

**Detection and characterization of DNA structural variants
in pediatric brain tumors using optical genome mapping**

Inaugural-Dissertation

zur Erlangung des Doktorgrades
der Mathematisch-Naturwissenschaftlichen Fakultät
der Heinrich-Heine-Universität Düsseldorf

vorgelegt von

Nadezhda Kubon, geb. Bogodukhova
aus Volzhsky

Düsseldorf, November 2025

Aus dem Institut für Neuropathologie
der Heinrich-Heine-Universität Düsseldorf

Gedruckt mit der Genehmigung der
Mathematisch-Naturwissenschaftlichen Fakultät der
Heinrich-Heine-Universität Düsseldorf

Berichterstatter:

1. Prof. Dr. Guido Reifenberger
2. Prof. Dr. Gunnar Klau

Tag der mündlichen Prüfung: 30.03.2026

Table of contents

Summary	I
Zusammenfassung	II
1 Introduction	1
1.1 Brain tumors	2
1.1.1 Medulloblastoma	3
1.1.1.1 WNT-activated medulloblastoma	6
1.1.1.2 SHH-activated medulloblastoma	6
1.1.1.3 Non-WNT/non-SHH (Group 3/4) medulloblastoma	9
1.1.2 Atypical teratoid/rhabdoid tumor	12
1.1.2.1 ATRT–TYR	15
1.1.2.2 ATRT–SHH	15
1.1.2.3 ATRT–MYC	16
1.2 Structural variants of DNA	16
1.2.1 Mechanisms of the formation of DNA structural variants	17
1.2.2 Classification of DNA structural variants	19
1.2.3 Detection of DNA structural variants	21
1.3 Aims of the thesis	23
2 Materials and Methods	24
2.1 Devices and software	24
2.2 Patient-derived tumor tissue and blood samples	25
2.3 Cell lines and culture conditions	27
2.4 CNS tumor classification by DNA methylation profiling	30
2.4.1 Copy-number variation analysis from DNA methylation array data	31
2.5 Bionano Optical Genome Mapping	32
2.5.1 Ultra-high molecular weight genomic DNA extraction from frozen cell pellets	34
2.5.2 Ultra-high molecular weight genomic DNA extraction from frozen blood samples	34
2.5.3 Ultra-high molecular weight genomic DNA extraction from solid brain tumor tissue samples	35
2.5.4 Genomic DNA quantifications and direct labelling and staining	36
2.5.5 Chip loading and data collection	36
2.5.6 Detection of structural DNA variants by optical genome mapping	37
2.5.6.1 Annotated Rare Variant Analysis	37
2.5.6.2 Annotated <i>De novo</i> Assembly Pipeline	37

2.5.6.3	Dual Variant Annotation Pipeline	38
2.5.7	Data analysis and visualization	38
2.6	RNA sequencing	39
2.6.1	Sample processing for RNA sequencing	39
2.6.2	RNA sequencing data processing, visualization and gene fusion calling	39
2.7	Targeted panel next generation sequencing	40
2.8	Immunohistochemistry	41
3	Results	42
3.1	Setup of the optical genome mapping workflow	42
3.1.1	Processing of different sample types and assessment of ultra-high molecular weight genomic DNA quantity	42
3.1.2	Assessment of optical genome mapping data quality and association with different sample types.....	48
3.2	Implementation and optimization of secondary optical genome mapping- based DNA copy number variation and structural variation analyses.....	56
3.2.1	Identification of DNA structural variants and copy number variants by optical genome mapping	57
3.2.1.1.	Analysis of the annotated Rare Variant Analysis results	57
3.2.1.2	Analysis of annotated <i>De novo</i> Assembly Pipeline results	61
3.2.2	Integration of DNA structural variants and copy number variants detected by optical genome mapping	62
3.3	Characterization of medulloblastoma cell lines and tumors.....	66
3.3.1	DNA methylation-based classification of medulloblastoma samples.....	66
3.3.2	OGM-based analysis of aneuploidies and global DNA copy number variants in medulloblastoma samples	66
3.3.3	Global copy number variation analysis of medulloblastoma samples derived from DNA methylation array data	69
3.3.4	OGM-based analysis of focal DNA copy number variants and structural variants in medulloblastoma samples	78
3.3.5	Identification of somatic DNA structural variants and copy number variation via the dual variant annotation pipeline	85
3.3.6	Identification and validation of novel gene fusions in medulloblastomas	87
3.4	Characterization of ATRT cell lines and tumors	95
3.4.1	DNA methylation-based classification of ATRT samples	95
3.4.2	Detection of aneuploidies and copy number variants by optical genome mapping in ATRT samples.....	95

3.4.3	Global copy-number variation analysis of ATRT samples based on DNA methylation array data	97
3.4.4	Identification of focal DNA copy number variants and structural variants in ATRT samples by optical genome mapping	100
3.4.5	Identification and validation of novel gene fusions in ATRT	105
4	Discussion.....	108
4.1	Evaluation of the optical genome mapping workflow and sample processing with regard to ultra-high molecular weight genomic DNA quantity and quality	108
4.2	Comparison of DNA copy number variant analysis by optical genome mapping versus EPIC array-based analysis	110
4.3	Evaluation of DNA structural variants and copy number variants in ATRT and medulloblastoma samples by optical genome mapping	114
7	References.....	129
8	Appendix.....	150
8.1	Abbreviations.....	150
8.2	Supplementary figures and tables	158
8.3	List of figures	218
8.4	List of tables	219
	Curriculum Vitae	III
	Acknowledgements	V
	Affirmation	VII
	Eidesstattliche Erklärung	VII

Summary

Medulloblastoma (MB) and atypical teratoid/rhabdoid tumor (ATRT), both malignant pediatric brain tumors, are classified into distinct subgroups/subtypes characterized by specific patterns of genetic and epigenetic alterations. In addition to single nucleotide variants (SNVs), larger structural variants (SVs) of DNA, including deletions, duplications, focal gene amplifications, translocations and inversions may contribute to ATRT and MB pathogenesis. However, comprehensive profiling for SVs is challenging, as established cytogenetic methods such as karyotyping and fluorescence *in situ* hybridization are limited by low sensitivity or restriction to detection of predefined SVs. Moreover, commonly used short-read gene panel or exome-wide next-generation sequencing may not reveal larger and complex SVs. To comprehensively characterize SVs in ATRT and MB, a novel technique for genome-wide SV detection was applied, namely optical genome mapping (OGM, Bionano Genomics®). OGM reliably detected genome-wide DNA copy number (CN) changes in ATRT and MB, as demonstrated by comparison to microarray-based DNA CN profiling. In addition, OGM allowed for the characterization of novel genomic alterations including chromosomal translocations, putative gene fusions and other SVs affecting cancer-associated genes as well as non-coding DNA segments, and revealed novel molecular alterations involved in ATRT and MB pathogenesis and tumor progression. Thus, OGM represents a promising novel approach for large-scale profiling of SVs in pediatric malignant brain tumors.

Zusammenfassung

Atypische teratoide und rhabdoide Tumoren (ATRT) und Medulloblastome (MB) sind maligne pädiatrische Hirntumoren, die nach unterschiedlichen und charakteristischen genetischen und epigenetischen Veränderungsmustern in verschiedene Subgruppen unterteilt werden. Neben Einzelnukleotidvarianten können größere strukturelle Genomvarianten (SVs), einschließlich Deletionen, Duplikationen, fokaler Genamplifikationen, Translokationen und Inversionen, zur Pathogenese von ATRT und MB beitragen. Während kleinere Variationen, die beispielsweise nur einzelne Nukleotide betreffen, durch Gen-Panel-basierte oder Exom- bzw. Genom-weite Next-Generation-Sequenzierung (NGS) mit hoher Präzision detektiert werden können, stellt die Erfassung größerer struktureller Variationen mittels „shortread“-basierter Sequenzieretechnologien eine methodische Herausforderung dar. Hingegen weisen die klassischen, etablierten zytogenetischen Verfahren wie Karyotypisierung und Fluoreszenz-*in-situ*-Hybridisierung (FISH) entweder eine geringe Sensitivität auf oder sind auf die Detektion vorab definierter SVs beschränkt.

Im Rahmen dieser Arbeit wurde zur Charakterisierung von SVs in ATRT und MB eine innovative und hochauflösende Methode zur genomweiten SV-Detektion, die optische Genomkartierung (OGM) von Bionano Genomics®, angewandt. Der Vergleich mit mikroarray-basierten DNA-Kopienzahlanalysen bestätigte, dass OGM zuverlässig genomweite Kopienzahlveränderungen in ATRT und MB detektiert. Darüber hinaus ermöglichte OGM die Identifizierung neuartiger genomischer Veränderungen, einschließlich chromosomaler Translokationen, potenzieller Genfusionen sowie weiterer SVs, die sowohl onkogene Treiber als auch nicht-kodierende genomische Regionen betrafen. Die erzielten Befunde lieferten neue Erkenntnisse zu den molekularen Mechanismen des Wachstums und der malignen Progression von ATRT und MB. Zusammenfassend lässt sich sagen, dass OGM einen vielversprechenden und innovativen Ansatz zum umfassenden und spezifischen Nachweis struktureller Genomvarianten in pädiatrischen Hirntumoren darstellt.

1 Introduction

Cancer is a group of diseases resulting from uncontrolled growth of abnormal cells, which develop through a combination of genetic factors and environmental influences^{1,2}. The abnormal proliferation and subsequent division of neoplastic cells leads to formation of cell clusters or tumors. Albeit originating from a progenitor cell that originally gives rise to a tumor, cancer development and progression occur gradually whereas neoplastic cell clones become malignant through the accumulation of genomic somatic mutations¹⁻³. The somatic mutations in proto-oncogenes and tumor suppressor genes drive oncogenesis through clonal expansion and selection for cells with progressive capability of proliferation and survival. The capacity to invade surrounding healthy tissues and organs, and eventually spread throughout the body via the blood or lymphatic systems into distant areas to form metastases, is the hallmark feature of malignant tumors¹⁻⁴.

Cancer may occur in different tissues of the body and is classified histologically, according to the type of tissue involved (carcinoma, sarcoma, myeloma, leukemia, lymphoma), or characterized based on the primary location of origin (e.g. skin, lung, breast, etc.)³. Most cancers develop later in life and their incidences increase markedly between the ages 50–85⁵. Thus, the increase of cancer incidence with age is consistent with the contemporary understanding of cancer development and progression, which describes cancer as a genetic disease resulting from accumulation and selection of mutations over the lifetime⁶. Indeed, with advances in genome sequencing technologies, large-scale genetic profiling studies have revealed different signatures of mutational processes and confirmed a particularly high mutational burden for adult cancers⁶⁻⁹. While the same molecular mechanisms that regulate aging also may be involved in the pathogenesis of cancer¹⁰, it cannot be considered an age-related disease alone^{11,12}. This consideration is particularly relevant for malignancies with an early onset as it is the case for childhood cancers. Global studies on different subtypes of pediatric neoplasms report relatively low mutational frequencies for single-nucleotide variants (SNVs), overall 14 times lower than in adult cancers, but relatively high prevalence of DNA structural variants (SVs)^{6,9,13-15}. In this context, different mechanisms leading to tumor initiation and formation of adult and pediatric cancers are acknowledged^{13,16,17}.

Generally, SVs are classified as large (≥ 50 bp) deletions, insertions, inversions, duplications and translocations and represent DNA losses, gains or rearrangements^{18,19}. SVs significantly contribute not only to inter-individual diversity of the human genome, but in case of translocations and more complex DNA rearrangements (e.g. chromothripsis, chromoplexy) also frequently result from genomic instability of cancer cells^{13,20-23}. In different tumor entities, SVs in cancer predisposition genes have been identified as driving events of

tumorigenesis^{8,17,24,25}. Consequently, a comprehensive landscape of genomic SVs may harbor reliable diagnostic relevance and therapeutic implications for a specific subset of pediatric tumors.

1.1 Brain tumors

Primary tumors of the central nervous system (CNS) originate in the brain or spinal cord and constitute less than 1.5% of all cancers annually diagnosed world-wide^{5,26}. At present, there are over 130 distinct CNS malignancies recognized and summarized in the fifth edition of the World Health Organization Classification of Tumors of the Central Nervous System (WHO CNS5)²⁷.

Traditionally, the WHO classification categorized clinically and biologically diverse CNS tumor types based only on their histological features²⁸. The grading ranged from benign tumors, which are curable if they can be surgically removed (CNS WHO grade 1), to highly malignant tumors that do not respond well to any available therapy (CNS WHO grade 4). Over the past decades, diagnostic characterization and classification of CNS tumors greatly improved due to comprehensive large-scale molecular genetic studies of brain tumor cohorts, including targeted genetic analyses as well as high-throughput molecular profiling, and the development of novel bioinformatics tools²⁸. This allowed for better understanding of the distinct clinical features, cellular behavior and molecular characteristics of the highly heterogeneous spectrum of CNS tumors^{27,28}. In 2018, one particular method, i.e., bead chip array-based DNA methylome profiling, has significantly advanced CNS tumor classification and has become a standard practice in daily CNS tumor diagnostics²⁹.

Nowadays, conventional and well-established histological and immunohistochemical methods are complemented by modern, orthogonal molecular techniques that are based on the analysis of genomic, epigenomic and transcriptomic tumor signatures. The integration of these sensitive and accurate methods has been found to reliably improve the diagnostic categorization and grading of CNS tumors (as implemented in WHO CNS5) as well as the risk stratification and treatment planning. The subsequent application of targeted therapies may reduce side effects and improve patient care and disease management in selected CNS tumor entities^{30,31}.

According to the recent data from 2019/2020 by the Association of Population-based Cancer Registries in Germany (GEKID) and the German Centre for Cancer Registry Data (ZfKD) at the Robert Koch Institute, about 7,000 new cases of malignant CNS tumors are diagnosed per year in Germany³². This accounts for an annual incidence³² rate of ~ 8.4/100,000 persons per year and coincides with data from different other countries²⁶. Although malignant primary CNS tumors are relatively rare in adults, they usually carry dismal prognosis and low survival rates³². In children and young adults however, primary CNS tumors represent the most common solid

tumors accounting for approximately 24% of all diagnosed cancers, and are the leading cause of cancer mortality in this age group (Figure 1)³³. The most commonly diagnosed pediatric CNS tumors are astrocytomas, in particular pilocytic astrocytomas (10.4%), intracranial and intraspinal embryonal tumors (3.9%), and ependymomas (1.5%)³³. Unlike many pediatric-type astrocytomas, which are typically slow growing, well-confined tumors of glial origin that are manageable by total resection and associated with a favorable prognosis (CNS WHO grade 1 or 2), the embryonal CNS tumors are very aggressive and classified as CNS WHO grade 4 even though some neoplasms carry a more favorable prognosis than others²⁷. The most common malignant embryonal CNS tumor, medulloblastoma (MB), and another highly malignant but even more rare embryonal CNS tumor, atypical teratoid/rhabdoid tumor (ATRT), are the subjects of this thesis and are addressed in more detail within the following paragraphs.

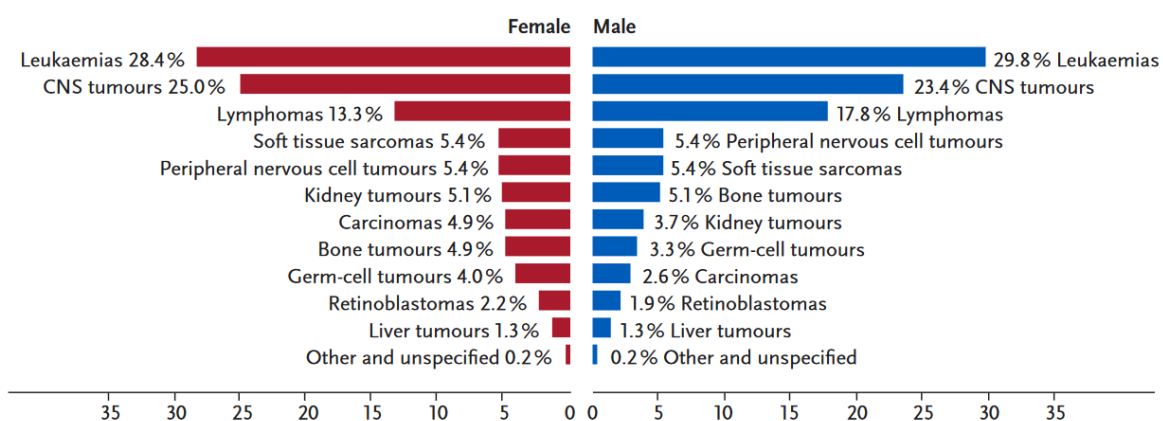


Figure 1. Most common tumors in childhood (< 18 years) of all cancer cases during the period of 2012–2021 in Germany. Adapted from “Cancer in Germany 2019/2020-Cancer in Children”³³.

1.1.1 Medulloblastoma

Medulloblastoma (MB), a malignant cerebellar tumor of embryonal origin (CNS WHO grade 4), is the most common malignant pediatric CNS tumor^{27,34}. It is commonly known to occur in childhood with a peak incidence at approximately 5 years of age, however, one quarter of all MB are documented in adults^{27,28}. MB more commonly affect males than females (ratio 1.8:1), and are typically aggressive and fast-growing tumors with a high metastatic potential by seeding of tumor cell via the cerebrospinal fluid (CSF)^{27,34,35}.

MB have the ability to spread from its primary site of origin and infiltrate cerebellar structures of the posterior fossa and the adjacent brain stem, and may disseminate via the CSF into the leptomeninges and the brain, while hematogeneous metastases to extraneural sites are rare²⁷. Originating from neuronal stem or progenitor cell populations during early neurogenesis of the cerebellum^{27,36,37}, the classic MB variant accounts for ~ 70% of all MB and is

histomorphologically characterized by densely packed sheets of poorly differentiated, highly proliferative tumor cells with sparse cytoplasm and hyperchromatic nuclei. The desmoplastic/nodular (D/N) MB variant, histologically characterized by the formation of reticulin-free nodular islands of more differentiated, less proliferative tumor cells within desmoplastic tumor areas with reticulin formation and poorly differentiated, highly proliferative tumor cells, contributes to approximately 15% of all MB^{27,38}. The least common but most aggressive type of MB, the large-cell anaplastic (LCA) MB, demonstrates anaplastic features upon histology, including tumor cells with enlarged nuclei of irregular size and shape, prominent nucleoli, and frequent nuclear molding. LCA MB also presents with high mitotic and apoptotic activity and may exhibit large necrotic regions^{27,39}.

Based on distinct DNA methylation and gene expression profiles, four molecular MB groups were originally identified: MB WNT-activated, MB SHH-activated, MB Group 3 and MB Group 4^{27,40}. To date, however, the classification of MB developed beyond the four principal molecular groups presenting a broader spectrum of MB subtypes with a high level of intragroup heterogeneity with respect to clinical phenotype and behavior. Genome-wide transcriptional- and methylation profiling together with novel bioinformatic approaches improved MB tumor classification, enabling further segregation of MB subgroups within the pre-defined molecular groups⁴¹⁻⁴⁴. Overall, there are 2 subgroups of MB WNT, 4 subgroups of MB SHH and 8 subgroups within the MB non-WNT/non-SHH Group 3/4⁴¹⁻⁴⁴. MB thus represents a highly heterogeneous disease entity with different molecular subgroups that can be linked to diverse clinical manifestation, prognosis and outcome⁴⁵.

The diagnosis of MB is currently based on clinical assessment and magnetic resonance imaging (MRI) where MB are visualized as a solid mass in the posterior fossa. The extent of disease and patients' age at diagnosis greatly affects the treatment plan and therefore the control of MB. Thus, patients are stratified into average-risk and high-risk groups, as summarized in Figure 2. The first-line treatment for all MB patients is the maximal safe surgical resection of the tumor⁴⁶. The amount of residual tumor after surgery is considered an important prognostic factor. The average-risk patients with MB present less than 1.5 cm² post-operative residual tumor and no metastatic dissemination at the time of diagnosis⁴⁶. In contrast, high-risk MB patients either already present metastatic lesions at the time of diagnosis or/and more than 1.5 cm² post-operative residual tumor⁴⁶. The subsequent histological and molecular examination performed on the excised tumor tissue enables specific tumor and molecular group classification, risk stratification and therapy planning⁴⁶. Utilizing the cumulative diagnosis of clinical and biological parameters, the subsequent standard of care treatment of MB may include adjuvant chemotherapy, alone or in combination with craniospinal irradiation (CSI).

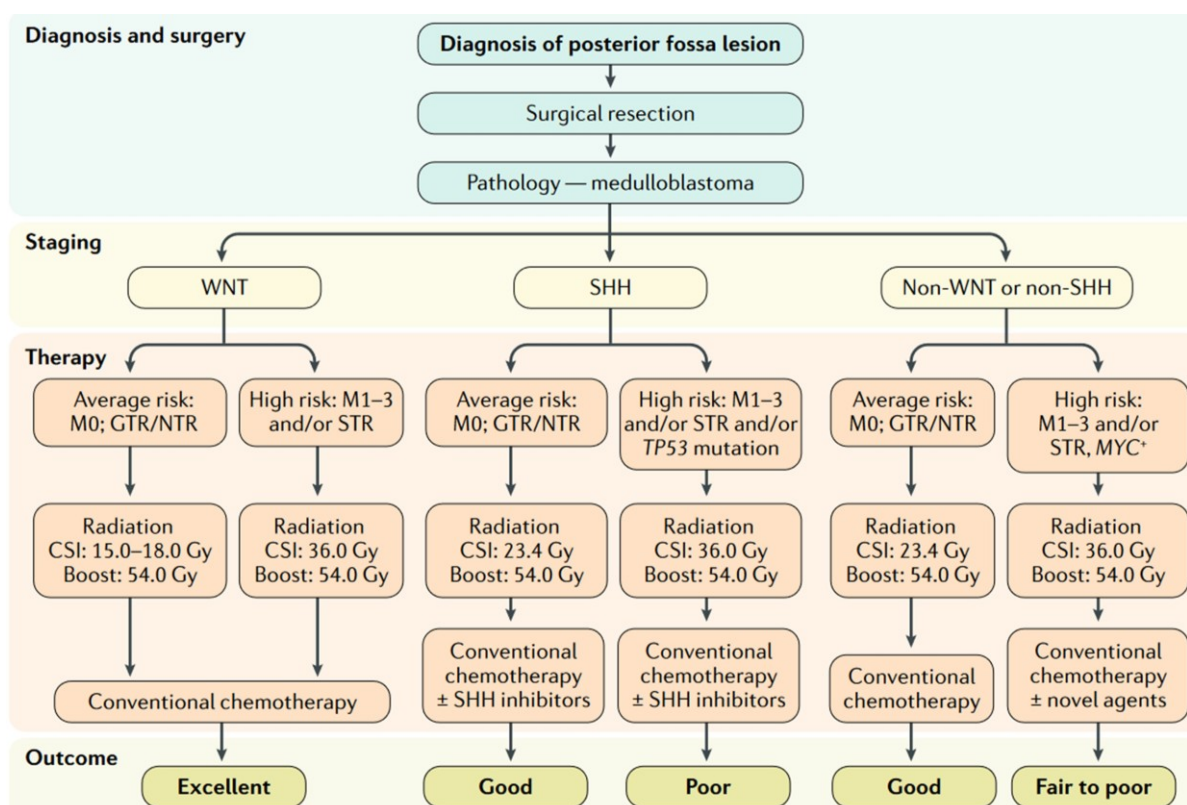


Figure 2. Current standard clinical management scheme for medulloblastoma patients. *M0*, no metastatic evidence; *M1–3*, grades of metastatic presence according to the Chang⁴⁷ staging system. *GTR*, gross total resection; *NTR*, near-total resection; *STR*, subtotal resection. Figure adapted from Northcott *et al.*³⁵.

Unfortunately, numerous adverse side effects of this extensive therapy may lead to lifelong sequelae diminishing the patients' quality of life. Even in remission, survivors may face chronic treatment-related medical conditions, impairments in neurocognitive and neuroendocrine function and low physical fitness and independence⁴⁶. Thus, optimal treatment protocols for young patients diagnosed with MB rely on maximal safe neurosurgery accompanied by chemotherapy ideally avoiding CSI to preserve as many aspects of patients' quality of life as possible⁴⁶. This optimized treatment strategy has led to 5-year survival rates over 70% for average-risk and over 50% for high-risk group patients^{44,48}. However, long-term survival rates after relapse are exceedingly low. Many joint initiatives have set the common objective to advance survival and quality of life outcomes for children with MB and other childhood CNS tumors⁴⁹. Promising modern clinical trials and novel precision medicine-based treatment strategies are co-evolving with the improved classification of the disease⁴⁶. The highly complex combination of the inter- and intragroup heterogeneity of MB in association with the intra- and inter-patient heterogeneity emphasizes the urgent need for individualized therapy.

1.1.1.1 WNT-activated medulloblastoma

Tumors of the WNT group constitute ~ 10% of all MB and typically occur in older children and young adults with a slight predominance in females²⁷. WNT-activated MB originate from the dorsal brainstem, are rarely metastatic and present a favorable long-term prognosis when treated with standard therapy protocols leading to survival rates above 90%. The vast majority of all MB WNT display a classic MB histology⁵⁰. Although MB WNT have been described to present low inter-patient heterogeneity with respect to their morphological and molecular features, two molecular subtypes, WNT- α and WNT- β , are distinguished (Figure 3). Both subtypes have been documented to differ in the age at diagnosis (median age of 10 vs. 20 years, respectively) and the frequency of chromosome (chr) 6 monosomy, which is the signature chromosomal alteration of the MB WNT group present in up to 90% of all cases^{34,42}. Albeit having the second highest burden of somatic genome-wide SNVs of all MB groups, other prominent large-scale chromosomal copy number alterations (CNAs) are very uncommon in MB WNT⁵¹.

While commonly mutated genes in MB WNT include *TP53*, *SMARCA4*, *KMT2D* and *DDX3X*, the hallmark genetic feature observed in ~ 90% of MB WNT cases consist of somatic activating mutations in exon 3 of the *CTNNB1* gene (encodes Catenin Beta 1)⁴². These mutations lead to formation of a degradation-resistant form of β -catenin, which in turn induces the eponymous constitutional activation of the WNT signalling pathway. In cases when MB WNT lack activating *CTNNB1* mutations, pathogenic loss-of-function mutations in the *APC* gene are typically detected⁴². These alternative and less frequent genomic alterations ultimately lead to the same result – the prevention of APC-dependent degradation of Catenin beta-1.

1.1.1.2 SHH-activated medulloblastoma

The SHH group constitutes ~ 30% of all MB and is twice as frequent in males than females²⁷. MB SHH predominantly arise in the cerebellar hemispheres. Histologically, classic and desmoplastic/nodular (D/N) variants occur at similar frequencies, both contributing to ~ 40% of cases, and the LCA variant makes up the remaining cases^{34,50}. MB SHH display a bimodal age distribution upon diagnosis. It represents the most common MB group in infants (< 4 years) as well as in adults (> 16 years) with only a small proportion of cases diagnosed during childhood (3–16 years)³⁴.

While the majority of all MB SHH either harbor germline or somatic mutations and copy number alterations in critical genes of the eponymous SHH signalling pathway (*PTCH1*, *SUFU*, *SMO*, *GLI1*, *GLI2*), infant, childhood and adult MB SHH represent clinically and biologically distinct MB subgroups with high levels of inter-tumoral heterogeneity (Figure 3). Thus, the prognosis

for patients with MB SHH is strongly associated with the molecular subgroup and dependent on the underlying genetic alterations^{44,51,52}.

The general landscape of somatically altered genes in MB SHH includes, among SHH-related genes, components for signal transduction (*PTEN*, *TERT*), chromatin modifiers (*KMT2C*, *KMT2D*, *CREBBP*, *KANSL1*) and transcriptional regulators (*MYC*, *MYCN*)^{42,52}. Frequent large-scale chromosomal alterations are also commonly found in MB SHH including loss of chr9q (*PTCH1* location), chr10q (*SUFU* location), chr14q, and chr17p, and gains of chr2 and chr9p^{42,53}.

Two distinct tumor subgroups, SHH- β and SHH- γ (equivalent to iSHH-I and iSHH-II), have been identified among infant MB SHH^{41,44}. Both subgroups display different cytogenetic features and therefore different outcomes. MB SHH- β are frequently metastatic, present focal amplifications, gain of chr2 and loss-of-function mutations or deletions in *SUFU* and *PTEN*, and are found in the youngest patients⁴¹. The long-term prognosis for patients with this MB subtype is unfavourable, as indicated by 5-year survival rates of $\sim 27\%$ ^{41,54}. SHH- γ tumors, however, present comparably high 5-year survival rates ($\sim 75\%$)⁵⁴ and are enriched for mutations in *SMO* and *KMT2D*^{41,42}. Within this subgroup, a rare histologic variant, namely, medulloblastoma with extensive nodularity (MBEN) is documented, which was found to present a more clinically indolent behaviour⁵⁵. In contrast to the infantile tumors, the SHH- δ subgroup is predominantly found in adults (median age of 26 years)⁴¹. Patients with SHH- δ generally exhibit a higher burden of genome-wide SNVs compared to younger patients with MB SHH^{34,51}. Almost all diagnosed cases of adult SHH- δ ($\sim 98\%$) contain somatic *TERT* mutations and over 80% have alterations in either *PTCH1* or *SMO*^{41,52}. The last distinct subgroup, SHH- α , mainly occurs in children and is enriched for patients harboring loss-of-function *TP53* mutations^{41,56}. The *TP53*-mutant SHH tumors are associated with particularly high-risk disease⁵⁶ and dismal prognosis due to chromothripsis-driven oncogenic amplification of *MYCN*, the dysregulation of which is known to strongly contribute to tumor initiation, maintenance and progression⁵⁷. Additional gene amplifications affecting in *GLI1*, *GLI2* or *YAP1* are documented^{41,52}. These tumors tend to exhibit resistance to standard therapy protocols, thus, radical, high-risk treatment protocols have to be implemented. Correspondingly, these tumors are considered as a distinct molecular subtype of MB referred to as "Medulloblastoma, SHH-activated and TP53-mutant"²⁷.

Group		WNT		SHH			
Subgroup		WNT α	WNT β	SHH α	SHH β	SHH γ	SHH δ
Subgroup proportion							
Subgroup relationship							
Clinical data	Age						
	Histology			LCA Desmoplastic	Desmoplastic	MBEN Desmoplastic	Desmoplastic
	Metastases	8.6%	21.4%	20%	33%	8.9%	9.4%
	Survival at 5 years	97%	100%	69.8%	67.3%	88%	88.5%
Copy number	Broad	6 ⁻		9q ⁻ , 10q ⁻ , 17p ⁻		Balanced genome	
	Focal			MYCN amp, GLI2 amp, YAP1 amp	PTEN loss		10q22 ⁻ , 11q23.3 ⁻
Other events				TP53 mutations			TERT promoter mutations

Age (years): 0-3 >3-10 >10-17 >17

Figure 3. Overview of the MB WNT and MB SHH groups. The MB WNT group consists of two subgroups, WNT-α and WNT-β, whereas the MB SHH group is subdivided into four subgroups, SHH-α, SHH-β, SHH-γ, and SHH-δ. The distinct MB subgroups are summarized by clinico-demographic and molecular features. The age groups are: infant, 0–3 years; child, > 3–10 years; adolescent, > 10–17 years; adult, > 17 years. *LCA*, large cell anaplastic; *MBEN*, medulloblastoma with extensive nodularity. Figure adapted and modified from Cavalli *et al.*⁴¹.

1.1.1.3 Non-WNT/non-SHH (Group 3/4) medulloblastoma

MB devoid of a molecular signature associated with activation of WNT or SHH pathway signalling are summarized under the term "Medulloblastoma, non-WNT/non-SHH" in the CNS5 WHO classification²⁷ and include the Groups 3 and 4 of MB. As determined by DNA methylation profiling, the "MB non-WNT/non-SHH" spectrum can be further characterized into eight molecular subgroups (IV–III)⁴³, associated to MB Group 3 (II, III, IV), MB Group 4 (VI, VIII) and a group with mixed MB Group 3/4 characteristics (I, V, VII) (Figure 4).

Mostly located in the midline and expanding into the fourth ventricle, these tumors frequently present metastatic spread into distant areas of the CNS at time of diagnosis. Depending on the combination of clinical and genetic factors at time of diagnosis, patients are stratified as standard or extremely high-risk with intermediate (< 80%) and low overall survival rates (< 60%), respectively^{44,48}. While MB Group 3/4 commonly demonstrate classic morphology, depending on the subtype, large-cell anaplastic (LCA) variants and very rarely desmoplastic/nodular (D/N) variants are also documented^{43,53}. Cytogenetically, MB Group 3/4 are predominantly characterized by high frequencies of isochromosome (isochr) 17q observed across most subtypes⁵³. Additionally, aneuploid karyotypes with (partial) losses and/or gains of different chromosomes are common in MB Group 3/4^{43,53}. Thus, these tumors are considered to be mainly driven by copy number aberrations.

1.1.1.3.1 Group 3 medulloblastoma

Group 3 tumors comprise ~ 25% of all MB and typically occur during infancy and early childhood with twice as high prevalence in males compared to females²⁷. Considered the most aggressive MB group, Group 3 tumors frequently present high prevalence of metastatic dissemination at time of diagnosis contributing to a 5-year overall survival of only < 60%⁴⁸. MB Group 3 are rare in adults.

While the landscape of genes demonstrating recurrent alterations in MB Group 3 is relatively sparse⁴², somatic high-level amplification of the proto-oncogene *MYC* is recognized as the hallmark copy number abnormality that is found in ~ 17% of MB Group 3^{43,53}. Aberrant activation of *MYC* regulates multiple cellular pathways in a pro-tumorigenic manner thereby strongly affecting mRNA processing, protein translation and cell cycle progression, and represents a molecular indicator of high-risk disease comparable to the *TP53*-mutant MB SHH^{41,43,56}. Additional somatic gene level amplifications in MB Group 3 may affect the paralog, *MYCN*⁵⁸, and the master transcription factor in neurodevelopment, *OTX2*⁵⁹. Another common feature found in ~ 15% of MB Group 3 is the hyper-activation of transcriptional repressors, *GFI1* and its paralog *GFI1B*, by a mechanism called enhancer hijacking⁶⁰. The repositioning of either *GFI1* or *GFI1B* next to active enhancer or super-enhancer elements, which results from

distinct patterns of somatic structural rearrangements, was shown to induce their overexpression, thereby promoting oncogenic activity⁶⁰. Otherwise, most MB Group 3 tumors present extensive aneuploidy and are enriched for recurrent chromosomal copy number abnormalities, including isochr17q, gains of chr1q and chr7, as well as losses of chr8, chr10, chrX and chr16q^{41,43}.

1.1.1.3.2 Group 4 medulloblastoma

Group 4 represents the most abundant group, accounting for up to 40% of all MB cases²⁷. Commonly occurring during adolescence, MB Group 4 tumors are approximately three times more likely to develop in males than females⁴³. Although regarded as intermediate in terms of survival, one third of patients present metastases at time of diagnosis^{27,43}. Comparable to the genetic landscape of MB Group 3, recurrent somatic gene mutations are also relatively sparse in MB Group 4⁴². The putative driver gene with the highest prevalence, as detected in ~ 17% of MB Group 4 cases, is *PRDM6*, encoding a transcriptional repressor implemented in chromatin modification^{42,53}. Other less commonly mutated genes, *KDM6A* (7%), *ZMYM3* (6%), and *KMT2C* (6%), also belong to the group of chromatin modifiers⁴². These findings suggest a role of epigenetic dysregulation in tumorigenesis of MB Group 4. Aside from somatic mutational changes, many copy number alterations and large-scale chromosomal aberrations are found in MB Group 4. Gene amplifications of *MYCN*, *OTX2* and *CDK6* are documented in small proportions of cases, the latter found exclusively in MB Group 4 but not in any other MB subgroup^{42,43}. Similar to many MB Group 3, the most common cytogenetic aberration is the formation of isochr17q and high prevalence of chrX monosomy in female patients^{42,43}. Otherwise, losses of chr8, chr10, chr11, and chr17q, as well as gains of chr4, chr7, and chr19 are also observed, albeit less frequently⁴¹⁻⁴³.

























Group		Group 3						Group 4	
Subgroup		1	2	3	4	5	6	7	8
Demographics	Frequency	3-5%	10-15%	10-15%	8-10%	8-10%	8-10%	15-20%	25-28%
	Age								
	Sex	♂♂♂ ♀♀	♂♂♂ ♀	♂♂♂ ♀	♂♂ ♀	♂♂♂ ♀	♂♂ ♀	♂♂ ♀	♂♂♂ ♀
Clinical features	Histology	Classic	LCA, Classic	Classic > LCA	Classic	Classic	Classic > LCA	Classic	Classic
	Metastasis								
	5-year OS	~75%	~55%	~45%	~85%	~60%	~80%	~85%	~75%
Molecular features	Cytogenetics	 balanced	 8+ 1q+ i17q	 7+ i17q 10q- 16q-	 14+ 7+ 8- 10- 11- 16-	 7+ i17q 16q-	 7+ i17q 8- 11-	 7+ i17q 8-	 i17q
	Driver events	<i>GF11/GF11B</i> activation <i>OTX2</i> amplification	<i>MYC</i> amplification <i>GF11/GF11B</i> activation <i>KBTBD4</i> , <i>SMARCA4</i> , <i>CTDNEP1</i> , <i>KMT2D</i> mutation	<i>MYC</i> , <i>MYCN</i> amplification	Unknown	<i>MYC</i> , <i>MYCN</i> amplification	<i>PRDM6</i> activation <i>MYCN</i> amplification	<i>KBTBD4</i> mutation	<i>PRDM6</i> activation <i>KDM6A</i> , <i>ZMYM3</i> , <i>KMT2C</i> mutation

Figure 4. Overview of the complex spectrum of MB, non-WNT/non-SHH, Group 3/4. Schematic representation of demographics, key clinical and molecular features for the eight subgroups (I–VIII) of Group 3/4 medulloblastoma. LCA, large cell anaplastic. Adapted from Ellison and Taylor²⁷.

1.1.2 Atypical teratoid/rhabdoid tumor

Atypical teratoid/rhabdoid tumor (ATRT) is a rare and aggressive embryonal CNS tumor (CNS WHO grade 4) accounting for 1–2% of all pediatric brain malignancies²⁷. Predominantly occurring early in life, it affects infants and young children with ~ 90% of cases reported before 3 years of age and documented slightly more frequently in males than females^{27,61}. ATRTs are fast growing and invasive tumors that commonly spread via the CSF and metastatic dissemination is found in approximately one third of patients at initial presentation^{61,62}. Thus, the prognosis for patients with ATRTs is reported as particularly poor, with a 3-year overall survival (OS) of ~ 25%^{61,62}.

Albeit being highly malignant, ATRTs display remarkably simple and balanced genomes. The main and often only recurrent genetic event occurring in > 95% of ATRT cases is a biallelic inactivation of the *SMARCB1* gene, caused by either loss-of-function mutations or larger structural variants leading to a partial or complete loss of chr22^{63–65}. Alongside somatic alterations in *SMARCB1*, germline *SMARCB1* mutations are also documented in up to 30% of ATRT patients, who suffer from the rhabdoid tumor predisposition syndrome 1 (RTPS1), and thus may present rhabdoid tumors synchronously in more than one location^{66–68}. In rare ATRT cases (< 5%) that lack deleterious alterations in *SMARCB1*, inactivating mutations in *SMARCA4* are detectable⁶⁹. Both, *SMARCB1* and *SMARCA4*, are essential components of the ATP-dependent chromatin remodelling SWI/SNF complex, which regulates the presence and positioning of nucleosomes on DNA, allowing binding of transcription factors, enhancers and other regulatory elements^{70–72}. Intact SWI/SNF complexes are macromolecular assemblies containing multiple different subunits that enable combinatorial assembly and context-specific functional implication, such as transcription, lineage specification and cell differentiation. Generally, human SWI/SNF complexes consist of a single ATPase, either *SMARCA2* or *SMARCA4*, three core subunits, *SMARCB1*, *SMARCC1*, and *SMARCC2*, and seven variable subunits^{70–72}. Thus, disruption of protein formation of a single subunit, particularly the ATPase or the core unit, changes the composition of the SWI/SNF complex and alters its' functionality. At least nine distinct SWI/SNF subunits have been documented to harbour recurrent mutations and are found in more than 20% across various cancer types⁷².

Although *SMARCB1* loss is a nearly universal feature presenting the only common genetic tumorigenic event across largely uniform ATRT genomes, multiple studies have revealed remarkable differences in ATRT biology. Distinct transcriptomic and epigenetic landscapes of ATRTs have reinforced the concept of three molecular ATRT subtypes (Figure 5)^{73–76}. Based on this consensus, the WHO recognizes three ATRT subtype that depend on cellular and molecular context with different implications on prognosis and therapy: ATRT–TYR, ATRT–SHH, ATRT–MYC^{27,28}.

Clinically, ATRT is indistinguishable from MB or from other types of embryonal CNS tumors. Thus, like with other CNS tumors, the diagnosis of ATRT begins with MRI and staging, and depends on the location, spread and the age of the patient²⁷. The first-line treatment for ATRT patients, if feasible, is the maximal safe surgical resection of the tumor⁶¹. The subsequent histological and molecular examination performed on the biopsy enables specific tumor and subtype classification.

Typically composed of rhabdoid cells intermixed with variable components of primitive neuroectodermal, mesenchymal, and epithelial cells, ATRTs present as a large heterogeneous mass that can originate in any compartment of the CNS⁷⁷. Due to the aggressiveness, invasiveness and heterogeneity of localization and size of ATRTs, no definite standard-of-care treatment is available at present. The implemented therapeutic strategies for ATRTs generally include intensive multimodality regimens combining CSI with chemotherapy consisting of various drug combinations or single agents⁷⁸⁻⁸⁰. Although the multimodal approaches have significantly improved the patients' survival rates, the toxic side effects of the treatment remain substantial and most children succumb to the long-term complications of the therapy. Thus, the largely dismal prognosis and the rarity of ATRT still facilitates the need for both, novel trials and personalized therapy approaches.

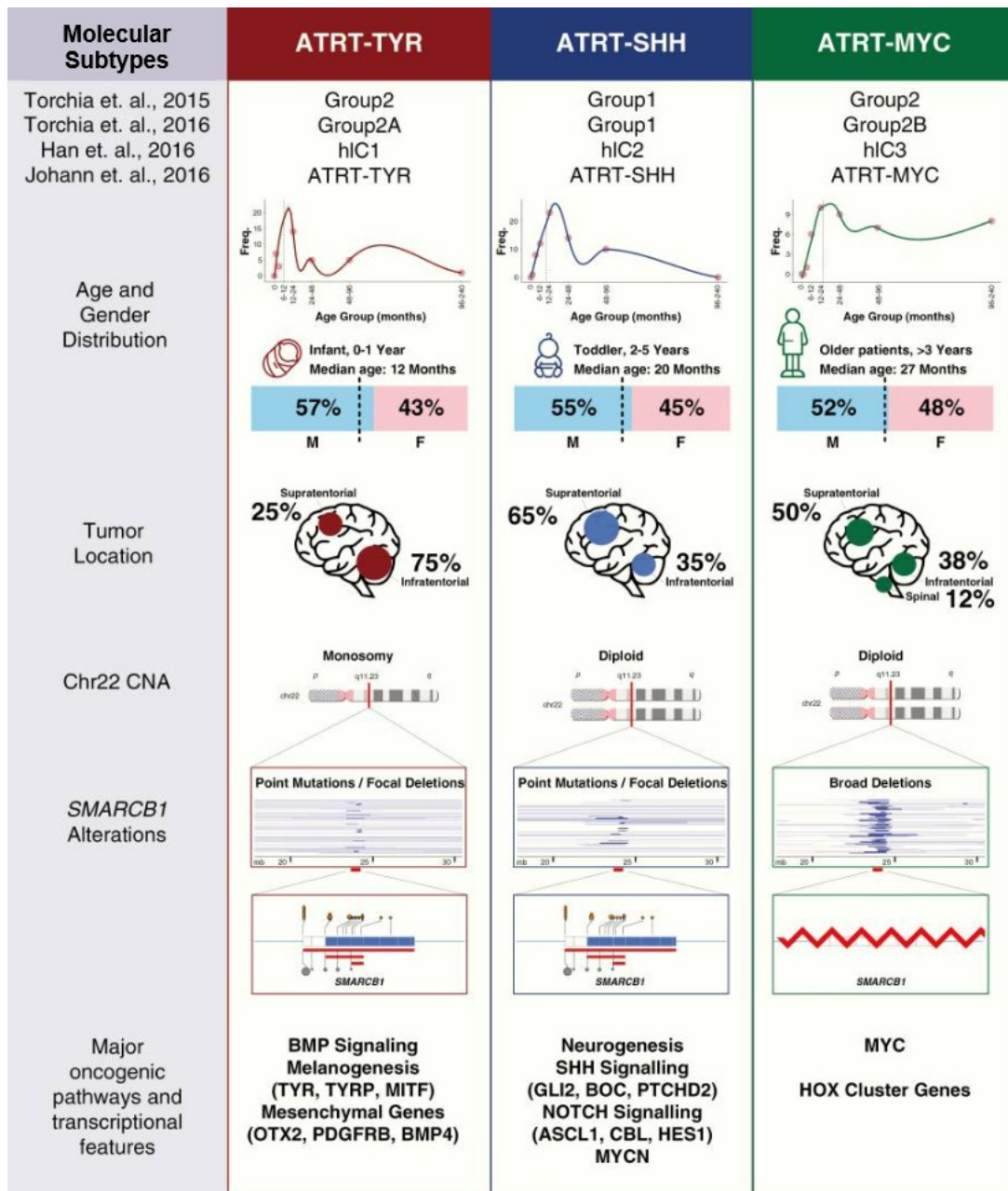


Figure 5. Overview of ATRT molecular subtypes. Three molecular ATRT subtypes are recognized: ATRT-TYR, ATRT-SHH and ATRT-MYC. The distinct subtypes are summarized by clinico-demographic and molecular features. Figure adapted and slightly modified from Ho *et al.*⁷⁶.

1.1.2.1 ATRT–TYR

The ATRT–TYR molecular subtype constitutes ~ 34% of all ATRT and typically presents in infants (≤ 1 years of age) with a slightly higher prevalence in males than females^{73,75}. ATRT–TYR patients older than 1 year were reported to have the best overall prognosis compared to patients with one of the other molecular ATRT subtypes⁸¹. ATRT–TYR commonly arises in the infratentorial brain compartment, although supratentorial localization is documented in 25% of cases⁷⁶.

Eponymous for this subtype is the enzyme tyrosinase (TYR), which catalyses the biosynthesis of melanin and is characteristically overexpressed in most ATRT–TYR cases, but specifically not in other subtypes of ATRTs⁷⁶. Alongside the upregulation of melanosomal pathways due to overexpression of melanosomal markers TYR, TYRP, MITF and DCT^{73,75,76}, the ATRT–TYR is also defined by upregulation of BMP, OTX2, FGFR2 and JAK-STAT pathways^{75,76,82}. Genetically, ATRT–TYR is primarily characterized by *SMARCB1* inactivation due to whole chromosome or partial loss of one copy of chr22 accompanied by an inactivating *SMARCB1* mutation on the second allele⁷⁶. Comprehensive epigenome analyses revealed signatures of global hypermethylation for ATRT–TYR cases compared to other brain tumors and healthy cerebellum⁷⁵. The particular pattern of promoter hypermethylation was indeed found to induce silencing and downregulation of several tumor-suppressor genes⁷⁵. Furthermore, ATRT–TYR-specific (super-)enhancer landscapes and transcription factors (TFs), such as OTX2 and MITF, and their gene targets *TYR*, *DCT* and *CCND1*, were defined⁷⁵.

1.1.2.2 ATRT–SHH

The ATRT–SHH represents the most abundant and heterogeneous molecular subtype of ATRT, accounting for up to 44% of all ATRT cases^{73,76}. Typically occurring in slightly older infants with a median age of 20 months at diagnosis, these tumors present either in supratentorial or infratentorial locations. Recent studies based on DNA methylation profiling facilitated further segregation within the ATRT–SHH subtype, whereas ATRT–SHH–I was shown to occur mostly supratentorially and ATRT–SHH–II mainly correlated with infratentorial localization⁸³.

SHH and NOTCH pathway members like BOC, GLI1, MYCN and PTCH1 (all SHH pathway members), and ASCL1, DTX1 and HES1 (all NOTCH pathway members) are typically overexpressed in ATRT–SHH^{73,75,76}. Most cases of ATRT–SHH display either biallelic inactivating point mutations or focal aberrations in *SMARCB1*⁷⁶. Compared to ATRT–TYR, ATRT–SHH harbors signatures of global hypermethylation and display the highest differences in DNA methylation compared to other brain tumors and healthy cerebellum⁷⁵. ATRT–SHH subtype-specific targets of enhancers are *GLI2*, *PTCH2*, *FOXK1*, *SOX11* and *MN1*⁷⁵.

1.1.2.3 ATRT–MYC

Occurring commonly during late infancy but also during childhood and adolescence (median age: ~ 27 months), ATRT–MYC comprise ~ 22% of all ATRTs^{73,76}. Approximately half of these tumors are localized supratentorially, however, some also arise infratentorially and rare cases are even of spinal origin⁷⁵.

Named after the aberrant, elevated expression of the proto-oncogene *MYC*, this molecular subtype of ATRTs also presents overexpression of several *HOXC* cluster genes^{75,76}. The overall common signature of *SMARCB1* inactivation in ATRT–MYC results from broad, homozygous deletions spanning several megabase pair (Mbp) around the genomic region of *SMARCB1*, thereby also affecting multiple neighbouring genes⁷⁵. In contrast to the global hypermethylation of ATRT–TYR and ATRT–SHH, epigenetic analyses found genome-wide CpG methylation levels in ATRT–MYC tumors to be more comparable to those in other brain tumors⁷⁵. Additionally, subtype-specific targets of enhancers include *HMGA2* and *HOXC9*, while *CEBPB*, *RARG* and *MYC* were identified as subtype-specific transcription factor-binding sites (TFBSs)⁷⁵.

1.2 Structural variants of DNA

Mutations that arise in somatic cells not only contribute to inter-individual diversity of the human genome but can also drive oncogenesis^{6,9}. Somatic mutations comprise single-nucleotide variants (SNVs) and insertions/deletions (indels) of a few nucleotides as well as large copy number variants (CNVs) and structural variants (SVs)⁸⁴. SVs are events of genomic rearrangements that alter chromosomal material through deletion, amplification or reorder of DNA at scales ranging from short genomic regions affecting at least 50 nucleotides (≥ 50 bp), to aneuploidies affecting whole chromosome arms (p/q) or even entire chromosomes^{18,19}.

Due to their size, SVs have a greater impact on nucleotide sequence differences than SNVs, on average accounting for 1% and 0.1% variability of the human genome, respectively^{85,86}. Although most alterations in nucleotide sequence represent shared variants and polymorphisms without functional impact⁸⁷, they can also influence phenotype through various mechanisms. In particular, large SVs can alter the intricate 3D-arrangement of the chromatin, thereby affecting the interactions of the genome, epigenome and proteins in a temporal and spatial manner^{88,89}. The mechanisms hereby occur through SV-mediated change of DNA dosage or through change of the DNA position⁹⁰. This effect can be of particular importance in genomic disorders that present an otherwise low mutational burden, such as pediatric malignancies.

Overall, multiple previous studies have highlighted the importance of SVs in the biology of various genetic diseases^{85,91–94}, and chromosomal aneuploidies are a longstanding genomic feature in heritable syndromes^{95,96}. Also in cancer genomes, SVs caused by genomic instability are frequent^{85,97–99}. Nevertheless, SVs have received less attention compared to SNVs, primarily because they are much more difficult to identify and interpret.

1.2.1 Mechanisms of the formation of DNA structural variants

While the mechanisms underlying the formation of SVs are intricate, in essence they involve different patterns and combinations of DNA breakage and re-joining (Figure 6)^{19,25,100}. Thus, the SVs themselves are junctions connecting two break-ends within the genome which can arise from natural processes of DNA recombination, DNA replication or DNA damage repair^{101,102}. Three primary mechanisms have been acknowledged for genomic rearrangements in the human genome (Figure 6): non-allelic homologous recombination (NAHR), non-homologous end-joining (NHEJ), as well as Fork Stalling and Template Switching (FoSTeS)^{100,102,103}.

During repair of genomic double-strand breaks (DSBs) in chromosomes, a template of DNA is used to restore the damaged region and seal the break ends. When a unique region is affected by a DSB, the mechanism of allelic homologous recombination (AHR) implements the same allelic region on the sister chromatid as the template, which is a nearly exact copy of the DNA altered by the DSB. However, DSBs occurring near or within repetitive regions can facilitate NAHR utilizing non-allelic but highly homologous regions of various origins as the repair template^{100,102}. Thus, many genomic rearrangements can result from NAHR-mediated DNA repair between two flanking low-copy repeats (LCRs) or two segmental duplications (SDs)^{88,100}. Consequently, the genomic region flanked by either LCRs or SDs is prone to genomic rearrangements. Despite seemingly distinct terminology, LCRs and SDs essentially represent the same structural events: they are DNA segments of at least 1 kilobase pair (kbp) in size that share sequence similarity (homology) of > 95%, constituting approximately 5% of the human genome^{104,105}. LCRs are usually located near chromosomal centromeres or telomeres¹⁰⁶ and they can contain fragments or series of genes, pseudogenes and endogenous retroviral or paralogous fragments¹⁰⁰. Due to the high degree of sequence similarity between two LCRs, erroneous assembly of homologous sequences can lead to misalignment of chromosomes or chromatids leading to a subsequent crossover. If the crossover event implements non-allelic homologous regions, it can cause either duplication or deletion of the genomic segment between the two directly oriented LCRs^{100,102}. However, misalignment between LCRs of opposite orientation results in inversions of the genomic segment flanked by them. Overall, the misalignment enabling NAHR strongly depends on the degree of LCR homology, the length of the LCR sequences, the distance between and the orientation of the implicated LCRs^{90,100}. The

same LCR pairs can also facilitate both mitotic and meiotic NAHR^{98,107,108}, and many large LCRs co-localize with large genomic regions that are prone to rearrangements and are associated with genomic disorders^{88,104}. Indeed, LCR/NAHR-mediated rearrangements are often observed within the same genomic segments among different individuals and are therefore considered shared, recurrent SVs^{87,100,101}.

In contrast to NAHR, other mechanisms, such as NHEJ and FoSTeS, maintain DNA repair in a nearly non-homologous manner and are commonly known to facilitate non-recurrent SVs^{109,110}. The DSB repair by NHEJ necessitates modification of DNA break-ends, which induces addition or cleavage of nucleotides to or from the ends, prior to direct ligation of DNA strands^{109,111}. Thus, the modification process at the DSB site can leave an imprecise NHEJ signature whereas the junctions can include microhomologies or small insertions^{110,111}. FoSTeS, on the other hand, is responsible for formation of non-recurrent SVs of higher complexity¹¹⁰. This model was proposed by Lee *et al.*¹¹⁰ and describes an event during DNA replication whereas the bare single-stranded DNA forms an intramolecular secondary structure upon absence of the repair template. Subsequently, the secondary structure physically inhibits the progression of the replication fork (“fork stalling”) leading to release and invasion of the actively replicated strand into another replication fork with the same microhomologies. This event can occur consecutively, juxtaposing and merging sequences from different genomic regions thereby generating complex SVs¹¹⁰.

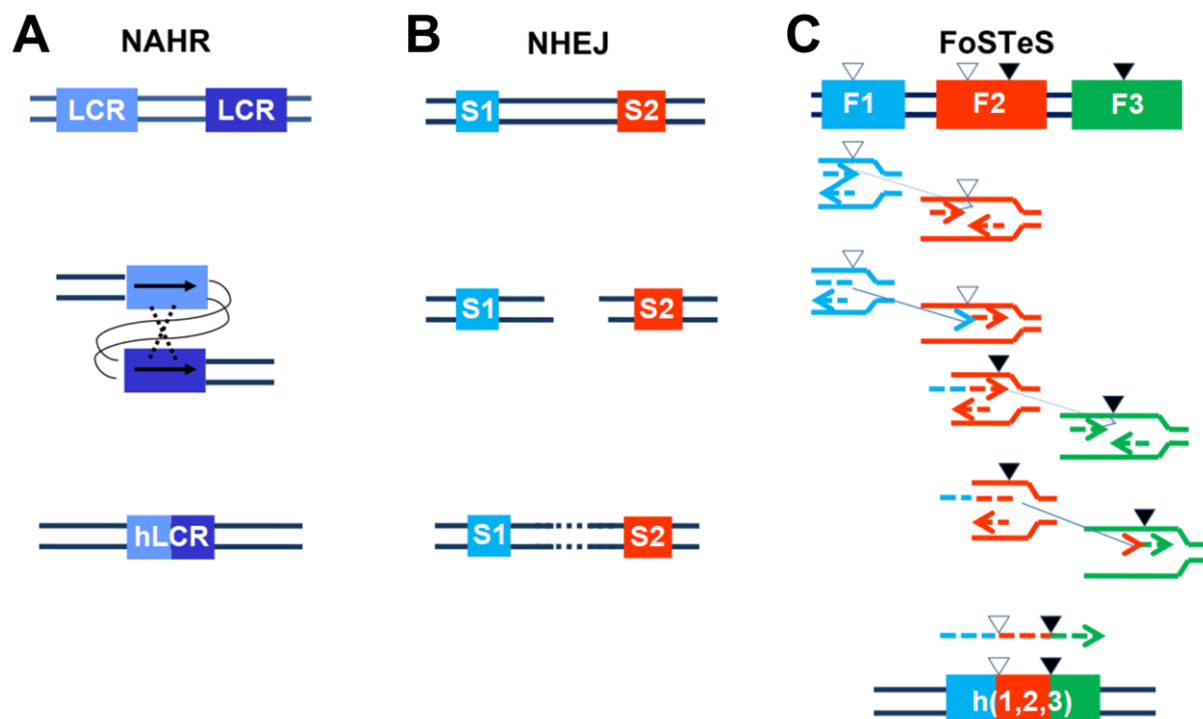


Figure 6. Three major mechanisms for SV formation in the human genome. Black parallel lines represent double-stranded DNA in all three schemes. (Figure legend continues on page 19.)

(A) Nonallelic homologous recombination (NAHR) between directly oriented low copy repeats (LCRs) with high sequence homology, as indicated by light and dark blue boxes, generates a deletion of the intermediate DNA segment leading to formation of a hybrid LCR (hLCR). **(B)** Non-homologous end-joining (NHEJ) does not require homologous templates for repair of a detected DSB, but mediates repair by modification and direct re-ligation of the two break ends. The modification of the DNA strands prior to ligation can lead to gain or loss of nucleotides, thereby altering the DNA sequence leaving behind a NHEJ “signature”. **(C)** Two cycles of Fork Stalling and Template Switching (FoSTeS) events cause complex partial deletions of genomic segments of F1, F2 and F3 rendering a hybrid genomic segment h(1,2,3) which can result in a gene fusion. No extensive homology is required between F1, F2 and F3, but microhomologies (2–5 bp) between F1 and F2, and F2 and F3 are depicted as small triangles. The original stalling of the replication fork of F1 induces the lagging strand (blue, dotted arrow) to disengage and anneal to a second fork F2 (red, dotted arrow) via common microhomology (white triangle), followed by extension of the now 'primed' second fork F2 and DNA synthesis (blue-red, dotted arrow). After disengagement of the second fork F2, the tethered original fork with its lagging strand (blue-red dotted arrow) can invade a third fork F3 (green, dotted arrow) via second common microhomology (black triangle). Dotted lines represent newly synthesized DNA. Series of replication fork disengagement and invasion of the lagging strand into another replication fork can occur consecutively (e.g. FoSTeS x 2, FoSTeS x 3, and so on) before replication on the original template is re-established. Figure adapted and modified from Gu *et al.*¹⁰³.

1.2.2 Classification of DNA structural variants

SVs can be subdivided into deletions, insertions, duplications, inversions and interchromosomal translocations (Figure 7, “Simple” SVs)^{18,19}. In cancer, however, SVs rarely occur as a singular event but most commonly arise in various combinations contributing to formation of more complex SVs^{19,23,97} (Figure 7, “Complex” SVs). Therefore, different subtypes of complex SVs have been documented across various cancers^{99,112–115}.

The typical case of chromothripsis, which literally means “chromosome shattering”, represents a massive number of breakpoints in a dense chromosomal region followed by random reshuffle and reassembly of the multiple chromosomal fragments¹¹⁶. Unlike the process of accumulation and selection of somatic mutations in cancers, chromothripsis occurs not gradually but rather as a “single-hit” event leading to a localized formation of various complex SV patterns¹¹⁶. These massive and dense chromosomal rearrangements are usually confined to one chromosome arm recombining the shattered fragments in random order and orientation and sometimes even between few localized regions of different chromosomes, which are then accompanied by interchromosomal translocations^{116,117}.

In contrast, chromoplexy involves reassembly of fragmented regions on multiple chromosomes (> 3) that are connected by interchromosomal translocations forming a closed chain of complex rearrangements^{118–120}. In prostate cancer, chromoplexy was documented to simultaneously disrupt several tumor suppressor genes (i.e., *PTEN*, *TP53*) and activate oncogenes through formation of gene fusions (i.e., *TMPRSS2::ERG*)^{118,119}. Since chromoplexy mechanisms are

found in regions of actively transcribed and open chromatin, it is not considered a random event¹¹⁸.

Overall, SVs can have a pronounced effect either on the gene position or the gene dosage⁹⁰. Firstly, SVs can physically reposition the genome and thus either connect two distal fragments together or separate integral genomic elements^{19,90,121}. In rearrangements affecting two distinct genes, novel gene fusions can form, giving rise to aberrant chimeric proteins¹²². Within the same chromosome, gene fusions can form, e.g., due to a deletion, whereas two genomic regions are joined through the removal of the intermediate genomic segment. Alternatively, translocations between different chromosomes can also be causative of gene fusions^{22,122,123}. Furthermore, SV-mediated genomic repositioning can alter the interactions between genes and regulatory elements. Thus, distal enhancers, for instance, can interact with genes that are otherwise physically inaccessible^{60,124,125}. Conversely, physical separation of continuous genomic elements can result in the disturbance of gene expression, which can harm the gene function. This effect of gene disruption becomes particularly relevant for genes that are considered as tumor suppressors^{126,127}. In cancer, inactivation of tumor suppressor genes results in elimination of negative regulatory proteins and consequently contributes to tumor growth¹²⁶. The principle of gene disruption has been implemented for a long time in genetic laboratories and is also referred to as “gene knock-out”¹²⁸.

Secondly, SVs can have a gene dosage effect^{90,129,130}. Events of deletions and duplications often coincide with CNVs, a subtype of unbalanced SVs, which reflects the loss or gain of the respective chromosomal segment^{101,131,132}. In the absence of CNVs, a diploid genome consists of two copies of each chromosome. It is therefore commonly represented by one whole genome segment with the corresponding absolute copy number (CN) of two (CN = 2). The gain of a particular genomic segment is usually reflected by an increase of the CN (CN > 2) whilst the decrease of CN (CN < 2) is indicative of a segmental loss. The gains or losses of genomic segments harboring important genes and regulatory elements influence their DNA dosage and therefore can affect phenotype and cause disorders^{90,133,134}.

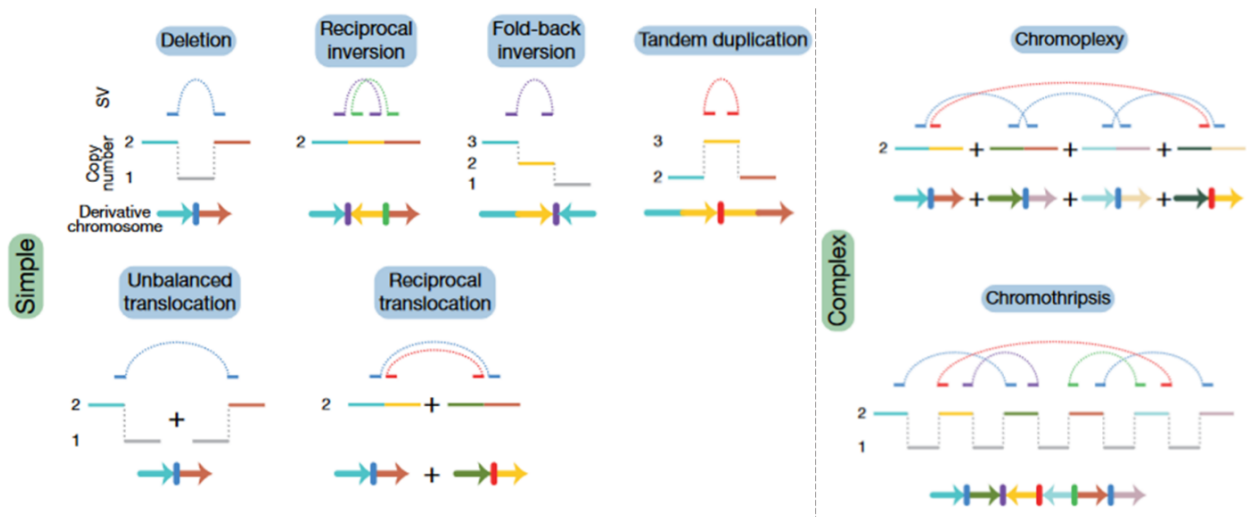


Figure 7. Classification of major SV subtypes in cancer genomes. Schematic representations of 8 types of SVs according to their rearrangement characteristics, i.e., “Simple” on the left side or “Complex” on the right side. Each graph consists of three parts: (1) SV: dotted arcs for each SV junction that joins two chromosomal segments, (2) Copy number: change in copy-number of a given SV-affected segment, and (3) Derivative chromosome: final configuration that results from the structural rearrangement. The colors of the second segment are identical to the colors of the third segment. Figure adapted and modified from Li *et al.*¹⁹.

1.2.3 Detection of DNA structural variants

Despite the overall significance of somatic SVs in cancer pathogenesis, their detection remains challenging¹³⁵. Furthermore, the identification and interpretation of SVs with respect to functionality and phenotypes poses an additional limitation. Thus, different classical and novel methods are currently used for SV detection in cancer. For decades, detection of gross structural abnormalities in the genome was achieved by G-band karyotyping, a well-established technique of classic cytogenetics¹³⁶. Although this conventional staining technique is still widely accepted and used in stem cell research and certain specific malignancies¹³⁷, it lacks resolution and throughput¹³⁸. Improvement in both, resolution and throughput of SV detection was achieved by application of fluorescence *in situ* hybridization (FISH) analysis^{123,139} and comparative genomic hybridization (CGH) microarrays¹⁴⁰. However, only the advances in genome-wide sequencing technologies enabled sensitive and specific SV detection and identification in cancer^{6,8}.

The current high-resolution whole genome analysis of cancer genomes is based on the method of next-generation sequencing (NGS), whereas massively parallel sequencing of short DNA fragments, usually from 50 to 300 bp of size, is performed¹⁴¹. The subsequent computational alignment of the generated genomic reads against the reference genome is essential for identification of changes within the investigated DNA sample¹⁴². This way, mutations can be inferred from abnormal alignment patterns and predictions can be made with respect to the

effect and phenotype of the detected aberration. Although much of the knowledge on genome-wide SVs in cancer result from short-read whole genome sequencing (WGS), this technique also presents several shortcomings like limited sensitivity due to the short read length (~150 bp), which also affects the accuracy of the read alignment to the reference genome¹⁴³. In contrast to SNVs and indels, SVs are usually significantly bigger in size covering a large portion of a sequencing read or even extending over the read length¹⁴⁴. This in turn complicates the alignment of the detected variant to the reference genome, which additionally can be prone to errors. The unambiguous identification of SVs can be even further complicated by similar patterns of individual rearrangements and variable combinations thereof^{25,144}. The resulting complex SV patterns preclude alignment and require computational assemblies of each genomic sample from scratch, or “*de novo*”¹⁴⁵. This is significantly more costly and difficult, and becomes almost unfeasible in repetitive genomic regions composed of similar or even identical stretches of DNA sequence. This issue is well reflected by the presence of large number of different SV annotation algorithms and absence of a gold standard method for SV detection and annotation¹²¹. While short-read sequencing technologies remain the most cost-efficient way to detect SNVs, indels, and screen for known/expected SVs, the technologies still struggle to reliably detect novel, large SVs¹⁴⁴. However, contemporary efforts of technological and methodological developments have managed to overcome many issues associated with short-read sequencing¹⁴⁶. The advent of long-read sequencing technologies, particularly Pacific Biosciences (PacBio) and Oxford Nanopore™ Technologies (ONT), greatly improved identification of novel SVs enabling detection of large DNA fragments (≥ 5 kbp) and thus ease the alignment of generated sequencing reads^{112,147}. The long continuous reads can indeed be aligned more precisely leaving fewer gaps compared to the reference, however, at increased cost and higher computational effort due to current lack of reliable and reproducible alignment and SV annotation algorithms¹²¹.

In addition to long-read sequencing, a cost-efficient and user friendly method, namely Optical Genome Mapping (OGM) provided by Bionano Genomics¹⁴⁸, became accessible. OGM is a non-sequencing, imaging-based technique that employs a restriction enzyme for labelling of a 7 bp motif sequence throughout the genome. OGM detects labeled ultra-high molecular weight (UHMW) DNA molecules and provides a high-resolution genome-wide profile highlighting DNA copy number and structural anomalies from 500 bp to one or more Mbp in length. It enables identification of simple SVs including deletions, insertions, inversions, and duplications as well as more complex genomic rearrangements, like translocations or chromothripsis events. The long-range genome analysis of labelled high-molecular weight DNA molecules (> 150 kbp) facilitates direct whole genome *de novo* assembly¹⁴⁹. This way, large SVs can be identified and directly visualized, without application of any additional computational tools. This

technique is considered to be particularly useful in conjunction with WGS (or even long-read sequencing), thereby complementing the shortcomings of the sequencing approach.

1.3 Aims of the thesis

Brain tumors are one of the leading causes of cancer-related death in children and young adults³³. In contrast to adult solid tumors, which usually present elevated mutational burden that results after accumulation of multiple sequential somatic mutations, studies on different types of pediatric solid tumors report comparably low mutational loads but relatively high prevalence of DNA SVs (≥ 50 bp)^{6,8,13}. Based on these findings, different mechanisms leading to tumor initiation and formation of adult and pediatric tumors are acknowledged^{6,8,13}.

The major aim of this thesis was to assess the role of SVs in malignant brain tumors from pediatric patients. The key aspects were:

- Establishment of the central technique for genome-wide SV detection, namely optical genome mapping (OGM), using the Bionano Genomics Saphyr™ OGM instrument^{148,149}.
- Optimization of the OGM wet-lab and SV analysis workflow.
- Comparison and validation of OGM findings with DNA methylation and copy-number profiling using the Infinium™ MethylationEPIC BeadChip v1.0 (“850k EPIC”) array platform, RNA sequencing and targeted panel NGS.
- Evaluation and interpretation of detected SVs and CNVs: known versus novel rearrangements in MB and ATRT.

2 Materials and Methods

2.1 Devices and software

The equipment used in this thesis is summarized in Table 1.

Table 1. List of laboratory devices and equipment.

Item	Catalog number, Distributor
Vi-Cell-XR Cell Viability Analyzer	Beckman Coulter (Krefeld, Germany)
IKA mini G tabletop centrifuge	#0003958000, IKA (Freiburg, Germany)
IKA ULTRA-TURRAX T 25 digital	#0003725000, IKA (Freiburg, Germany)
Eppendorf Centrifuge 5430	#5427000015, Eppendorf (Wesseling-Berzdorf, Germany)
Eppendorf Centrifuge 5810 R	#5811000015, Eppendorf (Wesseling-Berzdorf, Germany)
Analog Vortex Mixer	#444-0996, VWR International (Hannover, Germany)
Ion GeneStudio S5 System	#A38194, Thermo Fisher Scientific (Schwerte, Germany)
Ion Chef™ Instrument	#4484177, Thermo Fisher Scientific (Schwerte, Germany)
Biometra TRIO 48	#846-2-070-723, Analytik Jena
qTOWER ³ touch	#844-00555-2, Analytik Jena
Maxwell® RSC Instrument with Quantus™ Fluorometer	#AS4500, Promega (Mannheim, Germany)
QuantiFluor® ONE dsDNA System	#E4870, Promega (Mannheim, Germany)
DynaMag™-2 Magnet	#12321D, Thermo Fisher Scientific (Schwerte, Germany)
HulaMixer™ Sample Mixer	#15920D, Thermo Fisher Scientific (Schwerte, Germany)
Nanodrop ND-1000 Spectrophotometer	PEQLAB Biotechnologie (Erlangen, Germany)
Microbiological Safety Cabinet, Class II, MSC 1.2	#51025761, Thermo Fisher Scientific (Schwerte, Germany)
Incubator CB210	#9040-0013, BINDER (Tuttlingen, Germany)

The different types of software used in this thesis are listed in Table 2.

Table 2. Software and packages.

Software	Version, Distributor
Microsoft Office	Professional Plus 2016, Microsoft
Circa.Ink	v1.0 (2023), https://circa.omgenomics.com/
Bionano Access	v1.7.1.1, Bionano Genomics
Bionano Solve	vSolve3.7_03302022_283, Bionano Genomics
R	v.R-4-4, https://cran.r-project.org/
RStudio	v2024.09.1+394, 2009-2024 Posit Software, PBC, https://posit.co/downloads/
Minfi	v1.52.0, https://github.com/hansenlab/minfi
Conumee 2.0	v.2.1, https://github.com/hovestadtlab/conumee2
Torrent Suite™	v5.10, ThermoFisher Scientific
Ion Reporter	v5.10.2.0, ThermoFisher Scientific
Integrative Genomics Viewer (IGV)	v2.5.0, https://igv.org/

2.2 Patient-derived tumor tissue and blood samples

In total, 32 unfixed frozen primary brain tumor tissues from patients with either MB (29 patients, 18 male, 11 female, median age: 7 years, range: 1–42 years) or ATRT (3 patients, 1 male, 2 female, median age: 60 years, range: 1–70 years) were examined in this thesis. The respective tissue samples were obtained from the CNS tumor tissue bank and the institutional archive of the Institute of Neuropathology, Heinrich Heine University Düsseldorf. Peripheral blood samples for extraction of constitutive (leukocyte) DNA were available from 18 of the patients. All tumor, indicated by “t”, and blood samples indicated by “b”, were investigated in a pseudonymized manner to protect privacy of the patients (Table 3). The study was approved by the institutional review board (Ethikkommission of the Medical Faculty, Heinrich Heine University Düsseldorf, Ethikvotum #2021-1745, #2021-1745-1).

The diagnosis of each tumor was established by the combination of morphological and immunohistochemical features, followed by specific testing for genetic biomarkers by application of standard molecular diagnostics as required according to the current WHO classification of CNS tumors 2021²⁷. Based on this information, tumors were assigned to distinct molecular groups, so that it was possible to include at least three tumor samples from each of the four MB groups (Table 3). Due to the overall rarity of ATRT, deep frozen tumor tissue samples were available from only three patients, including two tumor specimens from adult patients with ATRT. Each tumor sample was histologically evaluated before nucleic acid

extraction to ensure that only tumor sections with > 80% tumor cell content were incorporated in this study.

Table 3. Overview of investigated ATRT and MB samples. The original assignment to distinct MB groups was based on immunohistochemical features. *n.a.*, not available.

Entity	Tumor ID	Blood ID	Assignment
ATRT	A1t	A1b	n.a.
ATRT	A2t	n.a.	n.a.
ATRT	A3t	n.a.	n.a.
MB	MB1t	MB1b	SHH
MB	MB2t	MB2b	Group 3/4
MB	MB3t	MB3b	Group 3/4
MB	MB4t	n.a.	Group 3/4
MB	MB5t	n.a.	Group 3/4
MB	MB6t	n.a.	Group 3/4
MB	MB7t	n.a.	Group 3/4
MB	MB8t	n.a.	WNT
MB	MB9t	MB9b	WNT
MB	MB10t	n.a.	WNT
MB	MB11t	n.a.	SHH
MB	MB12t	MB12b	SHH
MB	MB13t	n.a.	SHH
MB	MB14t	MB14b	Group 3/4
MB	MB15t	MB15b	SHH
MB	MB16t	MB16b	SHH
MB	MB17t	MB17b	Group 3/4
MB	MB18t	MB18b	Group 3/4
MB	MB19t	MB19b	SHH
MB	MB20t	MB20b	SHH
MB	MB21t	MB21b	Group 3/4
MB	MB22t	MB22b	Group 3/4
MB	MB23t	MB23b	Group 3/4
MB	MB24t	MB24b	SHH
MB	MB25t	n.a.	Group 3/4
MB	MB26t	MB26b	Group 3/4
MB	MB27t	n.a.	SHH
MB	MB28t	MB28b	SHH
MB	MB29t	n.a.	Group 3/4

2.3 Cell lines and culture conditions

Nineteen brain tumor cell lines were included in this thesis (Table 4; MB: n=6; ATRT: n=13). Human medulloblastoma cell lines D283 Med (RRID:CVCL_1155), MED-MEB-8A (RRID:CVCL_M137), ONS-76 (RRID:CVCL_1624) and UW228-3 (RRID:CVCL_0573) were kindly provided by Dr. Pablo Landgraf (Department of Pediatrics, University Hospital of Cologne) and Prof. Dr. Marc Remke (Department of Pediatric Oncology, Hematology and Clinical Immunology, University Hospital Düsseldorf, present address Department of Pediatric Oncology and Hematology, University Hospital Homburg/Saar). HD-MB03 (RRID:CVCL_S506) (PMID 23054560) was kindly provided by Prof. Dr. Till Milde (Department of Pediatrics, University Hospital Jena). The Daoy cell line (RRID:CVCL_1167) was obtained from American Type Culture Collection (ATCC, Manassas, USA). ATRT cell lines CHLA-02-ATRT, CHLA-04-ATRT, CHLA-05-ATRT, CHLA-06-ATRT were also purchased from ATCC. CHLA-266 and BT-12 cell lines were obtained from the Childhood Cancer Repository (<https://www.cccells.org/>). ATRT13808, JC-ATRT and VU397 were kindly provided by Dr. Siddhartha Mitra (University of Colorado, Denver Anschutz Medical Campus, Aurora, CO) and Prof. Dr. Marc Remke. The cell line BT-16 was a gift from Dr. Annie Huang (Department of Pediatrics, SickKids and University of Toronto, Canada). The xenograft cell lines ATRT-310-FHTC and ATRT-311-FHTC were obtained from the Brain Tumor Resource Laboratory (Fred Hutchinson Cancer Center, Seattle, WA). HHU-ATRT1 cells were generated by Prof. Dr. Marc Remke at the Department of Pediatric Oncology, Hematology and Clinical Immunology, University Hospital Düsseldorf from the primary tumor sample A3 (also studied in this thesis) as approved by the institutional review board (Ethikkommission der Medizinischen Fakultät, study number #2018-102).

A detailed description of all cell models and culture conditions is documented in Tables 4 and 5. In brief, cryopreserved cell culture stocks were removed from storage in liquid nitrogen vapor phase, thawed in a 37°C water bath and transferred into a culture flask with the respective complete medium. After appropriate incubation period (at 37°C, 5% CO₂), cell number and viability were determined by Vi-Cell-XR Cell Viability Analyzer. Subsequently, 1.5 x 10⁶ cells were pelleted and aliquots were stored at -80°C until further analysis.

Table 4. Overview of ATRT and MB cell line models and their culture conditions. M1–8 are cell culture media (M) used for the individual cell lines, see Table 5. *RRID*, Research Resource Identifier.

Entity	Cell line (RRID)	Culture condition	References
ATRT	ATRT13808	M1	unpublished
ATRT	ATRT310-FHTC	M2	unpublished
ATRT	ATRT311-FHTC	M2	unpublished
ATRT	BT-12 (CVCL_M155)	M4	150
ATRT	BT-16 (CVCL_M156)	M4	150
ATRT	CHLA-02-ATRT (CVCL_B045)	M5	151
ATRT	CHLA-04-ATRT (CVCL_0F38)	M5	151
ATRT	CHLA-05-ATRT (CVCL_AQ41)	M5	152
ATRT	CHLA-06-ATRT (CVCL_AQ42)	M5	152
ATRT	CHLA-266 (CVCL_M149)	M4	153
ATRT	HHU-ATRT1	M3	unpublished, established from primary tumor A3t
ATRT	JC-ATRT	M1	unpublished
ATRT	VU397	M1	unpublished
MB	Daoy (CVCL_1167)	M6	154
MB	HD-MB03 (CVCL_S506)	M7	155
MB	MED-MEB-8A (CVCL_M137)	M8	156
MB	ONS-76 (CVCL_1624)	M7	157
MB	UW228-3 (CVCL_0573)	M7	158
MB	D283 Med (CVCL_1155)	M7	159

Table 5. Overview of the different cell culture media (M) compositions. M1–M8, see Table 4.

Culture condition	Culture medium	Supplements
M1	1:1 DMEM/F-12 and Neurobasal™-A Medium	1% P/S, 1% Sodium bicarbonate, 1% Sodium pyruvate, 1% MEM NEAA 2% B-27 supplement, 10 ng/mL EGF, 10 ng/mL FGF, 10 ng/mL LIF, 0.25% Heparin
M2	NeuroCult™ NS-A Basal Medium (Human)	1% NeuroCult™ NS-A Proliferation Supplements, 1% P/S, 20 ng/mL EGF, 20 ng/mL FGF
M3	NeuroCult™ NS-A Basal Medium (Human)	1% L-Glutamine, 1% P/S, 75 µg/mL BSA, 1% N-2 supplement, 2% B-27 supplement, 10 ng/mL EGF, 10 ng/mL FGF, 0.25% Heparin
M4	IMDM	20% FBS, 1x ITS-G
M5	DMEM/F-12	2% B-27 supplement, 20 ng/mL EGF, 20 ng/mL FGF
M6	MEM, NEAA	10% FBS, 1% P/S
M7	DMEM	10% FBS, 1% P/S
M8	RPMI 1640	10% FBS, 1% MEM NEAA

The sources of cell culture media, supplements and consumables for in vitro cell cultivation are listed in Table 6.

Table 6. List of cell culture media, supplements and consumables.

Item	Supplier	Catalog-No.
DMEM, high glucose, GlutaMAX™ Supplement, pyruvate	Thermo Fisher Scientific (Schwerte, Germany)	31966021
DMEM/F-12	Thermo Fisher Scientific (Schwerte, Germany)	11320033
MEM Medium, NEAA, no glutamine	Thermo Fisher Scientific (Schwerte, Germany)	10370047
RPMI 1640 Medium, no glutamine	Thermo Fisher Scientific (Schwerte, Germany)	31870025
IMDM	Thermo Fisher Scientific (Schwerte, Germany)	12440061
Neurobasal™-A Medium	Thermo Fisher Scientific (Schwerte, Germany)	10888022
Insulin-Transferrin-Selenium (ITS-G) (100X)	Thermo Fisher Scientific (Schwerte, Germany)	41400045
HEPES (1M)	Thermo Fisher Scientific (Schwerte, Germany)	15630080
B-27™ Supplement (50X), minus vitamin A	Thermo Fisher Scientific (Schwerte, Germany)	12587010
L-Glutamine (200 mM)	Thermo Fisher Scientific (Schwerte, Germany)	25030024
Human EGF Recombinant Protein	Thermo Fisher Scientific (Schwerte, Germany)	PHG0311
MEM Non-Essential Amino Acids (NEAA) Solution (100X)	Thermo Fisher Scientific (Schwerte, Germany)	11140035
N-2 Supplement (100X)	Thermo Fisher Scientific (Schwerte, Germany)	17502048
Sodium Bicarbonate 7.5% solution	Thermo Fisher Scientific (Schwerte, Germany)	25080094
Sodium Pyruvate (100 mM)	Thermo Fisher Scientific (Schwerte, Germany)	11360070
Trypsin-EDTA (0.25%), phenol red	Thermo Fisher Scientific (Schwerte, Germany)	25200056
NeuroCult™ NS-A Basal Medium (Human)	Stemcell Technologies (Cologne, Germany)	05750
NeuroCult™ NS-A Proliferation Supplement (Human)	Stemcell Technologies (Cologne, Germany)	05753
Heparin Solution (0.2%)	Stemcell Technologies (Cologne, Germany)	07980
Penicillin (10.000 U/mL)-Streptomycin (10 mg/mL) (P/S)	Sigma-Aldrich (Taufkirchen, Germany)	P4333
Heat Inactivated Fetal Bovine Serum (FBS)	Sigma-Aldrich (Taufkirchen, Germany)	F9665
Dulbecco's phosphate buffered saline (PBS)	Sigma-Aldrich (Taufkirchen, Germany)	P5493
FGF basic, human recombinant (rHuFGF-basic)	Biomol (Hamburg, Germany)	50361.50
Small Cell Scraper	Corning (Wiesbaden, Germany)	3010

Stripette™ Serological Pipets	Corning (Wiesbaden, Germany)	4486, 4487, 4488, 4489, 4490
Falcon™ High Clarity PP Centrifuge Tube	Corning (Wiesbaden, Germany)	352196 352070
Falcon™ Round-Bottom Polypropylene Test Tubes With Cap	Thermo Fisher Scientific (Schwerte, Germany)	352059
Nunc™ Biobanking and Cell Culture Cryogenic Tubes	Thermo Fisher Scientific (Schwerte, Germany)	363401
Nunc™ Cell-Culture Treated Multidishes	Thermo Fisher Scientific (Schwerte, Germany)	140675 150628
Nunc™ EasYFlask™ Cell Culture Flasks	Thermo Fisher Scientific (Schwerte, Germany)	156367 156499
Suspension Culture Flasks	Greiner Bio-One (Frickenhausen, Germany)	658195
Glass Pasteur Pipettes	BRAND (Wertheim, Germany)	747720

2.4 CNS tumor classification by DNA methylation profiling

DNA methylation profiling using the Infinium™ MethylationEPIC BeadChip v1.0 (“850k EPIC”, Illumina, San Diego, CA) and subsequent analysis of the methylation data with the Heidelberg CNS tumor classifier has been shown to allow for histology-independent stratification of CNS tumors including MB and ATRT into distinct methylation family classes and subclasses²⁹. Therefore, all MB and ATRT tumors and cell lines included in this thesis were subjected to 850k EPIC-based DNA methylation and copy number profiling.

DNA extraction was carried out according to “Bionano Prep SP Tissue and Tumor DNA Isolation Protocol (#30339)”, Bionano Prep SP Frozen Human Blood DNA Isolation Protocol v2” (#30395, Rev B) and “Bionano Prep SP Frozen Cell Pellet DNA Isolation Protocol” (#30268) (Bionano Genomics, San Diego, USA) as described within the sections below. Hybridization of sodium bisulfite modified DNA to EPIC chips and scanning of the chips was performed at LIFE & BRAIN GmbH in Bonn. Briefly, the samples were subjected to bisulfite conversion followed by purification, hybridization to the 850k EPIC array and scanning. Typically, each analyzed CpG site on the array is represented by two probes: one for the methylated state (red) and one for the unmethylated state (green). As output of the DNA methylation analysis, a paired red-green (RG) DNA methylation dataset (two IDAT files) is generated per analyzed sample. Both files were then uploaded to the “Heidelberg CNS Tumor Methylation Classifier” (v12.8, www.moleculareuropathology.org, now available at <https://app.epignostix.com>)^{29,160}. The analysed brain tumors and cell lines were classified upon calibrated confidence score thresholds of ≥ 0.9 , which represent a probability estimation of a true-positive classification within a methylation class family or (sub)class¹⁶⁰.

The final classification results based on DNA methylation analysis of each analysed MB cell line and tumor sample are shown in Table 13 and each analysed ATRT cell line and tumor sample in Table 15. Additional information is listed in Supplementary Table I.

2.4.1 Copy-number variation analysis from DNA methylation array data

Beyond epigenetic information, genetic information in form of DNA CNV profiles can also be derived from the 850k EPIC-based DNA methylation data using the “conumee” package available in bioconductor¹⁶¹. Conumee provides seamLess integration with the widely used minfi package¹⁶² to facilitate the import of pre-processed datasets directly from raw DNA methylation data (IDAT files). The subsequent CNV analysis is conducted through a two-step process: (1) normalization of combined methylated and unmethylated intensities using a normal control reference set with a balanced genome and (2) the combination of individual neighbouring probes into genomic bins. The final segmentation process automatically implements the DNACopy package¹⁶³ and whole genome CNV profiles can be produced with pre-set plotting functions, whereas the copy-number ratio (sample to reference, in log₂) is plotted on the y-axis according to the respective chromosomal location on the x-axis (Figure 8). A high CN ratio (log₂ > 0) is color-coded as red/orange and represents a gain of chromosomal material (CN gain). A low CN ratio (log₂ < 0) is color-coded as blue and represents losses of chromosomal material (CN loss). All individual CNV profiles of cell lines, ATRT and MB tumors, as well as summary plots and heatmaps were produced with conumee 2.0 (v2.1) in RStudio (v2024.09.1+394).

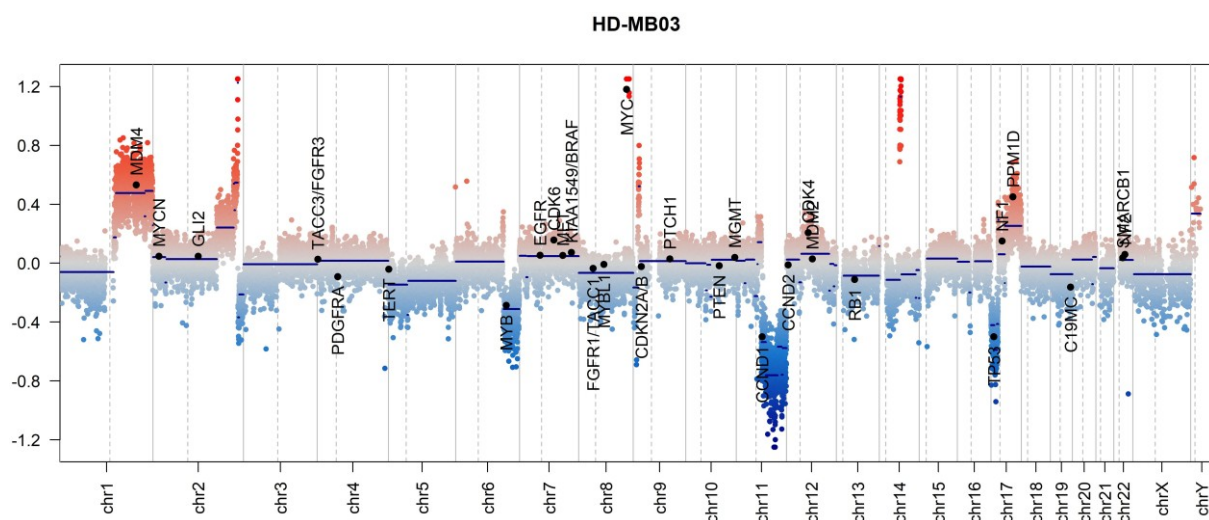


Figure 8. CNV profile of the MB cell line HD-MB03 calculated from 850k EPIC array data. Example of an individual CNV profile produced with conumee 2.0. The horizontal axis depicts chr1–22 and both sex chromosomes. The dashed vertical lines per chromosome indicate the locations of the centromeres, which separate the respective chromosomes into p-arm (left), and q-arm (right) segments. The vertical axis represents the CN ratio (in log₂), whereas CN gains are indicated in red and CN losses are indicated in dark blue around the baseline at 0.0. The CNV profile of this case shows gains on chr1q, chr2q, chr8q,

chr9p, chr14q, and chr17q as well as losses on chr6q, chr11q and chr17p. This CNV profile also shows an amplification of *MYC* (on chr8q), indicated by high focal shift of single red dots including the *MYC* locus above the log2 value of 0.8. Additionally, the typical signature of isochr17q (loss of chr17p and simultaneous gain of chr17q) is observed, which is frequent in Group 3/4 MB.

2.5 Bionano Optical Genome Mapping

The typical Bionano optical genome mapping (OGM) workflow consists of several sequential steps and is graphically summarized in Figure 9. Tables 7 and 8 list the required consumables. Firstly, the long ultra-high molecular weight (UHMW) genomic DNA (gDNA) molecules are extracted from an either fresh or cryopreserved sample. Subsequently, the homogenous UHMW gDNA is labelled with Bionano reagents by incorporation of fluorophores at the CTTAAG sequence motif throughout the genome. The labelled genomic UHMW DNA is then transferred into flowcells on a Saphyr™ chip and the chip is loaded into the Saphyr™ System. The Saphyr™ System gathers data by electrically pulling labelled UHMW gDNA molecules into nanochannel arrays, sequentially imaging the stretched and physically confined gDNA molecules while detecting the molecule backbone and label positions as fluorescence signals. The gDNA molecules are uniquely identifiable by distinct distribution of sequence motif labels and subsequent clustering of the imaging data generates a whole genome consensus map of the analysed sample.

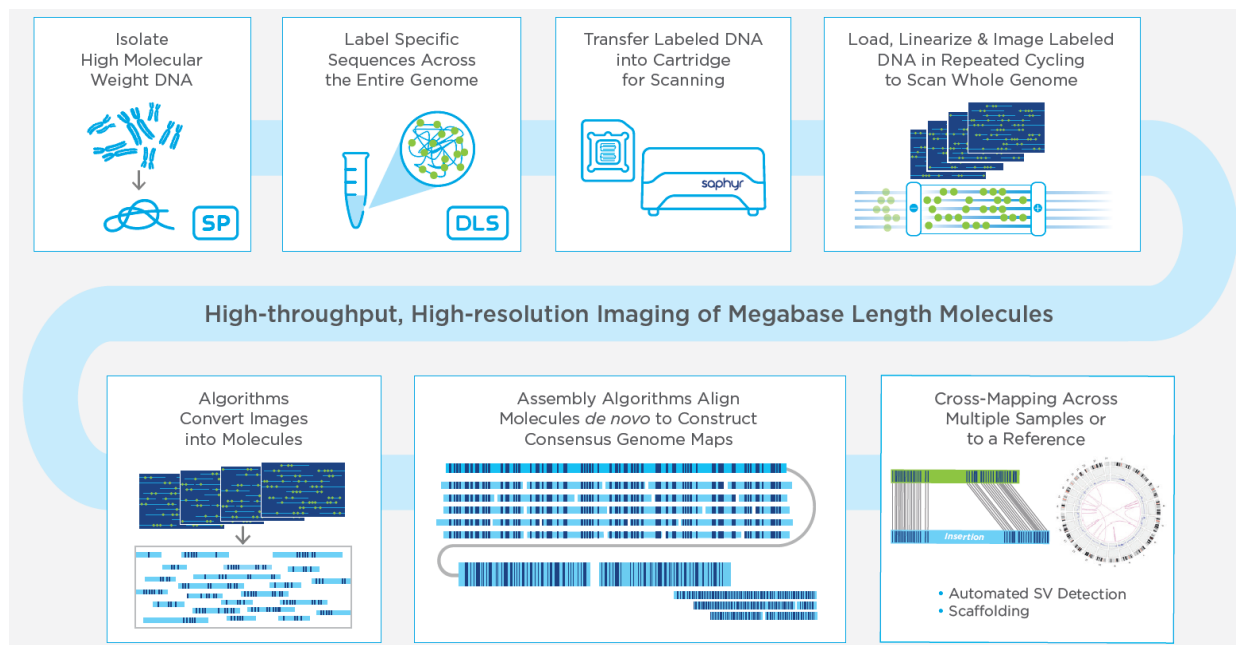


Figure 9. Bionano OGM workflow. From upper left to lower right: UHMW gDNA extraction, UHMW gDNA labelling, chip loading, gDNA imaging, digitization of signal, assembly of consensus map, SV calling. Figure adapted from Bionano Genomics (Saphyr™ System Brochure).

Table 7. List of Bionano consumables used for extraction and labelling and of UHMW gDNA.
All consumables were supplied by Bionano Genomics, San Diego, USA.

Item	Catalog No.
SP Blood and Cell Culture DNA Isolation Kit	80030 (new 80042)
SP Tissue and Tumor DNA Isolation Kit	80038
Bionano Prep SP Magnetic Retriever (2 pack)	80031
Direct Label and Stain (DLS) Kit	80005
Saphyr™ Chip G2.3	20366

Table 8. List of items and consumables used for extraction and labelling and of UHMW gDNA.
The consumables were not supplied by Bionano.

Item	Supplier	Catalog No.
Protein LoBind® Tubes	Eppendorf (Wesseling-Berzdorf, Germany)	0030108116 0030108132
Rainin Pos-D™ positive-displacement pipette MR-10	Mettler-Toledo (Gießen, Germany)	17008575
Pipette Tips C POSD 10µL 180/3	Mettler-Toledo (Gießen, Germany)	17012264
Wide-Bore Pipette Tips, fitered, 200µL	VWR International (Hannover, Germany)	732-3909
UltraFine Filter Tips, 1000µL	VWR International (Hannover, Germany)	732-0534
Phenylmethanesulfonyl fluoride solution (PMSF)	Sigma-Aldrich (Taufkirchen, Germany)	93482
Ethanol absolute VLSI	VWR International (Hannover, Germany)	85651.320
2-Propanol, ≥ 99,5%, Ph. Eur., extra pure	Carl Roth (Karlsruhe, Germany)	CP41.4
Puregene Proteinase K	Qiagen (Hilden, Germany)	158146

2.5.1 Ultra-high molecular weight genomic DNA extraction from frozen cell pellets

UHMW gDNA extraction from frozen cell line pellets was performed using the “SP Blood & Cell Culture DNA Isolation Kit (#80030)” according to the manufacturers’ manual “Bionano Prep SP Frozen Cell Pellet DNA Isolation Protocol” (#30268, Rev D, Bionano Genomics, San Diego, USA). Briefly, cell pellets with 1.5×10^6 cells were thawed at 37°C for 1 minute and directly resuspended in 40 μ L DNA Stabilizing Buffer (Bionano) to preserve UHMW DNA integrity. Subsequently, the cell homogenate was treated with Proteinase K (Bionano) at room temperature for 3 minutes, then Lysis and Binding Buffer (LBB, Bionano) was added and the cell lysate was mixed for 15 minutes at room temperature and 10 rpm on a HulaMixer (ThermoFisher Scientific) for homogenous release of gDNA. Following PMSF (Sigma-Aldrich) treatment for 10 minutes at room temperature, which was used for Proteinase K inactivation, one Nanobind Disc (Bionano) was added into the lysate. Isopropanol was added on top and the lysate was repeatedly mixed for 15 minutes at room temperature and 10 rpm on a HulaMixer to allow for homogenous gDNA binding to the Nanobind Disc. Four rounds of washing steps were followed by gDNA elution in 65 μ L of the provided elution buffer (EB, Bionano), followed by an incubation period of at least 20 minutes at room temperature. The gDNA eluate was collected from the Nanobind Disc by pipetting, transferred into a new tube, slowly mixed by pipetting up and down with a standard 200 μ L tip and finally mixed for one hour at room temperature and 15 rpm on a HulaMixer for final homogenization of UHMW gDNA. To increase homogeneity of the freshly extracted gDNA, the sample was repeatedly mixed by pipetting up and down with a wide-bore 200 μ L tip and kept overnight at room temperature.

2.5.2 Ultra-high molecular weight genomic DNA extraction from frozen blood samples

UHMW gDNA extraction from frozen blood aliquots was performed using the “SP Blood & Cell Culture DNA Isolation Kit (#80030)” according to the manufacturers’ manual “Bionano Prep SP Frozen Human Blood DNA Isolation Protocol v2” (#30395, Rev B, Bionano Genomics, San Diego, USA). In brief, a frozen whole blood aliquot of 500 μ L was thawed at 37°C for 1 minute, pelleted at 2,000 x g for 5 minutes, the supernatant removed and the leukocyte cell pellets resuspended in 40 μ L DNA Stabilizing Buffer (Bionano). The following procedure was carried out exactly as described above in the paragraph 2.5.1.

2.5.3 Ultra-high molecular weight genomic DNA extraction from solid brain tumor tissue samples

For each tumor sample, UHMW gDNA was extracted from ~10 mg of fresh frozen human tumor tissue using the “SP Tissue and Tumor DNA Isolation Kit (#80038)” according to the manufacturers’ manual “Bionano Prep SP Tissue and Tumor DNA Isolation Protocol” (#30339, Rev A, Bionano Genomics, San Diego, USA).

In detail, a pre-chilled 3 mm x 3 mm stencil punch was used to retrieve a piece of tumor tissue which was subsequently transferred into a 15 mL conical tube containing 4 mL of pre-chilled Homogenization Buffer (Bionano). The submerged tissue pieces were homogenized for 20 sec at maximal speed using the T 25 digital ULTRA-TURRAX homogenizer (IKA) with a pre-chilled mixing rod. Additionally, the homogenizer mixing rod was rinsed with 6 mL of ice-cold Homogenization Buffer using a pipette and collected in the same conical tube containing the cell homogenate. The homogenate was decanted through a 40 µm cell strainer (provided in the Bionano Kit) into a 50 mL conical tube and placed on ice. The 15 mL conical tube was washed with additional 5 mL chilled Homogenization Buffer to rinse cells and debris off the sides of the tube and again decanted through the 40 µm cell strainer into the 50 mL conical tube on ice. The entire tumor cell homogenate (~ 15 mL) was mixed by pipetting up and down twice, transferred into a new 15 mL conical tube and pelleted at 2,000 x g for 5 minutes at 4°C.

Subsequently, the supernatant was removed, the cell pellet resuspended in 1 mL of Wash Buffer A (Bionano) and the cell suspension was transferred into a pre-chilled 1.5 mL Protein LoBind tube (Eppendorf) for the final centrifugation step at 2,000 x g for 5 minutes at 4°C. Finally, the supernatant was removed, leaving approximately 40 µL for resuspension of the cell pellet. The cell suspension was treated with Proteinase K (Bionano), detergent-containing LBB (Bionano) was added and the cell lysate was mixed on a HulaMixer (ThermoFisher Scientific) for homogenous release of gDNA. Following PMSF (Sigma-Aldrich) treatment, Salting Buffer, one Nanobind Disc (both Bionano) and Isopropanol were added on top and the lysate was repeatedly mixed on a HulaMixer to allow for homogenous gDNA binding to the Nanobind Disc. Four rounds of washing steps were followed by gDNA elution in the provided EB (Bionano) and final mixing on a HulaMixer for homogenization of UHMW gDNA. To increase homogeneity of the freshly extracted gDNA, the sample was mixed by pipetting up and down with a wide-bore 200 µL tip and kept overnight at room temperature.

2.5.4 Genomic DNA quantifications and direct labelling and staining

Quantification of the extracted UHMW gDNA was performed in triplicates after homogenization using the QuantiFluor® ONE dsDNA System (Promega). The homogenous UHMW gDNA extracted from cell line, tumor and blood samples, was subsequently labelled by application of the “Bionano Prep DLS Labeling Kit” (#80005) as described in the protocol “Bionano Prep Direct Label and Stain (DLS) Protocol” (#30206, Rev F) (Bionano Genomics, San Diego, USA).

Briefly, 750 ng gDNA were treated with DL-Green fluorophores using the Direct Labelling Enzyme (DLE-1) which enables direct fluorescent labelling of double-stranded gDNA at CTTAAG sequence motif. Proteinase K (Qiagen) digestion and DL-Green (Bionano) clean-up consisting of two membrane adsorption steps followed. Each gDNA sample was applied to a membrane and incubated in the dark for one hour at room temperature. After one hour, each gDNA sample was carefully collected within a standard pipette tip, reapplied to a fresh membrane and incubated under the same conditions for 30 more minutes. The DLE-1-labelled UHMW gDNA samples were homogenized by mixing with a HulaMixer and gDNA backbone counterstaining protected from light was performed overnight at room temperature. The labelled gDNA was quantified in duplicates using the QuantiFluor® ONE dsDNA System (Promega). The quantified, labelled gDNA samples were temporary stored at 4°C protected from light and finally equilibrated to room temperature directly before loading into the flowcells of the G2.3 Saphyr Chip (Bionano, #20366).

2.5.5 Chip loading and data collection

Each used G2.3 Saphyr™ Chip contains three single flow cells. The labelled UHMW gDNA samples were each loaded into one flowcell of the chip for uniform linearization and imaging on the Saphyr Instrument (#60325, Bionano Genomics®, San Diego, USA). Each flowcell of the chip was set to generate the maximal throughput of raw genomic data, which was 1300 gigabase pair (Gbp) per labeled UHMW gDNA sample, and multiple cycles of imaging occurred. The maximal accumulated throughput and run time was pre-determined by the version of the Saphyr Instrument Control Software. A single, final, raw molecule file (BNX file) was generated per analysed UHMW gDNA sample. All subsequent downstream SV analyses, including the annotated *De novo* Assembly Pipeline (DNP), annotated Rare Variant Analysis (RVA) and the dual Variant Annotation Pipeline (dual VAP) have different data input requirements which are listed below in Table 9. All analyses were performed via Bionano Access Server (v1.7) and are addressed in more detail in the paragraphs below.

Table 9. Assembled OGM data collection parameters for different SV analysis pipelines.

SV Pipeline	Rare Variant Analysis	De Novo Assembly
Estimated Raw Coverage [X]	400	120
DNA Throughput [Gbp]	1300	480
N50 (\geq 150 kbp) [Mbp]	\geq 0.23	\geq 0.2
Map Rate to Reference [%]	\geq 70	\geq 70
Eff. Coverage of Reference [X]	\geq 300	\geq 80
Minimal SV Size [kbp]	5	0.5
Variant Allele Fraction (VAF) [%]	5	50

2.5.6 Detection of structural DNA variants by optical genome mapping

2.5.6.1 Annotated Rare Variant Analysis

Each raw molecule file of ~1300 Gbp was first submitted to the Rare Variant Analysis (RVA), which Bionano specifically designed to identify rare SVs even at low variant allele frequencies (VAF \geq 5%). Therefore, raw imaged single molecules were directly aligned to the provided reference genome, for example, human reference build GRCh38, and the labelling pattern of the DNA molecule maps was compared against the reference. The goal of the RVA is to find structural changes that occur in only a small fraction of cells at a low frequency but may still be biologically or clinically significant. This approach is particularly useful for cancer samples in which subclonal rearrangements may occur. The generated, annotated RVA managed to detect SVs based on the labelling pattern, implementing the “split-read” analysis¹⁶⁴, and partial CNVs and whole chromosome aneuploidies, implementing the CN analysis¹⁶⁴. The “split-read” analysis identifies SVs by assessing the molecule alignments while searching for highly similar clusters of molecules that either present alignment gaps or show multiple overlapping alignments. The CN analysis calculates the mean coverage of all labels, the so-called “baseline CN” state, and then identifies genomic CNVs, which present significant coverage deviations from the “baseline CN” state. The final RVA data was listed in Bionano CMAP format and subsequently visualized with the Bionano Access Server.

2.5.6.2 Annotated *De novo* Assembly Pipeline

The annotated *De novo* Assembly Pipeline (DNP) was conducted in parallel to the annotated RVA. The DNP is built on “the overlap-layout-consensus strategy with a maximum likelihood model for scoring alignments”¹⁶⁴. Meaning that, in contrast to the RVA, the DNP initially builds a new, reference-independent genome assembly from the raw imaged single molecules by comparison and subsequent alignment of the labelling patterns in the DNA molecule maps, thereby constructing pre-merged consensus maps. These consensus maps are iteratively refined, extended and merged, until the final, comprehensive stand-alone assembly of an

individual's genome is constructed. This iterative assembly process requires less raw genome coverage with still sensitive detection of SVs ≥ 500 bp in a diploid genome¹⁶⁴. The stand-alone genome assembly is then used for SV detection when a reference is provided. However, the DNP approach may miss SVs at low VAF frequencies.

With the aim to validate the RVA-identified SVs by a complementary and independent SV-calling algorithm and to detect both, large candidate SVs that were potentially missed by the RVA and small SVs below the RVA size threshold, the annotated DNP was applied. To this end, each raw molecule file of ~ 1300 Gbp was filtered down to ~ 480 Gbp with a custom minimal molecule length of 200 kbp, corresponding to an approximate raw genome coverage of $\sim 90X$, as recommended by Bionano. The filtered molecule file was submitted to the DNP. Similar to the RVP, the annotated DNP identified SVs based on the labelling pattern, and partial CNVs and whole-chromosome aneuploidies based on label coverage depth information. The final DNP data was listed in Bionano CMAP format and subsequently visualized with the Bionano Access Server.

2.5.6.3 Dual Variant Annotation Pipeline

Bionano's dual Variant Annotation Pipeline (VAP) was applied only as "matched tumor-normal pair" analysis for those cases, for which UHMW gDNA was available from both tumor (sample) and blood (control) of the same patient. In cases with available tumor gDNA but no matched blood gDNA, only RVA and DNP was used for evaluation of the analysed genomes. Within the dual VAP, call sets from each annotated RVA of a tumor was automatically compared against the corresponding annotated RVA call sets of the blood to determine whether the variants in the tumor can also be found in the blood assembly. If so, these variants were regarded as germline variants and disregarded as somatic events. For purpose of completeness, VAP was similarly applied to the data of the annotated DNPs of the same tumor-blood pair. The output was saved as a VAP analysis file and viewed as either dual RVA VAP or dual DNP VAP on the Bionano Access Server in Circos plot view.

2.5.7 Data analysis and visualization

All statistical analyses and visualization thereof were performed using R (v.R-4-3-2, <https://cran.r-project.org/>) with the RStudio interface (<https://posit.co/downloads/>)¹⁶⁵. The following publicly available packages were downloaded in RStudio and applied accordingly: dplyr, ggplot2¹⁶⁶, ggpubr, tidyverse¹⁶⁷, multcompView, rstatix, stats. All data were presented as mean (\pm sd) unless stated otherwise. The comparisons between groups were made by employing the one-way analysis of variance (ANOVA) and p-values < 0.05 were considered as being statistically significant. The Tukey's Honest Significant Difference (HSD) post hoc test was carried out for pairwise comparison of means between the examined groups as

appropriate. The summarized visualization of OGM-detected SVs in single samples occurred in Circos plot view and specific SVs were shown in the Genome Browser view in the Bionano Access Software. The Circos plots of each analysed cell line and tumor sample are shown as supplementary data (Supplementary Figure I). For cumulative visualization of OGM-detected SVs in multiple samples of the same groups, the Circa.Ink software (<https://circa.omgenomics.com>) was applied. Oncoprint diagrams were created using the OncoPrinter webtool (<https://www.cbioportal.org/oncoprinter>).

2.6 RNA sequencing

2.6.1 Sample processing for RNA sequencing

RNA sequencing (RNA-Seq) was performed for the MB tumor samples. Therefore, RNA was extracted from 29 fresh-frozen medulloblastoma tissues (MB1t–MB29t) and 12 ATRT cell lines using Maxwell® RSC simplyRNA Tissue Kit and Maxwell® RSC Instrument (both by Promega, Madison, Wisconsin, USA). At the Genomics & Transcriptomics Laboratory (BMFZ, Heinrich-Heine-University, Düsseldorf), short-read RNA libraries of 14 MB cases were prepared from 60 ng total RNA with Illumina Stranded Total RNA Prep, Ligation with Ribo-Zero Plus according to the manufacturer's instructions (Illumina, San Diego, CA, USA). The quality of the RNA and the libraries was assessed using Bioanalyzer (Agilent Technologies, Santa Clara, CA) and sequencing of the libraries was performed using Illumina NextSeq2000 (Illumina, San Diego, CA, USA) for 101 cycles. The other 15 MB libraries were prepared at the DKFZ NGS core facility (Heidelberg), whereas 500 ng of total RNA was prepared with the TruSeq RNA Sample Preparation v2 kit (Illumina) and sequenced using the NovaSeq6000 (Illumina) for 101 cycles.

RNA-Seq of the 13 ATRT cell lines was done prior to this study as described by Pauck *et al.*¹⁶⁸.

2.6.2 RNA sequencing data processing, visualization and gene fusion calling

RNA-Seq data pre- and post-processing, quality control (QC) and visualization were performed by Mirela Bălan, Core Unit Bioinformatics (CUBI), Medical Faculty and University Hospital Düsseldorf, Heinrich Heine University Düsseldorf. The expression data (Fastq files) of all samples were analysed using the nf-core-rnaseq nextflow pipeline (v.3.14.0)¹⁶⁹. Briefly, reads were trimmed with Trim Galore¹⁷⁰ and then aligned to the human genome GRCh38.p14 using STAR mapper¹⁷¹ on the Ensembl release v104 as annotation. An extensive quality control was done before and after mapping as part of the default execution of the nf-core rnaseq pipeline. The count matrix was generated as final product of the nf-core rnaseq pipeline using Salmon¹⁷². To compare the gene expression between sample groups of interest, the count

matrices were further analysed with the nf-core-differentialabundance nextflow pipeline (v.1.4.0)¹⁶⁹ that implements a differential analysis using the DeSeq2 package¹⁷³. Gene expression levels were plotted using ggplot2¹⁶⁶.

To detect gene fusions from structural rearrangements, Arriba (v.2.4.0)¹⁷⁴ was used on the STAR alignment from the nf-core-rnaseq pipeline and using the references distributed with Arriba for GRCh38.p14 and the Ensembl release v104 gene model (blacklist, known fusions and protein domains). Arriba extracts the sequence of supplementary alignments and discordant mates, followed by a set of filters set as in the workflow defaults that reduces the number of false positives. The output is a list of gene fusions candidates and a graphical depiction of each fusion. The second tool used for detection of novel somatic fusion genes was FusionCatcher (v1.33)¹⁷⁵ together with the Human Ensembl v102 annotation release. The resulting genes and summaries from FusionCatcher and Arriba's high-confidence calls were deduplicated and merged by gene symbol for each of the analysed datasets. All genes that were implicated in fusion events in the in the healthy controls were removed from the analysis as likely false positives, and the remaining genes were grouped by the tumoral classification. As a final filtering step, we kept only the calls that were reported by both Arriba and FusionCatcher. Same pipeline was applied to two publicly available medulloblastoma datasets from Azatyan and Zaphiropoulos¹⁷⁶ and Forget *et al.*¹⁷⁷ for means of independent comparison of the detected gene fusion events.

2.7 Targeted panel next generation sequencing

Targeted next-generation sequencing (NGS) was performed for selected ATRT cell lines and ATRT tumors that did not present any SVs within the *SMARCB1* gene upon OGM analysis. For this purpose, a gene panel originally designed for molecular diagnostics was used as this panel also covered the *SMARCB1* gene (NM_003073.5). Briefly, relative quantification of amplifiable gDNA was performed using the TaqMan Copy Number Reference Assay with human RNaseP (ThermoFisher Scientific) as described within the "TaqMan Copy Number Assays" protocol (Pub. No. 4397424, Rev. D). The amplicon libraries were created according to the "Ion AmpliSeq™ Library Kit 2.0 User Guide" using the IonAmpliSeq Library Kit 2.0 and subsequently quantified with the Ion Library TaqMan Quantitation Kit (both ThermoFisher Scientific). The sequencing of barcoded and pooled libraries was performed on the Ion GeneStudio™ S5 System" (ThermoFisher Scientific) and the analysis of the sequencing data was done using Torrent Suite 5.12.1.0, Ion Reporter v5.18.2.0 and IGV v2.5.0 with the reference genome GRCh37/hg19. The following public databases were used for interpretation of the variants: dbSNP (<https://www.ncbi.nlm.nih.gov/snp/>), COSMIC (<https://cancer.sanger.ac.uk/cosmic/>), cBioPortal (<https://www.cbioportal.org/>), cancerhotspots.org, ClinVar (<https://www.ncbi.nlm.nih.gov/clinvar/>) and OncoKB

(<https://www.oncokb.org/>). After filtering out artefacts and suspected germline variants, non-benign somatic variants that alter the amino acid sequence with allele frequencies $\geq 5\%$ were finally reported. Table 10 lists the items and consumables used for targeted panel NGS.

Table 10. List of items and consumables used for NGS library preparation.

Item / Consumable	Supplier	Catalog #
AMPure XP Bead-Based Reagent	Beckman Coulter (Krefeld, Germany)	A63881
PCR 96-Well TW-MT-Platte, weiß, breakable	Biozym Scientific (Hessisch Oldendorf, Germany)	712425
DNA LoBind® Tubes	Eppendorf (Wesseling-Berzdorf, Germany)	0030108051
Ion 540™ Chip Kit	Thermo Fisher Scientific (Schwerte, Germany)	A27766
Ion AmpliSeq™ Library Kit 2.0	Thermo Fisher Scientific (Schwerte, Germany)	4480441
TaqMan™ Genotyping Master Mix	Thermo Fisher Scientific (Schwerte, Germany)	4371355
Ion Library TaqMan™ Quantitation Kit	Thermo Fisher Scientific (Schwerte, Germany)	4468802
Ion Xpress™ Barcode Adapters 17-32 Kit	Thermo Fisher Scientific (Schwerte, Germany)	4474009
Ion Xpress™ Barcode Adapters 33-48 Kit	Thermo Fisher Scientific (Schwerte, Germany)	4474518
Low TE 10 mM Tris-HCl (pH 8.0), 0.1 mM EDTA	Thermo Fisher Scientific (Schwerte, Germany)	12090015
Polyolefin Sealing Film for qPCR, Self-Adhesive	Starlab (Hamburg, Germany)	E2796-9895
Ethanol absolute $\geq 99.8\%$, AnalaR NORMAPUR® ACS	VWR International (Hannover, Germany)	20821.330P

2.8 Immunohistochemistry

For selected cases of high-level gene amplifications, specifically *CCND2* and *MYCN*, immunohistochemistry staining of the respective formalin-fixed paraffin-embedded (FFPE) tissues was conducted at the Histopathology Laboratory in the Institute of Neuropathology. Cyclin D2 polyclonal antibody (Proteintech, 10934-1-AP) and N-Myc (D4B2Y) Rabbit monoclonal antibody (Cell Signaling Technology, #51705) were used as primary antibodies in 1:250 and 1:100 dilutions, respectively. Immunostaining was performed on a Dako Autostainer Link 48 immunostainer (Agilent Technologies, Santa Clara, California). Antigen binding of the primary antibodies was detected with the EnVision FLEX system (Agilent Technologies) using 3,3'-diaminobenzidine as horseradish peroxidase substrate and chromogen. Immunostained sections were counterstained with hemalum.

3 Results

3.1 Setup of the optical genome mapping workflow

3.1.1 Processing of different sample types and assessment of ultra-high molecular weight genomic DNA quantity

The quantification of the extracted UHMW gDNA was performed in triplicates the day after the extraction. As indicated in Table 11, the mean gDNA concentrations ranged between 42.70–264.30 ng/ μ L for all of the processed samples. The coefficient of variation ($CV = sd / mean$) of three measurement points of each sample was below the Bionano suggested threshold of 0.30 (range $CV = 0.01–0.24$) and was representative of gDNA homogeneity appropriate for subsequent gDNA labelling. In cases when the UHMW gDNA homogeneity was not initially reached overnight ($CV < 0.30$), appropriate dilution and additional mixing was performed as suggested in the troubleshooting section of the manual “Bionano Prep Direct Label and Stain (DLS) Protocol” (#30206, Rev F) (Bionano Genomics, San Diego, USA). For highly viscous samples, the dilution coefficient of 2–3x was implemented and the period of mixing and equilibration at room temperature was extended to a total of 72 hours (h).

To determine possible correlation between processing different sample types and the respective gDNA quantity, mean gDNA concentrations of different samples types (cell lines, tumors, blood) were compared within the one-way ANOVA. The results showed a significant difference of mean gDNA concentrations between the different sample types ($F(2, 66) = 6.85$, $p = 0.002$), as indicated in Figure 10 (“Pre-labelling”). Subsequently, specific pairwise comparison of the three groups was assessed with a post-hoc test in order to determine which specific sample types were significantly different from each other. The Tukey’s HSD test showed a significant difference between the mean gDNA concentrations of processed cell line ($c(\text{mean}) = 89.25$ ng/ μ L) and blood samples ($c(\text{mean}) = 132.63$ ng/ μ L) ($p = 0.016$, 95% CI = [-82.25, -7.02]), and between cell line and tumor samples ($c(\text{mean}) = 138.23$ ng/ μ L) ($p = 0.002$, 95% CI = [15.86, 82.1]). The processed cell lines presented significantly lower gDNA concentrations compared to blood samples (diff -43.38), and the tumor samples had significantly higher gDNA concentration compared to the cell lines (diff +48.98). No significant difference between the mean gDNA concentrations of processed tumor and blood samples was found ($p = 0.949$, 95% CI = [-29.35, 38.03]), suggesting that their mean gDNA concentrations were relatively similar. These differences of gDNA yield from cultivated (cell lines) and native (tumor and blood) cells could be attributed to a higher input number of tumor cells and leukocytes within the respective samples compared to the cell line samples. In concordance with the mean gDNA yield from all cell lines ($c(\text{mean}) = 89.25$ ng/ μ L) each

eluted in 110 μL EB, and the gDNA amount of a diploid human cell of $\sim 6 \text{ pg/cell}^{178}$, the mean cellular input for UHMW gDNA extraction from cultivated cells was approximately 1.64×10^6 cells. While the calculated cell number of cultured cells was comparable to the counted number determined by the ViXcell counter ($\sim 1.5 \times 10^6$ cells), no counting of leukocytes was performed before preparation of frozen blood pellets. Here, aliquots of fresh whole blood (500 μL) were frozen and directly processed upon thawing. Considering the mean gDNA yield from frozen blood aliquots ($c(\text{mean}) = 132.63 \text{ ng}/\mu\text{L}$) eluted in 65 μL EB, the mean cellular input for UHMW gDNA extraction from leukocytes was calculated as 1.44×10^6 cells per pellet. However, blood as well as tumor gDNA samples were often highly viscous and rarely homogeneously diluted overnight, therefore the dilution coefficient of 2–3x was implemented. The dilution coefficients would correct the previously calculated cell count to $\sim 2.87 \times 10^6$ and $\sim 4.31 \times 10^6$ cells, respectively and thus explain the significant difference of mean gDNA concentrations from blood samples as compared to the mean gDNA concentrations from cell lines. A similar observation was made for the mean gDNA yield from tumor tissues, as no tumor cell counting was performed prior to UHMW gDNA extraction. The processed pieces of tumors were removed from a larger cryopreserved tumor piece with a 3 mm x 3 mm punch, and directly used for gDNA extraction. The weighting was performed once, before processing of the first tumor sample ($\sim 15 \text{ mg}$), to ensure the input amount was comparable to the recommended amount for Bionano OGM analysis. Since the tumor pieces retrieved by the 3 x 3 mm punch were not individually weighted, the different input amount could account for intra- and intergroup differences. Nevertheless, gDNA homogeneity of all UHMW gDNA samples could have been achieved either overnight or 72 h after extraction.

The quantification of the labelled UHMW gDNA samples was performed in duplicates using the QuantiFluor ONE dsDNA System (Promega) as indicated in Table 11. The mean gDNA concentrations were within the range of 3.40–21.00 $\text{ng}/\mu\text{L}$ for all of the processed samples (manufacturers' recommended concentration range 4–12 $\text{ng}/\mu\text{L}$) and the coefficient of variation (CV) between two measurement points from each sample was < 0.3 (range CV = 0.00–0.24). Again, to determine possible correlation between processing of gDNA from different sample types and the respective gDNA yield, mean gDNA labelled concentrations of different samples types (cell lines, tumors, blood) were compared within the one-way ANOVA (Figure 10, "Post-labelling"). The results showed no significant differences in the mean gDNA labelled concentrations among any of the samples types ($F(2, 66) = 1.015$, $p = 0.368$). The lack of significant findings across all comparisons indicated uniformity in mean gDNA concentrations post-labelling. This suggests that although the initial mean gDNA yield was strongly dependent on the cell input, which varied between sample types, the homogenization of UHMW gDNA was nevertheless successful and thus, a comparable gDNA amount ($\sim 750 \text{ ng gDNA}$) was

processed during the labelling procedure finally yielding similar labelled mean gDNA concentrations for downstream analyses. In summary, gDNA extraction from more than $\sim 1.5 \times 10^6$ cells was successful and did not affect the final homogeneity of the UHMW gDNA samples.

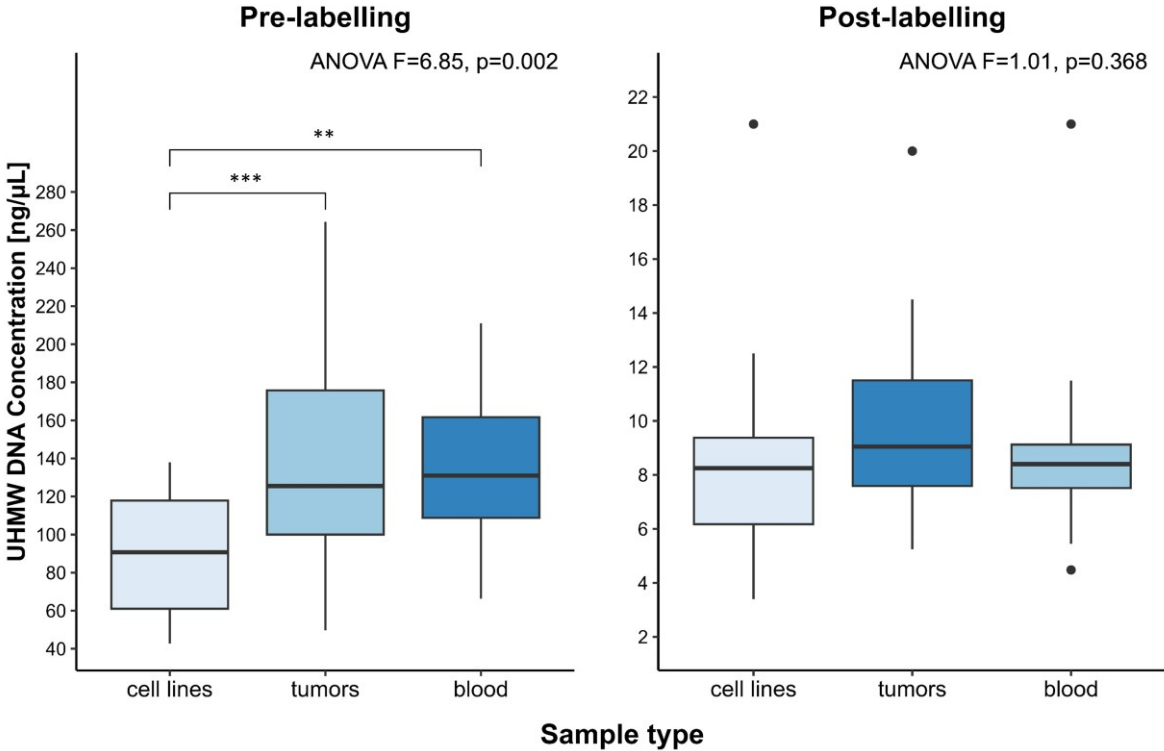


Figure 10. Mean UHMW gDNA concentrations according to sample types. UHMW gDNA concentrations were measured directly before labelling (left panel, Pre-labelling), and after labelling directly before chip loading (right panel, Post-labelling). The statistical method used to compare mean concentrations between different types of processed samples was the one-way ANOVA. Upon significant intergroup differences ($p = 0.002$), as in case of “Pre-labelling”, the post-hoc Tukey’s HSD test was performed. The mean concentrations were significantly different between processed cell line and peripheral blood samples, and between cell line and tumor samples. No significant differences in the mean gDNA labelled concentrations among any of the samples types were found. The intensity of the blue boxplots is dependent on the calculated median. **, $p < 0.01$; ***, $p < 0.001$

Table 11. Summary and statistics of UHMW gDNA concentrations for each analysed sample. gDNA concentrations were measured after extraction (Pre-labelling) and homogenization in triplicates (#1, #2, #3) and concentrations of labelled gDNA (Post-labelling) were measured in duplicates (#1, #2). The mean, sd and CV was calculated for each sample. *sd*, standard deviation; *CV*, coefficient of variation.

Case ID	Sample ID	Sample Type	UHMW gDNA Concentration (ng/μL)										
			Pre-labelling						Post-labelling				
			#1	#2	#3	mean	sd	CV	#1	#2	mean	sd	CV
ATRT13808	ATRT13808	ATRT Cell line	145	124	145	138.00	9.90	0.07	3.3	3.5	3.40	0.10	0.03
ATRT310-FHTC	ATRT310-FHTC	ATRT Cell line	100	78	102	93.33	10.87	0.12	5.5	5.9	5.70	0.20	0.04
ATRT311-FHTC	ATRT311-FHTC	ATRT Cell line	49	49	41	46.33	3.77	0.08	8.1	8.4	8.25	0.15	0.02
BT-12 (CVCL_M155)	BT-12	ATRT Cell line	60	65	61	62.00	2.16	0.03	7.8	11.0	9.40	1.60	0.17
BT-16 (CVCL_M156)	BT-16	ATRT Cell line	125	121	128	124.67	2.87	0.02	6.8	7.2	7.00	0.20	0.03
CHLA-02-ATRT (CVCL_B045)	CHLA-02	ATRT Cell line	113	80	97	96.67	13.47	0.14	8.3	8.6	8.45	0.15	0.02
CHLA-04-ATRT (CVCL_OF38)	CHLA-04	ATRT Cell line	53	59	47	53.00	4.90	0.09	9.0	9.7	9.35	0.35	0.04
CHLA-05-ATRT (CVCL_AQ41)	CHLA-05	ATRT Cell line	91	108	73	90.67	14.29	0.16	26.0	16.0	21.00	5.00	0.24
CHLA-06-ATRT (CVCL_AQ42)	CHLA-06	ATRT Cell line	71	75	73	73.00	1.63	0.02	5.9	7.4	6.65	0.75	0.11
CHLA-266 (CVCL_M149)	CHLA-266	ATRT Cell line	52	62	60	58.00	4.32	0.07	7.6	6.5	7.05	0.55	0.08
HHU01-ATRT	HHU01-ATRT	ATRT Cell line	138	120	124	127.33	7.72	0.06	7.1	7.0	7.05	0.05	0.01
JC-ATRT	JC-ATRT	ATRT Cell line	74	70	75	73.00	2.16	0.03	4.1	4.1	4.07	0.01	0.00
VU397	VU397	ATRT Cell line	58	59	63	60.00	2.16	0.04	4.6	4.0	4.79	0.17	0.04
D283 Med (CVCL_1155)	D283-MED	MB Cell line	71	77	66	71.33	4.50	0.06	8.4	8.8	8.60	0.20	0.02
Daoy (CVCL_1167)	Daoy	MB Cell line	112	103	126	113.67	9.46	0.08	9.9	7.7	8.80	1.10	0.13
HD-MB03 (CVCL_S506)	HD-MB03	MB Cell line	120	133	112	121.67	8.65	0.07	12.0	13.0	12.50	0.50	0.04

MED-MEB-8A (CVCL_M137)	MED8A	MB Cell line	122	159	133	138.00	15.51	0.11	11	9.8	10.40	0.60	0.06
ONS-76 (CVCL_1624)	ONS76	MB Cell line	105	97	134	112.00	15.90	0.14	4.6	3.9	4.29	0.36	0.08
UW228-3 (CVCL_0573)	UW-228-3	MB Cell line	36	44	48	42.67	4.99	0.12	9.7	9.1	9.40	0.30	0.03
A1	A1t	tumor	48	53	48	49.67	2.36	0.05	7.1	6.9	7.00	0.10	0.01
	A1b	blood	141	154	150	148.33	5.44	0.04	7.7	7.5	7.60	0.10	0.01
A2	A2t	tumor	56	54	55	55.00	0.82	0.01	5.4	5.1	5.25	0.15	0.03
A3	A3t	tumor	297	267	229	264.33	27.82	0.11	8.9	5.9	7.40	1.50	0.20
MB1	MB1t	tumor	78	126	90	98.00	20.40	0.21	12.0	12.0	12.00	0.00	0.00
	MB1b	blood	202	175	181	186.00	11.58	0.06	7.5	7.6	7.56	0.05	0.01
MB2	MB2t	tumor	95	121	134	116.67	16.21	0.14	6.8	6.3	6.55	0.25	0.04
	MB2b	blood	70	70	68	69.33	0.94	0.01	8.0	9.4	8.70	0.70	0.08
MB3	MB3t	tumor	75	90	75	80.00	7.07	0.09	9.2	8.4	8.80	0.40	0.05
	MB3b	blood	134	119	121	124.67	6.65	0.05	7.1	6.2	6.65	0.45	0.07
MB4	MB4t	tumor	146	190	183	173.00	19.30	0.11	8.2	10.0	9.10	0.90	0.10
MB5	MB5t	tumor	184	244	196	208.00	25.92	0.12	13.0	12.0	12.50	0.50	0.04
MB6	MB6t	tumor	112	180	187	159.67	33.83	0.21	5.6	5.2	5.40	0.20	0.04
MB7	MB7t	tumor	270	235	246	250.33	14.61	0.06	9.2	9.5	9.35	0.15	0.02
MB8	MB8t	tumor	120	99	107	108.67	8.65	0.08	17.0	23.0	20.00	3.00	0.15
MB9	MB9t	tumor	89	76	132	99.00	23.93	0.24	11.0	13.0	12.00	1.00	0.08
	MB9b	blood	154	165	157	158.67	4.64	0.03	7.0	8.0	7.50	0.50	0.07
MB10	MB10t	tumor	151	111	123	128.33	16.76	0.13	8.0	8.5	8.25	0.25	0.03
MB11	MB11t	tumor	93	124	87	101.33	16.21	0.16	12.0	11.0	11.50	0.50	0.04
MB12	MB12t	tumor	88	117	95	100.00	12.36	0.12	6.5	7.7	7.10	0.60	0.08
	MB12b	blood	69	66	64	66.33	2.05	0.03	4.7	4.3	4.48	0.18	0.04
MB13	MB13t	tumor	106	110	125	113.67	8.18	0.07	8.9	10.0	9.45	0.55	0.06
MB14	MB14t	tumor	122	118	109	116.33	5.44	0.05	9.3	10.0	9.65	0.35	0.04
	MB14b	blood	136	131	147	138.00	6.68	0.05	9.3	8.7	9.00	0.30	0.03
MB15	MB15t	tumor	180	156	131	155.67	20.01	0.13	10.0	9.4	9.70	0.30	0.03

	MB15b	blood	127	119	135	127.00	6.53	0.05	10.0	9.6	9.80	0.20	0.02
MB16	MB16t	tumor	189	202	198	196.33	5.44	0.03	8.0	7.9	7.95	0.05	0.01
	MB16b	blood	142	130	133	135.00	5.10	0.04	8.0	7.9	7.95	0.05	0.01
MB17	MB17t	tumor	139	107	122	122.67	13.07	0.11	12.0	12.0	12.00	0.00	0.00
	MB17b	blood	78	74	77	76.33	1.70	0.02	9.3	8.2	8.75	0.55	0.06
MB18	MB18t	tumor	144	146	142	144.00	1.63	0.01	10.0	8.9	9.45	0.55	0.06
	MB18b	blood	223	201	209	211.00	9.09	0.04	8.3	10.0	9.15	0.85	0.09
MB19	MB19t	tumor	139	174	182	165.00	18.67	0.11	12.0	11.0	11.50	0.50	0.04
	MB19b	blood	170	180	169	173.00	4.97	0.03	8.1	8.1	8.10	0.00	0.00
MB20	MB20t	tumor	80	66	59	68.33	8.73	0.13	9.3	7.9	8.60	0.70	0.08
	MB20b	blood	78	79	77	78.00	0.82	0.01	21.0	21.0	21.00	0.00	0.00
MB21	MB21t	tumor	114	89	97	100.00	10.42	0.10	14.0	13.0	13.50	0.50	0.04
	MB21b	blood	165	162	161	162.67	1.70	0.01	7.2	6.7	6.95	0.25	0.04
MB22	MB22t	tumor	41	65	53	53.00	9.80	0.18	8.0	11.0	9.50	1.50	0.16
	MB22b	blood	100	108	118	108.67	7.36	0.07	5.2	5.7	5.45	0.25	0.05
MB23	MB23t	tumor	187	217	190	198.00	13.49	0.07	8.5	6.8	7.65	0.85	0.11
	MB23b	blood	91	122	113	108.67	13.02	0.12	12.0	11.0	11.50	0.50	0.04
MB24	MB24t	tumor	117	123	93	111.00	12.96	0.12	9.0	8.0	8.50	0.50	0.06
	MB24b	blood	122	101	107	110.00	8.83	0.08	9.3	11.0	10.15	0.85	0.08
MB25	MB25t	tumor	184	180	189	184.33	3.68	0.02	6.4	8.3	7.35	0.95	0.13
MB26	MB26t	tumor	208	241	199	216.00	18.06	0.08	8.0	10.0	9.00	1.00	0.11
	MB26b	blood	123	130	127	126.67	2.87	0.02	8.6	9.5	9.05	0.45	0.05
MB27	MB27t	tumor	121	140	132	131.00	7.79	0.06	15.0	14.0	14.50	0.50	0.03
MB28	MB28t	tumor	202	216	204	207.33	6.18	0.03	8.3	8.9	8.60	0.30	0.03
	MB28b	blood	220	203	211	211.33	6.94	0.03	11.0	8.1	9.55	1.45	0.15
MB29	MB29t	tumor	150	152	153	151.67	1.25	0.01	7.5	7.1	7.30	0.20	0.03

3.1.2 Assessment of optical genome mapping data quality and association with different sample types

The assessment of the quality of generated OGM raw data retrospectively also provided information about the quality of the processed UHMW gDNA samples. As described within the methods sections above, each flowcell of the chip was set to generate the maximal throughput of raw data, ≥ 1300 Gbp per labeled UHMW gDNA sample (Table 12, “Total DNA [Gbp]”), and multiple cycles of imaging were aimed to reach the maximal possible genome coverage. The maximal throughput of ≥ 1300 Gbp per flow cell and the resulting maximal coverage were selected with the intent to apply every available secondary downstream analysis pipeline, as down-sampling of large datasets was possible by application of specific filtering parameters, however, generation of additional data required additional flowcell usage. After the primary analyses, an average throughput of 1313.63 (± 23.39) Gbp and an average mapping rate of 81.46% ($\pm 8.78\%$) was reached across all processed samples yielding an average estimated effective coverage of the reference of 343.7x. The time required for generation of the maximal amount of compatible raw data per scanned chip ranged from 24–36 h and was not always continuous, resulting in imaging termination. During non-continuous scans, some flow cells required rehydration due to evaporation or flow cell clogging and the generation of data was interrupted, yielding two separate raw molecule files (BNX format) per sample from the same run. It was not clear, whether the longer imaging period was causative of evaporation or flow cell clogging or whether evaporation or flow cell clogging led to increase of imaging time and premature termination of the imaging process. However, the two generated raw files were afterwards merged into a single raw data file, as indicated in the “comment” column of Table 12. In three cases of processed ATRT cell lines (BT-12, CHLA-02 and VU397) the maximal throughput was not reached during one run and thus, an additional chip was loaded with the same, labelled UHMW gDNA sample. Finally, per analysed UHMW gDNA sample, the final raw molecule file (BNX format) was generated either directly or upon merging of two separate raw molecule files, from either the same run (Table 12, “merged from 2 files”) or two separate runs (Table 12, “merged from 2 runs”).

To review the quality of the generated raw molecule file, the integrity and appropriate labelling density of the analysed UHMW gDNA molecules were examined. In order to ensure reliable SV calling and annotation via downstream secondary analyses, as described within the next section and indicated in Figure 11, post-run QC parameters were examined (Table 12).

To check for a possible effect of the processed sample type on the UHMW gDNA quality, few selected parameters (Table 12) were compared by one-way ANOVA. The distribution of the selected QC parameter values among sample types as well as the ANOVA results are

visualized in Figure 11A–E. For four out of five selected QC parameters, the ANOVA results presented no statistically significant differences among sample types, whereas only the “N50 for all Molecules \geq 150 kbp” was significantly different between the different sample types ($F(2, 67) = 7.183$, $p = 0.001$), as indicated in Figure 11D. Tukey’s HSD test revealed that the OGM data derived from UHMW gDNA of the cell lines (N50 \geq 150 kbp(mean) = 0.26 Mbp) and the tumor tissues (N50 \geq 150 kbp(mean) = 0.27 Mbp) presented significantly higher N50 compared to the blood samples (N50 \geq 150 kbp(mean) = 0.24 Mbp) ($p = 0.021$, 95% CI = [0.003, 0.047] and $p = 0.001$, 95% CI = [0.011, 0.05], respectively). No significant difference between N50 \geq 150 kbp of cell line and tumor samples was found ($p = 0.79$, 95% CI = [-0.014, 0.025]).

In the context of the application of the OGM data derived from blood samples, which were generally used as tumor-matched control data, the lower average N50 values of UHMW gDNA molecules were still above the Bionano recommended threshold of 0.23 Mbp and thus were still considered applicable. Overall, all QC parameters presented values within the acceptable ranges provided by Bionano and thus UHMW gDNA from all sample types were processed with sufficient quality for downstream analyses algorithms.

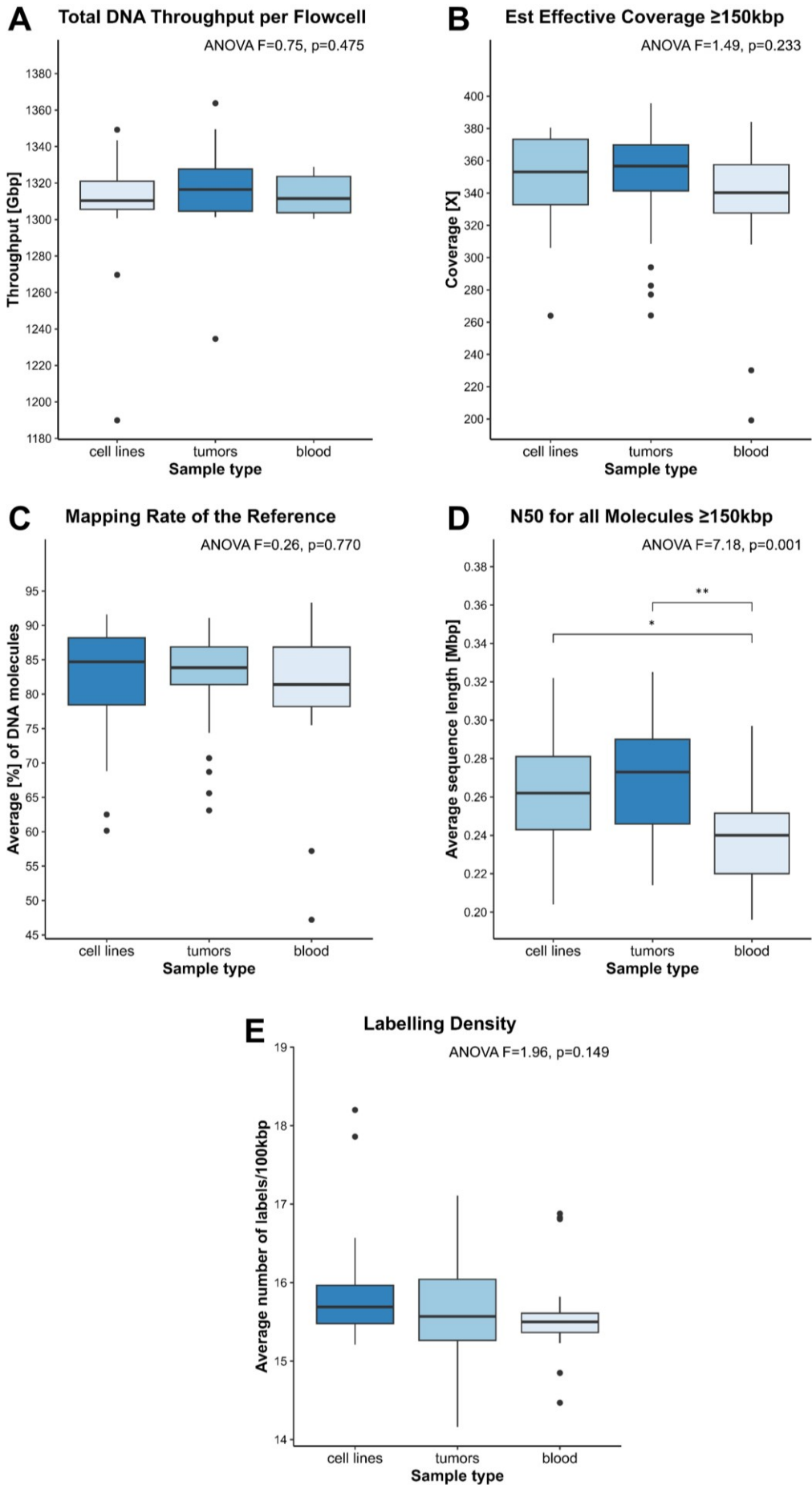


(Figure legend is on page 51.)

Figure 11. Post-run quality control parameters. Selected post-run QC parameters (**A–E**) were examined among files from different sample types. The statistical method used to compare QC parameters between different types of processed samples was the one-way ANOVA test. Upon significant intergroup differences ($p = 0.001$), as in case of “N50 for all Molecules ≥ 150 kbp” (**D**), the post-hoc Tukey’s HSD test was performed. The N50 for all Molecules ≥ 150 kbp was significantly different between processed cell line and blood samples, and between tumor and blood samples. The differences in A–C and E were not significant. The intensity of the blue boxplots is dependent on the calculated median. *, $p < 0.05$; **, $p < 0.01$; *kbp*, kilobase pair; *Mbp*, megabase pair; *Gbp*, gigabase pair.

Table 12. Summary of the OGM run and quality control metrics for all analysed samples. *Avg*, average; *Est*, estimated; *PLV*, positive labelling variance; *NLV*, negative labelling variance; *kbp*, kilobase pair; *Gbp*, gigabase pair; *Mbp*, megabase pair.

Case ID	Sample ID	Sample type	Reference	Total DNA [Gbp]	Avg N50 ≥ 150 kbp [Mbp]	Avg N50 ≥ 20 kbp [Mbp]	Avg Label Density [/100 kbp]	Avg Map Rate [%]	Est Effective Coverage [x]	Avg PLV [%]	Avg NLV [%]	Comment
ATRT13808	ATRT13808	ATRT Cell line	GRCh38	1308.87	0.26	0.16	15.4	88.10	373.3	5.1	8.8	
ATRT310-FHTC	ATRT310-FHTC	ATRT Cell line	GRCh38	1300.68	0.22	0.14	15.4	80.20	338.0	5.0	9.6	
ATRT311-FHTC	ATRT311-FHTC	ATRT Cell line	GRCh38	1310.32	0.24	0.18	15.6	86.00	365.1	4.7	9.1	
BT-12 (CVCL_M155)	BT-12	ATRT Cell line	GRCh38	1305.32	0.23	0.12	15.9	62.50	264.0	3.5	9.1	merged from 2 runs
BT-16 (CVCL_M156)	BT-16	ATRT Cell line	GRCh38	1314.55	0.25	0.16	15.9	79.40	338.1	3.2	9.7	
CHLA-02-ATRT (CVCL_B045)	CHLA-02-ATRT	ATRT Cell line	GRCh38	1304.45	0.24	0.12	15.2	60.15	318.9	3.5	14.7	merged from 2 runs
CHLA-04-ATRT (CVCL_OF38)	CHLA-04-ATRT	ATRT Cell line	GRCh38	1306.31	0.20	0.12	15.7	77.50	327.6	4.4	8.8	
CHLA-05-ATRT (CVCL_AQ41)	CHLA-05-ATRT	ATRT Cell line	GRCh38	1349.20	0.31	0.23	15.7	89.40	378.2	4.0	11.7	
CHLA-06-ATRT (CVCL_AQ42)	CHLA-06-ATRT	ATRT Cell line	GRCh38	1343.34	0.30	0.24	16.0	89.70	376.6	4.7	9.0	
CHLA-266 (CVCL_M149)	CHLA-266	ATRT Cell line	GRCh38	1338.54	0.28	0.20	15.9	87.30	378.5	4.9	8.8	
HHU-ATRT1	HHU-ATRT1	ATRT Cell line	GRCh38	1312.79	0.26	0.13	16.6	80.10	340.4	7.1	8.5	
JC-ATRT	JC-ATRT	ATRT Cell line	GRCh38	1305.79	0.26	0.19	15.6	88.30	373.4	5.2	9.0	
VU397	VU397	ATRT Cell line	GRCh38	1341.98	0.28	0.15	17.9	68.80	322.1	5.4	9.4	merged from 2 runs
D283 Med (CVCL_1155)	D283 Med	MB Cell line	GRCh38	1313.62	0.27	0.21	15.4	89.50	380.6	5.3	10.8	
Daoy (CVCL_1167)	Daoy	MB Cell line	GRCh38	1326.86	0.23	0.16	15.4	80.80	347.3	4.7	12.0	
HD-MB03 (CVCL_S506)	HD-MB03	MB Cell line	GRCh38	1269.65	0.28	0.19	16.3	86.00	354.4	5.3	11.2	
MED-MEB-8A (CVCL_M137)	MED-MEB-8A	MB Cell line	GRCh38	1315.17	0.27	0.17	15.6	84.70	360.7	4.9	11.6	

ONS-76 (CVCL_1624)	ONS-76	MB Cell line	GRCh38	1306.27	0.31	0.21	18.2	72.30	306.0	6.2	9.4	
UW228-3 (CVCL_0573)	UW228-3	MB Cell line	GRCh38	1189.90	0.32	0.26	16.0	91.60	353.1	4.8	9.0	
A1	A1t	ATRT tumor	GRCh38	1337.98	0.24	0.17	16.0	86.80	376.1	4.9	8.6	
	A1b	blood	GRCh38	1305.03	0.20	0.10	15.3	76.50	309.7	4.7	11.8	merged from 2 files
A2	A2t	ATRT tumor	GRCh38	1313.03	0.23	0.13	16.2	82.40	350.3	6.4	8.9	
A3	A3t	ATRT tumor	GRCh38	1314.26	0.27	0.20	15.1	81.80	348.0	4.0	14.2	
MB1	MB1t	MB tumor	GRCh38	1309.18	0.29	0.21	16.5	87.10	369.4	6.5	10.2	
	MB1b	blood	GRCh38	1315.50	0.22	0.13	15.5	80.00	329.8	4.2	11.7	merged from 2 files
MB2	MB2t	MB tumor	GRCh38	1302.00	0.29	0.22	16.1	82.60	348.3	5.7	11.7	
	MB2b	blood	GRCh38	1324.44	0.23	0.14	15.6	79.20	339.6	4.3	10.4	
MB3	MB3t	MB tumor	GRCh38	1301.31	0.29	0.21	16.2	88.30	372.3	5.3	9.6	
	MB3b	blood	GRCh38	1318.35	0.25	0.18	15.5	85.90	355.7	4.9	11.5	merged from 2 files
MB4	MB4t	MB tumor	GRCh38	1303.95	0.21	0.12	16.4	65.60	277.1	5.4	9.3	
MB5	MB5t	MB tumor	GRCh38	1302.33	0.28	0.17	17.1	77.40	326.5	7.8	12.8	
MB6	MB6t	MB tumor	GRCh38	1338.06	0.30	0.22	15.2	88.50	383.4	3.4	12.7	
MB7	MB7t	MB tumor	GRCh38	1320.94	0.28	0.21	16.3	88.30	377.5	6.3	9.7	
MB8	MB8t	MB tumor	GRCh38	1363.73	0.28	0.22	15.5	89.60	395.7	3.8	11.6	
MB9	MB9t	MB tumor	GRCh38	1316.85	0.31	0.26	15.8	91.10	388.6	4.3	10.0	
	MB9b	blood	GRCh38	1303.50	0.21	0.12	15.6	81.10	329.1	5.3	10.9	merged from 2 files
MB10	MB10t	MB tumor	GRCh38	1333.00	0.30	0.26	14.7	82.80	357.2	4.4	17.2	
MB11	MB11t	MB tumor	GRCh38	1301.76	0.33	0.27	15.9	88.00	370.9	6.3	9.4	
MB12	MB12t	MB tumor	GRCh38	1310.15	0.23	0.15	15.6	85.10	361.0	4.6	10.2	
	MB12b	blood	GRCh38	1312.12	0.22	0.13	14.9	84.70	344.4	4.7	11.5	merged from 2 files
MB13	MB13t	MB tumor	GRCh38	1316.04	0.28	0.19	15.6	88.20	375.8	4.5	11.0	
MB14	MB14t	MB tumor	GRCh38	1327.12	0.25	0.16	15.3	85.40	356.3	4.3	14.8	merged from 2 files

	MB14b	blood	GRCh38	1322.75	0.27	0.22	15.4	93.30	384.0	4.2	10.7	
MB15	MB15t	MB tumor	GRCh38	1344.79	0.25	0.16	15.4	82.50	359.4	4.3	13.0	
	MB15b	blood	GRCh38	1300.38	0.26	0.19	15.8	88.00	359.5	5.8	11.8	merged from 2 files
MB16	MB16t	MB tumor	GRCh38	1318.11	0.23	0.15	15.5	85.30	364.2	4.8	10.5	
	MB16b	blood	GRCh38	1328.83	0.24	0.17	15.7	89.30	372.4	4.8	10.2	merged from 2 files
MB17	MB17t	MB tumor	GRCh38	1329.25	0.23	0.14	15.5	84.20	362.6	3.9	10.7	
	MB17b	blood	GRCh38	1326.74	0.23	0.15	15.5	86.70	361.0	4.4	12.0	merged from 2 files
MB18	MB18t	MB tumor	GRCh38	1321.31	0.24	0.11	15.9	63.10	264.2	5.7	17.1	merged from 2 files
	MB18b	blood	GRCh38	1303.98	0.22	0.13	15.6	81.40	331.8	4.8	11.8	merged from 2 files
MB19	MB19t	MB tumor	GRCh38	1303.28	0.27	0.14	15.6	82.80	341.8	4.1	14.5	merged from 2 files
	MB19b	blood	GRCh38	1324.70	0.25	0.17	14.5	79.30	340.2	5.3	15.3	
MB20	MB20t	MB tumor	GRCh38	1321.97	0.25	0.17	14.3	68.70	294.0	5.6	19.8	
	MB20b	blood	GRCh38	1328.52	0.26	0.13	16.8	77.20	326.3	4.3	11.5	
MB21	MB21t	MB tumor	GRCh38	1349.42	0.30	0.22	14.8	86.40	369.5	4.9	14.4	
	MB21b	blood	GRCh38	1307.41	0.24	0.16	15.5	87.00	354.2	5.5	11.2	merged from 2 files
MB22	MB22t	MB tumor	GRCh38	1319.01	0.25	0.12	16.5	74.40	308.5	6.5	15.8	merged from 2 files
	MB22b	blood	GRCh38	1307.28	0.25	0.16	15.3	86.40	353.1	5.8	11.0	merged from 2 files
MB23	MB23t	MB tumor	GRCh38	1309.74	0.24	0.16	15.3	86.00	352.7	4.8	13.7	merged from 2 files
	MB23b	blood	GRCh38	1301.48	0.22	0.11	15.2	75.50	308.2	4.6	15.7	
MB24	MB24t	MB tumor	GRCh38	1325.02	0.29	0.20	15.0	85.50	355.6	5.4	16.3	merged from 2 files
	MB24b	blood	GRCh38	1311.49	0.30	0.23	15.5	91.90	371.0	4.7	10.6	merged from 2 files
MB25	MB25t	MB tumor	GRCh38	1336.31	0.29	0.21	15.6	83.50	361.2	7.9	13.1	
MB26	MB26t	MB tumor	GRCh38	1303.53	0.27	0.18	15.2	77.50	327.2	6.3	17.2	

	MB26b	blood	GRCh38	1303.27	0.24	0.12	16.9	47.20	199.2	6.0	20.5	
MB27	MB27t	MB tumor	GRCh38	1304.84	0.26	0.19	15.6	81.90	345.8	7.8	12.3	
MB28	MB28t	MB tumor	GRCh38	1310.21	0.26	0.19	15.3	80.20	340.1	8.0	13.1	
	MB28b	blood	GRCh38	1301.76	0.22	0.12	16.8	57.20	230.2	7.8	14.2	
MB29	MB29t	MB tumor	GRCh38	1234.56	0.30	0.22	14.2	70.70	282.6	7.3	17.4	merged from 2 files

3.2 Implementation and optimization of secondary optical genome mapping-based DNA copy number variation and structural variation analyses

Seventy raw molecule files were generated: 19 from cell line gDNA, 32 from tumor tissue gDNA and 19 from blood (leukocyte) gDNA. First, the 13 ATRT and 6 MB cell lines were examined for SVs and CNVs using the two available downstream analysis pipelines, the annotated DNP and the annotated RVA. Next, the three ATRT tumor, 29 MB tumor and the 19 matched blood molecule files were processed likewise, with both analysis pipelines being performed for each molecule file independently. Afterwards, matched tumor-normal pairs were processed in a pairwise fashion by application of the dual VAP. The workflow overview is visualized in Figure 12 and the analysis pipelines are addressed in more detail within the subsections below.

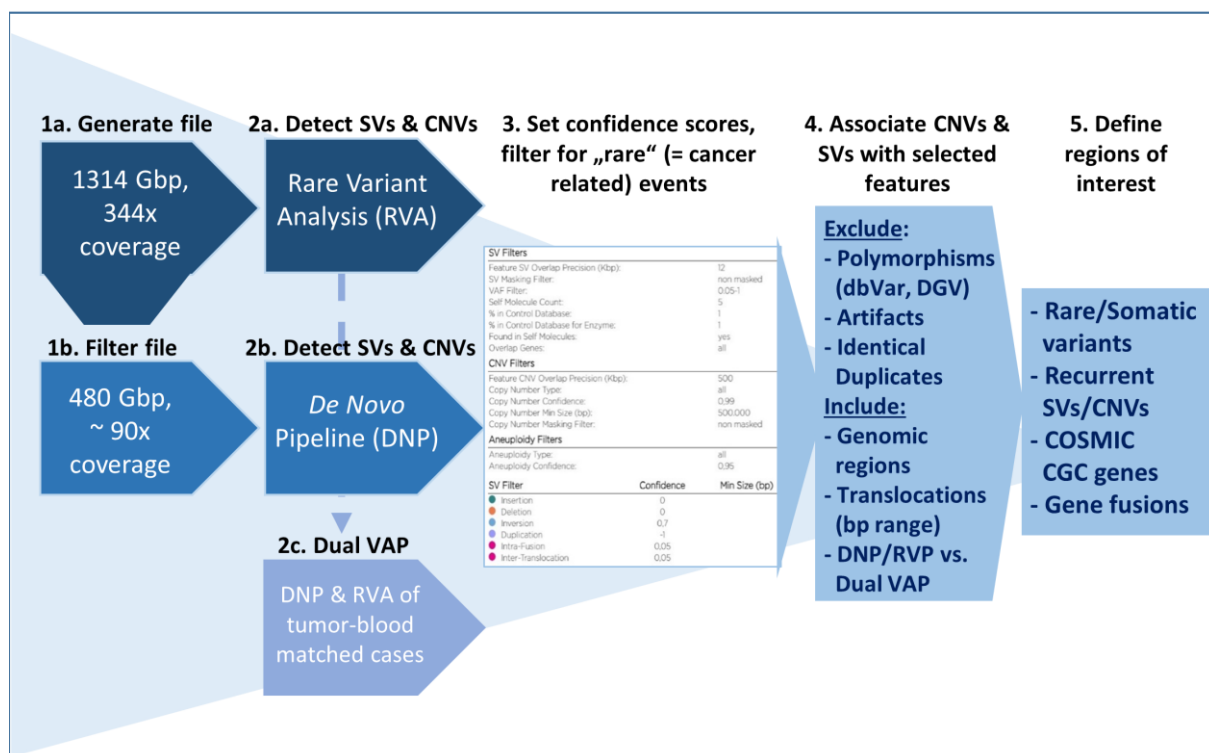


Figure 12. Illustration of the OGM data analysis workflow. Stepwise processing of OGM-generated raw molecule files (**1a, b**); application of SV-detection and annotation algorithms (**2a–c**), downstream manual filtering of annotated SVs from different assemblies (**3, 4**) and final integration into an output with defined regions of interest (**5**). *bp*, base pair; *Gbp*, gigabase pair; *VAP*, Variant Annotation Pipeline by Bionano Genomics; *dbVar*, NCBI's database of genomic structural variation; *DGV*, Database of Genomic Variants; *COSMIC*, Catalogue of Somatic Mutations in Cancer; *CGC*, Cancer Gene Census.

3.2.1 Identification of DNA structural variants and copy number variants by optical genome mapping

3.2.1.1. Analysis of the annotated Rare Variant Analysis results

Each raw molecule file of ~ 1300 Gbp was initially submitted to the RVA pipeline, which Bionano specifically designed to identify rare SVs at low variant allele frequencies (VAF \geq 5%), as for example in tumors, where cell heterogeneity is highly prevalent and subclonal DNA variants exist. The SV detection is based on direct overlapping alignments of few, raw single-molecules with the provided reference, whereas SVs of \geq 5 kbp are detected with high sensitivity¹⁶⁴. Upon visualization of the RVA with the Bionano Access Server, as shown in Figure 13, a low stringency SV filter with the following confidence scores for SV detection was applied: insertion = 0, deletion = 0, inversion = 0.7, duplication = -1, intra-fusion = 0.05, inter-translocation = 0.05, self molecule count = 5. The low stringency SV thresholds were designed by Bionano to balance between detection sensitivity and minimizing false positive calls, while still allowing the detection of low-confidence SVs that may be relevant in this exploratory context¹⁶⁴. Additionally, all SVs with a VAF < 0.05 were excluded. The targeted minimal SV size was 5 kbp, as pre-defined by the RVA algorithm, but the size threshold was set to 4500 bp to ensure reliable detection of SVs, taking into account that the methods' minimal resolution is 500 bp. This adaptation ensured that all SVs which did not specifically reach the 5 kbp threshold, due to possible resolution miscalculations, were still included within the RVA call-set. For detection of CNVs, the default filtering parameters were set: confidence = 0.99 and the minimal size = 0.5 Mbp. The applied SV and CNV confidence scores were recommended as default by Bionano Access Server and are based on confidence models that were trained using both simulated SVs/CNVs and detected SVs/CNVs from real samples where validation data were available. Additionally, a custom fractional copy number (CN) < 1.800 for losses and a fractional CN > 2.200 for gains was set arbitrarily to reduce the signal noise around the "baseline CN" state (estimated mean coverage of all labels) of the human diploid genome (CN = 2).

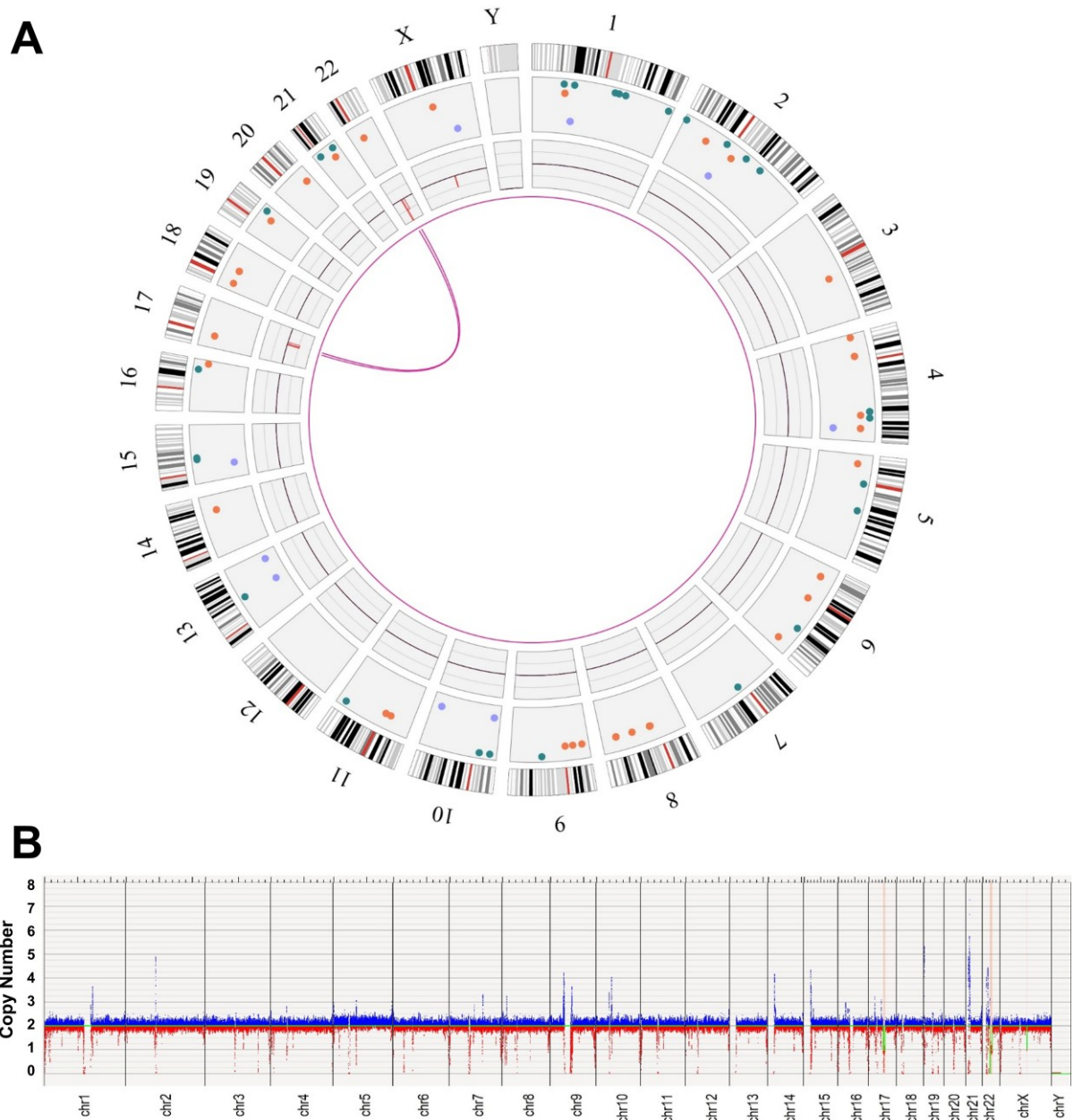


Figure 13. RVA-detected CNVs and SVs in the ATRT cell line JC-ATRT.

(A) Example of the OGM circos plot view, from outside to the center: chromosome ideograms, SVs represented as color-coded dots (*teal*, insertion; *orange*, deletion; *light-blue*, inversion; *purple*, duplication), large CNV segment alterations (*red*, loss; *blue*, gain), translocations or events of complex rearrangements in pink arcs. **(B)** Example of the whole genome CNV profile view. The y-axis lists the copy number range of 0–8 and the baseline is centered around CN of 2. The x-axis presents the respective chr1–22, chrX and chrY. DNA copy number values below 2 (CN < 2) are indicated by red and DNA copy number values above 2 (CN > 2) by blue colors.

The OGM-integrated SV calling algorithm of the RVA identified on average 1435.31 (± 212.98) SVs in ATRT cell lines and 1388.67 (± 137.13) SVs in ATRT tumors (Figure 14B; Suppl. Table IV). Among MB cell lines, significantly more SVs were detected as compared to MB tumors ($F(1, 34) = 7.232$, $p = 0.011$), on average 1812.67 (± 332.67) and 1512.79 (± 217.82) SVs, respectively (Figure 14A; Suppl. Table IV). Therefore, the detailed SV types of MB tumors and MB cell lines were presented separately (Figure 14C and 14E; Suppl. Table IV), whereas SVs of ATRT tumors and cell lines were visualized in a combined manner (Figure 14D). The absolute numbers of all detected SV types across individual samples are summarized in the Supplementary Table III and the statistics in Supplementary Table IV.

In both, ATRT and MB samples, deletions and insertions contributed to the majority of SVs identified with the RVA pipeline (Figures 14C–E, “DEL” and “INS”; Suppl. Table IV), followed by duplications and inversions (Figures 14C–E, “DUP” and “INV”). The minority of SV calls in ATRT samples and MB tumors was contributed by translocations: on average 0.38 (± 0.70) and 7.62 (± 15.21) translocation / sample were identified, respectively (Figure 14D and 14C, “TRANSL”; Suppl. Table IV). In MB cell lines, however, translocations contributed to a higher proportion of SVs, i.e., 147.67 (± 106.87) were identified on average per sample (Figure 14E, SV type “TRANSL”; Suppl. Table IV).

A custom pre-filter for variant annotation was then applied by defining a cut-off of $\leq 1\%$ allele frequency among the Bionano-integrated control database of > 200 healthy individuals, aiming to exclude common SVs and polymorphisms and setting the focus on rare variants only. For each analysed sample, the pre-filtered, rare SV, CNV and aneuploidy call-sets were downloaded, imported into Excel 2016 (Microsoft) and accompanied by parallel visualization and comparison of structural variants identified relative to the DLE-1 labelled reference genome GRCh38 on the Bionano Access Server.

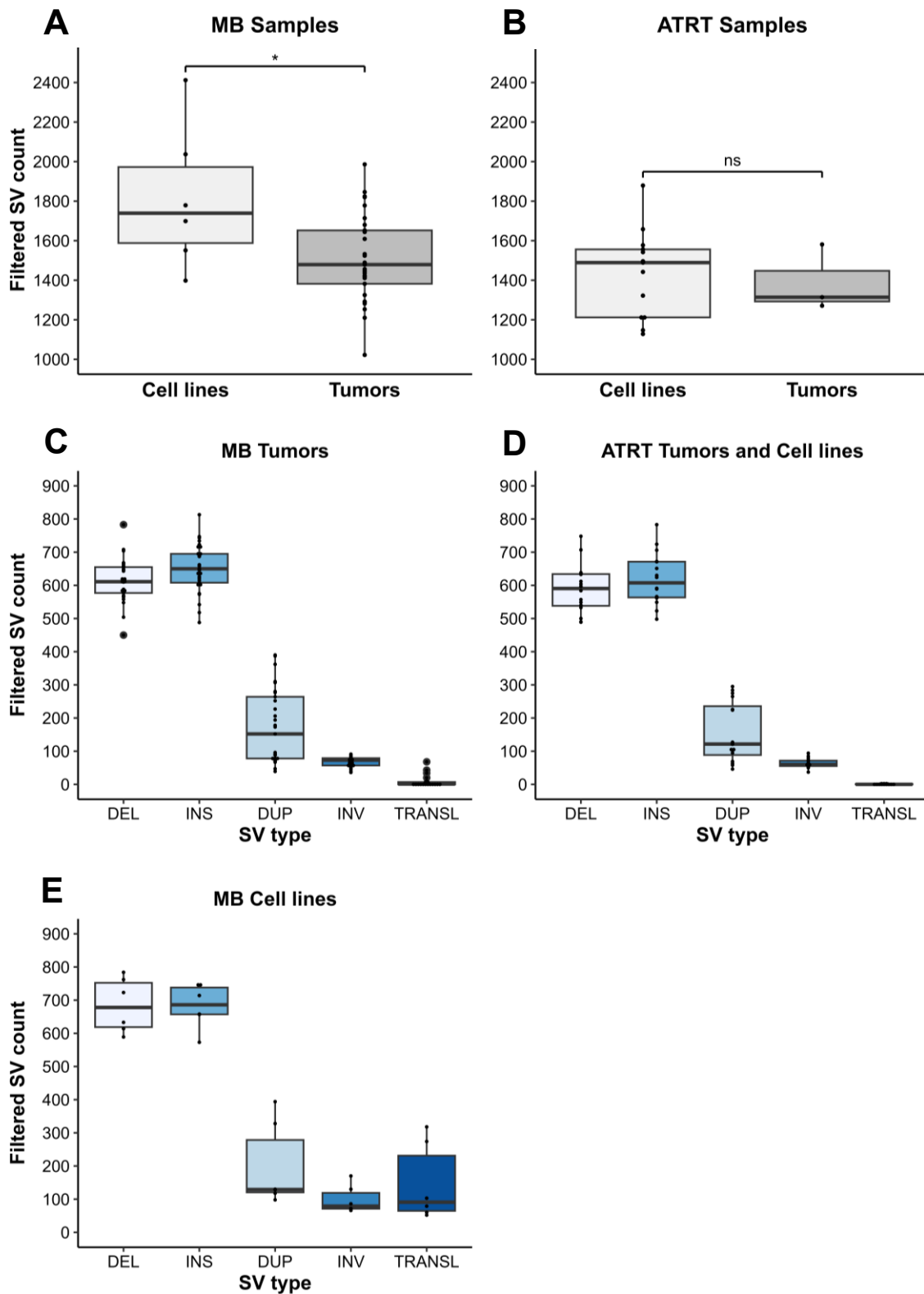


Figure 14. Absolute numbers of OGM RVA-detected SVs in MB (left column) and ATRT samples (right column). The upper panel represents the total number of filtered SVs after application of general SV confidence scores in MB (**A**) and ATRT (**B**) samples, independent of SV types. The lower panel includes three graphs (**C–E**) representing the filtered SV count in MB tumors (**C**), ATRT tumors and cell lines together (**D**) and MB cell lines (**E**), separated by the SV type. The distinction between MB tumor and cell lines was made based on the statistical difference in the one-way ANOVA: *ns*, not significant; *, $p < 0.05$. Distinct SV types are represented as following: *DEL*, deletion; *INS*, insertion; *DUP*, duplication; *INV*, inversion; *TRANSL*, intrachromosomal fusion/interchromosomal translocation.

3.2.1.2 Analysis of annotated *De novo* Assembly Pipeline results

In contrast to the above introduced RVA, the annotated DNP initially builds a new, reference-independent whole genome map from the raw imaged single molecules¹⁶⁴. The assembly approach is based on pairwise alignment of single-molecule maps creating longer and more continuous consensus maps¹⁶⁴. These maps are further refined into a continuous, stand-alone whole genome assembly, which is then used for SV detection when a reference is provided. Additionally, zygosity of individual SVs is estimated. The annotated DNP was conducted in parallel aiming to validate the RVA-identified SVs by a complementary and independent SV calling algorithm and to detect potentially missed candidate SVs. Therefore, the previously constructed DNP was compared to the provided reference, GRCh38, and SVs were annotated.

Upon visualization of the annotated DNP results within the Bionano Access Server, the same low stringency SV filter with the following confidence scores for SV detection was applied, as in the RVA (Figure 13): insertion = 0, deletion = 0, inversion = 0.7, duplication = -1, intra-fusion = 0.05, inter-translocation = 0.05, self molecule count = 5. However, the targeted minimal SV size was set to 500 bp, as pre-defined by both, the minimal resolution of the OGM and the minimal sensitivity of the DNP algorithm¹⁶⁴. Due to this adaptation, all SVs down to the size of 500 bp were included within the DNP call-set. The confidence score for CNVs was set at 0.99 and the VAF range was defined as 0–1, as prior recommended by Bionano. Additionally, the same pre-filtering variant annotation cut-off of $\leq 1\%$ allele frequency among the Bionano-integrated control database of > 200 healthy individuals was applied to exclude common SVs and polymorphisms. The pre-filtered, rare SV, CNV and aneuploidy call-sets were downloaded, imported into Excel and accompanied by parallel Bionano Access Server visualization and manual examination of individual SVs, as described in the RVA paragraph above.

The absolute numbers of DNP-detected, pre-filtered, rare SVs in MB and ATRT samples were somewhat, but not significantly higher as compared to the absolute, pre-filtered, rare SV count of the RVA (data not shown). However, on average 15% of DNP-detected, pre-filtered, rare SVs were below the RVA threshold of 4500 bp. Therefore, these smaller DNP-detected SVs could not be used for validation of the RVA-detected SVs, but were reviewed separately later on (see paragraph 3.3.5).

3.2.2 Integration of DNA structural variants and copy number variants detected by optical genome mapping

Examination of the RVA and DNP SV call-sets was performed manually using the USCS Genome Browser (GENCODE, release 42, GRCh38.p13, https://www.gencodegenes.org/human/release_42.html). Therefore, regions of SVs overlapping with known polymorphisms within the TCAG DGV Curated Catalogue of Human Structural Variation (https://dgv.tcag.ca/dgv/docs/GRCh38_hg38_variants_2020-02-25.txt) above 1% allele frequency and NCBI dbVAR Curated Common SVs (<https://www.ncbi.nlm.nih.gov/dbvar/studies/nstd186/>) databases, as well as all centromeres and p-arms of acrocentric chromosomes (chr13, chr14, chr15) were excluded. Identical SVs with respect to genomic size and position appearing in more than two samples were considered either polymorphisms or methodological artefacts, and were thus excluded as well. Multiple identical SVs within one sample were considered duplicates and their total number was reduced to a single entry. In cases where SV breakpoints were detected on different chromosomes (interchromosomal translocations), the so-called “breakpoint region”, encompassing the last detected label and the first non-detected label, was defined and individually examined. The “breakpoint regions” were considered affected by an interchromosomal rearrangement, as no precise breakpoint localization was possible due to the resolution of the OMG method. Low confidence SVs (confidence score ≤ 0.5) were removed from the dataset if not otherwise supported by the CNV algorithm or by both pipelines simultaneously. Additionally, the RVA- and DNP-identified SVs of the respective sample were compared among each other and summarized in one final list of high-confidence, rare SVs per analysed case. The final absolute numbers of high-confidence, rare SVs in individual cases are summarized within the Supplementary Table III and the statistics in Supplementary Table V.

Upon intersection of the high-confidence rare SVs with GENCODE (V42) annotations (https://www.gencodegenes.org/human/release_42.html), 248 events affecting coding sequence, 137 events in untranslated regions (UTRs), 112 events in introns, and 115 intergenic events were detected in the 16 ATRT samples (Suppl. Table III). Of those, 53 SVs overlapped with either exonic or intronic regions of cancer-associated genes from the Cancer Gene Census of the Catalogue Of Somatic Mutations In Cancer (COSMIC CGC, <https://cancer.sanger.ac.uk/census;v98>). In 29 MB tumors, 433 events affecting coding sequence, 154 events in UTRs, 165 events in introns, and 192 intergenic events were detected (Suppl. Table III). Of those, 90 SVs were intersecting either exonic or intronic regions of cancer-associated genes. In contrast, 861 events affecting coding sequence, 166 events in UTRs, 280 events in introns, and 168 intergenic events were detected in 6 MB cell lines, among which

241 SVs affected either exonic or intronic regions of cancer-associated genes from the COSMIC CGC.

The absolute numbers and individual types of cumulative RVA and DNP-identified, filtered, high-confidence, rare SVs ≥ 4.5 kbp in MB and ATRT samples are visualized in Figure 15. On average $40.46 (\pm 11.47)$ and $26.67 (\pm 5.56)$ SVs could be identified as high confidence, rare SV events in ATRT cell lines and ATRT tumors, respectively (Figure 15B; Suppl. Table V). The overall number of detected SVs among MB cell lines remained significantly higher as compared to MB tumors ($F(1, 34) = 148.9$, $p = 8.9 \times 10^{-14}$), whereas $246.00 (\pm 79.06)$ and $32.52 (\pm 23.31)$ SVs were identified, respectively (Figure 15A; Suppl. Table V). Thus, the detailed high-confidence, rare SVs found in MB tumors and MB cell lines were again presented separately (Figure 15C and 15E). The types of high-confidence, rare SVs in ATRT tumors and ATRT cell lines, however, were visualized together in Figure 15D.

Although the integrated cut-offs and the subsequent filtering steps greatly reduced the overall number of detected SVs among all analysed samples, deletions still contributed to the majority of identified rare SVs (Figures 15C–E; Suppl. Table V). In combined ATRT samples, rare deletions (“DEL” = 19.06 ± 4.34) were followed by insertions (“INS” = 11.19 ± 5.67), duplications (“DUP” = 6.56 ± 4.95), inversions (“INV” = 0.69 ± 0.77) and lastly translocations (“TRANSL” = 0.38 ± 0.70), including both, intrachromosomal fusions and interchromosomal translocations (Figure 15D). In MB tumors (Figure 15C), the prevalence of rare SVs was comparable to ATRT samples, whereas rare deletions (“DEL” = 13.41 ± 8.06) were also followed by insertions (“INS” = 7.55 ± 2.61) and duplications (“DUP” = 4.90 ± 5.39). However, the minority of rare SVs in MB tumors was contributed to inversions (“INV” = 2.24 ± 5.42) instead of translocations (“TRANSL” = 4.45 ± 7.70). In contrast, in MB cell lines (Figure 15E), translocations were the second most frequently detected type of high confidence, rare SVs after deletions (“TRANSL” = 58.33 ± 23.00) followed by duplications (“DUP” = 54.83 ± 32.96), insertions (“INS” = 35.00 ± 14.79) and finally, inversions (“INV” = 26.33 ± 18.98).

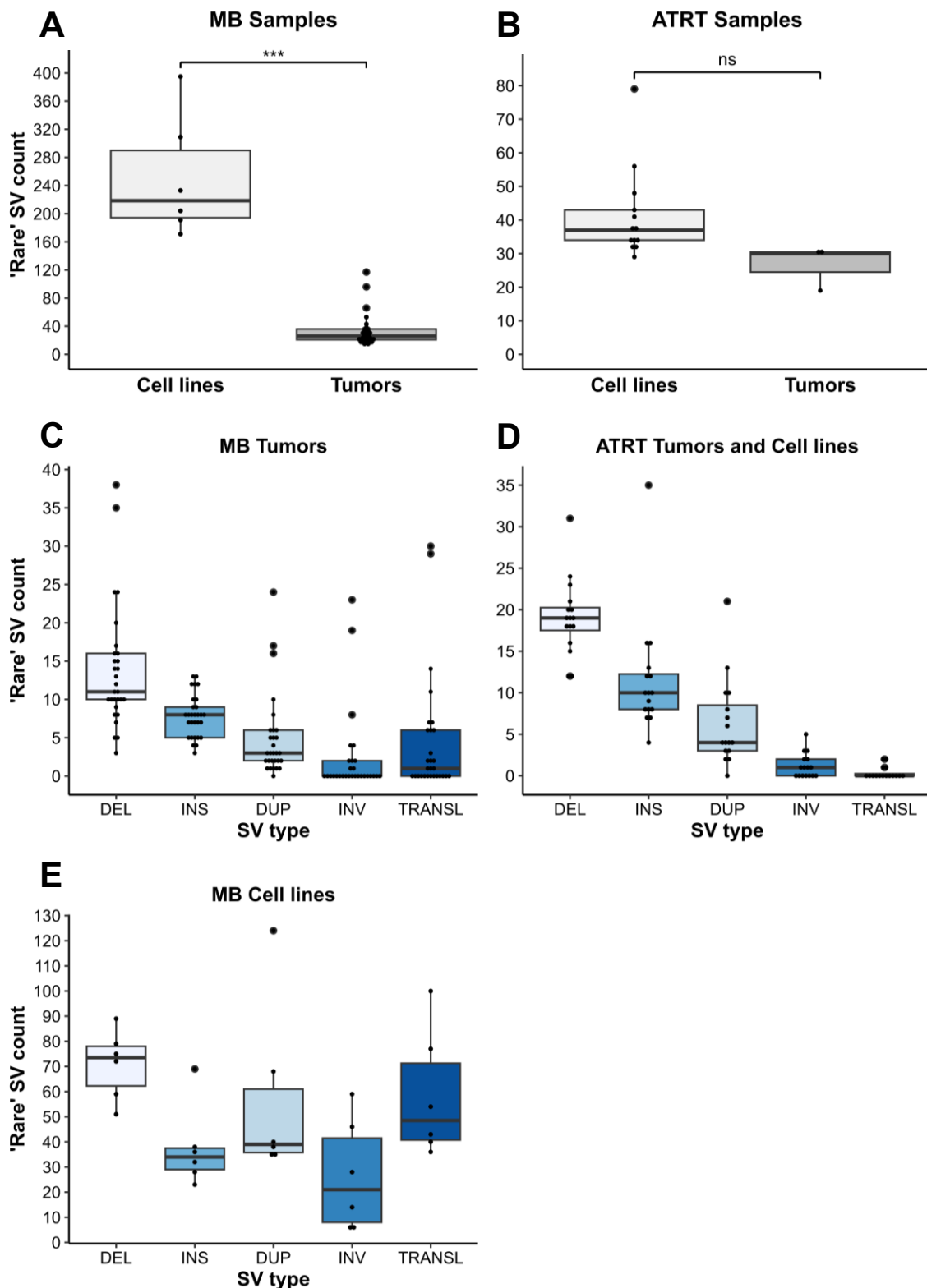


Figure 15. Absolute numbers of rare SVs in MB (left column) and ATRT samples (right column). The upper panel represents the total number of rare SVs in MB (**A**) and ATRT (**B**) samples, independent of SV types, after the exclusion of common variants present in the OGM-integrated control database (> 1% freq). The lower panel includes three graphs (**C–E**) representing the ‘rare’ SV count in MB tumors (**C**), ATRT tumors and cell lines together (**D**) and MB cell lines (**E**), separated by SV type. The distinction between MB tumor and cell lines was made based on the statistical difference of the one-way ANOVA: ***, $p < 0.001$; *ns*, not significant. Distinct SV types are represented as following: *DEL*, deletion; *INS*, insertion; *DUP*, duplication; *INV*, inversion; *TRANSL*, intrachromosomal fusion/interchromosomal translocation.

For the RVA/DNP CNV and aneuploidy call-sets, the global thresholds for CN gains and losses are pre-defined within the CNV algorithm of the analysis pipelines which examine the genome coverage depth. Therefore, the relative abundance of DNA fragments from each chromosome is measured and compared to a “normal” (diploid) reference. Any deviations from the normal diploid state are identified by comparison of the relative copy number of the respective chromosome regions from the sample against the reference. If a whole chromosome is present in more or fewer copies than expected (e.g., trisomy, monosomy), a detectable and uniform increase or decrease in the coverage signal for the respective chromosome is detected and is referred to as an “aneuploidy”¹⁷⁹. The same applies to the partial or segmental CNVs such as duplications/deletions, but the coverage signal is more localized to a specific chromosomal region. The final CNV and aneuploidy results of each analysed tumor sample and cell line are summarized in Supplementary Table II.

All OGM-identified CN segments without detected alterations within the range of $1.800 < CN \leq 2.200$ were considered diploid and were excluded from the CNV call-set. Those CN segments are referred to as “balanced”. The CN segments, which were explicitly listed within the OGM CNV call-set, were automatically assigned a fractional CN (Suppl. Table II, “fractCN”) and defined as “gain” type, when $CN > 2.200$, or as “loss” type, when $CN < 1.800$. For detailed distinction of specific and localized regions affected by CNVs within the framework of the analyses, “CN gain” was designated when $2.200 < CN \leq 3.500$ and “amplification” when $CN > 3.500$. Conversely, $CN < 1.800$ was termed as “hemizygous deletion” and $CN < 0.800$ as “homozygous deletion”. Similar successive fractional CN values on one chromosome, which were assigned to the overall same CN, were combined in one entry within the Supplementary Table II, whereas the starting (Suppl. Table II, “Start”) and ending coordinates (Suppl. Table I, “End”) on the respective chromosome were concatenated. Furthermore, CNV segments were differentiated into “focal” and “partial” dependent on the size of the affected region (Suppl. Table II, “Size”), which was calculated as the difference of the starting and ending coordinates. As suggested by Bierkens *et al.*¹⁸⁰, “focal” CN aberrations were designated upon size < 3 Mbp and “partial” CN aberration upon CN size ≥ 3 Mbp but not exceeding the length of an entire chromosomal arm. Therefore, the fractional chromosomal length of the respective fractional CN (Suppl. Table II, “fractCNsize”) was calculated as the relative proportion of the affected region to the total length of the respective GRCh38 reference chromosome. Monosomies or trisomies, which are aneuploidies affecting whole chromosomes, were designated upon calculated fractional CN size ≥ 0.630 . Partial aneuploidies of whole chromosomal arms were designated upon calculated fractional CN size ≥ 0.315 . Finally, in cases where alternating fractional CN values with overall distinct CNs were assigned to different segments on the same chromosome (e.g. fractCN = 2.323, fractCN = 1.645 and fractCN = 2.884), a “complex” CN signature was designated. Detailed CNV data are listed in Supplementary Table II.

3.3 Characterization of medulloblastoma cell lines and tumors

3.3.1 DNA methylation-based classification of medulloblastoma samples

Six MB cell lines and 29 MB tumors were subjected to DNA methylation profiling by application of Illumina 850k EPIC array. The DNA methylation-based CNS tumor methylation classifier (v12.8) assigned 25 of 29 investigated MB tumors to one of the three medulloblastoma methylation families (MF: MB WNT, MB SHH, MB non-WNT/non-SHH) with calibrated confidence scores ≥ 0.9 ¹⁶⁰. Twenty-one MB tumors were further assigned to distinct MB methylation (sub)classes (MC) based on calibrated classifier scores ≥ 0.9 : “Medulloblastoma, WNT-activated” (MB WNT, n = 3), “Medulloblastoma, SHH-activated, subclass 1 or 2” of the infant subgroup (MB SHH–infant, n = 5), “Medulloblastoma, SHH-activated, subclass 3 or 4” of the non-infant subgroup (MB SHH–child, n = 1), “Medulloblastoma, non-WNT/non-SHH, Group 3 subtype, subclass I–IV” (MB Group 3, n = 3), and “Medulloblastoma, non-WNT/non-SHH, Group 4 subtype, subclass V–VIII” (MB Group 4, n = 9). Eight MB tumors were not assigned to any of the MB methylation (sub)classes with a classifier score ≥ 0.9 , however, could also be stratified based on classifier scores between 0.44 and 0.86 (Table 13; Suppl. Table I).

The HD-MB03 cell line was assigned to the “Medulloblastoma, non-WNT/non-SHH” methylation family with a MF classifier score of 0.68 and the “Medulloblastoma, non-WNT/non-SHH, subclass II” with a MC classifier score of 0.53 (Table 13). For the five remaining MB cell lines, no classifier scores of ≥ 0.3 were obtained. Thus, these cell lines could not be assigned to any specific MB methylation (sub)class (Table 13; Suppl. Table I).

3.3.2 OGM-based analysis of aneuploidies and global DNA copy number variants in medulloblastoma samples

Following DNA methylation-based classification of the MB samples and their segregation into molecular groups and subgroups, OGM-detected genome-wide CNV profiles of six MB cell lines and 29 MB tumors were assessed. Therefore, the annotated OGM analyses were performed for each processed sample as described in paragraph 2.5.6. An overview of all MB cell lines and tumors as classified by 850k EPIC DNA methylation analysis as well as the OGM-identified structural DNA alterations are summarized in Table 13. The individual OGM-detected genome-wide CNV profiles of each individual MB tumor and cell line are provided in Supplementary Figure I. All OGM-identified chromosomal regions affected by focal or partial CNVs, or whole-chromosome aneuploidies, are summarized in Supplementary Table II.

As indicated in Figure 16A, the CNV prevalence, here defined as number of chromosomes affected by CNVs per analysed case, was significantly different between the distinct groups of

MB tumors (ANOVA, $F(4, 24) = 7.81$, $p = 0.00035$). Based on the significant result of the analysis of variance, the Tukey's HSD test was applied to determine and compare significant differences between specific MB groups. MB Group 3 harboured genomes with significantly higher prevalence of CNVs (14.25 ± 3.30) as compared to MB SHH–infant ($p = 0.00027$, 95% CI = [-19.28, -5.22]), MB WNT ($p = 0.00341$, 95% CI = [-19.90, -3.26]) and MB SHH–child ($p = 0.04420$, 95% CI = [-14.76, -0.14]), as determined by Tukey's HSD test (Figure 16A). However, no significant difference in CNV prevalence was found between MB Group 3 and Group 4.

A simplified overview of OGM-detected CNVs (Figure 16B) is graphically sorted by individual cases of distinct MB groups on the horizontal axis, and the presence of CNVs on the respective chromosome on the vertical axis. Many different CN alterations were detected by OGM in MB Group 3 reflecting frequent occurrence of chromosomal rearrangements in this particular group of tumors. Also, in three out of four MB Group 3, isochr17q was detected (Figure 16B, indicated as “Complex” CN). In contrast, the overall least CNV prevalence (2.00 ± 1.10) was found in MB SHH–infant cases (Figure 16A). Although five out of six SHH–infant tumors presented CNVs on at least one chromosome, the CN alterations were mainly focal. Only three SHH–infant tumors presented whole-chromosome aneuploidies: two tumors had trisomy of both chr2 and chr3, and another tumor contained chr9 monosomy. Otherwise, the genomes of MB SHH–infant tumors were mostly balanced (Figure 16B).

The CNV prevalence in MB WNT (2.67 ± 0.58) was similar to MB SHH–infant tumors, whereas the following whole-chromosome aneuploidies were detected: monosomy of chr6 was present in all three analysed tumors and monosomy of chrX and chr11, and loss of chrY was each observed once (Figure 16B). Among the five MB SHH–child cases, $6.80 (\pm 3.49)$ chromosomes were affected per individual case. In addition to other detected CNVs, one particular MB SHH–child tumor presented CNV patterns which were consistent with isochromosome formation of 9p and 10p (Figure 16B, indicated as “Complex CN”). The highest intra-group heterogeneity of CNVs was present in MB Group 4 (8.00 ± 4.90) and chr17 was affected in all analysed Group 4 tumors. The typical isochr17q pattern was found in 9/11 MB Group 4 cases and the remaining two tumors presented trisomy of chr17. Additionally, many complex CNVs manifested within the CN profiles of individual Group 4 cases as repetitive, sub-chromosomal CN alterations or simultaneous gains and losses of whole chromosome arms (indicative of isochromosome presence). These complex patterns of OGM-detected CNVs were almost exclusively found in MB Group 3 and 4.

No cumulative visualization of CN profiles of the MB cell lines was performed due to the presence of multiple, highly alternating CN segments across whole cell line genomes, which did not allow for simplification. Otherwise, each chromosome would be simply labelled as

“complex” and no distinction of rearrangement patterns would be possible. Also, since no ambiguous classification was achieved for any of the 6 MB cell lines, the MB-group affiliations were also not definite. Nevertheless, the OGM-identified specific chromosomal regions affected by focal/partial CNVs or aneuploidies (Suppl. Table II) and individual CN profiles of MB cell lines are depicted in Supplementary Figure I.

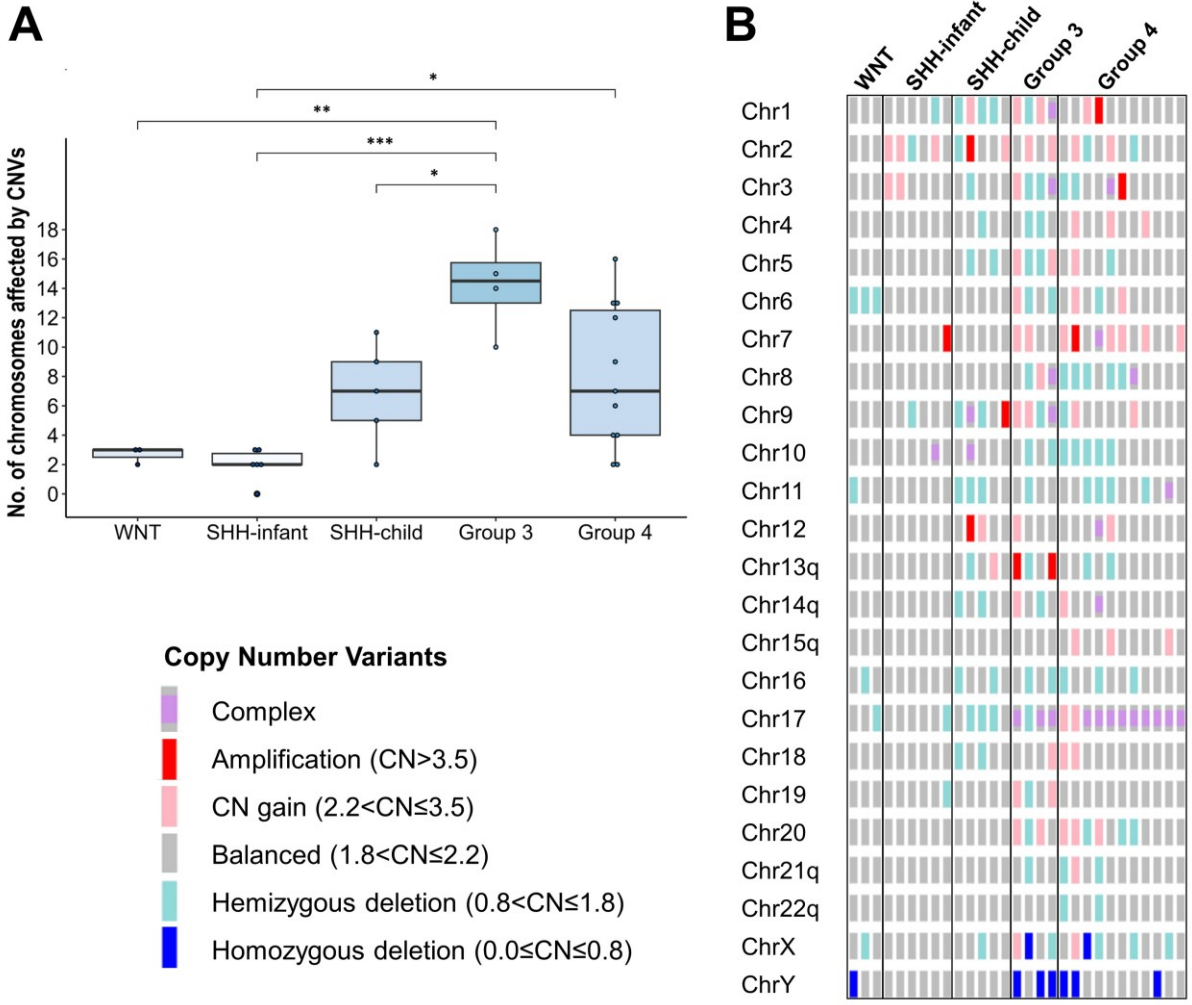


Figure 16. OGM-detected copy number variants in 29 MB tumors. **(A)** Group-wise comparison of the number of chromosomes affected by CNVs using ANOVA and Tukey’s test at 5% level of significance: *, $p < 0.05$; **, $p < 0.01$; ***, $p < 0.001$. **(B)** Simplified overview of CNVs sorted by MB groups presenting the detected CNV on the respective chromosome. Each column represents one MB tumor.

3.3.3 Global copy number variation analysis of medulloblastoma samples derived from DNA methylation array data

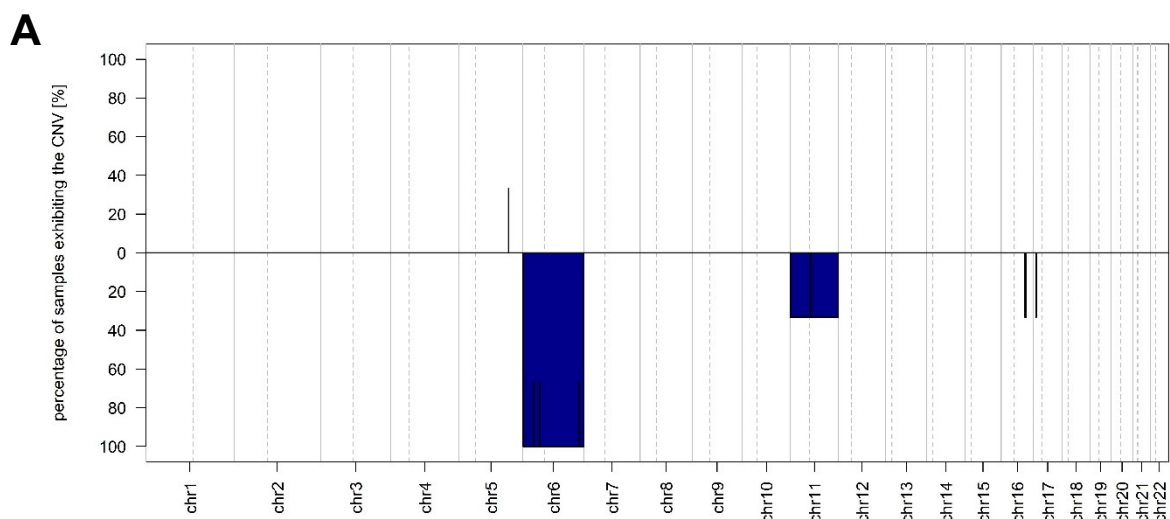
In addition to OGM-derived analysis of aneuploidies and global CNVs, global CNV profiles were inferred from DNA methylation array-based datasets of six MB cell lines and 29 MB tumors. The respective individual CNV profiles of each MB tumor and cell line cases are provided in Supplementary Figure I. For an overview of the chromosomal aberrations characteristic for the respective MB group tumors as well as MB cell lines, summary CNV plots were created with “conumee 2.0” (Figure 17). Unlike in individual CNV profiles of single cases, where the CN ratio is indicated by the y-axis and is plotted according to the chromosomal location on the x-axis (example in Figure 8), and the summary CNV plots visualize the percentage of changes in cumulated cases on the y-axis at the respective chromosomal location on the x-axis. Thus, the y-axis has a baseline of 0% corresponding to zero cases and a range from 0–100% above and below the baseline, representing the percentage of cumulated cases showing the respective DNA copy number gain or loss, respectively. Shifts below the baseline at the respective chromosomal location are blue and indicate CN losses whereas the magnitude of the shift represents the frequency of the identified CN loss among all cases. This also applies to CN gains, visualized in red/orange, only the shifts are shown above the baseline (Figure 17A–F).

In all three MB WNT tumors loss of whole chr6 was identified (Figure 17A), as indicated in the summary CNV profile by the blue bar with the frequency corresponding to 100%. Furthermore, loss of the whole chr11 was detected in ~ 33%, which corresponds to one out of three samples (Figure 17A). In six MB SHH–infant tumors, only very few CNVs were detected, none of which was recurrent (Figure 17B). In 16.7% of combined SHH–infant cases, corresponding to a single tumor, partial gains and losses affecting chr2, partial losses on chr10 and chr11p and a loss of whole chr9 was detected. MB SHH–child cases were particularly enriched for cases with loss of chr9q, with three of five analysed tumors (60%) presenting this CNV (Figure 17C). Furthermore, in 40% of MB SHH–child (2/5 tumors), losses of chr11p, chr14q and chr18q were prevalent. Also, large losses affecting whole chr2, chr4, chr11, chr16 and chr18 or complete chromosomal arms of chr3p, chr5q, chr10q and chr11q, and larger gains affecting complete chromosomal arms of chr9p, chr10p and chr13q were documented in one SHH–child tumor. The signature of chr9p and chr10p gains in combination with losses of the respective long chromosomal arms, chr9q and chr10q, suggests a presence of isochromosomes, isochr9p and isochr10p.

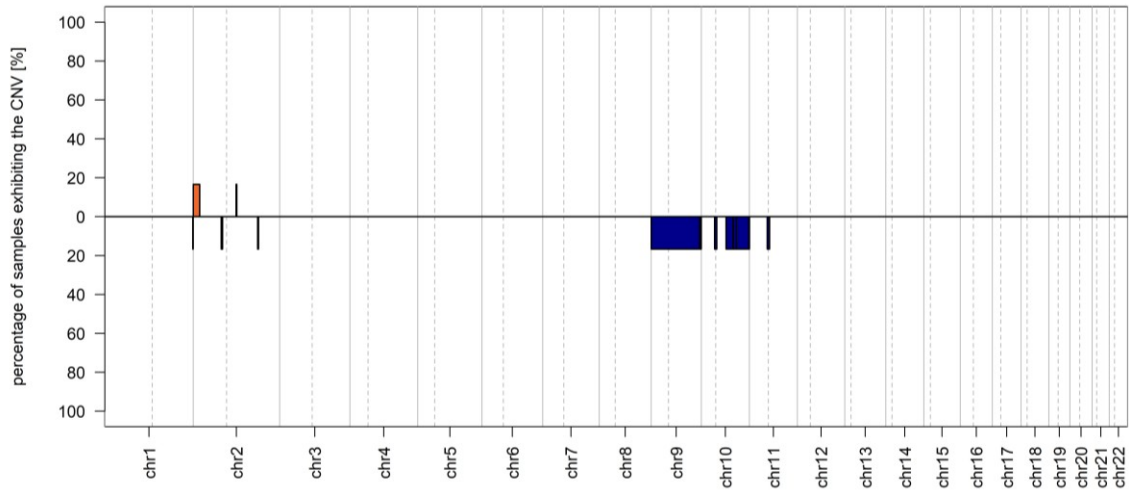
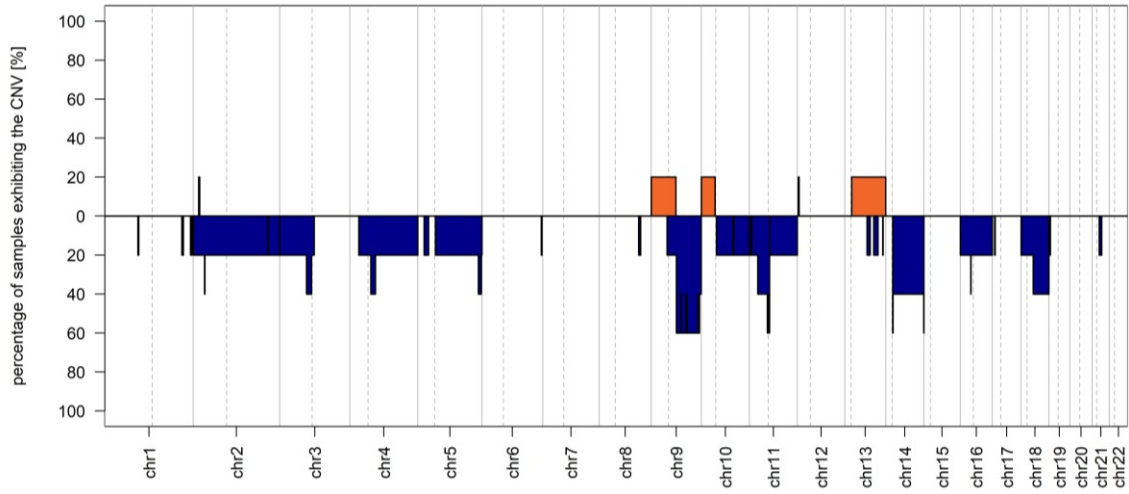
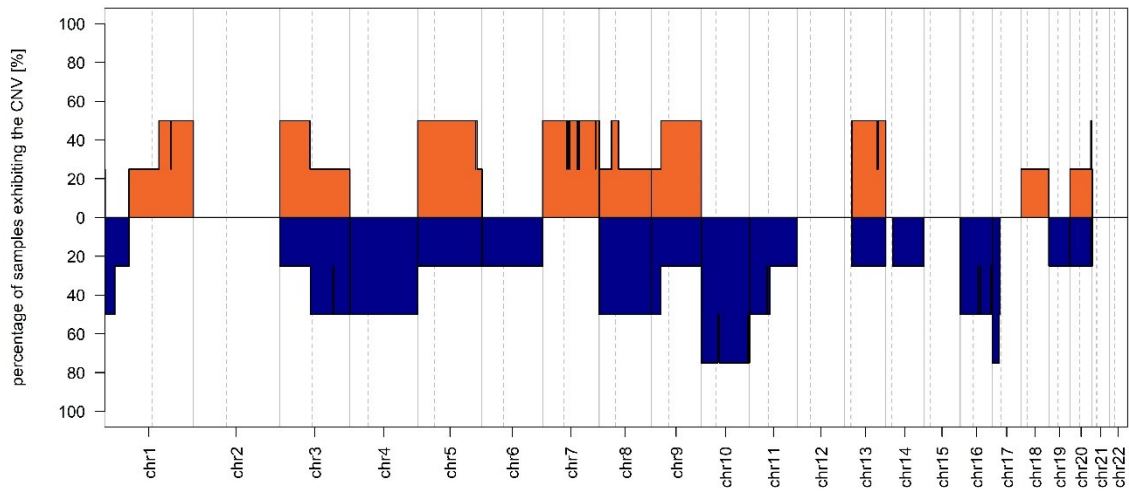
Among four analysed MB Group 3 tumors, multiple CN alterations affected either whole chromosomal arms or complete chromosomes (Figure 17D). In 75% of cases, corresponding

to three out of four tumors, losses of both whole chr10 and chr17p were detected. Also, in 50% of cases, corresponding to 2 tumors, gains of chr1q, chr3p, chr5, chr7, chr8q(part), chr9, chr13 and losses of chr1p(part), chr3q, chr4, chr8, chr11p, and cr16, were identified. Only chr2, chr12, chr15, chr21 and chr22 remained unaffected by CN alterations among all MB Group 3. MB Group 4 tumors were particularly enriched for cases with a typical CN signature indicative of isochr17q (Figure 17E), in 82% (9/11 tumors) loss of chr17p was accompanied with gain of chr17q. The second frequent CNV present in 45.5% (5/11 tumors) was the gain of chr7 and partial losses of chr8pq, chr10q and chr11p. In addition, other partial CN losses and gains were detected at lower frequencies, ranging from 9.1% (1/11 tumors) to 36.4% (4/11 tumors). CN losses of whole chr8 and chr10 were observed in 36.4% (4/11 tumors) and 27.3% of cases (3/11 tumors), respectively. Also, whole chr4 was affected by CN gains in 27.3% of MB Group 4 (3/11 tumors).

In six analysed MB cell lines, a multitude of partial and whole chromosome CN alterations was present, whereas not a single chromosome remained unaffected (Figure 17F). The most abundantly identified CN alteration was the gain of chr1, ranging to up to 83.3% of cases and thus corresponding to five of the six MB cell lines. Also, partial losses of distal regions of chr11q and chr14q were detected in up to 83.3% (5/6 cell lines) as well. Interestingly, both chr1 and chr2 were least affected by CN losses and displayed only partial chromosomal regions affected by CN losses in 16.7% of cases (1/6 cell lines). Conversely, chr10 was least affected by CN gains, displaying a partial CN gain on chr10p in 16.7% of cases (1/6 cell lines).



(Figure legend is on page 72.)

B**C****D**

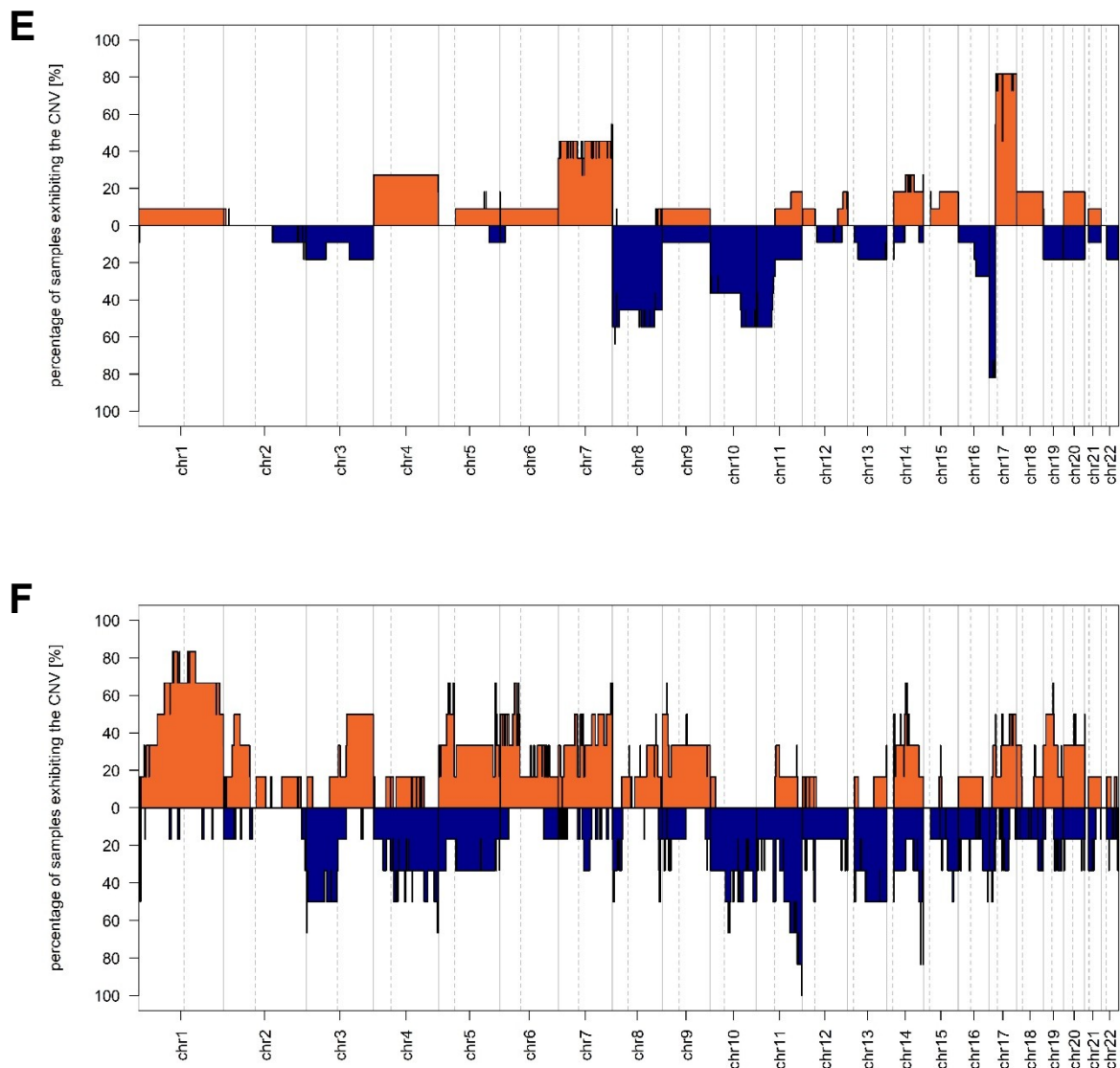


Figure 17. Summary CNV profiles of MB samples derived from DNA methylation array data. Three cases of MB WNT (A), six MB SHH–infant (B), five MB SHH–child (C), four cases of MB Group 3 (D), eleven MB Group 4 (E), and six MB cell lines (F). The y-axis of each summary plot represents the frequency of changes in % of the cumulated cases in each group at the respective chromosomal location (x-axis). The dashed vertical lines indicate the locations of the centromeres and separate the respective chromosomes into p-arm (left) and q-arm (right) segments. CN gains are represented in orange/red above, and CN losses are represented in dark blue below the baseline. Sex chromosomes are not included.

To summarize the CNV results of all analysed MB cases, a cumulative overview of CNV profiles of the individual MB tumors and cell lines was plotted in a clustered genome heatmap (Figure 18). The cumulated genome heatmap is a visualization where rows represent individual CNV profiles of 29 MB tumors and 6 MB cell lines, which are stacked on top of each other and clustered according to common features as indicated by the dendrogram on the y-axis of the plot. As in individual CNV profiles of single cases, the CN ratio in the cumulative profile is plotted according to the chromosomal location on the x-axis. CN ratios above the baseline, determined by a balanced, healthy reference, represent CN gains and are labeled in

orange/red. CN ratios below the baseline represent CN losses and are labelled in blue. The x-axis in Figure 18 depicts chr1–22, visually separated by vertical black lines. The sex chromosomes were purposely excluded, in order to prevent possible clustering based on sex.

The cases on the upper and lower rim of the heatmap in Figure 18, MB20t, a MB tumor of SHH–infant subtype and Daoy, a MB cell line, represent samples with the highest dissimilarity and exhibit least common features. The individual cases ordered within the frame of the heatmap are most similar to the neighbouring cases above and below, and the complexity of the CNV profiles increases from top to the bottom of the heatmap. Within the upper heatmap section, mostly balanced CNV profiles with only few intensive-coloured CNVs can be observed. Here CNV profiles of all six SHH–infant tumors (MB20t, MB16t, MB27t, MB12t, MB28t and MB24t), three out of five SHH–child tumors (MB13t, MB19t and MB11t) and three out of eleven Group 4 tumors (MB3t, MB14t and MB17t) are located. In the middle of the heatmap, cases with multiple intensive-coloured CNVs of similar chromosomal localizations are presented. Among them are CNV profiles of four other Group 4 tumors (MB21t, MB2t, MB25t and MB22t), two of four Group 3 tumors (MB23t and MB29t), all three MB WNT (MB10t, MB9t and MB8t) and the two remaining MB SHH–child tumors (MB1t, MB15t). The bottom of the heatmap includes CNV profiles with a multitude of different CNVs indicated by intensive red and blue colouring. Here, the CNV profiles of four Group 4 (MB26t, MB6t, MB7t and MB5t), two Group 3 tumors (MB18t and MB4t), and all of the MB cell lines (HD-MB03, UW288-3, MED8A, ONS76, D283 and Daoy) are clustered.

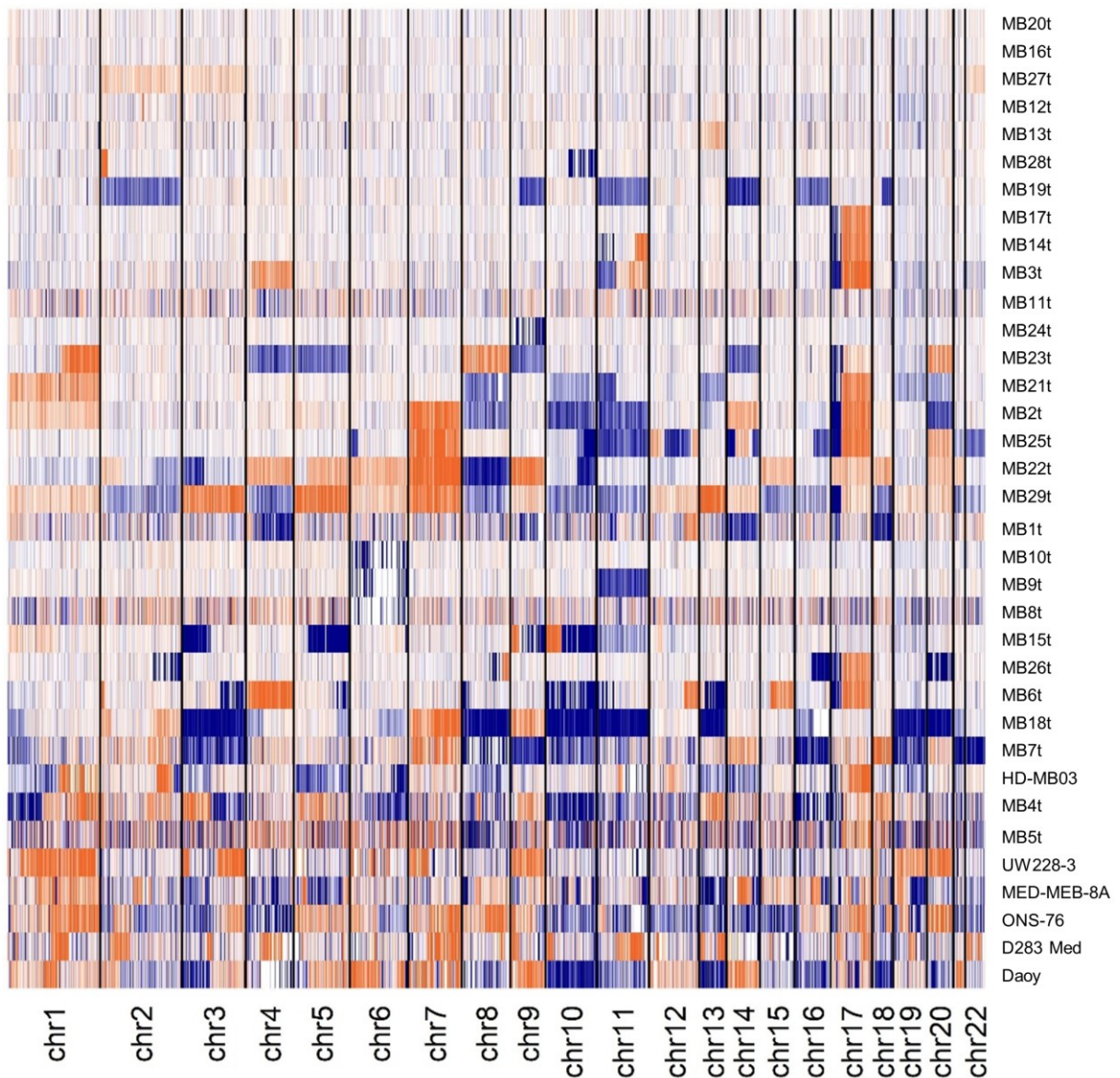


Figure 18. Summary genome heatmap of CNV profiles of MB samples as derived from DNA methylation array data. Shown is a clustered, cumulative overview of individual CNV profiles of MB tumors (MB1t–MB29t) and MB cell lines. The vertical axis shows the individual CNV profiles of the respective cases, labelled on the right. The horizontal axis depicts chr1–22, visually separated by the vertical black line. CN gains are orange/red and CN losses are dark blue. Sex chromosomes are not included.

Table 13. Summary of investigated MB cell lines and primary tumors as classified by EPIC 850k DNA methylation analysis and OGM-detected SVs, aneuploidies and subchromosomal CNVs. A “balanced genome” is diploid and has a CN = 2, “gain” represents $2.2 < CN \leq 3.5$, “amplification” has $CN \geq 3.5$, “hemizygous deletion” has $0.8 < CN < 1.8$ and a “homozygous deletion” represents the total loss of the respective genomic region, $CN < 0.8$.

Sample Type	Sample ID	Brain tumor classification, Heidelberg classifier version v12.8 (calibrated score)	OGM Aneuploidies and CNVs	Nr. of rare SVs/ somatic SVs
Cell line	D283 Med	No assignment (no score ≥ 0.3)	Highly complex CN patterns; many gains, amplifications and losses across the whole genome, many inter- & intrachromosomal rearrangements	307
Cell line	Daoy	No assignment (no score ≥ 0.3)	Complex CN patterns; many gains, amplifications and losses across the whole genome, several inter- & intrachromosomal rearrangements present	187
Cell line	HD-MB03	Medulloblastoma, non-WNT/non-SHH, Group 3 subtype, subclass II (0.52865)	Isochr17q; partial amplification on: chr1q, chr2q, chr9p; focal amplification on: chr2q, chr8q, chr14q; inter- & intrachromosomal rearrangements present	193
Cell line	MED-MEB-8A	No assignment (no score ≥ 0.3)	Highly complex CN patterns; many gains, amplifications and losses across the whole genome, many inter- & intrachromosomal rearrangements	391
Cell line	ONS-76	No assignment (no score ≥ 0.3)	Isochr17q; complex CN patterns; many gains, amplifications and losses across the whole genome, several inter- & intrachromosomal rearrangements present	231
Cell line	UW228-3	No assignment (no score ≥ 0.3)	Trisomy: chr1, chr9, chr19, chr20; partial gain on: chr3q, chr3q; partial amplification on: chr5p, chr7p; focal gain on chr7q; chr6 chromothripsis; partial hemizygous deletion on: chr7q, chr11q	167
Tumor	MB1t	Medulloblastoma, SHH-activated, subclass 4 (0.81579)	Monosomy: chr4q, chr14, chr18, chrXp; focal hemizygous deletion on chr1p; partial hemizygous deletion on: chr9q, chr11p, chr17p; partial homozygous deletion on chr9q; partial gain on chr12q; several translocations	36/15
Tumor	MB2t	Medulloblastoma, non-WNT/non-SHH, Group 4 subtype, subclass V (0.92546)	Isochr17q; chr7 trisomy; partial gain on chr4p; partial hemizygous deletion on chr11p (chr4p-11p translocation)	17/6
Tumor	MB3t	Medulloblastoma, non-WNT/non-SHH, Group 4 subtype, subclass VIII (0.99992)	Isochr17q; homozygous deletion of chrY	36/2
Tumor	MB4t	Medulloblastoma, non-WNT/non-SHH, Group 3 subtype (0.94463) (no clear subclass)	Isochr17q; trisomy: chr3p, chr5, chr13, chr18; monosomy: chr3q, chr6q, chr10, chr16; homozygous deletion of chrY; complex: chr1, chr8, chr9; focal hemizygous deletion on chrXq; partial gain on chr2q; focal gain on chr7q, chr19p; focal amplification on chr13q (focal high-level GPC5 amplification (CN=19)); translocations: chr1p-1q, chr3q-9p	117
Tumor	MB5t	Medulloblastoma, non-WNT/non-SHH, Group 4 subtype (0.73809)	Isochr17q; trisomy: chr6, chr7; monosomy: chr8, chr20; focal amplification on chr3p; chr2q-9q translocation	29
Tumor	MB6t	Medulloblastoma, non-WNT/non-SHH, Group 4 subtype, subclass V (0.90828)	Isochr17q; chr4 trisomy; monosomy: chr10, chr11p, chr13; complex chr3p; partial hemizygous deletion on: chr5q, chr8p; focal gain on: chr2p, chr7q; partial gain on: chr12q, chr15q; several translocations	53

Tumor	MB7t	Medulloblastoma, non-WNT/non-SHH, Group 4 subtype, subclass VII (0.99867)	Trisomy: chr7, chr14, chr17, chr18, chr20; monosomy: chr3, chr8, chr9, chr16, chr21, chr22; homozygous deletion of chrY; partial hemizygous deletion on chr10q	15
Tumor	MB8t	Medulloblastoma, WNT-activated (0.99482)	Monosomy: chr6, chrX; focal hemizygous deletion on chr16q	13
Tumor	MB9t	Medulloblastoma, WNT-activated (0.99958)	Monosomy: chr6, chr11; homozygous deletion of chrY	24/1
Tumor	MB10t	Medulloblastoma, WNT-activated (0.99988)	Chr6 monosomy; focal hemizygous deletion on chr17p	20
Tumor	MB11t	Medulloblastoma, SHH-activated, subclass 4 (0.44044)	Focal gain on chr2p; focal amplification on chr9p	42
Tumor	MB12t	Medulloblastoma, SHH-activated, subclass 1 (0.99998)	Trisomy: chr2, chr3	16/4
Tumor	MB13t	Medulloblastoma, SHH-activated, subclass 3 (0.71393)	Chr13 trisomy, partial hemizygous deletion on: chr1q, chr5q; focal hemizygous deletion on: chr16p, chr17p; chr6p-19q translocation	25
Tumor	MB14t	Medulloblastoma, non-WNT/non-SHH, Group 4 subtype, subclass VIII (0.99993)	Isochr17q, chrX monosomy, complex chr11 (chr11p-q translocation); focal gain on chr15q	22/5
Tumor	MB15t	Medulloblastoma, SHH-activated, subclass 3 (0.59341)	Chr1p trisomy, monosomy: chr3p, chr5q; complex: chr9, chr10 (both isochromosome signature); partial hemizygous deletion on chr11pq; focal hemizygous deletion on: chr6q, chr13q, chr17p; focal homozygous deletion on: chr5q, chrXp; high-level amplification of <i>MYCN</i> (CN=140 on chr2p) & <i>CCND2</i> (CN=19 on chr12p); chr2p-12p translocation	96/81
Tumor	MB16t	Medulloblastoma, SHH-activated, subclass 1 (0.99621)	Balanced genome	18/2
Tumor	MB17t	Medulloblastoma, non-WNT/non-SHH, Group 4 subtype, subclass VIII (0.99990)	Isochr17q; focal gain on chr7q	27/3
Tumor	MB18t	Medulloblastoma, non-WNT/non-SHH, Group 3 subtype, subclass IV (0.99990)	Trisomy: chr7q, chr9; monosomy: chr3, chr8, chr10, chr11, chr13, chr16p, chr19, chr20; homozygous deletion of: chr16q, chrX; partial hemizygous deletion on: chr1p, chr4p, chr5q, chr6q, chr17p, chr21q; focal hemizygous deletion on chr17q; partial gain on: chr2p, chr2q, chr7p, chr9p,chr9q; several translocations	28/10
Tumor	MB19t	Medulloblastoma, SHH-activated, subclass 4 (0.99227)	Monosomy: chr2, chr9q, chr11, chr14, chr16; partial hemizygous deletion on: chr1q, chr18q	25/4
Tumor	MB20t	Medulloblastoma, SHH-activated, subclass 2 (0.95996)	focal amplification on chr7p; focal hemizygous deletion on: chr17q, chr19p; chr3q-Xq translocation	23/9
Tumor	MB21t	Medulloblastoma, non-WNT/non-SHH, Group 4 subtype, subclass V-association (0.77007)	Isochr17q; chr1 trisomy, monosomy: chr8, chr10, chr11p, chr13, chr20; focal hemizygous deletion on: chr2p, chr2q; partial hemizygous deletion on chr8q; homozygous deletion of chrX; several chr2q-8q translocations	32/22

Tumor	MB22t	Medulloblastoma, non-WNT/non-SHH, Group 4 subtype, subclass VII (0.99992)	Trisomy: chr4, chr5q, chr6, chr7, chr9, chr15, chr17, chr18, chr20, chr21; chr8 monosomy, partial hemizygous deletion on: chr3p, chr10q; homozygous deletion of chrY, partial gain on: chr2p, chr7q, chrXq; several translocations	21/14
Tumor	MB23t	Medulloblastoma, non-WNT/non-SHH, Group 3 subtype, subclass II (0.99804)	Isochr17q, trisomy: chr1q, chr8, chr20; monosomy: chr4, chr5, chr9, chr14; focal hemizygous deletion on chr3q; homozygous deletion of chrY	22/6
Tumor	MB24t	Medulloblastoma, SHH-activated, subclass 2 (0.63980)	Chr9 monosomy; focal hemizygous deletion on chr2q	15/3
Tumor	MB25t	Medulloblastoma, non-WNT/non-SHH, Group 4 subtype, subclass VI (0.99949)	Isochr17q; complex: chr7 (chromothripsis?), chr12, chr14q; chr20 trisomy, monosomy: chr11, chr16q, chr21, chr22, chrX; focal amplification on: chr1q, chr12p; partial hemizygous deletion on: chr6p, chr10q; chr1q-chr12p translocation with focal breakpoint amplifications	66
Tumor	MB26t	Medulloblastoma, non-WNT/non-SHH, Group 4 subtype, subclass VIII (0.86189)	Isochr17q; complex chr8q; monosomy: chr16q, chr20, chrX; focal homozygous and partial hemizygous deletion on chr2q; focal gain on chr9p; several chr2q-8q translocations	31/16
Tumor	MB27t	Medulloblastoma, SHH-activated, subclass 1 (0.99996)	Trisomy: chr2, chr3	19
Tumor	MB28t	Medulloblastoma, SHH-activated, subclass 2 (0.99631)	Focal hemizygous deletion on chr1q; partial hemizygous deletion on chr10q; partial gain on chr2p; focal gain on chr10p; chr2-10-4 translocation	35/8
Tumor	MB29t	Medulloblastoma, non-WNT/non-SHH, Group 3 subtype, subclass IV (0.99821)	Isochr17q: trisomy: chr1, chr3, chr5, chr6, chr7, chr9, chr12, chr14, chr19, chr20; gain of chrX; homozygous deletion of chrY; amplification of chr13	22

3.3.4 OGM-based analysis of focal DNA copy number variants and structural variants in medulloblastoma samples

Six MB cell lines, 29 MB tumors and 18 corresponding blood samples were examined for focal CNVs and SVs. The annotated OGM analyses were performed for each sample as described in paragraph 2.5.6, and the respective SV datasheets were downloaded and analysed as described in paragraph 3.2. The rare SVs detected in MB tumors are summarized as cumulative SV profiles stratified according to MB group and MB cell lines in Figure 19.

In the three analyzed MB WNT tumors, 57 unique, rare SVs were identified (Figure 19, “WNT”; Suppl. Table V). Among others, these included a hemizygous deletion covering the *CBFB*, *CTCF* and *CHD1* gene loci on chr16 (chr16:66,886,992–69,305,254; ~ 2.4 Mbp) in MB8t (Suppl. Figure I), and a hemizygous deletion on chr17p (chr17:7,286,494–7,840,671; ~ 0.5 Mbp) spanning the TP53 gene locus in MB10t (Suppl. Figure I).

In the six investigated MB SHH–infant cases, 125 unique, rare SVs including deletions, duplications, insertions, inversions and translocations were detected by OGM (Figure 19, “SHH–infant”; Suppl. Table V). Four SVs affected exonic regions of cancer-related genes such as *STAG2* (a hemizygous deletion of 7 Mbp at chrX:123,995,348–130,952,538 and a chr3::chrX translocation t(3;X)(3q28;Xq25), *NPIP2* (an approximately 5 kbp deletion at chr16:11,917,019–11,962,114) and *NOTCH2* (an approximately 6 kbp insertion at chr1:119,960,225–119,969,033). Two MB SHH–infant tumors, MB20t and MB28t, carried distinct interchromosomal translocations. In MB20t, chr3 and X were involved, and in MB28t, chr2, 4 and 10 (Suppl. Figure I). Recurrent SVs were not found among the MB SHH–infant tumors.

The five MB SHH–child tumors presented an overall higher abundance of SVs compared to the MB WNT and MB SHH–infant tumors, and an increased complexity of structural genomic rearrangements. In total, 224 unique, rare SVs were detected (Figure 19, “SHH–child”; Suppl. Table V). Multiple SVs affected exonic regions of cancer-associated genes in individual tumors, such as *RPL5* (hemizygous deletion of ~ 2.4 Mbp at chr1:92,491,106–94,918,675), and *SET*, *FNBP1*, *ABL1*, *TSC1* (hemizygous deletion of ~ 4.6 Mbp at chr9:128,376,902–132,947,376) in MB1t, *FOXP1* (~ 5 kbp deletion at chr3:71,465,253–71,476,913) in MB11t, *RGS7*, *FH*, and *AKT3* (hemizygous deletion of ~ 4.4 Mbp at chr1:241,009,879–245,374,670) in MB13t, and *ABL2* (~ 5 kbp insertion at chr1:179,201,431–179,219,468) in MB19t (Suppl. Figure I). In two cases (MB15t and MB1t), large deletions at chr9 (chr9:94,811,772–95,606,427; chr9:95,392,140–98,655,497) were detected that covered the *FANCC* and *PTCH1* loci in MB15t, and *PTCH1* and *XPA* loci in MB1t. MB15t (Figure 20) displayed a

particularly high SV load affecting multiple loci of cancer-associated genes including *CCND2*, *MYCN*, *FGFR10P*, *AFDN*, *FANCC*, *PTCH1*, *PTEN*, *FAS*, *YWHAE*, *TP53* and *MAP2K2*. Notably, this case contributed to two thirds of all translocations detected in this MB group (Figure 19, “SHH–child”; Figures 20B, C). Multiple interchromosomal translocations between chr2 and chr12, t(2;12)(p24.2;p13.32), coincided with highly rearranged genomic regions which led to the amplification of a region on chr2 including *CCND2* and another high-level amplification of a region on chr12 including *MYCN*, yielding copy numbers of 19 and 140, respectively (Figure 20A–C). RNA-Seq and immunohistochemical staining supported the enhanced mRNA and protein expression of both amplified genes (Figure 20D and E; Suppl. Figure III).

In the four MB Group 3 tumors (MB4t, MB18t, MB23t, MB29t), 188 unique, rare SVs were detected (Figure 19, “Group 3”; Suppl. Table V), most of which were found in MB4t (Figure 21). This particular tumor presented multiple different SVs on chr13 (chr13q31.1) leading to focal amplification (CN = 19) of the cancer-associated gene *GPC5* (Figure 21E), which in turn led to enhanced *GPC5* mRNA expression levels, as demonstrated by RNA-Seq (Figure 21F; Suppl. Figure III). Furthermore, multiple intrachromosomal translocations were detected on chr8 and chr17 suggesting complex chromosomal rearrangements like chromothripsis (Figure 20C, D). In MB23t, a SV affected the exonic region of the cancer-associated gene *ATRX* (~ 5 kbp hemizygous deletion at chrX: 77,507,310–77,524,034), and in MB29t a hemizygous deletion of *CDKN2A* (~ 275 kbp at chr9:21,923,701–22,208,558) was detected (Suppl. Figure I). No recurrent SVs were found among the MB Group 3 tumors.

The MB Group 4 was the most representative among all MB groups comprising 11 tumors and accounting for approximately 40% of all MB tumors in the investigated MB cohort. Within this group, 349 unique, rare SVs of varying complexity were detected (Figure 19, “Group 4”; Suppl. Table V). Although several cancer-related genes were affected by those rearrangements, only few recurrent SV regions were observed. Two MB Group 4, MB2t (subclass V) and MB22t (subclass VII) presented a duplicated region affecting *SNCAIP* and surrounding genes on chr5 (chr5:122,331,469–122,529,437 and chr5:122,349,574–122,554,212, respectively). Two other Group 4 tumors, MB6t and MB21t (both subclass V), presented a deletion and an insertion affecting an overlapping region including *GSTA1* and *GSTA6P* on chr6 (chr6:52,799,051–52,827,174 and chr6:52,757,730–52,827,174, respectively). MB21t and MB26t (subclass VIII) exhibited an insertion and a duplication affecting an overlapping region including *CASC19* and *PCAT1* on chr8 (chr8:127,207,751–127,219,380 and chr8:125,611,155–129,327,914, respectively). Approximately 40% of the detected rare SVs affected only intronic or intergenic genomic regions. Several of those SVs were recurrent among two MB Group 4 cases, MB21t and MB26t, and three MB Group 3 cases, MB4t, MB18t

and MB29t, and clustered on chr2p16.3. As summarized in the Supplementary Table VI, these deletions overlapped with either *NRXN1* or *NRXN1-DT* introns, while in MB18t an *MSH2* intron was affected. Interestingly, similar deletions overlapping with *NRXN1* or *NRXN1-DT* were also observed in the MB cell lines D283 Med and UW228-3, where both exonic and intronic genomic regions were affected (Suppl. Table VI). In the Daoy cell line, *NRXN1* was affected by an interchromosomal chr2::chr7 translocation, t(2;7)(p16.3;q36.3) (Suppl. Figure I; Suppl. Table VI). Regarding complex genomic events or translocations, three MB Group 4 tumors (MB5t, MB21t and MB26t) featured intra- and interchromosomal rearrangements affecting chromosome arm 2q (q22.2, q22.3). Additionally, MB21t and MB26t presented complex rearrangements affecting regions on chromosome arm 8q (q21.13, q24.13, q24.21) (Suppl. Figure I).

In the six analysed MB cell lines, 1476 unique, rare SVs were found, which corresponded to an average of 256.00 (± 79.06) rare SVs per MB cell line (Figure 19, "Cell lines"; Suppl. Table V). On average 40.17 (± 28.38) highly rearranged regions per cell line overlapped with exonic regions of at least 70 different cancer-associated genes from the COSMIC CGC database. The most frequently affected gene was *LRP1B* (chr2q22.1–chr2q22.2), which was targeted by multiple SVs of different sizes leading to its' hemi- or homozygous losses in five of six MB cell lines. Only HD-MB03 showed no SVs in *LRP1B*. In contrast, the only MB tumor with rearrangements affecting the *LRP1B* region was MB21t, which presented an intra-chromosomal rearrangement forming a putative *NRXN1-DT::LRP1B* fusion fus(2)(p16.3q22.2) (Suppl. Table VII). The second most commonly targeted gene among MB cell lines was *FHIT* (chr3), which was subjected to hemizygous deletions in four cases, namely in Daoy, HD-MB03, MED-MEB-8A and UW228-3. Furthermore, in MED-MEB-8A it formed a deletion-dependent, putative *SFMBT1::FHIT* gene fusion del(3)(p21.1p14.2)). In three cell lines, D283 Med, HD-MB03 and MED-MEB-8A, multiple complex rearrangements affected a region on chr8 including *MYC*. These events led to focal, high-level amplifications of the *MYC*-associated genomic region. In three cell lines, Daoy, MED-MEB-8A and ONS-76, *PTPRD* (chr9) was affected by multiple different SVs. Multiple exonic regions of *PTPRK* (chr6) were affected by either a duplication or a deletion in Daoy, HD-MB03 and UW228-3. In addition, homozygous deletions affected a large region including *MLLT3* and *CDKN2A* (chr9) in Daoy, D283 Med, MED-MEB-8A. An intronic region of *DCC* (chr18) was affected by an inverted duplication in MED-MEB-8A whereas in ONS-76, a deletion-dependent, putative *SLC14A2::DCC* gene fusion, del(18)(q12.3q21.2), was found. The following genes were also affected by SVs in two different MB cell lines: *ETV6* (chr12) in D283 Med and Daoy, *GPC5* (chr13) in D283 Med and ONS-76, *QKI* (chr6) in D283 Med and ONS-76, and *YWHAE* (chr17) in Daoy and HD-MB03.

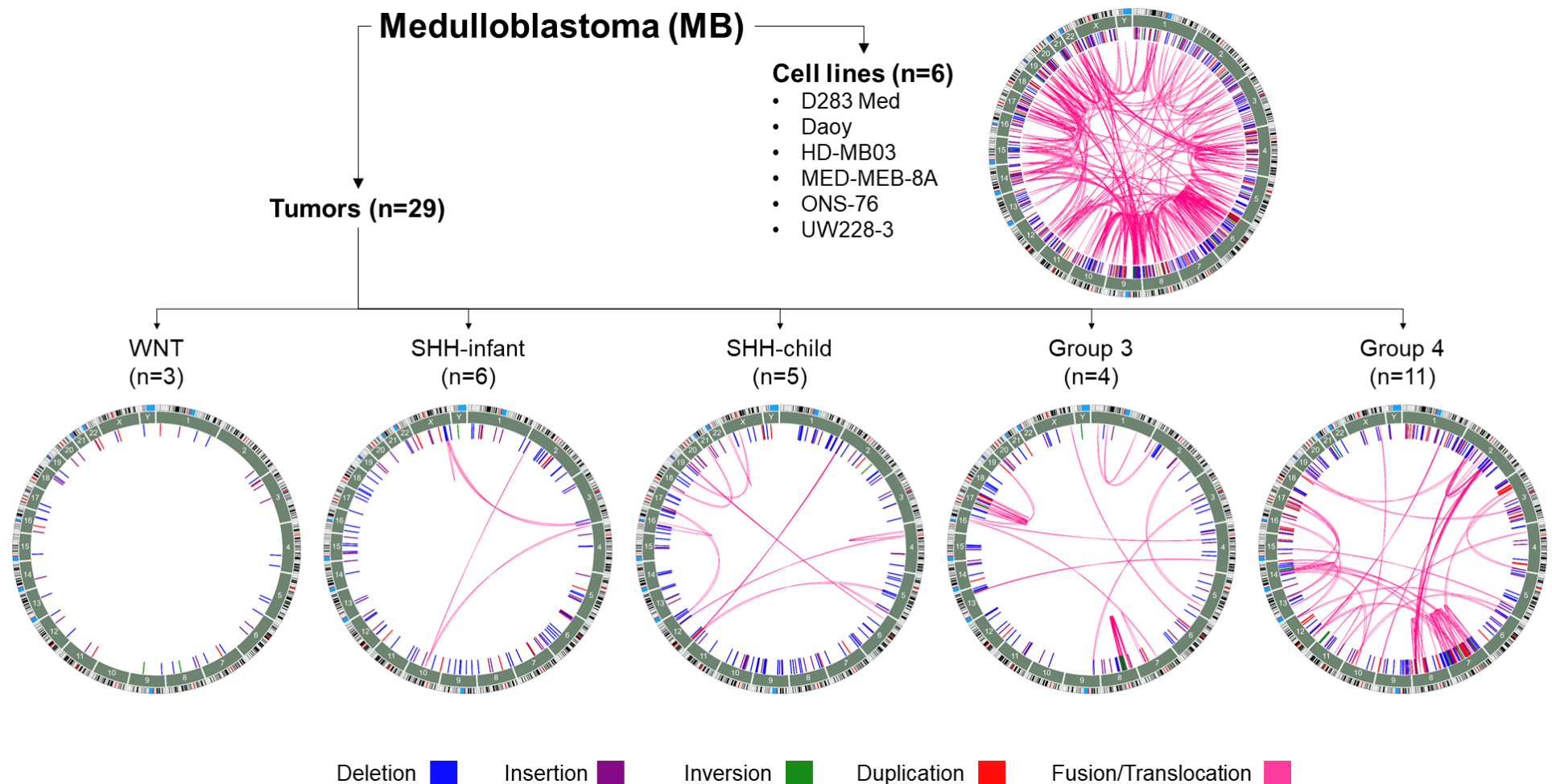


Figure 19. Cumulative SV profiles detected by OGM in 29 MB tumors stratified according to the distinct MB groups and six MB cell lines. The outer circle of each plot shows the ideogram of the respective chromosome with the centromere labelled in red and gaps in light-blue according to the GRCh38 reference genome. The numbered rectangles in the circle further inside represent each chromosome. SVs (deletions in blue, insertions in purple, inversions in green, and duplications in red) are visualized as lines inside the circle indicating the involved genomic positions. Complex SV events (translocations, chromothripsis) are shown as pink arcs connecting either the same (intrachromosomal SVs) or two different chromosomes (interchromosomal SVs). WNT MB (n = 3, SVs = 57), MB SHH–infant (n = 6, SVs = 125), MB SHH–child (n = 5, SVs = 224), MB Group 3 (n = 4, SVs = 188), MB Group 4 (n = 11, SVs = 349) and MB cell lines (n = 6, SVs = 1476).

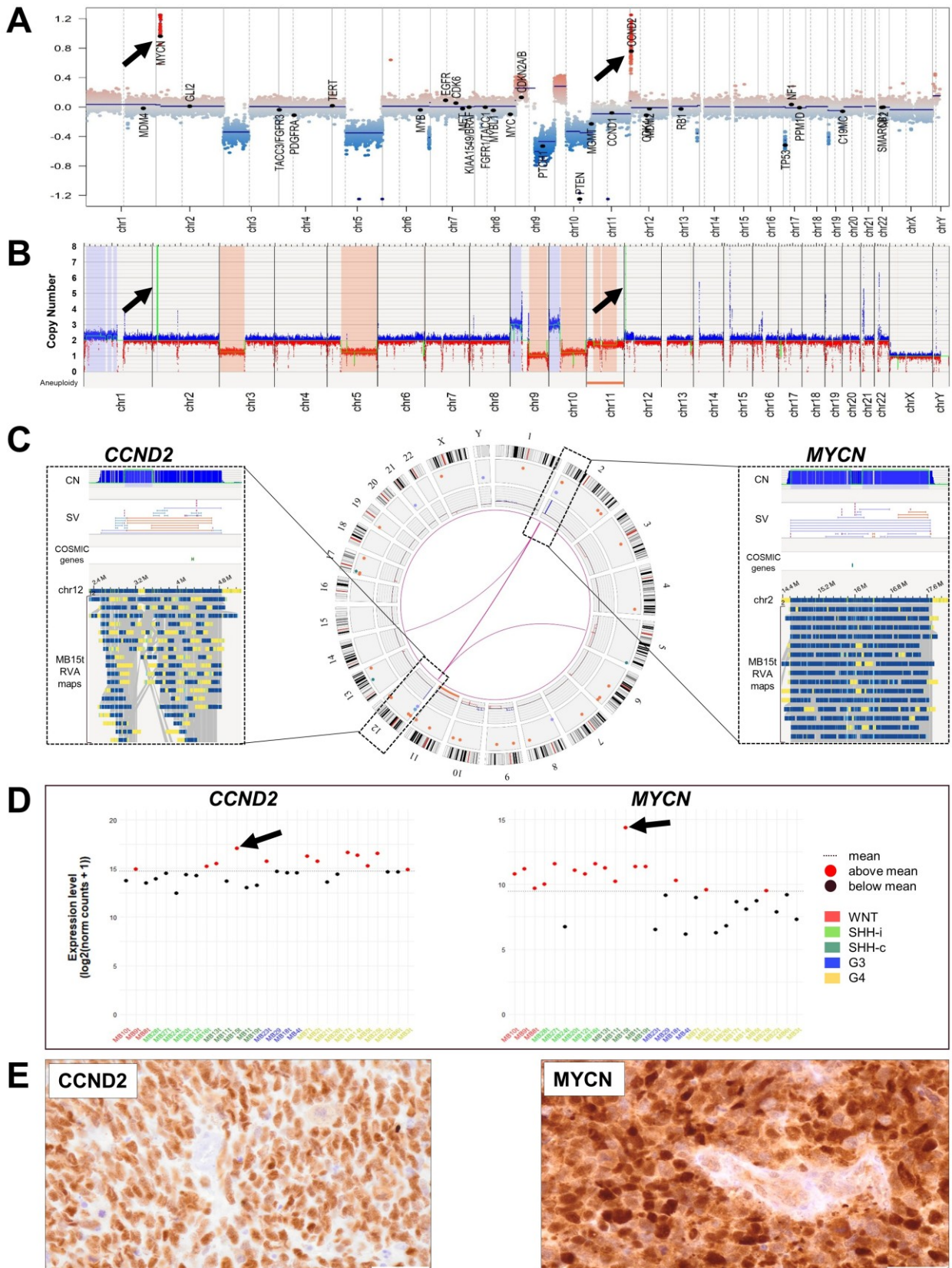


Figure 20. Overview of SVs and selected genes in the MB SHH-child tumor MB15t.

(A) Whole genome CN profile of MB15t as detected by EPIC analysis with losses (blue) and gains (red) of chromosomal regions. y-axis, \log_2 median segment intensity in the interval $[-1.2, 1.2]$; x-axis, chr1–22 plus sex chromosomes. **(B)** Corresponding whole genome CN profile of MB15t as detected by OGM showing similar losses (red) and gains (blue) of chromosomal regions. y-axis, CN in the interval $[0, 8]$; x-axis, Aneuploidy indicators showing whole-chromosome monosomies or total losses (red) and whole-

chromosome trisomies or amplifications (blue), and chr1–22 plus sex chromosomes. **(C)** Circos plot of OGM findings in MB15t showing from the outside in the individual chromosomes with their ideograms, SVs as color-coded dots (*red*, deletion; *purple*, duplication; *light-blue*, insertion), large CN alterations, and translocations/events of complex rearrangements as pink arcs. Translocation events between chr5 and chr12, as well as chr2 and chr12 were detected. The latter translocation colocalized with two amplified regions on chr2 and 12. The boxes flanking the circos plot display a more detailed view of the amplified regions that included the proto-oncogenes *CCND2* on chr12 (left) and *MYCN* on chr2 (right). **(D)** *CCND2* (left plot) and *MYCN* (right plot) mRNA expression levels calculated based on RNA-Seq data across all analysed MB tumors and sorted by MB groups. The increased *CCND2* and *MYCN* mRNA expression levels in MB15t are indicated by black arrows. y-axis, ($\log_2(\text{norm counts} + 1)$) in the interval [0, 15]; x-axis, individual MB cases separated by group: MB WNT in red, MB SHH in green, MB Group 3 in blue and MB Group 4 in yellow. **(E)** Immunohistochemical staining of *CCND2* (left) and *MYCN* (right) shows positive and strong protein expression in the tumor cells of MB15t.

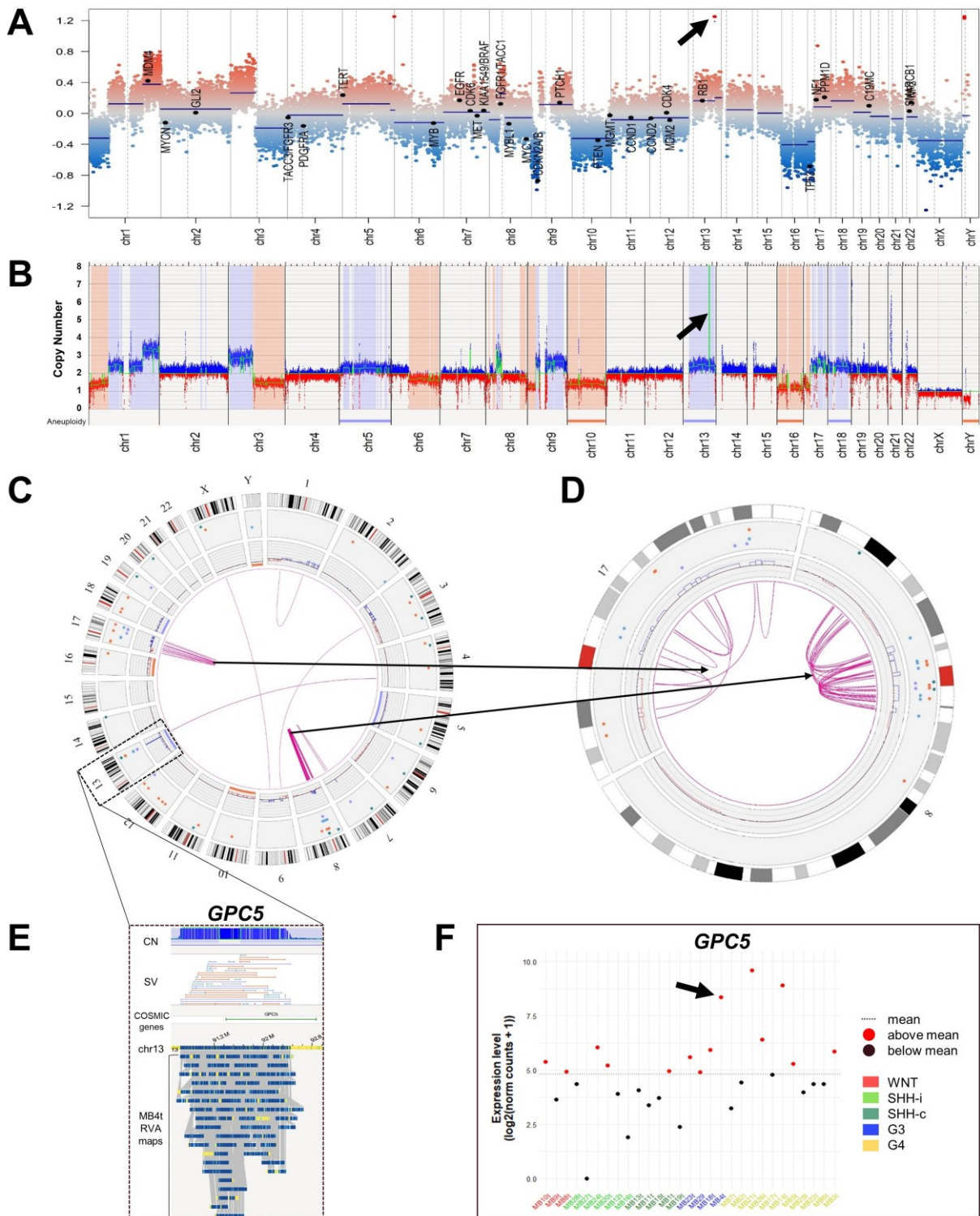


Figure 21. Overview of SVs and selected genes in the MB Group 3 tumor MB4t.

(A) Whole genome CN profile of MB4t as detected by EPIC array analysis with losses (blue) and gains (red) on different chromosomes. y-axis, log₂ median segment intensity in the interval [-1.2, 1.2]; x-axis, chr1–22 plus sex chromosomes. **(B)** Corresponding whole genome CN profile as detected by OGM with losses (red) and gains (blue) of similar chromosomal regions. y-axis, CN in the interval [0, 8]; x-axis, Aneuploidy indicators showing whole-chromosome monosomies or total losses (red) and whole-chromosome trisomies or amplifications (blue), and chr1–22 plus sex chromosomes. Many chromosomes show copy number aberrations and an isochr17q is present. Arrows in **(A)** and **(B)** point to a circumscribed high-level copy number gain corresponding to *GPC5* gene amplification on chr13. **(C)** A circos plot of MB4t shows from the the outside in, the chromosome ideograms, SVs as color-

coded dots (red, deletion; purple, duplication; light-blue, insertion), large CN alterations, and translocations/events of complex rearrangements as pink arcs. Two clusters of such complex rearrangements are detected on chr8 and 17, as shown in mor detail in the circos plot **(D)** for both chromosomes. In addition, an amplification of a 1580887 bp region on chr13 (chr13:90,684,670–92,265,557) including the *GPC5* locus is present. **(D)** Enlarged view of the highly amplified region detected by OGM on chr13 including *GPC5*. **(E)** *GPC5* mRNA expression levels across all MB tumors sorted by groups. The increased *GPC5* expression in MB4t is indicated by an arrow. Expression levels were calculated based on RNA-Seq data. The three tumors with increased *GPC5* mRNA levels are indicated by red dots between 7.5 and 10.0. y-axis, ($\log_2(\text{norm counts} + 1)$) in the interval [0, 10]; x-axis, individual MB cases separated by group: MB WNT in red, MB SHH in green, MB Group 3 in blue and MB Group 4 in yellow.

3.3.5 Identification of somatic DNA structural variants and copy number variation via the dual variant annotation pipeline

Bionano's dual VAP was applied only as "matched tumor-normal pair" analysis for those cases, from which both tumor (sample, designated as "t") and blood (control, designated as "b") from the same patient were available. Among the ATRT samples, a single matched tumor-normal pair, A1t and A1b, was available. Among the MB samples, 18 matched tumor-normal pairs were analysed. As input for the dual VAP analysis, the RVA and the DNP files of the tumors and the matched blood samples were used. Using the dual VAP, SVs and CNVs from each RVA of a tumor were automatically compared against the SVs and CNVs detected by the RVA of the matched blood. Variants present in both tumor and blood genomes were regarded as germline variants and not as tumor-specific events, and were therefore filtered out of the dual VAP analysis call-set. For purpose of completeness, the dual VAP was also applied to the DNP files of each tumor-blood pair. The output was saved as a VAP analysis file and viewed as either dual RVA VAP or dual DNP VAP in the Bionano Access Software. The filtered SV, CNV and aneuploidy call sets were downloaded, imported into Excel and visualized with the Bionano Access Software. For validation purposes, manual comparisons of matched tumor-normal RVA and DNP data were performed for selected cases.

To quantitatively assess the proportion of somatic SVs among the identified high-confidence rare SVs and thus evaluate the significance of the VAP analysis, the absolute numbers of RVA-detected (rare SVs) and RVA-VAP-detected SVs (somatic SVs) of the 18 matched MB tumor-normal pairs were compared by one-way ANOVA. This revealed a significant reduction of the absolute number of SVs upon application of the VAP analysis as indicated in Figure 22 ("total": $F(1, 34) = 1.015$, $p = 0.0053$). Particularly for deletions (Figure 22, "DEL") and insertions (Figure 22, "INS"), the differences between the detected "rare SVs" and "somatic SVs" were highly significant ("DEL": $F(1, 34) = 16.36$, $p = 3 \times 10^{-4}$; "INS": $F(1, 34) = 88.64$, $p = 5 \times 10^{-11}$). For duplications (Figure 22, "DUP") and inversions (Figure 22, "INV"), no significant differences between the detected rare SVs and somatic SVs were found ("DUP": $F(1, 34) = 1.08$, $p = 0.31$;

“INV”: $F(1, 34) = 0.001$, $p = 0.97$). In cases of intrachromosomal fusions and interchromosomal translocations (Figure 22, both summarized as “TRANSL”), no statistical difference was detected (“TRANSL”: $F(1, 34) = 0$, $p = 1$). In summary, although constituting high confidence, rare SVs, a significant number of deletions and insertions was finally excluded from the list of somatic SVs due to their presence in the matched blood genomes. In contrast, all of the intrachromosomal fusions, interchromosomal translocations and most of the inversions and duplications were tumor-specific alterations that were retained in the final list of somatic SVs. Furthermore, application of the paired tumor-blood DNP-VAP analyses delivered insights into the properties of high-confidence, rare SVs within the range of 500–4500 bp. The initial idea to detect candidate SVs below the 5 kbp size threshold of the RVA and therefore decipher a more complete and comprehensive genomic landscape with respect to SVs did not prove successful. All of the detected SVs < 4.5 kbp were filtered out from the final list of somatic SVs due to their co-presence within the matched blood genomes (data not shown), indicating germline variants. The absolute SV counts, types and characteristics are summarized in Supplementary Table III. With regard to the CNV and aneuploidy call sets generated by the dual VAP analyses, all detected CNVs and aneuploidies were found in tumor genomes only and not in the matched blood assemblies, indicating somatic variants. These CNV and aneuploidy findings are summarized in Supplementary Table II.

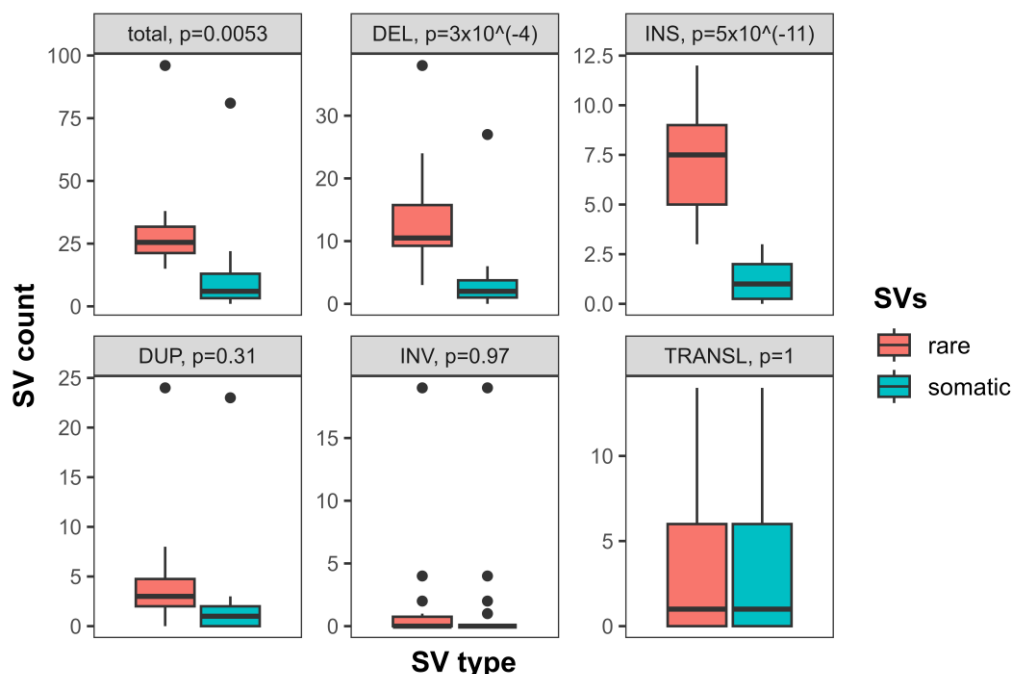


Figure 22. Numbers of high-confidence SVs ≥ 4.5 kbp detected in MB tumor/peripheral blood DNA pairs of 18 patients. Comparison of absolute SV counts per SV type after exclusion of common SVs stratified as rare SVs detected in the MB tumor tissues without subtraction of constitutive SVs also present in the corresponding blood sample (red boxplots), and somatic SVs detected exclusively in the MB tumor tissues (turquoise boxplots) SVs. The one-way ANOVA was used to compare SV numbers in the two groups. *kbp*, kilobase pairs; *total*, total SV count; *DEL*, deletions; *INS*, insertions; *DUP*, duplications; *INV*, inversions; *TRANSL*, intrachromosomal fusions/interchromosomal translocations.

3.3.6 Identification and validation of novel gene fusions in medulloblastomas

Along with detection and identification of CNVs and SVs, OGM algorithms enable mapping of the SV breakpoints to known gene locations thereby inferring whether two distinct genes are newly joined at these sites, resulting in the formation of a hybrid gene, i.e., causing a “putative gene fusion”. All OGM-called putative gene fusions are summarized in Supplementary Table VII.

OGM identified six distinct, putative gene fusions among three MB WNT, all of which were formed through deletions of a DNA segment that joined two genes. In four out of six MB SHH–infant tumors, seven distinct putative gene fusions were identified, four of which also were deletion-dependent. The other two gene fusion events were both formed after tandem duplications, with the large, copied DNA segments being inserted directly adjacent to the original segments. Only one putative gene fusion, *SH3BP2::CTNNA3*, was formed by an interchromosomal translocation, t(4;10)(p16.3;q21.3), which was detected in MB28t (Figure 23B). Among the five MB SHH–child tumors, 36 OGM-called putative gene fusions were identified, with at least two independent fusion events being present per tumor. In total, 75% of the detected fusion events were either deletion- or duplication-dependent, and only 25% were formed by either intrachromosomal fusions or interchromosomal translocations. However, the majority of the total fusion calls (~ 60%) resulted from the chr2-12 rearrangement and the co-localized *CCND2* and *MYCN* amplification in the case MB15t (Figure 20).

A similar observation was made for the MB Group 4 cases: among 11 tumors, 37 putative gene fusions were detected, with at least one independent fusion event being present per tumor. Approximately 60% of the detected gene fusions were either deletion- or duplication-dependent events and 40% were formed by either intrachromosomal fusions or interchromosomal translocations. Approximately half of all Group 4 gene fusion events were contributed by one particular case (MB25t) which presented multiple intrachromosomal translocations on chr7 (Figure 19, “Group 4”; Suppl. Figure I). In MB Group 3 tumors, 23 out of total 24 putative gene fusions were detected in a single tumor, MB4t. In line with prior results shown in Figure 21, most of these fusion events were localized to chr8, chr13 and chr17. One putative gene fusion resulted from an interchromosomal translocation, t(4;13)(q31.23;q31.3), and affected *GPC5*.

In order to validate selected OGM-detected gene amplifications and putative gene fusions resulting from translocations or other SVs, RNA-Seq data of the respective MB tumors were analyzed. Fusion transcripts from RNA-Seq data were identified by Arriba¹⁷⁴ and compared to the final list of high confidence rare SVs identified in the respective MB tumors, as well as the

cumulative putative gene fusion list (Suppl. Table VII). As summarized in the Supplementary Table VIII, in 22 of 29 analyzed MB tumors, 64 high-confidence gene fusions with two coding gene partners were found by Arriba (confidence: “high”). Most of the Arriba-identified high confidence fusion transcripts resulted from deletions ($n = 25$), followed by duplications ($n = 21$), translocations ($n = 9$) and inversions ($n = 9$). Upon comparison of Arriba-detected fusions with the final list of OGM-detected rare SVs, several fusion events detected by Arriba and labelled as “high-confidence”, overlapped with OGM-detected SVs (Suppl. Table VII). Upon reduction of stringency parameters (e.g. confidence, gene partners), additional Arriba-detected fusion transcripts (Suppl. Table VIII, confidence: “medium”) were found to overlap with a total of 35 OGM-detected SVs in MB tumors, as indicated in Supplementary Table VII.

All potentially relevant, novel gene fusions identified by OGM and validated by RNA-Seq using Arriba¹⁷⁴ and FusionCatcher¹⁷⁵ are discussed below and visualized in Figure 23, as well as three novel gene fusions validated by Arriba only, which are visualized in Supplementary Figure II and also discussed below. Each subfigure of Figure 23 (A–F) and Supplementary Figure II (A–C) is separated into two representations of the same gene fusion event, whereas the upper circos plot and SV view is derived from OGM and the lower circos plot and SV view from Arriba analyses. Both circos plots emphasize the structural rearrangement in the respective sample, whereas the specific SV event is designated either by an arrow or a colored highlight. Both SV views present a detailed visualization of the specific gene fusion event (OGM) or fusion transcript (Arriba). In OGM, the reference regions are indicated in green with the respective whole-chromosomes on the outer rims of the window. The OGM consensus map incorporating the SV is indicated in light blue, showing the partial alignment to the reference region. In Arriba, a schematic visualisation of the detected transcripts of fusion partners, their coverage, orientation and the retained exons contributing to the fusion transcript, are visualized (Figure 23).

Six novel gene fusions were identified by OGM and supported by both fusion callers, as summarized in Table 14. Among SHH–infant tumors, two novel gene fusions were identified: a deletion-dependent $\text{del}(X)(q25q26.1)$ *STAG2::ARHGAP36* fusion in MB20t (Figure 23A) and a translocation-dependent $\text{t}(4;10)(p16.3;q21.3)$ out-of-frame *SH3BP2::CTNNA3* fusion in MB28t (Figure 23B). Among two SHH–child tumors, two deletion-dependent gene fusions were found: an in-frame *RANBP17::CANX* fusion $\text{del}(5)(q35.1q35.3)$ in MB13t (Figure 23C) and an out-of-frame *ATF7IP::PTPRO* fusion $\text{del}(12)(p13.1p12.3)$ in MB15t (Figure 23D). Two gene fusions, the *ITGA9-AS1::EIF1B-AS1* fusion (Figure 23E) and an out-of-frame *MYRIP::ITGA9* fusion (Figure 23F), were found in a single Group 4 tumor (MB5t) resulting from the same duplication-dependent SV event $\text{dup}(3)(p22.1p22.2)$. Also, three additional, novel gene fusions were identified by OGM and confirmed only by Arriba-detected fusion transcripts (Suppl. Figure

IIA–C). Two out of the three novel fusion events were translocation-dependent and affected recurrent chromosomal regions among two independent Group 4 tumors (Table 14): the out-of-frame *NRXN1::NUDCD1* fusion t(2;8)(p16.3;q23.1) in MB21t (Suppl. Figure IIA), as well as two out-of-frame gene fusions in MB26t, *NSMCE2::ZEB2* t(8;2)(q24.13;q22.3) and an inversion-dependent *RUNX1T1::HPYR1* fus(8)(q21.3q24.22) (Suppl. Figure IIB, C). The mRNA expression levels of all the gene fusion-implicated genes are available in the Supplementary Figure III.

While the majority of the gene fusions were unambiguously identified by OGM and RNA-Seq based callers, the *STAG2::ARHGAP36* and the *RUNX1T1::HPYR1* gene fusions were not specifically called as a putative gene fusion event in OGM, because in OGM analyses, the second breakpoint overlapped an intergenic region (Table 14). Nevertheless, both *STAG2* and *RUNX1T1* are listed as cancer-associated genes in the COSMIC CGC database, and the respective SV calls were matched to the *STAG2::ARHGAP36* and the *RUNX1T1::HPYR1* fusion transcripts detected in the corresponding RNA-Seq data.

In addition to the cohort of this study, two publicly available medulloblastoma datasets were inspected and compared with this MB cohort for recurrent fusion events^{176,177}. These analyses revealed that the *STAG2::ARHGAP36* gene fusion previously detected by OGM and RNA-Seq (ENST0000371145.8(STAG2):e.1::ENST0000370922.5(ARHGAP36):e.2_12) in a single MB SHH–infant tumor of our cohort (MB20t) was also detectable in a single case of the cohort published in Forget *et al.*¹⁷⁷ (Figure 23A; Table 14). In contrast, the other gene fusions detected in this study were not present in the two independent MB RNA-Seq datasets, thus representing rare, novel gene fusions in MB.

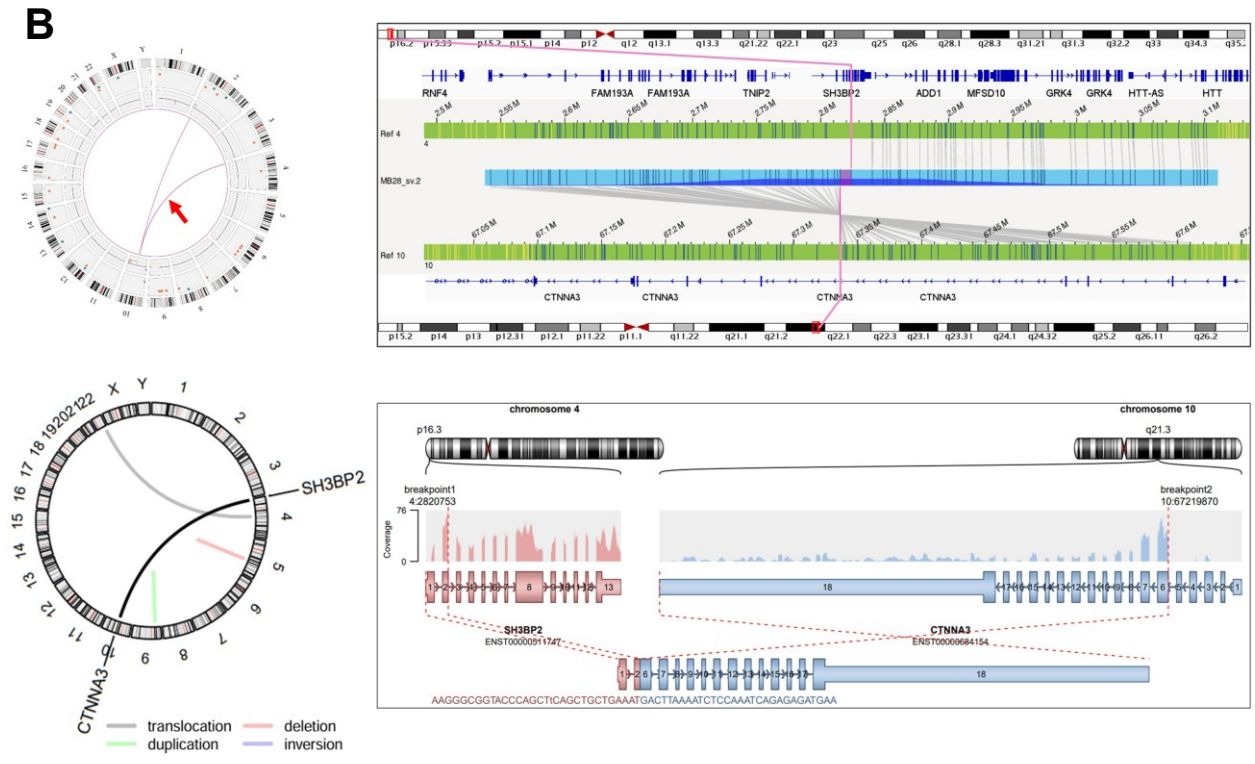
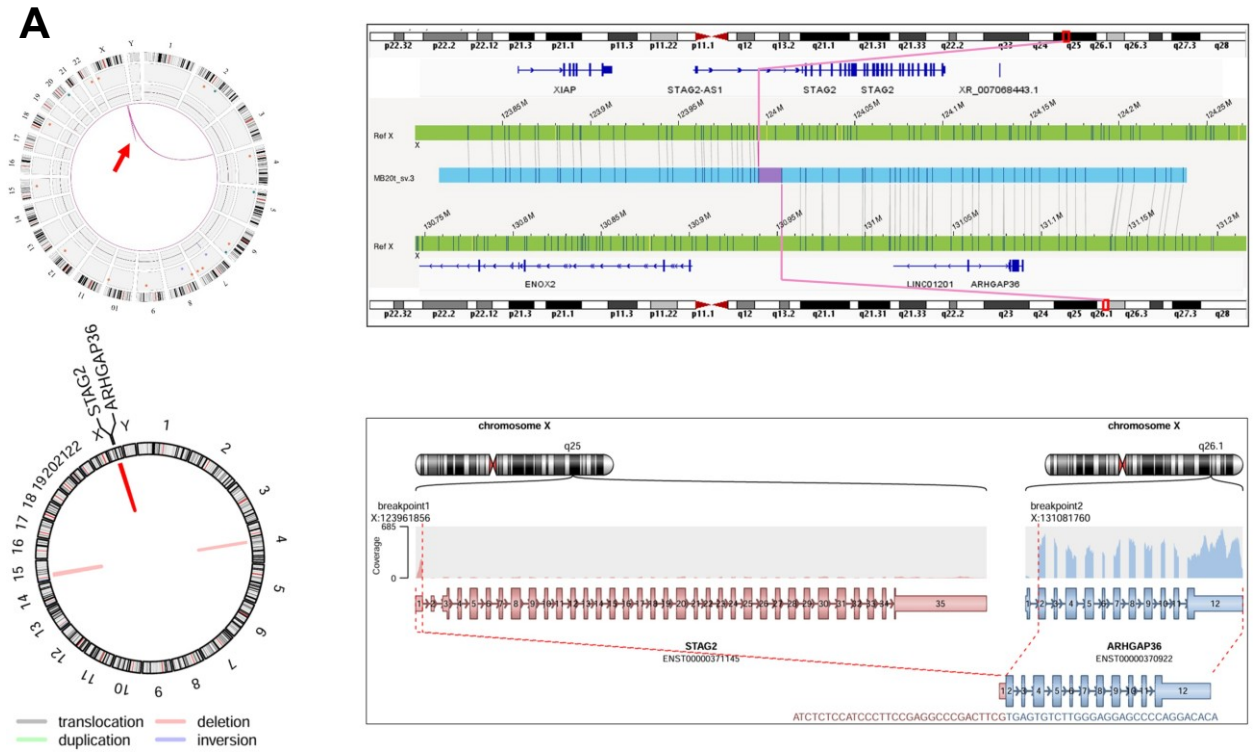
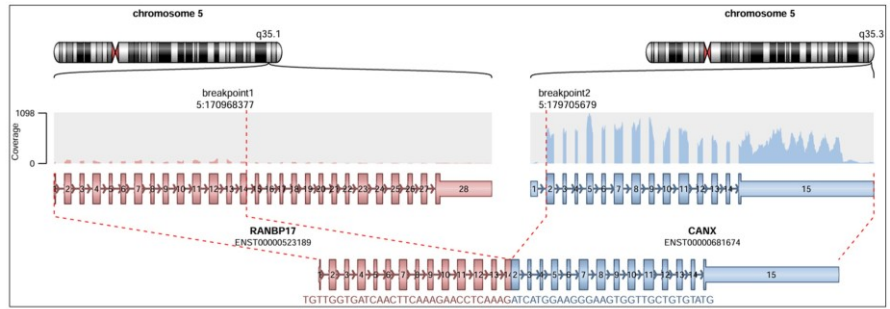
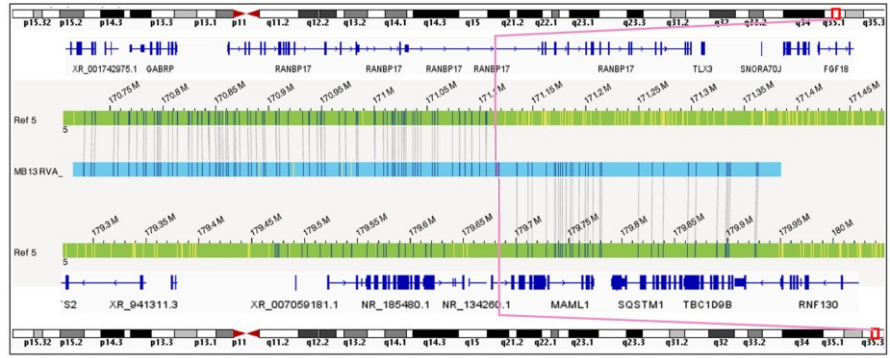
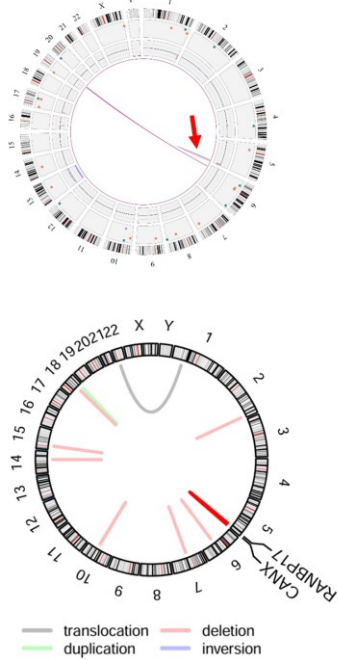
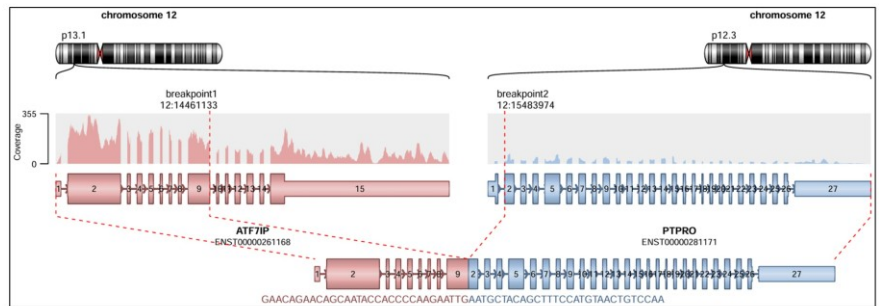
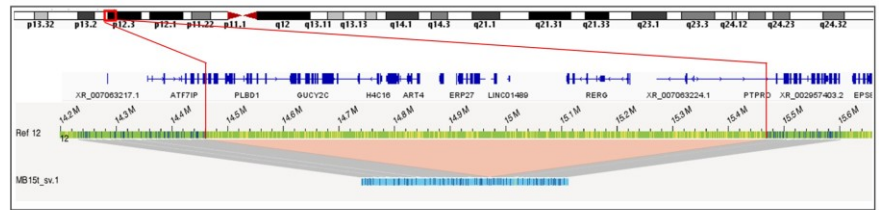
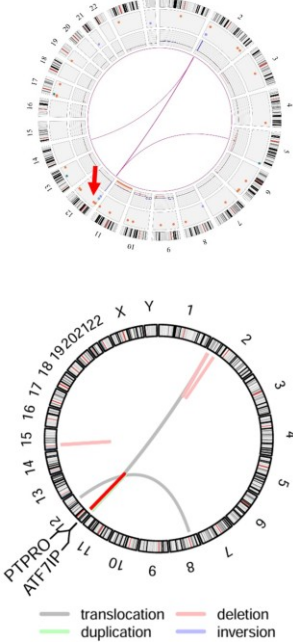


(Figure legend is on pages 92-93.)

C



D



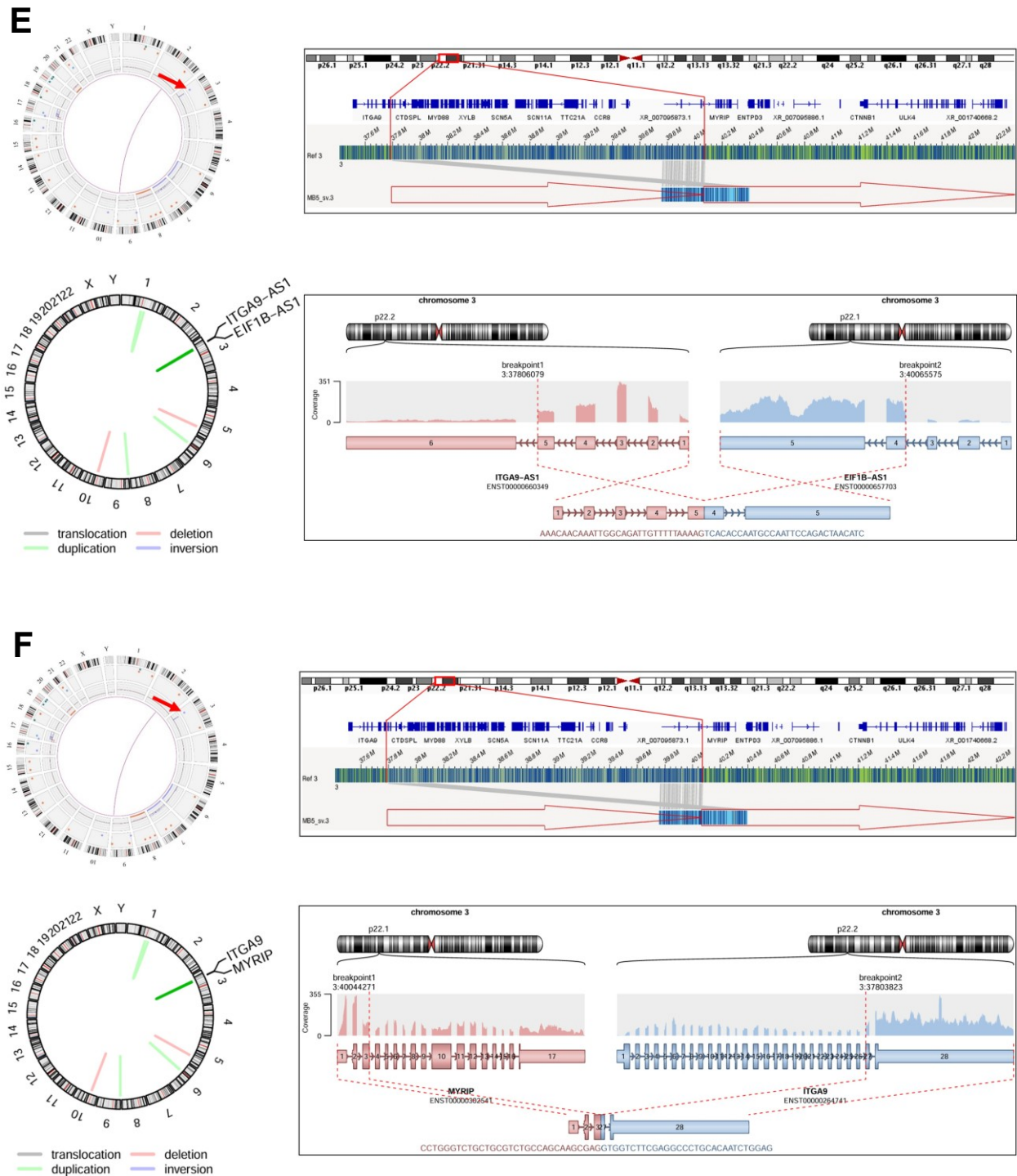


Figure 23. Novel gene fusions in MB detected by OGM and RNA-Seq of the same tumors. For each analysed sample in A–F, two representations of the same gene fusion event are given. The upper circo plots (left) and SV-views (center-right) are derived from OGM and the lower circo plots (left) and SV-views (center-right) from RNA-Seq data evaluated by Arriba. The circo plots emphasize all structural rearrangements of the analyzed sample, whereas the SV event of interest is designated and both SV views zoom into the specific SV event. In OGM SV view, the reference regions are indicated in green with the respective whole-chromosome on the other rims of the window and in the middle the light blue OGM consensus map (map incorporating the SV), indicating the partial alignment to the reference region. In the Arriba SV view, a schematic visualisation of detected transcripts of the fusion partners, their coverage, orientation and the retained exons contributing to the fusion transcript are visualized. (Figure legend continues on page 93.)

(A) OGM detected an intrachromosomal translocation affecting the q-arm of chrX in MB20t (MB SHH–infant). The breakpoints are within the *STAG2* gene and an intergenic region. Based on RNA-Seq data, Arriba predicted ENST0000371145.8(*STAG2*):e.1::ENST0000370922.5(*ARHGAP36*):e.2_12 fusion transcripts formed by an intrachromosomal deletion on chrX.

(B) OGM detected in MB28t (MB SHH–infant) a partially inverted, interchromosomal translocation between the p-arm of chr4 and the q-arm of chr10, t(4;10)(p16.3;q21.3), overlapping with the *SH3BP2* gene and a large, intronic region of the *CTNNA3* gene. The *SH3BP2*::*CTNNA3* gene fusion predicted by OGM was confirmed by ENST00000511747.6(*SH3BP2*):e.1_2::ENST00000684154.1(*CTNNA3*):e.6_18 fusion transcripts detected by RNA-Seq.

(C) In MB13t (MB SHH–child), OGM detected a deletion-co-localized, intrachromosomal translocation affecting the q-arm of chr5. The breakpoints were within the genes *RANBP17* and *CANX* and OGM identified a *RANBP17*::*CANX* putative gene fusion. This gene fusion was supported by RNA-Seq demonstrating ENST00000523189.6(*RANBP17*):e.1_14::ENST00000681674.1(*CANX*):e.1_15 fusion transcripts.

(D) In MB15t (MB SHH–child), OGM revealed a large deletion affecting a highly rearranged region on the p-arm of chr12. The deletion breakpoints mapped within the genes *ATF7IP* and *PTPRO*. This gene fusion was supported by RNA-Seq demonstrating ENST00000261168.9(*ATF7IP*):e.1_9::ENST00000281171.9(*PTPRO*):e.2_27 fusion transcripts.

(E, F) OGM identified a duplicated region on the p-arm of chr3 in MB5t (MB Group 4). The duplication breakpoints mapped within genomic regions overlapping the genes *EIF1B-AS1* and *ITGA9-AS1* (E), as well as *MYRIP* and *ITGA9* (F). Thus, OGM revealed the two duplication-dependent putative gene fusions, which were both supported by detection of the respective ENST00000660349.1(*ITGA9-AS1*):e.1_5::ENST00000657703.1(*EIF1B-AS1*):e.4_5 (E) and ENST00000302541.11(*MYRIP*):e.1_3::ENST00000264741.10(*ITGA9*):e.27_28 (F) fusion transcripts upon RNA-Seq.

Table 14. Gene fusions / translocations detected by OGM in the investigated MB and ATRT cohort of this study that affected potentially cancer-relevant genes and were validated by RNA-Seq based fusion callers.

Dataset	Sample ID	Classification	OGM				RNA-Seq				
			SV	Gene 1	Gene 2	SV type	Caller	Breakpoint 1	Breakpoint 2	Fusion transcript	SV type
This study	MB20t	SHH-infant	del(X)(q25q26.1)	STAG2	-	intrachr. fusion/deletion	Arriba, FusionCatcher	X:123961856	X:131081760	ENST0000371145.8(STAG2):e.1::ENST0000370922.5(ARHGAP36):e.2_12	deletion; exon-exon fusion junction
Forget <i>et al.</i> ¹⁷⁷	MT161	SHH	-	-	-	-	Arriba, FusionCatcher	X:123961856	X:131081760	ENST0000371145.8(STAG2):e.1::ENST0000370922.5(ARHGAP36):e.2_12	as above
This study	MB28t	SHH-infant	t(4;10)(p16.3;q21.3)	SH3BP2	CTNNA3	interchr. translocation	Arriba, FusionCatcher	4:2820753	10:67219870	ENST00000511747.6(SH3BP2):e.1_2::ENST00000684154.1(CTNNA3):e.6_18	translocation; out-of-frame exon-exon fusion junction
This study	MB13t	SHH-child	del(5)(q35.1q35.3)	RANBP17	CANX	deletion	Arriba, FusionCatcher	5:170968377	5:179705679	ENST00000523189.6(RANBP17):e.1_14::ENST00000681674.1(CANX):e.1_15	deletion; in-frame exon-exon fusion junction
This study	MB15t	SHH-child	del(12)(p13.1p12.3)	ATF7IP	PTPRO	deletion	Arriba, FusionCatcher	12:14461133	12:15483974	ENST00000261168.9(ATF7IP):e.1_9::ENST00000281171.9(PTPRO):e.2_27	deletion; out-of-frame exon-exon fusion junction
This study	MB5t	Group 4	dup(3)(p22.1p22.2)	ITGA9-AS1	EIF1B-AS1	duplication	Arriba, FusionCatcher	3:37806079	3:40065575	ENST00000660349.1(ITGA9-AS1):e.1_5::ENST00000657703.1(EIF1B-AS1):e.4_5	duplication; exon-exon fusion junction
This study	MB5t	Group 4	dup(3)(p22.1p22.2)	MYRIP	ITGA9	duplication	Arriba, FusionCatcher	3:40044271	3:37803823	ENST00000302541.11(MYRIP):e.1_3::ENST00000264741.10(ITGA9):e.27_28	duplication; out-of-frame exon-exon fusion junction
This study	MB21t	Group 4	t(2;8)(p16.3;q23.1)	NRXN1	TRHR / NUDCD1	interchr. translocation	Arriba	2:50346691	8:109172681	ENST00000342183.9(NRXN1):e.1	translocation; CDS/splice-site: intergenic; out-of-frame
This study	MB26t	Group 4	t(2;8)(q22.3;q24.13)	NSMCE2	ZEB2	interchr. translocation	Arriba	8:125182256	2:144492065	ENST00000287437.8(NSMCE2):e.1_5::ENST00000636471.1(ZEB2):e.2_1	translocation; CDS/splice-site: intron; out-of-frame
This study	MB26t	Group 4	fus(8)(q21.3q24.22)	RUNX1T1	-	intrachr. fusion	Arriba	8:92005116	8:132544809	ENST00000520978(RUNX1T1):e.1_2	inversion; CDS/splice-site: intron; out-of-frame
This study	JC-ATRT	ATRT-MYC	del(22)(q11.2q11.23)	PPIL2	SMARCB1	deletion	Arriba, FusionCatcher	22:21675115	22:23816770	ENST00000335025.12(PPIL2):e.1_6::ENST00000644036.2(SMARCB1):e.6_9	deletion; in-frame exon-exon fusion junction

3.4 Characterization of ATRT cell lines and tumors

3.4.1 DNA methylation-based classification of ATRT samples

Thirteen ATRT cell lines and three ATRT primary tumors were subjected to DNA methylation profiling by application of Illumina 850k EPIC array hybridization. DNA methylation-based CNS tumor classification using the Heidelberg Brain Tumor classifier version 12.8 assigned 10/16 ATRT samples to the methylation family (MF) of “Atypical teratoid/rhabdoid tumor” with classifier scores ≥ 0.9 ¹⁶⁰. Of those, six ATRT samples were unambiguously classified according to distinct ATRT methylation (sub)classes (MC) based on the calibrated classifier scores ≥ 0.9 : “Atypical teratoid/rhabdoid tumor, MYC-subtype” (ATRT–MYC, n = 3) and “Atypical teratoid/rhabdoid tumor, SHH-subtype” (ATRT–SHH, n = 3). Nine ATRT samples, were not assigned to any of the medulloblastoma methylation (sub)classes with a classifier score ≥ 0.9 , however, could also be stratified based on classifier scores between 0.49 and 0.89 (Table 15; Suppl. Table I).

Finally, nine ATRT samples, including one tumor and eight cell lines, were assigned to the ATRT–MYC subtype and six ATRT samples, including one tumor and five cell lines, were assigned to the ATRT–SHH subtype. For one of the three analyzed ATRT tumors (A1t), no classifier scores ≥ 0.3 could be calculated. Thus, neither classification, nor association with the respective CNS tumor entity could be made. Also, no methylation class family members of ATRT–TYR subtype were identified among the ATRT samples of this cohort. All classification results are summarized in Table 15 and Supplementary Table I.

3.4.2 Detection of aneuploidies and copy number variants by optical genome mapping in ATRT samples

Following DNA methylation-based classification of the ATRT samples, OGM-based genome-wide CNV profiles of the 13 ATRT cell lines and the three ATRT primary tumors were assessed. The annotated OGM analyses were performed for each sample and the respective CNV and aneuploidy call-sets were examined as described in paragraph 2.5.6. An overview of the ATRT cell lines and tumors as classified by EPIC 850k DNA methylation analysis as well as the OGM-identified aneuploidies, CNVs and SVs are provided in Table 15. The OGM-detected genome-wide CNV profiles of individual ATRT tumor and cell line cases are provided in Supplementary Figure I. All OGM-identified chromosomal regions affected by focal/partial CNVs, or by whole-chromosome aneuploidies, are summarized in Supplementary Table II.

As described in paragraph 3.2.1. and presented in Figures 12B and 13B, no significant differences between ATRT cell lines and tumors were observed with regard to the detected

absolute SV numbers. Similarly, the number of chromosomes affected by CNVs did not differ between primary tumors and cell lines, as determined by a one-way ANOVA ($F(1, 14) = 1.031$, $p = 0.213$). Thus, the distinction of ATRT CNV results is not based on the sample type, cell line versus tumor, but is instead based on the distinct classification, ATRT–MYC versus ATRT–SHH (Figure 24). As indicated in Figure 24A, the CNV prevalence, defined as number of chromosomes affected by CNVs per analysed case, was significantly different between the identified subtypes of ATRT (ANOVA, $F(1, 13) = 5.9580$, $p = 0.0297$). ATRT–MYC cases harboured genomes with higher prevalence of CNVs (2.78 ± 1.23) as compared to ATRT–SHH cases (1.17 ± 1.07).

In Figure 24B, a simplified overview of OGM-detected CNVs is graphically sorted by individual ATRT samples of the MYC-subtype and SHH-subtype, which are visualized on the horizontal axis, and the CNV location on the respective chromosome, visualized on the vertical axis. The respective thresholds for distinction among the CNVs was applied as discussed in paragraph 3.2.2. Individual CNV profiles of each sample are depicted in Supplemental Figure II.

The most frequently occurring CNVs among all ATRT cases were affecting chr5, whereas in three out of four ATRT cases focal hemizygous deletions of a distal region on chr5q were identified (Figure 24B). The fourth ATRT case presented a trisomy of chr5p and a partial trisomy of chr5q, accompanied by a focal amplification on chr5q. The CNVs affecting chr5 were exclusively detected among ATRT–MYC samples (Figure 24B). The second frequent CNV, which was also exclusively identified among ATRT–MYC cases, mapped to the long arm of chr22 (chr22q). Of those, two cases presented homozygous focal deletions on chr22q, and chr22 monosomy was identified in the last case. Also, partial CNVs were affecting chrXq in three ATRT cases, whereas a focal hemizygous deletion was identified in one ATRT–MYC case and focal CN gains were identified among two ATRT–SHH samples, the tumor A3 and the cell line established from it, HHU-01. Otherwise, all remaining CNVs were only detected in single ATRT cases, were of sub-chromosomal length, and affected only particular regions of chromosomes or chromosomal arms. Noteworthy, the pattern of ATRT–MYC and ATRT–SHH CNVs was mutually exclusive (Figure 24B). Of all analyzed ATRT cases, only two ATRT–MYC cases, the cell lines CHLA-06 and CHLA-266, presented whole-chromosome aneuploidies, namely chr8 trisomy and chr22 monosomy (Figure 24B and Suppl. Figure I).

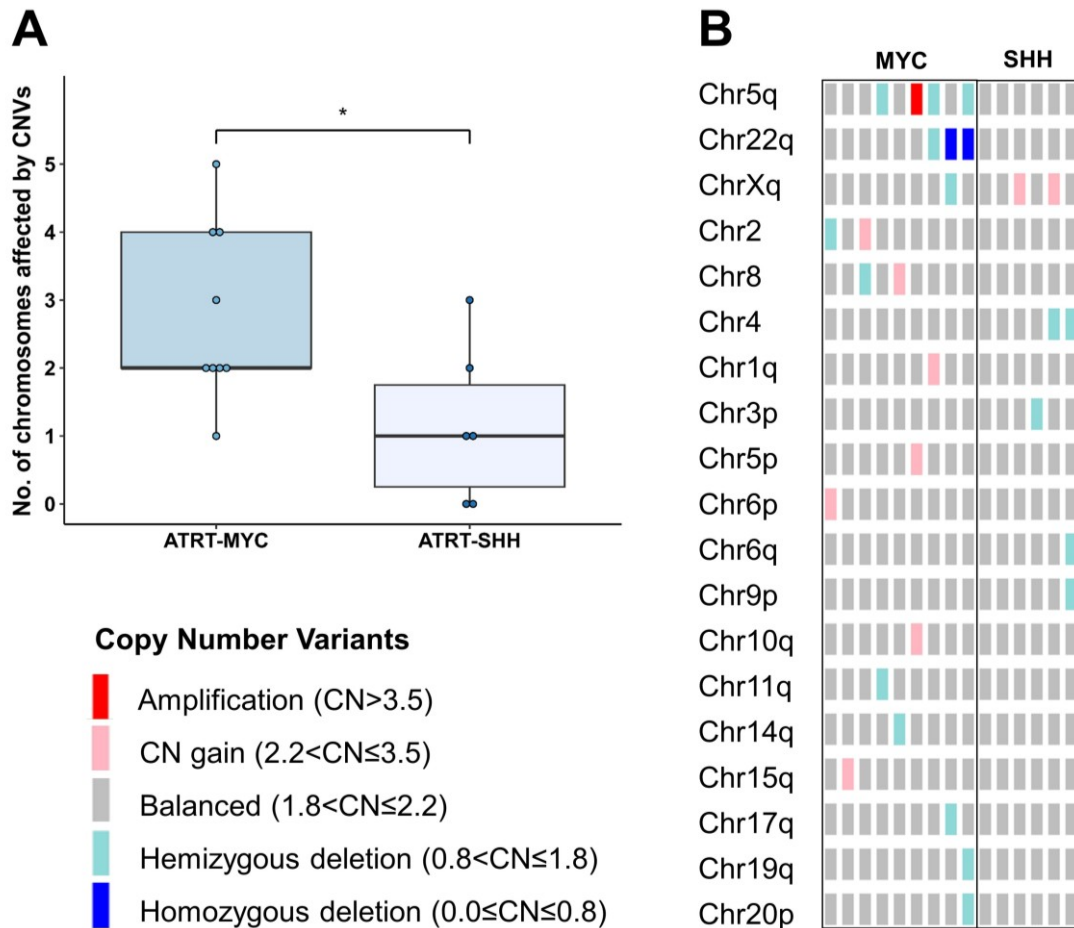


Figure 24. OGM-detected copy number variants in 15 ATRT samples, separated by ATRT subtype. (A) ATRT subtype-wise comparison of number of chromosomes affected by CNVs determined by ANOVA: *, $p < 0.05$. **(B)** Simplified overview of CNVs sorted by ATRT subtypes, ATRT–MYC and ATRT–SHH, presenting the detected CNV on the respective chromosome.

3.4.3 Global copy-number variation analysis of ATRT samples based on DNA methylation array data

Genome-wide CNV profiles were inferred from DNA methylation array-based datasets of the classified ATRT cell lines ($n = 13$) and ATRT tumors ($n = 2$). The respective individual CNV profiles of all ATRT cases are provided in the Supplementary Figure I. For an overview of the chromosomal aberrations characteristic for the nine cases of ATRT–MYC as well as the six cases of ATRT–SHH, summary CNV plots were created with “conumee 2.0” and are presented in Figure 25. As explained in paragraph 3.3.3., the summary CNV plots visualize the percentage of cumulative CNVs on the y-axis and the respective chromosomal location on the x-axis. Thus, the y-axis has a baseline of 0% corresponding to zero cases and a range from 0–100% above and below the baseline, representing the percentage of cumulative cases with a CNV on the particular chromosome. Shifts below the baseline indicate CN losses in blue and

shifts above indicate CN gains in orange/red. The magnitudes of the shifts represent the frequency in % of the identified CN loss among all cases.

In both summary plots of ATRT–MYC and ATRT–SHH cases, most ATRT genomes were devoid of recurrent or particularly prominent CNVs, as shown in Figure 25A and 25B, respectively. Only among ATRT–MYC cases, trisomies of chr8 and chr5, accompanied by a partial trisomy of chr5q, indicated by the wide orange/red bars at the respective locations, was observed in 11% (1/9) of cases (Figure 25A). Additionally, broad chr8p and chr22q losses, as indicated by the dark blue bar at the respective locations, were also identified once.

To summarize the CNV results of all analysed ATRT cases, a cumulative overview of CNV profiles of all three tumors and 13 cell lines was plotted in a clustered genome heatmap, as presented in Figure 26. The summary heatmap is a visualization where rows represent individual CN profiles of ATRT cases, which are stacked on top of each other and clustered according to common features as indicated by the dendrogram on the y-axis the plot. As in individual CN profiles of single cases, the CN ratio is plotted according to the chromosomal location on the x-axis. High CN ratios represent CN gains in orange/red whereas low CN ratios with represent CN losses in blue. The x-axis in Figure 26 depicts chr1–22, visually separated by vertical black lines. The sex chromosomes were purposely excluded, in order to prevent possible clustering based on sex.

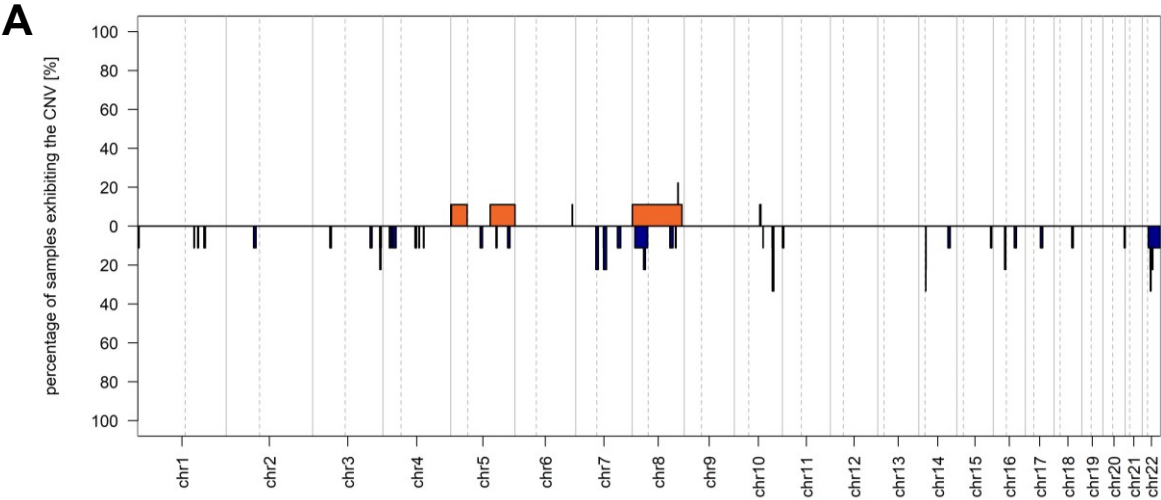


(Figure legend is on page 99.)

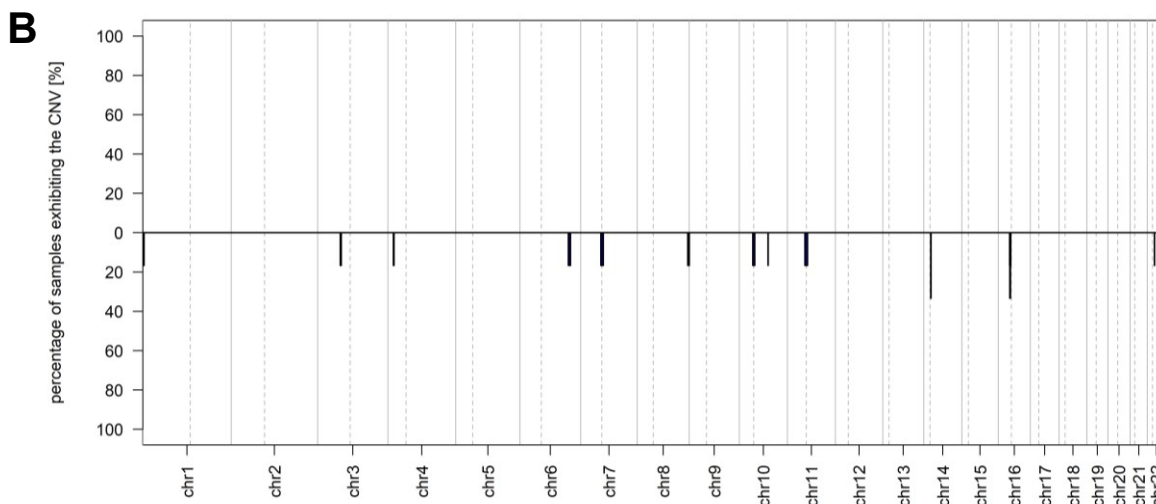


Figure 25. Summary CNV profiles of ATRT samples derived from DNA methylation array data. Nine cases of ATRT–MYC (A) and six cases of ATRT–SHHs (B). The y-axis of each summary plot represents the frequency of changes in % of all cases at the respective chromosomal location (x-axis). The dashed vertical lines indicate the locations of the centromeres and separate the respective chromosomes into p-arm (left) and q-arm (right) segments. CN gains are represented in orange/red above and CN losses are represented in dark blue below the baseline. Sex chromosomes are not included.

The heatmap of individual CNV profiles of ATRT cases in Figure 26 summarizes the genomes of individual cases, which present the CNVs discussed above. Apart from that, no evident clustering based on ATRT subtype can be conferred from the heatmap. The three ATRT–MYC cell lines presenting aneuploidies, CHLA-266, CHLA-06 and BT-12, cluster at the bottom of the heatmap followed by two other ATRT–MYC cell lines, BT-16 and VU397 (Figure 26, from bottom to top). After, CNV profiles of four ATRT–SHH cell lines (CHLA-04 – ATRT311-FHTC) follow. Only then, the CNV profile of the only ATRT–MYC-classified tumor, A2t, follows, presenting chr8p monosomy (Figure 26). Although without an assigned classification, the CNV profile of the tumor A1t is located between the CNV profiles of A2t and ATRT-13808, both cases assigned to the ATRT–MYC subtype. Then, the CNV profiles of two ATRT–SHH cases, HHU-ATRTO1 and its' original primary tumor, A3t, follow. At the top of the heatmap, the CNV profiles of two remaining ATRT–MYC cell lines, CHLA-02 and JC-ATRTO1, complete the illustration.

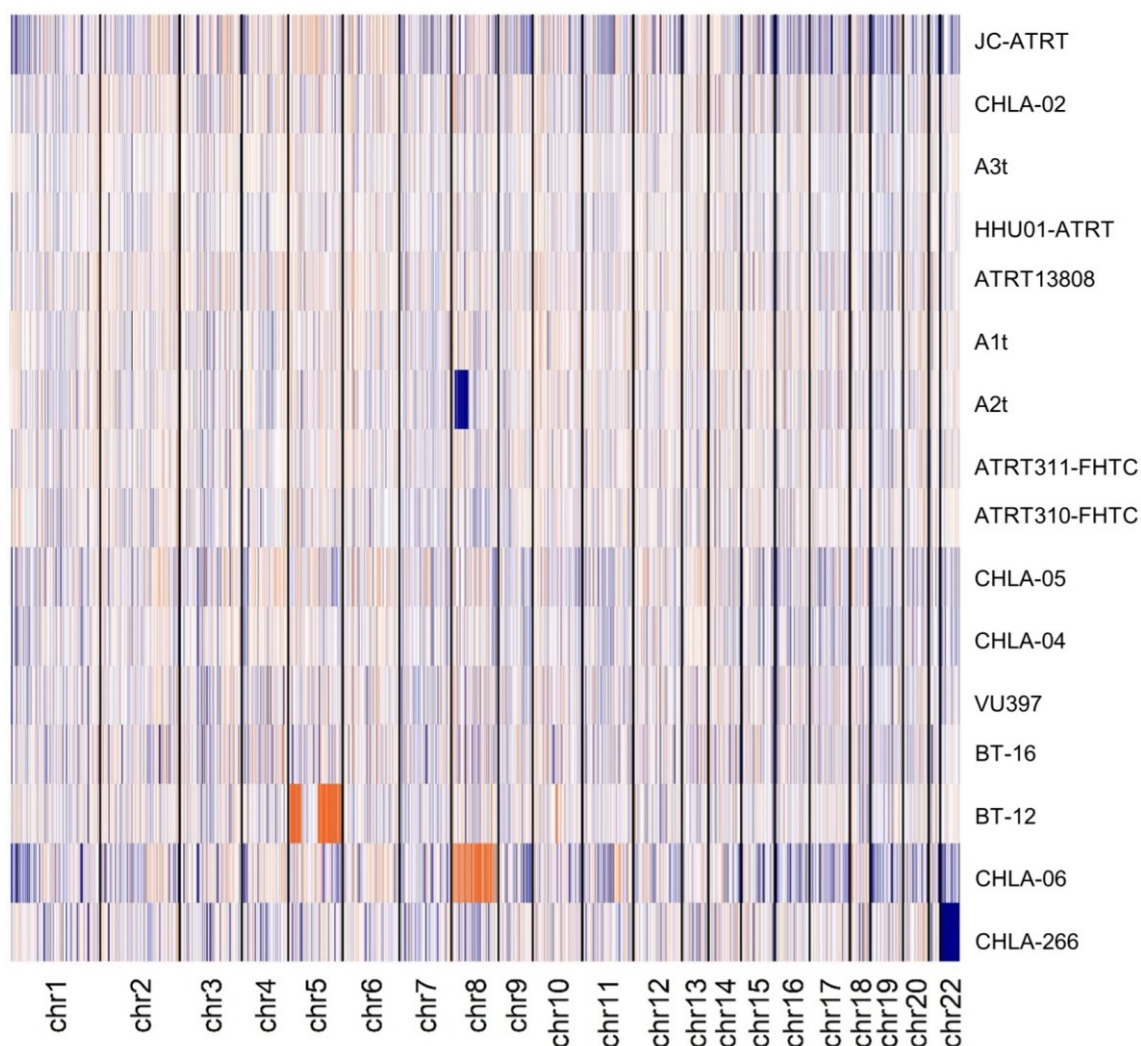


Figure 26. Summary genome heatmap of CNV profiles of ATRT samples as derived from DNA methylation array data. Shown is a clustered, cumulative overview of individual CNV profiles of ATRT tumors (A1t, A2t and A3t) and ATRT cell lines. The vertical axis shows the samples within the margins of the heatmap. The horizontal axis depicts chr1–22, visually separated by vertical black lines. CN gains are orange/red and CN losses are dark blue. Sex chromosomes are not included.

3.4.4 Identification of focal DNA copy number variants and structural variants in ATRT samples by optical genome mapping

Thirteen ATRT cell lines, three ATRT tumors and one matched blood sample were examined by OGM to detect focal CNVs and SVs. Therefore, the annotated OGM analyses were performed for each processed sample as described in paragraph 2.5.6, and the respective SV datasheets were downloaded and analysed as described in paragraph 3.2. As presented in Figure 27, the final high-confidence, rare SVs identified across ATRT samples were visualized according to their chromosomal location in a cumulative circos plot per ATRT subtype, i.e., ATRT–MYC or ATRT–SHH. Thus, the ATRT tumor without assigned classification (A1t) was not included.

Among nine ATRT–MYC cases, 378 (42.00 ± 13.16) unique rare SVs, including deletions, duplications, insertions, inversions and translocations were detected (Figure 27, “ATRT–MYC”; Suppl. Table V). In total, 31 SVs overlapped with exonic regions of different cancer-associated genes from the COSMIC CGC database (Suppl. Table III). The most frequently affected cancer-associated gene was *SMARCB1* (chr22q), targeted by SVs of different sizes leading to hemi- or homozygous losses in four ATRT–MYC cell lines, CHLA-02, CHLA-06, CHLA-266 and JC-ATRT. In CHLA-02, a large, homozygous deletion of 1.8 Mbp (chr22:22,183,401–23,997,045) affected the cancer-associated loci *IGL*, *BCR* and *SMARCB1*. In CHLA-266, the 21 kbp deletion in chr22q11.23 (chr22:23,769,856–23,791,276) overlapped genes *MMP11* and *SMARCB1*, with a putative *MMP11::SMARCB1* gene fusion being identified by OGM (Suppl. Table IV). Furthermore, as shown in Figure 27 within the cumulative ATRT–MYC circos plot, a translocation between chr17 and chr22, t(17;22)(q21.33;q11.22), led to additional rearrangements of both implicated chromosomes, which resulted in a total loss of the genomic regions overlapping with *SMARCB1* in the cell line JC-ATRT. Within the same, rearranged genomic region on chr22, a putative *PPIL2::SMARCB1* gene fusion (del(22)(q11.21q11.23); chr22:21,674,056–23,818,528) was identified by OGM.

In four other ATRT–MYC samples, ATRT-13808, BT-12, BT-16 and A2t, no SVs were detected to overlap with the genomic region of *SMARCB1*, however, *SMARCB1* mutations were identified by panel NGS as summarized in Table 16. In A2t, a hemizygous nonsense mutation in exon 1 of *SMARCB1* was detected, accompanied by a hemizygous loss of the wildtype *SMARCB1* allele. In the cell line VU397, no genomic rearrangements overlapping with *SMARCB1* could be detected neither by OGM nor by NGS. In three ATRT–MYC cell lines, BT-12, CHLA-06 and CHLA-266, deletions overlapped with intronic regions of *CTNNA2*. In two other ATRT–MYC cell lines, BT-16 and ATRT-13808, deletions and insertions were affecting either exonic or intronic regions of *FHIT* (chr3:60,187,941–60,574,671). In the CHLA-06 cell line and in the tumor A2t, deletions of intronic regions of *ROBO2* were present. Additionally, a translocation between chr2 and chr3, t(2;3)(p24.2;p12.3), was detected within the intronic region of *ROBO2* (Figure 27, “ATRT–MYC”; Suppl. Figure I).

Among six ATRT cases of the SHH-subtype, 209 (34.83 ± 4.91) unique, rare SVs including deletions, duplications, insertions, inversions and one deletion-dependent, intrachromosomal fusion were identified by OGM algorithms (Figure 27, “ATRT–SHH”; Suppl. Table V). The only recurrently SV-affected genomic region was found on chr22q in 50% of ATRT–SHH cases, A3t, HHU01-ATRT and ATRT-310-FHTC, which overlapped with the genomic region of *SMARCB1*. In ATRT-310-FHTC, a large 610 kbp hemizygous deletion on chr22q11.23 (chr22:23,422,948–24,033,240) was detected concomitant with a 5 kbp insertion on chr22q11.23 in *SMARCB1*. In both A3t and HHU01-ATRT, smaller hemizygous deletions (5–

8 kbp) were detected, whereas a putative *MMP11::SMARCB1* gene fusion was also identified (del(22)(q11.23q11.23)) (Table 16; Suppl. Table VII). In three remaining ATRT–SHH cases, ATRT-311-FHTC, CHLA-04 and CHLA-05, no SVs were detected to overlap with the genomic region of *SMARCB1*. Nevertheless, *SMARCB1* mutations were identified by panel NGS as summarized in Table 16. Furthermore, multiple very similar SVs were detected between A3t and HHU01-ATRT, as for example a 40 kbp duplication affecting three exons of *PLAG1* (chr8:56,139,808–56,179,106) and a 5 kbp deletion affecting one exon of *TCF7L2*. No other recurrent SVs across different samples were identified among ATRT–SHH cases. In the non-classified tumor A1t, no genomic rearrangements overlapping with *SMARCB1* could be detected neither by OGM nor by NGS.

In total, 14 of 16 ATRT samples presented either SVs or SNVs in combination with SVs on the other allele overlapping with exonic regions of *SMARCB1* (Table 16). OGM identified large deletions, insertions, and translocations often encompassing the *SMARCB1* gene region. Homozygous frameshift deletions and nonsense mutations in *SMARCB1* were identified by NGS. In case of the tumor sample A2t, NGS detected a hemizygous nonsense mutation and OGM identified a copy-number drop in the region overlapping with *SMARCB1*. Among samples of both, the ATRT–MYC and ATRT–SHH subtype, a recurrent putative, deletion-dependent *MMP11::SMARCB1* gene fusion, del(22)(q11.23q11.23), was identified (Table 16). Apart from this, no other recurrent events of genomic rearrangements were detected by OGM. However, another putative gene fusion affecting *SMARCB1*, del(22)(q11.21q11.23), *PPIL2::SMARCB1* (chr22:21,674,056–23,818,528) was identified in JC-ATRT, the ATRT–MYC cell line.

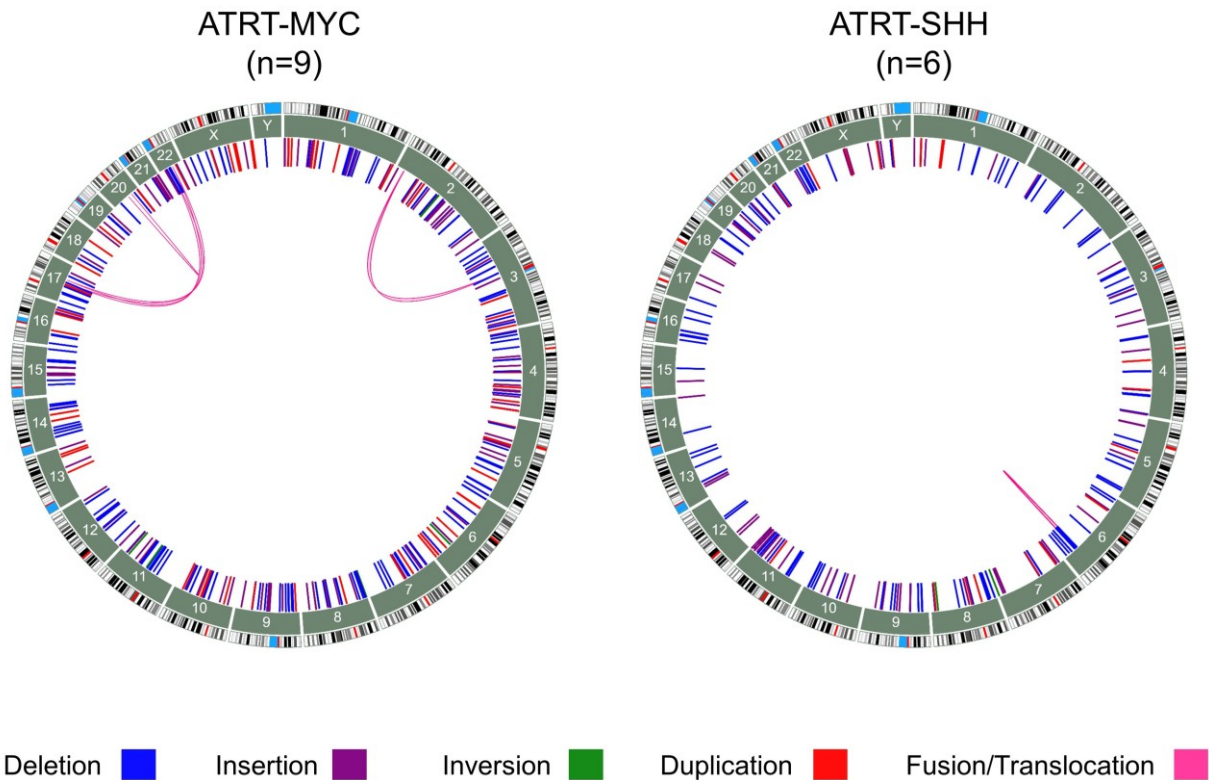


Figure 27. Cumulative SV profiles of 13 ATRT cell lines and two ATRT tumors separated according to the ATRT-MYC or ATRT-SHH subtype. The outer circle of each plot shows the ideogram of the respective chromosome with the centromere labelled in red and gaps in light-blue according to the GRCh38 reference genome. The numbered rectangles in the circle further inside represent each chromosome. SVs (deletions in blue, insertions in purple, inversions in green, and duplications in red) are visualized as lines inside the circle indicating the involved genomic positions. Complex SV events (translocations, chromothripsis) are shown as pink arcs connecting either the same (intrachromosomal SVs) or two different chromosomes (interchromosomal SVs). Alterations detected in the ATRT-MYC subtype (n = 9, SVs = 378) are summarized in the left and alterations detected in the ATRT-SHH subtype (n = 6, SVs = 209) are summarized on the right side of the figure.

Table 15. Summary of investigated ATRT cell lines and tumors as classified by EPIC 850k DNA methylation analysis and OGM-detected SVs, aneuploidies and subchromosomal CNVs. A “balanced genome” is diploid and has a CN = 2, “gain” represents $2.2 < CN \leq 3.5$, “amplification” has $CN \geq 3.5$, “hemizygous deletion” has $0.8 < CN < 1.8$ and a “homozygous deletion” represents the total loss of the respective genomic region, $CN < 0.8$.

Sample type	Sample ID	Brain tumor classification v12.8 (calibrated score)	OGM Aneuploidies and CNVs	Nr. of rare SVs/ somatic SVs
Cell line	ATRT13808	ATRT, MYC-subtype (0.96201)	Focal hemizygous deletion on chr2q; focal gain on chr6p	55
Cell line	ATRT310-FHTC	ATRT, SHH-subtype (0.99484)	Focal hemizygous deletion on: chr4p, chr6q, chr9p	42
Cell line	ATRT311-FHTC	ATRT, SHH-subtype (0.49257)	Focal hemizygous deletion on chr3p	28
Cell line	BT-12	ATRT, MYC-subtype (0.66682)	Chr5p trisomy; focal amplification and partial gain on chr5q; focal gain on: chr6q, chr10q	39
Cell line	BT-16	ATRT, MYC-subtype (0.77544)	Focal gain on chr15q	42
Cell line	CHLA-02-ATRT	ATRT, MYC-subtype (0.50433)	Focal hemizygous deletions on: chr5q, chr19q, chr20p; focal homozygous deletion on chr22q	24
Cell line	CHLA-04-ATRT	ATRT, SHH-subtype (0.75624)	Balanced genome	38
Cell line	CHLA-05-ATRT	ATRT, SHH-subtype (0.81965)	Balanced genome	36
Cell line	CHLA-06-ATRT	ATRT, MYC-subtype (0.85933)	Chr8 trisomy; focal hemizygous deletion on chr14q	49
Cell line	CHLA-266	ATRT, MYC-subtype (0.88673)	chr22 monosomy; focal gain on chr1q; focal hemizygous deletion on chr5q; chr3q-5q translocation	39
Cell line	HHU01-ATRT	ATRT, SHH-subtype (0.99343)	Focal hemizygous deletion on chr4q; focal gain on chrXq	36
Cell line	JC-ATRT	ATRT, MYC-subtype (0.82479)	Focal hemizygous deletion on: chr17q, chrXq; partial homozygous and focal hemizygous deletion on chr22q; chr17q-22q translocation	69
Cell line	VU397	ATRT, MYC-subtype (0.99160)	Focal hemizygous deletion on: chr5q, chr11q	29
Tumor	A1t	No assignment (no score ≥ 0.3)	Balanced genome	19/8
Tumor	A2t	ATRT, MYC-subtype (0.99999)	Focal gain on chr2p; hemizygous deletion of most chr8p; chr2p-3p translocation	32
Tumor	A3t	ATRT, SHH-subtype (1.00000)	Focal gain on chrXq	29

3.4.5 Identification and validation of novel gene fusions in ATRT

OGM identified 45 distinct, putative gene fusions among the 14 ATRT samples, as listed in the Supplementary Table IX. Of those, 38 belonged to the nine ATRT–MYC cases. Seven fusions were found among five of the six ATRT–SHH cases. All of the OGM detected putative gene fusions were formed either through deletion or duplication of a DNA segment. In order to validate the OGM-detected putative gene fusions resulting from SVs, previously published RNA-Seq dataset¹⁶⁸ of the same ATRT cell lines was analyzed. Fusion transcripts from RNA-Seq data were identified by Arriba¹⁷⁴ and compared to the final list of high-confidence, rare SVs detected in the respective ATRT cell lines as well as the cumulative putative gene fusion list identified by OGM (Suppl. Table VII). In 7 of 13 cell lines, 23 gene fusions with two coding gene partners were found by Arriba (Suppl. Table IX). The Arriba-identified gene fusions labelled as “high-confidence” resulted from duplications (n = 12), followed by deletions (n = 8), inversions (n = 1) and a translocation (n = 1) (Suppl. Table IX). Five of those overlapped with OGM-identified putative gene fusions (Suppl. Table VII), whereas only one was validated by both, Arriba¹⁷⁴ and FusionCatcher¹⁷⁵, independently. The presence of the *PPIL2::SMARCB1* (chr22:21,674,056–23,818,528) gene fusion formed through a deletion event del(22)(q11.21q11.23) in the ATRT–MYC cell line JC-ATRT could be confirmed through the respective fusion transcript, ENST00000335025.12(PPIL2):e.1_6::ENST00000644036.2(SMARCB1):e.6_9 (Figure 28, Table 14 and Suppl. Table VII). This fusion transcript was of high confidence, with in-frame orientation within the coding sequences and involved the retention of 83% of the SNF5/SMARCB1 domain (Table 14). The other OGM-identified and *SMARCB1*-implicated gene fusion, *MMP11::SMARCB1*, previously detected in the cell lines HHU01-ATRT, CHLA-266, and the tumor A3t could not be confirmed through RNA-Seq data by neither caller (Suppl. Table VII; Suppl. Table IX).

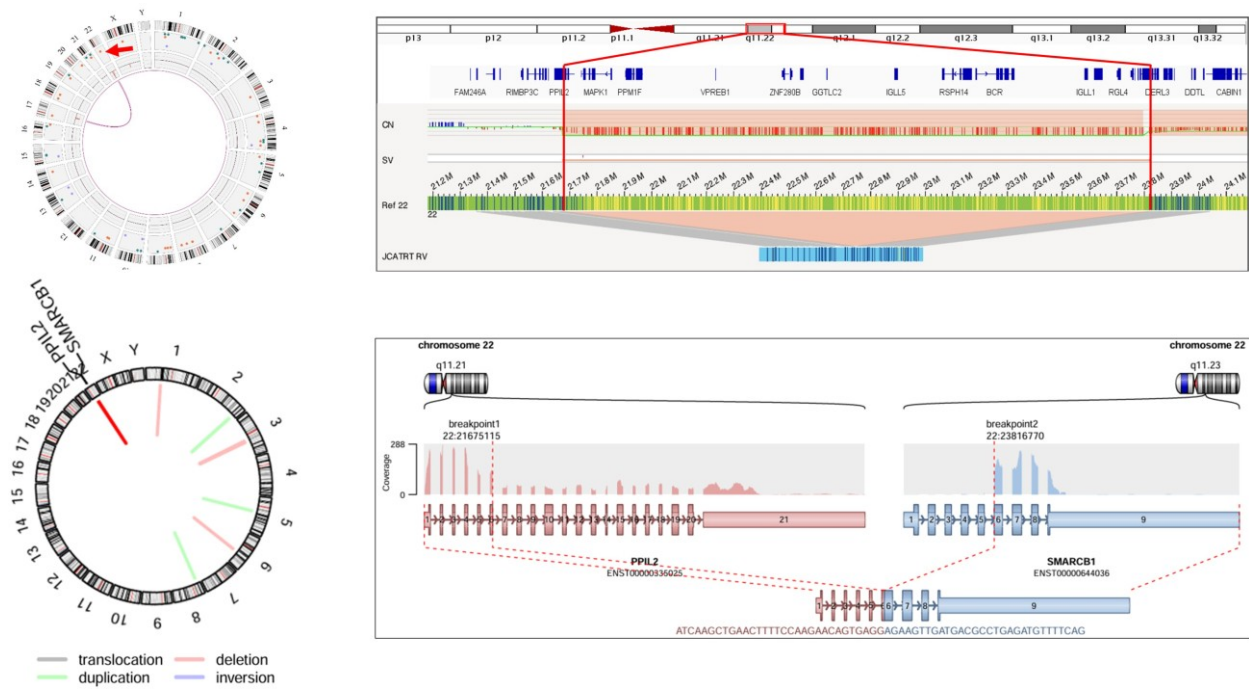


Figure 28. Novel *PPIL2::SMARCB1* gene fusion in the cell line JC-ATRT detected by OGM and RNA-Seq. Two representations of the same gene fusion event are given. The upper circos plot (left) and SV-view (right) are derived from OGM data and the lower circos plot (left) and SV-view (right) from Arriba analysis of RNA-Seq data. The circos plots emphasize all structural rearrangements of the analyzed sample. The SV event of interest is indicated by a red arrow (OGM) or a red line (Arriba), and both SV-views zoom into the specific SV event. In OGM-SV-view, the reference regions are indicated in green with the respective whole chromosome on the upper rim of the window and below the light blue OGM consensus map (map incorporating the SV), indicating the partial alignment to the reference region including the deletion. In the Arriba SV view, a schematic visualisation of detected transcripts of the fusion partners, their coverage, orientation and the retained exons contributing to the fusion transcript are visualized. OGM detected a deletion-dependent gene fusion, del(22)(q11.21q11.23), on the q-arm of chr22. The breakpoints were 2.1 Mbp apart and within the genes *PPIL2* and *SMARCB1* (chr22:21,674,056–23,818,528). Based on RNA-Seq data, Arriba predicted a ENST00000335025.12(*PPIL2*):e.1_6::ENST00000644036.2(*SMARCB1*):e.6_9 fusion transcript formed through a deletion. This gene fusion was independently validated by FusionCatcher.

Table 16. *SMARCB1* alterations in ATRT samples as detected by OGM and NGS.
AF, allele frequency

Sample ID	<i>SMARCB1</i> status
A1t	Wild-type
A2t	OGM: Loss of region (CN = 1.59) overlapping with <i>SMARCB1</i> NGS: Hemizygous nonsense mutation, likely pathogenic <i>SMARCB1</i> :NM_003073.5:exon1:c.90_91delCGinsTT:p.Ser30;Glu31* (AF = 33,05%)
A3t	OGM: Homozygous deletion on chr22q11.23 (chr22:23,783,774–23,796,274) with <i>MMP11</i> , <i>SMARCB1</i> gene overlap forming a putative <i>MMP11::SMARCB1</i> gene fusion
ATRT13808	NGS: Homozygous frameshift deletion leading to premature termination after 25 amino acids, likely pathogenic <i>SMARCB1</i> :NM_003073.5:exon3:c.351delC:p.Thr118ProfsTer25 (AF = 100%)
ATRT310-FHTC	OGM: homozygous 5 kbp insertion on chr22q11.23 (chr22:23,769,856–23,856,402) and 610 kbp hemizygous deletion on chr22q11.23 (chr22:23,422,948–24,033,240) including <i>SMARCB1</i>
ATRT311-FHTC	NGS: Homozygous nonsense mutation, likely pathogenic <i>SMARCB1</i> :NM_003073.5:exon5:c.618G>A:p.Trp206*(AF = 98,7%)
BT-12	NGS: Homozygous frameshift deletion leading to premature termination after 10 amino acids, likely pathogenic <i>SMARCB1</i> :NM_003073.5:exon2:c.178_179delAG:p.Arg60GlufsTer10 (AF = 100%)
BT-16	NGS: Homozygous frameshift deletion leading to premature termination after 28 amino acids, likely pathogenic <i>SMARCB1</i> :NM_003073.5:exon1:c.80delT:p.Met27ArgfsTer28 (AF = 100%)
CHLA-02-ATRT	OGM: Homozygous deletion of 1.8 Mbp on chr22q11.22–q11.23 (chr22:22,183,401–23,997,045, CN=0) with <i>SMARCB1</i> gene overlap
CHLA-04-ATRT	NGS: Homozygous nonsense mutation, likely pathogenic <i>SMARCB1</i> :NM_003073.5:exon6:c.769C>T:p.Gln257* (AF = 99,66%)
CHLA-05-ATRT	NGS: Homozygous frameshift deletion leading to premature termination after 10 amino acids, likely pathogenic <i>SMARCB1</i> :NM_003073.5:exon6:c.655delT:p.Ser219GlnfsTer10 (AF = 100%)
CHLA-06-ATRT	OGM: Homozygous 13.5 kbp deletion on chr22q11.23 (chr22:23,796,274–23,856,119) with <i>SMARCB1</i> gene overlap
CHLA-266	OGM: chr22 monosomy, homozygous deletion on chr22q11.23 (chr22:23,769,856–23,791,276) with <i>MMP11</i> , <i>SMARCB1</i> gene overlap forming a putative <i>MMP11::SMARCB1</i> gene fusion
HHU01-ATRT	OGM: Homozygous deletion on chr22q11.23 (chr22:23,783,774–23,796,274) with <i>MMP11</i> , <i>SMARCB1</i> gene overlap forming a putative <i>MMP11::SMARCB1</i> gene fusion
JC-ATRT	OGM: Homozygous deletion of 2.1 Mbp on chr22q11.21–q11.23 (chr22:21,674,056–23,818,528; CN = 0) with <i>SMARCB1</i> gene overlap and a putative <i>PPIL2::SMARCB1</i> gene fusion (fusion transcript: ENST00000335025.12(PPIL2):e.1_6::ENST00000644036.2(SMARCB1):e.6_9 validated by RNA-Seq)
VU397	Wild-type

4 Discussion

4.1 Evaluation of the optical genome mapping workflow and sample processing with regard to ultra-high molecular weight genomic DNA quantity and quality

As described in detail within the results, the mean gDNA concentrations of processed samples across sample types were distributed across a wide range (42.7–264.3 ng/ μ L) and varied significantly ($F(2, 66) = 6.85, p = 0.002$); suggesting that processed cell lines yielded significantly less gDNA than cells from blood or tumor tissue samples, independent of the tumor entity (MB and ATRT). The differences in gDNA yield could be attributed to variation in the input number of cells, whereas cell lines had an overall approximately similar input of 1.63×10^6 cells, but samples from blood or tissue likely had higher effective cell inputs, thus explaining their higher yields. The processed tumor samples, all derived from 3 x 3 mm punch biopsies, likely varied in cell density, which finally contributed to differences in gDNA yield. This variability arises from the intrinsic nature of tumors, which are often highly diverse in both their cellular composition and density^{1,4,41,181}. Factors such as the proportion of cancerous, stromal, and immune cells, necrotic regions, extracellular matrix, and other components can impact the gDNA yield^{41,181}. Although all tumors were histologically examined for appropriate tumor cell content being $\geq 80\%$ prior to gDNA extraction, a certain level of variability was still present. In tumor matched blood samples, the lack of leukocyte counting potentially introduced the highest variability across all samples, although approximately similar volumes of whole blood were used for gDNA extractions. Patient-specific factors, including age, health status, recent treatments, along with infections, inflammation, or haematological disorders can influence leukocyte counts and thus may contribute to variability in leukocyte numbers, which eventually affects the final gDNA yield¹⁸². Furthermore, the handling and storage of whole blood samples may influence cell integrity and recovery of intact UHMW gDNA¹⁸². Although whole blood samples subjected to more than one freeze-thaw cycle were not recommended for extraction of UHMW gDNA, and were thus not processed, variability of pre-processing storage conditions and duration could also affect blood sample quality.

The processed tumor and blood samples showed higher variability, which was most likely due to non-standardized input, though the homogenization steps finally ensured consistency in subsequent analyses. Despite the initial differences, post-labelling mean gDNA concentrations were more uniform across all sample types (3–21 ng/ μ L; $F(2, 66) = 1.015, p = 0.368$) and within the recommended range for chip loading and scanning, indicating successful dilution and that equilibration processes were effective in standardizing gDNA quality and concentration.

Therefore, adjustments in processing, such as dilutions, mixing and extended equilibration times for viscous samples, were critical for achieving gDNA homogeneity.

The quality of the OGM generated raw molecule files derived from labelled, homogenous UHMW gDNA samples, were evaluated through several quality control (QC) metrics, yielding insights into the gDNA integrity and its suitability for downstream analyses. Most QC parameters, including throughput, effective coverage (x), mapping rate, and labelling density, did not show statistically significant differences among sample types (cell lines, tumor tissues, blood samples). The observed QC differences among the sample types were interpreted as random variation rather than a systematic bias of sample types. Since the maximal throughput was pre-set at 1300 Gbp and the resulting maximal coverage (x) was dependent on both, the throughput and the mapping rate of the selected reference, the non-significant ANOVA results of these three QC parameters indicate an expectedly similar and good gDNA quality across processed sample types.

In the context of genome analysis, coverage (x) is a measure of depth that represents the average number of detected molecules at a given locus in the genome. It can be calculated as the quotient of the total amount of throughput data and the predicted haploid genome size. Therefore, the GRCh38 genome assembly was selected as reference for assessment of sample quality and calculation of the expected genome coverage (x). With the maximal throughput of 1300 Gbp and the predicted haploid genome size of the GRCh38 reference of ~ 3.2 Gbp, the maximal genome coverage was expected around $\sim 400x$. However, since not every molecule perfectly represents a given locus and aligns to the given reference, the “Estimated Effective Coverage of the Reference (x)” is used by Bionano as a proxy (Table 12, “Est Effective Coverage [x]”). It is defined as the total DNA of “cumulative length of DNA molecules that are ≥ 150 kbp and have ≥ 9 labels” multiplied with the mapping rate (=alignment to the reference), divided by the given reference size. The final mapping rate to the GRCh38 reference was similar across all processed samples yielding an average estimated effective coverage of the reference of 344x.

The QC parameter “Labelling Density” (Figure 11E) represented the average number of labels per 100 kbp for total DNA molecules that are 150 kbp or longer. This metric is indicative of the grade of DLE-1 enzyme activity and accessibility for efficient UHMW gDNA labelling, which is dependent on both, the gDNA homogeneity and the presence of inhibitory substances in the gDNA. Since the labelling density was both, within the Bionano recommended range of 8–25 labels/100 kbp and uniform across the analysed gDNA from different sample types, the DLE-1 efficiency was considered as good.

The QC parameter “N50”, which was lower for blood samples as compared to tumor and cell line samples, is a commonly used statistical measure in the context of genome assembly from sequencing data¹⁸³ but in this particular case, the OGM data. It is defined as the length of the shortest continuous sequence in a set of sequences that together contain at least 50% of the total length of the genome¹⁸³. Therefore, the N50 metric provides an indication of the assembly quality and contiguity, meaning the higher the N50 value, the longer the sequences, suggesting fewer gaps and a higher-quality genome assembly. These findings indicate that the UHMW gDNA molecules with at least 150 kbp of size extracted from cell lines and tumor tissues were generally longer and more continuous as compared to UHMW gDNA molecules extracted from blood samples, thus enabling higher quality genome assembly. From biological point of view, this could suggest specific cell characteristics present in the cell lines and tumors, which result in higher N50 values compared to peripheral blood leukocytes. These characteristics may be related to the shared origin of both tumors and cell lines, as both essentially represent malignant cells formed within the brain as compared to the leukocyte fraction extracted from whole blood. Alternatively, it could also simply indicate that gDNA from both tumors and cell lines was generally more stable upon handling, which can sometimes lead to DNA fragmentation, or simply that gDNA extracted from leukocytes was generally more prone to fragmentation.

Although the results underline the importance of cell input standardization in gDNA extraction protocols, a certain grade of variability persists even with standardized cell input, as observed across the initial gDNA concentrations of cell lines. Nevertheless, successful homogenization and comparable final labelled UHMW gDNA concentrations highlight the robustness of the UHMW gDNA preparation and labelling protocols across diverse biological sources, providing individual adjustments for gDNA homogenization are made. Additionally, the consistency in the QC metrics of OGM generated data underscores that UHMW gDNA extracted from all sample types was processed with sufficient quality for reliable genome analyses.

4.2 Comparison of DNA copy number variant analysis by optical genome mapping versus EPIC array-based analysis

OGM CNV algorithms revealed significant differences with regard to the CNV prevalence between distinct subtypes of ATRT, ATRT–MYC and ATRT–SHH: genomes of ATRT–MYC cases exhibited a higher prevalence of genomic rearrangements as compared to the ATRT–SHH cases. Whole-chromosome aneuploidies (e.g., chr8 trisomy and chr22 monosomy) were observed exclusively among the ATRT–MYC subtype (in CHLA-06 and CHLA-266) and common focal/partial CNVs affected chr5q and chr22q. Among the ATRT–SHH subtype, no common CNVs were identified, being sub-chromosomal and observed only in single cases.

In concordance with the OGM findings, DNA methylation-based CNV analysis by conumee 2.0 highlighted similar results, such as chr8 trisomy, gains on the p- and q-arm of chr5, and chr22q loss among cases of ATRT–MYC. All remaining conumee-identified shifts within the cumulative CNV profiles of both ATRT subtypes were sub-chromosomal and either frequently located in close proximity to the centromeric indicators of the respective chromosomes or again, observed only in individual cases. As these features could not be supported by the OGM results, one could argue them as methodological limitation of the DNA methylation-based analysis and the subsequent, cumulative visualization thereof. In the original “Summary CNV plots” from Capper *et al.*¹⁶⁰, these centromeric CNV peaks can also be observed independent of tumor entity.

Next, the comprehensive visualization of chromosomal variants across all analyzed ATRT cases was integrated within the cumulative, whole genome CNV heatmap (Figure 26). At first glance, no clear clustering based on ATRT subtype could be conferred from the heatmap. However, five ATRT–MYC cell lines were separated within the heatmap, whereas three cases exhibiting chromosomal aneuploidies were clustered at the bottom (BT-12, CHLA-06 and CHLA-266) and two other cases, JC-ATRT and CHLA-02, clustered on the complete opposite side, at the top of the heatmap. According to OGM, these two cell lines contained large, megabase pair long, homozygous deletions of the region on chr22q11.23, including not only the *SMARCB1* gene, but also the cancer-associated loci *IGL* and *BCR*. Here, the genomic similarity and thus the separate clustering of both ATRT cell lines becomes evident. However, it is very interesting to note that the classification of the cell line CHLA-02 is somewhat ambiguous, as some studies still consider it as an ATRT–SHH cell line^{76,184} but others also defined a MYC-association after classification with the DNA methylation-based CNS tumor methylation classifier (former MNP classifier)¹⁸⁵. Altogether, the cumulative results are in line with the current consensus, whereas multiple studies describe more extensive CNV patterns and a general higher genomic instability among the ATRT–MYC subtype as compared to the more restricted and focal alterations in ATRT–SHH^{75,76,186,187}.

Among analysed MB tumors, both OGM and conumee 2.0 CNV algorithms detected chr6 monosomy in all three MB WNT and chr11 monosomy in a single WNT tumor. Concordantly, monosomy of chr6 is universally recognized as the signature CNV of MB WNT^{42,53}. However, copy number alterations of chr11 were not specifically reported before and are thus not supported as a characteristic event among MB WNT. The occurrence of chr11 monosomy in a single WNT case likely represents intertumoral heterogeneity and ultimately does not contradict the classification.

According to OGM, an overall low CNV prevalence with few focal alterations and mostly balanced genomes was identified among six MB SHH–infant tumors. In three cases, either

whole or parts of chr2 were affected by CN gains, whereas the same cases also presented either gains on chr3 or loss on chr10. Chr9 monosomy was detected once, as well. In concordance with OGM, conumee 2.0 also detected minimal CN alterations and partial gains/losses on chr2, chr3p, chr10q and loss of the entire chr9 in 20% of cases, corresponding to a single tumor of six MB SHH–infant. These findings align well with previous large-scale genomic analyses, which consistently showed lower frequency of CNVs and a general higher genomic stability among MB SHH of infant subtype as compared to MB SHH of children and adolescents^{42,52,53}. This observation is also recapitulated among the MB SHH–child cases of this study, whereas the overall CNV prevalence was higher and CN signatures consistent with isochr9p and isochr10p were identified both by OGM and conumee 2.0. Additionally, enrichment for chr9q loss and frequent losses affecting chr11, chr14q, and chr18q were highly concordant between both methods. Interestingly, these results go in line with a more recent study also documenting occasional deletions of chr10q, chr9q and chr11q among SHH-activated MB¹⁸⁸.

Widespread CN alterations across all chromosomes, with expectedly the most frequent signature of chr17p loss and chr17q gain, representing isochr17q, was found by OGM in three of four MB Group 3 (75%) and nine of eleven MB Group 4 tumors (82%). In contrast, conumee 2.0 detected losses of chr17p but failed to identify chr17q gains among MB Group 3 cases. Nevertheless, both OGM and conumee 2.0 frequently identified gain of chr7 and losses of chr8, chr10, and chr11p among MB Group 4. Losses of whole chr4, chr10, and chr16 and gain of chr1q were particularly frequent in MB Group 3 cases, as identified by both, OGM and conumee 2.0. Among MB cell lines, conumee 2.0 identified the most frequent gains to affect chr1 and losses in distal regions of chr11q and chr14q. In contrast, identification of clear patterns among MB cell lines by OGM proved challenging due to the highly complex nature of the detected rearrangements. These findings are highly consistent with the genomic results reported in large MB Group 3/4 cohorts^{42,43,53,189,190}.

Upon direct comparison of individual CN profiles obtained by either OGM or conumee 2.0 across all cases (Suppl. Figure I), the overall concordance between both methods became evident. The highest agreement was observed when coverage changes were highly pronounced, as in cases of high-level amplifications (MB15t, Suppl. Figure I) or unambiguous aneuploidies (MB10t, Suppl. Figure I). In contrast, subtle changes in fractional CN (e.g. fractCN = 2.23; CN = 2) were missed by conumee 2.0 in some instances and therefore no overall CN change was detected, as observed in the tumor MB12t (Suppl. Figure I). This particular difference in CN detection sensitivity can be largely explained by the nature of the DNA methylation array data and its' processing by conumee 2.0. Unlike OGM-integrated algorithms that define a baseline for a CN neutral state according to the inferred allele

frequencies, the conumee 2.0 package relies on a statistical method calculating the log₂-ratio of probe intensities of a query sample versus the linear combination of control samples (normalized intensities)¹⁹¹. Thus, the CN neutral baseline is defined as the line where the median absolute deviation to all data points is minimal, which reflects the predominant CN state in the sample. The accuracy of the baseline calculation also heavily depends on the quality of the tumor sample and the samples within the control dataset. On the one hand, poor-quality sample/control data may lead to imprecise baseline estimation, impacting the reliability of the CNV calls. On the other hand, it's recommended to include CN neutral samples of lower-quality (e.g. higher noise profiles) as part of the control dataset, to improve correction and estimation of the baseline CN neutral state for low-quality query samples¹⁹¹. This would also imply that upon comparison of CN profiles of distinct samples of different qualities, as in the summary genome heatmaps in Figures 18 and 26, the clustering could also possibly be biased not only by the actual, biological similarity/difference of the samples, but also by the quality of the sample itself. This needs to be considered upon evaluation of CN profiles.

For the majority of cases, CN profiles generated from DNA methylation array data are highly valuable and easily interpretable. Nevertheless, the reliance on the predominant CN state can be particularly problematic in cases with multiple significant chromosomal aberrations, as those cases may lack a clear CN neutral state, rendering final interpretation more challenging. Additionally, the CN gains and losses are visualized as shifts in log₂ ratio of normalized signal intensity (red for gains and blue for losses), which have to be interpreted as CN proxy. According to Capper *et al.*¹⁶⁰, the log₂ values can be evaluated as follows: values within the range of 0 ± 0.4 represent gains/losses of ~ 1 copy of chromosomal material with respect to the balanced reference and values within the range of $\pm 0.4 - (\pm 1.2)$ represent gains/losses of ≥ 2 copies of chromosomal material with respect to the balanced reference. For CN losses, the interpretation is aided by the biological restriction that the CN cannot fall below zero. Thus, a log₂ value below -0.4 would indicate a homozygous deletion with the complete loss of the respective region. However, the interpretation of CN gains above 0.4 can be more delicate, as the CNs can potentially range from two to multiple extra copies of chromosomal material, as in cases of focal high-level amplifications.

The biological interpretation within the scope of this thesis was based on the following log₂ ranges: 0.0 – (-0.4) was designated a hemizygous deletion and < 0.4 as homozygous deletion, 0.0–0.4 concluded a trisomy or sub-chromosomal gain of one additional chromosomal copy, 0.4–0.8 was considered an amplification and > 0.8 , a high-level amplification. The overall high concordance of both focal, circumscribed and broad, large-scale CNVs across both methods demonstrates the reliability of the findings in these regions, reinforcing the diagnostic utility of both approaches. OGM complements DNA methylation-based CNV analysis by providing

additional granularity, allowing for validation of subtle and more complex CNV findings. In contrast, the conumee 2.0 package for analysis of DNA methylation data provides group-level summaries and insights into frequently altered regions, which may not always be apparent in individual OGM CN profiles. These findings reinforce the diagnostic utility of both methods, highlighting OGM's ability to validate complex CNVs and conumee 2.0's efficiency in summarizing group-level genomic alterations.

4.3 Evaluation of DNA structural variants and copy number variants in ATRT and medulloblastoma samples by optical genome mapping

With regard to overall SV detection, the average number of unfiltered SVs identified by the RVA was similar in ATRT cell lines and ATRT tumors. Traditionally, ATRTs are described as having a low mutational burden, primarily based on the limited number of SNVs and small indels^{74,76}. However, when SVs are included in the analysis, the concept of mutational burden becomes more nuanced. Here, the RVA method's ability to detect SVs provides a broader snapshot of genomic alterations. While ATRTs lack the higher SNV prevalence documented for other cancer types⁶⁻⁸, the still substantial number of SVs (1435 ± 213 in ATRT cell lines and 1389 ± 137 in ATRT tumors) could indicate that genomic instability in ATRTs more likely manifests through structural changes, rather than point mutations or small indels. The similar SV counts identified across cell lines and tumors suggest that ATRT cell lines resemble the structural mutational landscape of the original ATRT tumors, enhancing their utility and underscoring their compatibility as models for studying ATRT pathogenesis. For this reason, ATRT cell lines were further analysed along with ATRT tumors. Nevertheless, a more detailed annotation was necessary to differentiate actual pathogenic SVs from passenger SVs, polymorphisms or artefact variants.

In MB samples, however, the RVA detected significantly more SVs in MB cell lines (1813 ± 333) compared to MB tumors (1513 ± 218 ; $p = 0.011$). Generally, several factors can plausibly contribute to the larger number of SVs detected in the cell lines as compared to primary tumors. First, unlike primary tumors, which often present high cellular heterogeneity, cell lines are established from a single clone. The selection of *a priori* highly proliferative clones can lead to favorable growth and accumulation of certain SVs over time¹⁹²⁻¹⁹⁴. Secondly, cell lines are usually propagated over many passages *in vitro*, allowing for the accumulation of additional DNA alterations due to replication errors, oxidative stress, and lack of repair mechanisms, leading to higher mutational rates and thus overall increased genomic instability¹⁹²⁻¹⁹⁴. Thus, MB cell lines were analysed separately from MB tumors in the present study.

Overall, deletions were consistently the most frequent SVs across all sample types. Following, SVs of various but increasing complexity, such as insertions, duplications and inversions were identified. Translocations or other more complex rearrangements were rare among ATRT samples and MB tumors but significantly more common in MB cell lines, averaging 148 (± 107) events per cell line. With regard to identification of high-confidence, rare SVs ≥ 4.5 kbp, which were identified by both RVA and DNP algorithms, in ATRT samples deletions predominated, followed by insertions, duplications and only very few inversions. Translocations or complex rearrangements were nearly absent, suggesting relatively stable genomes for ATRT samples in this context, in line with previous studies^{73,75,186}. In MB samples, high-confidence, rare SVs of higher complexity, such as various inter- and intrachromosomal rearrangements, were more frequently found in cell lines compared to primary tumors.

The majority of identified rare SVs among all sample types affected coding sequences (CDS), again with the highest prevalence observed in MB cell lines (861 CDS events in 6 samples), followed by MB tumors (433 CDS events in 29 samples) and ATRT samples (248 CDS events in 16 samples). This enrichment in CDS overlap suggests that SVs are likely to have direct impacts on protein-coding regions, potentially altering protein function and contributing to altered tumor growth and survival. While less likely to disrupt coding regions, intronic and intergenic SVs may have an impact on gene expression by interfering with splicing or recruitment and action of regulatory elements such as enhancers and silencers. Additionally, a subset of identified high-confidence, rare SVs overlapped with regions of multiple different cancer-associated genes, emphasizing their potential relevance to tumorigenesis by contributing to oncogenic activation, loss of tumor suppressor function, or other aberrant cellular pathways.

Generally, the overall higher prevalence of SVs as well as the higher number of SVs overlapping with cancer-associated genes indicates an overall higher mutational burden and increased genomic instability in MB cell lines compared to MB tumors and ATRT samples. The difference particularly between MB cell lines and MB tumors suggests that while cell lines provide a model for studying tumor biology, they may effectively overestimate the prevalence and the actual impact of identified SVs. To this end, additional analysis of paired tumor-normal samples was performed with OGM's dual VAP. The VAP was designed for identification of tumor-specific rearrangements (somatic SVs), by comparison of variants detected in tumor gDNA against tumor-matched blood gDNA, which ultimately serves as germline control. SVs present in both tumor and blood genomes are classified as germline alterations and excluded from the tumor-specific call set. Thus, only SVs not identified in blood gDNA resulted in a refined list of high-confidence, somatic SVs. The VAP analysis significantly reduced the number of rare SVs identified in matched tumor-normal pairs of MB samples ($F(1, 34) = 1.015$,

$p = 0.0053$), whereas the most significant reductions were observed for deletions and insertions. These findings suggest that while deletions and insertions constituted a significant proportion of the initially detected rare SVs, the majority of those were shared between tumor and blood genomes, thus representing germline events rather than tumor-specific alterations. For rare duplications and inversions, no significant reduction in numbers was observed, indicating that these SVs were of somatic origin and hence tumor-specific. These events may contribute to tumor-specific oncogene amplification or disruption of regulatory regions. Nevertheless, unambiguous identification of true somatic duplications, inversions, and particularly deletions and insertions would still necessitate parallel analysis of tumor and matched control samples. No statistical reduction was observed for intra- and interchromosomal translocations ($F(1, 34) = 0, p = 1$), indicating that these complex rearrangements are unique to tumor genomes and very unlikely to occur as germline variants in healthy, diploid genomes. Same findings were observed with regard to CNVs and aneuploidies, which were detected in tumor genomes only, and were entirely absent in the respective blood assemblies. The consistency of this observation across all paired tumor-normal samples suggests that CNVs and aneuploidies are robust markers of tumor-specific genomic instability, confirming their somatic origin. In contrast, SVs within the 500–4500 bp range, initially expected to refine the genomic landscape, were ultimately excluded as somatic SVs due to their co-presence in blood genomes. This indicates that the smaller SVs were primarily of germline origin and less likely to contribute to tumor-specific processes. These findings corroborate prior observations, agreeing that complex rearrangements are unique to tumor genomes and rarely occur in the healthy germline^{99,195,196}.

In summary, while the VAP findings underline the necessity of matched controls to distinguish between somatic and germline deletions, insertions, duplications and inversions, they also suggest that large-scale genomic alterations, such as broad CNVs and aneuploidies alongside with circumscribed SVs of higher complexity, like different types of translocations, are indeed true somatic events. These findings influenced the evaluation of complex SVs for those tumor samples, where no tumor-matched blood samples were available. Thus, the OGM-identified CNVs, aneuploidies, intrachromosomal fusions and interchromosomal translocations were considered somatic variants, also including those identified in ATRT samples and MB tumors without the respective blood controls. Also, only rare SVs > 4.5 kbp were included within the final lists for unpaired ATRT and MB tumors and somatic SVs for tumor-normal paired ATRT and MB samples.

According to expectations, both ATRT subtypes, ATRT–MYC and ATRT–SHH, exhibited frequent and recurrent alterations affecting *SMARCB1*, highlighting its key role in ATRT biology^{64,73,75}. The bi-allelic *SMARCB1* inactivation was hence supported as the central

mechanism in ATRT pathogenesis, with alterations affecting *SMARCB1* observed in 14 out of 16 samples, as supported by both OGM and NGS. According to NGS, homozygous frameshift deletions and nonsense mutations in *SMARCB1* resulted in premature termination of the protein and therefore directly influenced its tumor-suppressive functions. In cases where NGS detected only a hemizygous nonsense mutation, OGM simultaneously identified a copy-number drop in the region overlapping with *SMARCB1*. This indicates bi-allelic inactivation of *SMARCB1* through a combinatorial mechanism, where an SNV inactivates one allele and an SV/CNV the second allele. Otherwise, OGM found large deletions, insertions, and translocations to encompass the genomic region of *SMARCB1*, whereas two novel gene fusions with both *SMARCB1* as fusion partner were identified: *PPIL2::SMARCB1* and *MMP11::SMARCB1*.

The deletion-dependent *PPIL2::SMARCB1* gene fusion could be validated through a respective fusion transcript (ENST00000335025.12(*PPIL2*):e.1_6::ENST00000644036.2(*SMARCB1*):e.6_9) by two RNA-Seq-based callers, whereas a high-confidence, in-frame, exon–exon fusion was reported. Although *PPIL2* is not commonly known for its role in tumor suppression or oncogenesis, it encodes the protein Peptidylprolyl Isomerase Like 2, a transferase implicated in mRNA processing, mRNA splicing, and ubiquitination of proteins, which is broadly expressed across various tissues and in the brain¹⁹⁷. Since *PPIL2* is located upstream of *SMARCB1* and both coding sequences are fused together through a genomic deletion event, whereas according to Arriba, the first five 5'-terminal *SMARCB1* exons are lost, it is very likely that *PPIL2*'s promoter drives aberrant expression of a chimeric/truncated, and if at all, only partially functional *SMARCB1* isoform. Therefore, this fusion would act as a substitute for the classical biallelic *SMARCB1* inactivation.

The *MMP11::SMARCB1* gene fusion was identified in three ATRT cases, suggesting a novel and recurrent gene fusion event. The identification of recurrent *MMP11::SMARCB1* fusions in one ATRT–SHH tumor sample (A3t), the cell line established from the same tumor (HHU01-ATRT, ATRT–SHH), and an additional, unrelated cell line of a distinct subtype (CHLA-266, ATRT–MYC), could potentially indicate a novel mechanism of *SMARCB1* inactivation. However, this particular gene fusion could not be validated through RNA-Seq, neither by Arriba nor by FusionCatcher, indicating that this event might rather represent a recurrent structural genomic rearrangement leading to *SMARCB1* disruption, than a functional hybrid transcript. Indeed, a series of deletion-associated genomic SVs encompassing *SMARCB1* were also previously reported^{198,199}. Interestingly, two samples, VU397 and A1t, were identified as being wildtype for *SMARCB1*, with no detectable SVs or SNVs affecting this gene. This could implicate alternative pathways or genetic alterations, as for instance previously documented

SMARCA4 mutations among a rare subset of *SMARCB1*-intact ATRT tumors^{69,200}, further emphasizing the heterogeneity of this disease. The final integration of DNA methylation-based classification with OGM- and complementary NGS data revealed critical insights into the genomic alterations underlying ATRT pathogenesis, thereby confirming the predominant role of *SMARCB1* inactivation in ATRT pathogenesis^{64,73,75}.

Also for MB, the presented findings were largely consistent with known and already documented features in different, leading scientific publications, thereby strengthening the understanding of subgroup-specific molecular features of MB^{34,42,43,51,201}. As already mentioned, genomic instability is known to be a characteristic of cancer and is reflected by presence and higher frequency of pathogenic alterations (SNVs and SVs) and more complex chromosomal aberrations (translocations and chromothripsis)^{6,13,17,202}. The level of SV/CNV manifestation in examined MB cell lines represents an appropriate example for highly altered and spurious cancer genomes, which, if at all, are mostly resembled by several highly rearranged MB Group 3 and Group 4 tumors. This particular similarity was supported by the visualization of chromosomal variants across 29 MB tumors and six MB cell lines integrated within the cumulative CNV heatmap, as shown in Figure 18. The clustering of several highly rearranged MB Group 3 and Group 4 cases together with the MB cell lines emphasized common Group 3/4 CNV patterns, thereby suggesting common genomic alterations with potential biological similarities, but also higher aggressiveness and malignancy of the tumors.

MB Group 3 and Group 4 are usually more complex and aggressive, compared to MB WNT and most MB SHH (p53-mutant SHH excluded) tumors, frequently carry a dismal prognosis, and pose many clinical challenges due to their molecular complexity and intra- as well as intergroup heterogeneity³⁴. In line with this, the four analysed MB Group 3 presented complex patterns of chromosomal rearrangements and multiple aneuploidies. These SV and CNV patterns varied strongly from case to case. The isochr17q formation was observed in three cases and multiple intra- and interchromosomal translocations were detected. In one particular Group 3 case, MB4t, all of the mentioned features were observed. Here, multiple chromosomes showed extensive rearrangements, particularly chr8 and chr17. Furthermore, the formation of isochr17q coincided with multiple events of intrachromosomal translocations, which are indicative of chromothripsis, the recognized hallmark of highly unstable genomes^{99,117}. Chromothripsis is known to cause multiple DNA double-strand breaks (DSBs) during a single catastrophic event, leading to extensive and often complex chromosomal rearrangements¹¹⁶. Furthermore, chromothripsis induces chromosomal shattering whereas subsequent erroneous DNA reassembly and repair can lead to excision of chromosomal segments, which upon circularization, can form acentric, extrachromosomal DNA (ecDNA) segments^{99,117,203,204}. The circular ecDNA structure allows for extrachromosomal replication

within the cell and the absence of centromeres leads to random distribution of ecDNAs during cell division²⁰⁴. When ecDNA contains oncogenes, this results in generation of high copy number of proto-oncogenes significantly enhancing their expression levels^{117,205,206}. The overexpression of proto-oncogenes, in turn, contributes to tumor initiation and progression, driving uncontrolled cell proliferation and survival²⁰⁷. However, ecDNA formation is not exclusively a consequence of chromothripsis but is more commonly associated with various genomic instability events and DNA repair processes²⁰⁸.

Within the MB Group 3 tumor MB4t that contained chromothriptic genomic rearrangements, an additional high-level amplification of the *GPC5* gene on chr13 was observed, which also was validated by demonstration of *GPC5* overexpression using RNA-Seq analysis. The *GPC5* gene encodes Glypican-5, a member of the glypican family of cell surface heparan sulfate proteoglycans (HSPG)^{209,210}. These transmembrane proteins are documented to act as co-receptors in developmental cell signalling pathways (including SHH and WNT signalling) and are implicated in regulation of cellular growth, differentiation and modulation of growth factors^{209,210}. Thus, activating mutations or other genomic alterations leading to overexpression of glypicans are associated with developmental abnormalities and tumor progression. For instance, changes in the expression of *GPC3*, a paralog of *GPC5*, were documented to induce cell growth and simultaneously inhibit cell differentiation in pediatric embryonal tumors²¹¹. So far, amplification and overexpression of *GPC5* has been documented in several adult and pediatric tumors^{212–214}. In rhabdomyosarcoma, amplification and overexpression of *GPC5* was linked to increased cell proliferation via potentiation of FGF2, HGF and Wnt1A signaling without induction of cell differentiation²¹². Also in salivary adenoid cystic carcinoma (SACC) it is documented to act in a tumor-promoting way²¹⁵. Conversely, a study on uterine sarcomas reported no difference in cell proliferation but alteration in cell differentiation upon *GPC5* overexpression²¹⁴. In non-small cell lung cancer, *GPC5* is described as a tumor suppressor, indicating that the effects of altered *GPC5* expression may be strongly dependent on the context and tumor entity²¹⁶.

Notably, two other tumors of MB Group 4 (MB14t, MB21t) also presented increased levels of *GPC5* mRNA expression based on RNA-Seq data (Suppl. Figure IIIA), although no amplification of the corresponding genomic region was detected by OGM. Interestingly, one particular case, MB21t, also presented an increased *HGF* mRNA expression along with the *GPC5* mRNA overexpression (Suppl. Figure IIIA, B). These findings indicate, that the increased *GPC5* levels could be a recurrent event among Group 3 and Group 4 MB, which also implicates different molecular mechanisms in regulation of gene expression, aside the OGM-detected genomic amplification of the respective gene region on chr13q31.1. Interestingly, unlike MB SHH and MB WNT, MB Group 3/4 do neither exhibit aberrant SHH-

nor aberrant WNT-signalling. However, GPC5 is known to influence both developmental signalling pathways, which in turn may still be important in tumor development and progression of MB Group 3/4. Consequently, the mechanism of action and functional relevance of *GPC5* overexpression in MB still needs to be interrogated.

MB Group 4 is known to be the most commonly represented and heterogeneous molecular group accounting for approx. 40% of all MB cases^{27,28,40}. Group 4 tumors also comprised the majority of our MB patient cohort (n = 11) with the overall highest levels of SV and CNV heterogeneity, ranging from low to high genomic complexity as observed in MB3t/MB17t and MB5t/25t, respectively (Suppl. Figure I). The genomic heterogeneity was emphasized within the summary heatmap in Figure 18, where several Group 4 tumors were shown to cluster closer to some MB SHH-child tumors than to other MB Group 4 or Group 3 cases. These findings accentuate the high level of heterogeneity among MB Group 4 complying with other studies^{34,43,53}.

A common feature identified among three MB Group 4 was the presence of co-localized intra- and interchromosomal rearrangements affecting the q-arms of chr2 and chr8. In MB26t, two events of complex SVs, one interchromosomal translocation, t(8;2)(q24.13;q22.3), and one intra-chromosomal translocation fus(8)(q21.3;q24.22) resulted in two novel putative gene fusions, *NSMCE2::ZEB2* and *RUNX1T1::HPYR1*, respectively. According to Arriba, the fusion event between *NSMCE2* and *ZEB2* occurred with out-of-frame consequence, thus suggesting a potential loss-of-function (LOF) of the fusion transcript (Suppl Figure IIB). In line, *ZEB2* mRNA expression levels were the lowest in MB26t, as compared to all analysed MB tumors (Suppl. Figure IIID). *ZEB2* encodes the Zinc Finger E-Box Binding Homeobox 2 transcription factor, which acts as a DNA-binding transcriptional repressor in promoters and plays a crucial role in neuronal development^{217,218}. *ZEB2* is expressed in multiple tissues, particularly the central nervous system, and is known to contribute to metastasis of various cancers by repressing E-cadherin and inducing epithelial-mesenchymal transition (EMT)²¹⁹. *NSMCE2* encodes an E3 small ubiquitin-like modifier (SUMO) ligase, a component of the SMC5/6 complex²²⁰. This complex plays a key role in DNA repair, maintenance of genomic stability, and proper chromosome segregation during cell division²²⁰⁻²²³. In conclusion, given that the gene fusion detected by OGM likely caused the *NSMCE2::ZEB2* LOF fusion transcript, both DNA repair and regulation of EMT could potentially be impaired. This in turn would increase the genomic instability of the tumor and impact cell differentiation and migration. Similarly, the second gene fusion also putatively formed a LOF *RUNX1T1::HPYR1* fusion transcript, as identified by Arriba (Suppl Figure IIC). While the exact biological role of *HPYR1* is characterized insufficiently, *RUNX1T1* encodes RUNX1 Partner Transcriptional Co-Repressor 1, which is commonly investigated for its role in acute myeloid leukemia (AML) as part of the

RUNX1::RUNX1T1 fusion gene²²⁴. However, *RUNX1T1* is also implicated in neural development acting as a regulator in hippocampal neurogenesis and promoting the differentiation of neural stem cells (NSCs) into neurons²²⁵. In glioblastoma, *RUNX1T1* was described as tumor suppressor gene whose gene product targets and degrades HIF1 α , a protein that promotes tumor growth and survival under low oxygen conditions²²⁶. In this context, genomic rearrangements that inactivate *RUNX1T1* and facilitate the LOF *RUNX1T1::HPYR1* fusion transcript, would contribute to tumor progression by impairing cell differentiation and promoting tumor growth and survival. However, *RUNX1T1* expression levels in MB26t were the highest among all analysed samples (Suppl. Figure IIIE). This could indicate that the fusion affects only one allele, while the other remains functional and even upregulated as a possible compensatory response.

Multiple fusion events in a different MB Group 4 sample, MB5t, affected coding (*MYRIP::ITGA9*) and non-coding genomic regions (*ITGA9-AS1::EIF1B-AS1*), whereas both del(3)(p22.1p22.2) fusions were confirmed by OGM, Arriba and FusionCatcher. However, increased transcriptional expression of both fusion partners were detected only in case of both lncRNAs (Suppl. Figure IIIS, T). The fusion of lncRNAs could play biologically relevant regulatory roles and by affecting adjacent protein coding genes through epigenetic modifications, chromatin remodelling, enhancer hijacking or sterically prevent gene expression^{227,228}. Although *EIF1B-AS1* is yet lacking characterization, it has been recently associated with cuproptosis, the pathway of copper-induced cell death^{229,230}. Similarly, *EIF1AX-AS1* was documented to suppress proliferation and promote apoptosis of endometrial cancer cell by affecting *EIF1AX* mRNA stabilization²³¹. *ITGA9-AS1*, the *ITGA9* (Integrin Alpha-9) antisense RNA, has been associated with regulation of *ITGA9*, which is known to contribute to cell adhesion, migration and metastasis²³². Furthermore, it also seems to be implicated in cell proliferation and apoptosis in non-small cell lung cancer (NSCLC) cells²³³. Given the upregulation of both long-noncoding genes, this fusion may act as an oncogenic regulatory element, contributing to tumor aggressiveness through alteration of both, integrin-mediated and apoptotic pathways.

Additionally, multiple SVs were identified in a specific region on the p-arm of chr2, 2p16.3, among several MB Group 4 and Group 3 cases. Most deletions overlapped with either *NRXN1* or *NRXN1-DT* introns, whereas in case of MB21t, a translocation-dependent, t(2;8)(p16.3;q23.1), *NRXN1::NUDCD1* putative gene fusion was identified (Suppl. Figure IIA). So far, deletions/mutations affecting the p16.3 band of chr2, and particularly the key gene *NRXN1*, have been implicated in various neurodevelopmental and psychiatric disorders^{234,235}. However, genomic rearrangements affecting *NRXN1* and their role in tumorigenesis remain largely unexplored. *NRXN1* encodes Neurexin-1, a presynaptic cell-surface receptor that

interacts with multiple intracellular signalling proteins and is critical for neuronal development and function²³⁶. Thus, a disrupted *NRXN1* transcript, due to deletion or a LOF fusion, could impair its' normal role in synaptic adhesion, signalling and neuronal differentiation, potentially even contributing to tumorigenesis²³⁷. A very recent study on colorectal cancer proposed *NRXN1* as tumor suppressor gene and associated NRXN1 loss with decreased patient survival²³⁸. Additionally, the study indicated that loss of NRXN1 function may promote an undifferentiated cellular state, allowing tumor cells to retain proliferation and undergo EMT which would enhance the metastatic potential of the tumor cells²³⁸. In this context, the discovery of *NRXN1* loss among a subset of MB Group 3/4 could indicate a possible novel mechanism relevant for MB pathogenesis. However, no evident pattern of differential *NRXN1* mRNA expression was evident among analysed MB tumors (Suppl. Figure IIIG).

In contrast to the highly heterogeneous and rearranged genomes of MB Group 3 and 4, WNT-activated tumors presented mostly balanced genomes and an overall low genomic instability^{13,53}. WNT MB are characterized by aberrantly activated WNT pathway signalling and are known to exhibit chr6 monosomy^{13,27,40,53}. This is also reflected in the OGM results and coincides with an overall good prognosis upon treatment with current therapeutics and thus a favorable outcome for patients with MB WNT⁴¹.

SHH-activated MB exhibit an aberrant activation of the Sonic Hedgehog pathway and are associated with an intermediate prognosis, which is, however, strongly subgroup-dependent^{34,41,53}. Additionally, a clear age-dependent segregation of MB SHH into SHH–infant and SHH–child is common, with better overall survival for the younger subgroup⁴⁴. This segregation is also comprehensively underlined by the difference in SV and CNV alterations in the OGM-analysed MB SHH cases. Although slightly more tumors of SHH–infant (n = 6) than SHH–child (n = 5) were studied, the occurrence of CNVs was lower in MB SHH–infant cases pointing towards higher genomic stability and therefore presumably less aggressive/morbid feature of this subgroup. In addition, it appeared that among MB SHH–infant, the observed SVs manifested either as CNVs affecting whole chromosomes without additional complex rearrangements (MB12t/MB24t) or a singular SV event with otherwise balanced genomes. One of these SVs among SHH–infant MB was found in MB20t, as the intrachromosomal, deletion-dependent exon–exon fusion on chromosome X, del(X)(q25q26.1), in which *STAG2* and *ARHGAP36* were implicated. Additionally, both genes presented expression level changes, as compared to other MB tumors (Suppl. Figure IIIU, V). *STAG2* Cohesin Complex Component is the protein encoded by *STAG2*, which is the integral element of the cohesion complex crucial for chromosomal segregation during cell division²³⁹. Therefore, disruption of normal *STAG2* function could lead to chromatin remodelling defects, genomic instability and aneuploidy. Generally, *STAG2* is considered a tumor suppressor and

defects in *STAG2* are associated with increased rates of aneuploidy and accelerated tumor progression^{240,241}. The lower expression of *STAG2* in MB20t, as compared to other MB, could also be indicative of lower *STAG2* activity in this particular case. However, the MB20t did not present any aneuploidy, suggesting the *STAG2* fusion could potentially play another role in this case. Interestingly, some *STAG2*-mutant cancers were also documented to exhibit normal chromosomal structures^{242,243}. The second fusion-implicated gene, *ARHGAP36*, encodes the Rho GTPase Activating Protein 36 which is known to activate the SHH pathway, the key driver of MB SHH^{244,245}. *ARHGAP36* is specifically documented to enhance transcriptional activation of *GLI*²⁴⁶. Thus, overexpression of *ARHGAP36* could potentially lead to hyperactivation of *GLI* and enhanced SHH-signalling, contributing to tumor proliferation. Consequently, the detected, increased transcriptional expression of *ARHGAP36* could serve as a biomarker for a more aggressive MB subtype among the MB SHH–infant tumors. If the *STAG2::ARHGAP36* fusion would not directly impact *STAG2* function but instead place *ARHGAP36* under the control of the *STAG2* promoter causing the *ARHGAP36* mRNA overexpression observed in MB20t, it could lead to amplified SHH pathway signalling and thus drive tumor proliferation and aggressiveness.

Another novel, out-of-frame *SH3BP2::CTNNA3* gene fusion was formed upon an interchromosomal translocation, t(4;10)(p16.3;q21.3), in MB28t, a MB SHH–infant tumor. *SH3BP2* encodes the scaffolding SH3 Domain Binding Protein 2 that is crucial for regulation of intracellular signaling pathways of immune and skeletal systems^{247,248}. Loss of *SH3BP2* has been connected to some cancer types^{249,250}. *CTNNA3* encodes Catenin Alpha 3, a cell-cell adhesion protein responsible for maintenance of the structural integrity in a multitude of tissues²⁵¹. Deletions/mutations affecting *CTNNA3* have been implicated in neurodevelopmental disorders, indicating a role in neural development²⁵². Interestingly, *CTNNA3* mutation is currently being used as one of several biomarker criteria in a clinical trial for MB (ClinicalTrials.gov ID NCT02066220; https://www.mycancergenome.org/content/clinical_trials/NCT02066220/), emphasizing the potential relevance of the detected gene fusion. The fusion may potentially contribute to tumorigenesis of MB SHH–infant by disrupting cell adhesion, due to *CTNNA3* LOF, and enhancing inflammatory responses through *SH3BP2* dysregulation. However, both *SH3BP2* and *CTNNA3* gene expression levels were not particularly altered in comparison to other MB tumors (Suppl. Figure IIIJ, I).

In contrast to the mostly stable genomes of MB SHH–infant tumors, MB SHH–child presented a moderate genomic complexity and a decent level of intragroup variability comparable to some MB Group 4 tumors, which is also reflected by the mixed clustering patterns of both groups within the summary heatmap (Figure 18). This suggests a broader spectrum of MB

SHH-child behavior, ranging from less aggressive SHH-infant-like cases, as MB13t, to more genomically unstable, Group 3-like cases, as MB15t. Particularly in MB15t, co-amplification and enhanced expression levels of two known and crucial oncogenes of MB pathogenesis, *MYCN* and *CCND2*, were identified (Figure 20 and Suppl. Figure IIIK, L)⁴². Both co-amplified regions on chr2q and chr12p showed extensive rearrangements in form of multiple interchromosomal translocations and co-localized deletions, inversions and duplications, along with highly elevated CN values. These high-level amplifications could be linked to ecDNA-driven oncogenesis^{206,207} and might be associated with particularly aggressive behavior of this MB SHH-child case²⁵³⁻²⁵⁵. Interestingly, a deletion-dependent *ATF7IP::PTPRO* LOF gene fusion event was identified on chr12p in the same MB tumor. *ATF7IP* encodes the chromatin regulator Activating Transcription Factor 7 Interacting Protein that modulates heterochromatin formation, epigenetic gene silencing and stability^{256,257}. *PTPRO* encodes a known tumor suppressor, the Protein Tyrosine Phosphatase Receptor Type O, that is frequently downregulated in various cancers and is involved in cell cycle regulation and signalling control²⁵⁸⁻²⁶⁰. Both genes play a role in neurodevelopment and neuronal differentiation suggesting that this deletion-induced fusion event alone might have implications for CNS tumors²⁶¹⁻²⁶⁴. Additionally, the *ATF7IP::PTPRO* LOF fusion could also be mechanistically linked to ecDNA formation and co-amplification of *CCND2* and *MYCN* through multiple genomic instability pathways. For instance, the *ATF7IP::PTPRO*-fusing deletion might act as a catalyst for the *CCND2* and *MYCN* co-amplification, given that disruption of *ATF7IP* could lead to a breakdown in chromatin architecture, allowing genomic instability and breakage-fusion-bridge (BFB) cycles inducing ecDNA formation^{115,265}. The BFB rearrangement is driven by repeated cycles of the BFB that are initiated with a fold-back inversion and fusion of two sister chromatids at their fragile sites due to telomere loss^{115,265,266}. This fusion forms a bridge connecting both chromatids that result in an abnormal, dicentric chromosome. During anaphase, both centromeres are pulled toward opposite poles and the bridge undergoes a DSB. Since the resulting daughter cells inherit chromatids unprotected by telomeres, the cycle can repeat. The recurrence of BFB cycles leads to a complex genomic signature where inversions, duplications, and deletions co-localize and result in stepwise increase in CN amplifications²⁵. This exact SV patterns could be observed at genomic locations of both, *CCND2* and *MYCN* (Figure 20). Also, both genes are located close to subtelomeric regions of chr12p and chr2p, respectively, which also supports the idea of BFB-driven rearrangements with subsequent ecDNA-mediated *CCND2* and *MYCN* co-amplification. The simultaneous lack of tumor suppression by *PTPRO* could further promote conditions favorable for DNA amplification, thereby accelerating tumor progression. Furthermore, other gene fusion transcripts from chr12p revealed genes involved in calcium signalling and cellular transport, as identified by Arriba, that overlap with OGM-detected SVs (Suppl. Table VII). In particular, gene fusions affecting *CACNA1C* and *CRACR2A* suggest

alterations in calcium-dependent pathways in MB15t. In this context, mRNA overexpression of *CRACR2A*, but not *CACNA1C*, could be supported (Suppl. Figure IIIM, N). Both genes are regulators of neural function and tumor growth and thus, dysregulation of calcium-dependent pathways has been implicated in tumor progression and MB-associated tumorigenesis^{34,267–270}. In line with the literature, few genes encoding subunits of calcium channel complexes were differentially expressed across MB subgroups. For instance, *CACNB4* and *CACNA2D1* were significantly higher expressed among MB SHH compared to MB WNT, which in turn had significantly higher expression of *CACNG5*, *CACNA2D4* and *CACNA1F*. Among MB Group 3/4 MB, *CACNA1F*, *CACNA1G*, *CACNA1G-AS1* and *CACNA2D4* were significantly higher expressed compared to MB SHH (data not shown).

In the presumably less aggressive SHH-child case, MB13t, an in-frame *RANBP17::CANX* gene fusion was identified, formed through a ~ 8.7 Mb deletion within the distal region on chr5. *RANBP17* encodes RAN Binding Protein 17, a member of the importin- β superfamily regulating nucleocytoplasmic transport, a key process of cellular physiology²⁷¹. Calnexin 1, encoded by *CANX*, is a calcium-binding chaperone protein within the endoplasmic reticulum (ER) that interacts with newly synthesized glycoproteins, assisting protein folding, assembly and facilitating retention of erroneously assembled proteins within the ER for subsequent degradation²⁷². Proper protein folding and quality control are crucial for preserving cellular stability. Thus, disruptions in these processes have been linked to neurodevelopmental and neurodegenerative disorders, tumorigenesis and progression^{273–275}. Given that the in-frame *RANBP17::CANX* gene fusion can potentially form a chimeric fusion protein, alteration of nucleocytoplasmic transport mechanisms, impaired protein folding and mislocalization of proteins could induce stress response within the ER and initiate oncogenic signalling.

So far, multiple studies have demonstrated the high potential of OGM to reliably detect SVs with higher resolution and sensitivity than classical cytogenetic methods like fluorescence in situ hybridization and karyotyping^{276–282}. However, the application of OGM is currently more established for hereditary genetic disorders^{283,284} and hematological malignancies^{277–281,285,286}, with only few studies emerging in the field of solid tumors^{287–289}. In brain tumor research and diagnostics, usage of OGM still remains particularly rare, even though the utility has already been demonstrated^{290,291}. Bornhorst *et al.*²⁹⁰ applied OGM to a single case of a pediatric embryonal brain tumor and identified a novel *ZNF532::NUTM1* gene fusion, not previously described in pediatric CNS tumors. Singh *et al.*²⁹¹ analysed 10 glioma cases and documented a full concordance of OGM findings with SVs and CNVs previously characterized with chromosomal microarrays. While OGM has clearly shown to outperform classical cytogenetic techniques and in this study particularly excelled at detecting rare and complex SVs not detectable by DNA-methylation microarrays, its methodologic limitation in size of SV detection

(> 500 bp) and lack of sequence-level resolution have to be mentioned. Additional OGM limitations such as the higher sample quality requirements (UHMW gDNA), lower sample throughput (3 samples per chip) and lack of functional information, make it difficult to establish this method as a standalone technique in routine diagnostics of solid tumors, and thus still facilitate the need for complementary molecular methods. Parallel application of OGM and sequencing-based techniques such as targeted NGS and RNA-Seq could complement the detection of the mutational landscape and enable FFPE tissue-compatible analysis and detection of SNVs, small indels (< 50 bp), fusion transcripts, TFBSs with single nucleotide resolution, thereby enhancing the general applicability for routine diagnostics^{292,293}. These insights into gene expression and/or epigenetic regulation could aid functional interpretation and final diagnosis^{289,294}.

With rapidly advancing sequencing technologies and declining costs, integrating OGM and long-read sequencing is now more feasible than ever^{295,296}. Table 17 summarizes the key features of the five major technologies for detection of (epi-)genomic alterations with regard to input requirements, detection limits, costs, accuracy and data analysis complexity. The choice of platform, or combination of platforms, should be guided by the specific requirements of the intended application and the available resources. For instance, parallel application of OGM with a long-read WGS technique of choice could ideally resolve structural complexity and elevate the SV breakpoint resolution to the sequence-level²⁹⁷, however, also substantially raise the costs, the overall resource requirements²⁹⁸ (e.g., standardised protocols, quality control measures, integration into existing clinical workflows and infrastructure) and bioinformatics challenges²⁹⁹. With progressing development of long-read sequencing technologies it has also become evident that extraction of high-quality gDNA and preparation of high-quality sequencing libraries is more limiting for the length of the sequenced reads, than the actual platform²⁹⁹. For instance, Oxford Nanopore™ Technologies (ONT) is critically dependent on the generation of long sequencing reads starting with high-quality gDNA of high-molecular weight, as degraded or fragmented samples significantly reduce achievable read lengths³⁰⁰. Simultaneously, shearing of UHMW gDNA in viscous samples is required for uniform barcoding during ONT library preparation and subsequent pore engagement during sequencing³⁰¹. This in turn, ultimately reduces the potential and full utility of long-read sequencing. Therefore, advancements in both high-molecular weight gDNA extraction and high-quality library preparation techniques will be required before full implementation of such platforms in a routine tumor diagnostic setting³⁰⁰.

Table 17. Detailed comparison of five major technologies for detection of (epi-)genomic alterations.

Feature	Bionano OGM^{164,302}	Short-read NGS	EPIC Array³⁰³	ONT Long Reads³⁰⁴	PacBio HiFi^{304,305}
Input DNA Requirement	High ($\geq 1\text{--}2\ \mu\text{g}$ UHMW DNA)	Low (10–100 ng)	250 ng DNA	High ($> 1\ \mu\text{g}$ HMW DNA)	Moderate ($\geq 500\text{ng}$ HMW DNA)
Output	Optical maps (structural info)	Short sequencing reads	Methylation β -values (CpG sites)	Long sequencing reads	Long, highly accurate reads
Read Length	0.15–1 Mb molecules	100–300 bp	Single CpG resolution (850–935k sites)	20 bp to $> 4\ \text{Mbp}$	0.5–20 kbp
SV Detection	Excellent for $\geq 500\ \text{bp}$ SVs	Moderate	Moderate	Excellent	Excellent
SNV/Indel Detection	No	Yes/Yes	No	Yes/No	Yes/Yes
Epigenetics	No	After bisulfite conversion	Yes (5mC at predefined CpG sites)	Yes (5mC, 5hmC, 6mA)	Yes (5mC, 6mA)
Transcript/Splice Analysis	No	Yes (RNA-seq)	No	Yes (direct RNA-Seq)	Yes (Iso-Seq)
Data & Analysis Complexity	Moderate (specialized, integrated SV tools)	Low (mature pipelines)	Low (developed tools)	High (basecalling, polishing, SV & epigenetics tools)	High (assembly, phasing)
Cost (approx.; storage of big data not included)	Moderate, $\sim 400\text{€}/\text{sample}^{306}$	Moderate, 200–700€ ³⁰⁷	Low/Moderate, $\sim 350\text{€}/\text{sample}$	High, 800–1200€ but strongly platform- & coverage dependent ³⁰⁷	High, 700–1000€ but platform-dependent ³⁰⁷
Turnaround Time	3–5 days	2–4 days	3–5 days	3–5 days	2–4 days
Strenghts	Large balanced & unbalanced SVs, genome scaffolding	SNVs, indels, expression profiling ³⁰⁰	Genome-wide DNA methylation & CNV profiling ³⁰⁰	SVs, SNVs, methylation, isoforms, assembly ³⁰⁰	SNVs, SVs, high-accuracy assembly & phasing ³⁰⁰

To conclude, the combinatory approach of integrating genomic (OGM, panel NGS), transcriptomic (RNA-Seq) and epigenomic (850k EPIC array) analysis within this study provided deeper insights into molecular mechanisms underlying ATRT and MB heterogeneity, with potential implications for further functional research and targeted therapies. The parallel application of OGM and NGS confirmed bi-allelic *SMARCB1* inactivation as a key driver event in 14 of 16 analysed ATRTs, whereas OGM alone identified bi-allelic structural loss of *SMARCB1* only in seven of 16 cases (Table 16). RNA-Seq further aided identification and validation of OGM-detected putative gene fusions. In the cell line JC-ATRT, a novel, deletion-dependent *PPIL2::SMAPRCB1* gene fusion was verified through presence of the respective chimeric transcript. Within the MB cohort of this study, the inter- and intra-group heterogeneity across MB groups was further emphasized by OGM and supported by the CNV analysis of 850k EPIC arrays. High genomic complexity including isochr17q formation, events of chromothripsis and a high-level *GPC5* amplification were identified among MB Group 3. Also, a recurrently rearranged region affecting *NRXN1* or *NRXN1-DT* on chr2p16.3 was detected by OGM among several MB Group 4 and Group 3 tumors. In MB SHH-child, OGM identified oncogene co-amplification of *MYCN* and *CCND2* and increased expression levels of the respective transcripts were supported by RNA-Seq. Furthermore, several novel gene fusions across different MB subgroups were discovered, which could contribute to tumor pathogenesis through disrupted DNA repair, cell adhesion, or calcium signalling pathways.

7 References

1. Cooper GM. *The Cell: A Molecular Approach*. 2nd edition. Sunderland (MA): Sinauer Associates; 2000. *The Development and Causes of Cancer*. Available from: <https://www.ncbi.nlm.nih.gov/books/NBK9963/>.
2. Stratton MR, Campbell PJ, Futreal PA. The cancer genome. *Nature*. 2009;458(7239):719-724. doi:10.1038/nature07943
3. SEER Training Modules, What Is Cancer? U. S. National Institutes of Health, National Cancer Institute. 08.08.2024, <https://training.seer.cancer.gov/disease/cancer/>.
4. Hanahan D, Weinberg RA. Hallmarks of Cancer: The Next Generation. *Cell*. 2011;144(5):646-674. doi:10.1016/j.cell.2011.02.013
5. Association of Population-based Cancer Registries in Germany (GEKID) and the German Centre for Cancer Registry Data (ZfKD) at the Robert Koch Institute. *Cancer in Germany 2019/2020*.
6. Australian Pancreatic Cancer Genome Initiative, ICGC Breast Cancer Consortium, ICGC MML-Seq Consortium, et al. Signatures of mutational processes in human cancer. *Nature*. 2013;500(7463):415-421. doi:10.1038/nature12477
7. Lawrence MS, Stojanov P, Polak P, et al. Mutational heterogeneity in cancer and the search for new cancer-associated genes. *Nature*. 2013;499(7457):214-218. doi:10.1038/nature12213
8. Vogelstein B, Papadopoulos N, Velculescu VE, Zhou S, Diaz LA, Kinzler KW. Cancer Genome Landscapes. *Science*. 2013;339(6127):1546-1558. doi:10.1126/science.1235122
9. The ICGC/TCGA Pan-Cancer Analysis of Whole Genomes Consortium, Aaltonen LA, Abascal F, et al. Pan-cancer analysis of whole genomes. *Nature*. 2020;578(7793):82-93. doi:10.1038/s41586-020-1969-6
10. López-Otín C, Blasco MA, Partridge L, Serrano M, Kroemer G. The Hallmarks of Aging. *Cell*. 2013;153(6):1194-1217. doi:10.1016/j.cell.2013.05.039
11. White MC, Holman DM, Boehm JE, Peipins LA, Grossman M, Jane Henley S. Age and Cancer Risk. *Am J Prev Med*. 2014;46(3):S7-S15. doi:10.1016/j.amepre.2013.10.029
12. Aunan JR, Cho WC, Søreide K. The Biology of Aging and Cancer: A Brief Overview of Shared and Divergent Molecular Hallmarks. *Aging Dis*. 2017;8(5):628. doi:10.14336/AD.2017.0103
13. ICGC PedBrain-Seq Project, ICGC MML-Seq Project, Gröbner SN, et al. The landscape of genomic alterations across childhood cancers. *Nature*. 2018;555(7696):321-327. doi:10.1038/nature25480
14. Rahal Z, Abdulhai F, Kadara H, Saab R. Genomics of adult and pediatric solid tumors.
15. Ma X, Liu Y, Liu Y, et al. Pan-cancer genome and transcriptome analyses of 1,699 paediatric leukaemias and solid tumours. *Nature*. 2018;555(7696):371-376. doi:10.1038/nature25795

16. Downing JR, Wilson RK, Zhang J, et al. The Pediatric Cancer Genome Project. *Nat Genet.* 2012;44(6):619-622. doi:10.1038/ng.2287
17. Vogelstein B, Kinzler KW. Cancer genes and the pathways they control. *Nat Med.* 2004;10(8):789-799. doi:10.1038/nm1087
18. Sudmant PH, Rausch T, Gardner EJ, et al. An integrated map of structural variation in 2,504 human genomes. *Nature.* 2015;526(7571):75-81. doi:10.1038/nature15394
19. Li Y, Roberts ND, Wala JA, et al. Patterns of somatic structural variation in human cancer genomes. *Nature.* 2020;578(7793):112-121. doi:10.1038/s41586-019-1913-9
20. Iafrate AJ, Feuk L, Rivera MN, et al. Detection of large-scale variation in the human genome. *Nat Genet.* 2004;36(9):949-951. doi:10.1038/ng1416
21. Sebat J, Lakshmi B, Troge J, et al. Large-Scale Copy Number Polymorphism in the Human Genome. *Science.* 2004;305(5683):525-528. doi:10.1126/science.1098918
22. Mitelman F, Johansson B, Mertens F. The impact of translocations and gene fusions on cancer causation. *Nat Rev Cancer.* 2007;7(4):233-245. doi:10.1038/nrc2091
23. Levy-Sakin M, Pastor S, Mostovoy Y, et al. Genome maps across 26 human populations reveal population-specific patterns of structural variation. *Nat Commun.* 2019;10(1):1025. doi:10.1038/s41467-019-08992-7
24. Stransky N, Cerami E, Schalm S, Kim JL, Lengauer C. The landscape of kinase fusions in cancer. *Nat Commun.* 2014;5(1):4846. doi:10.1038/ncomms5846
25. Yi K, Ju YS. Patterns and mechanisms of structural variations in human cancer. *Exp Mol Med.* 2018;50(8):1-11. doi:10.1038/s12276-018-0112-3
26. SEER Cancer Stat Facts: Brain and Other Nervous System Cancer U. S. National Institutes of Health, National Cancer Institute. 08.08.2024, <https://seer.cancer.gov/statfacts/html/brain.html>.
27. WHO Editorial Board, *Central Nervous System Tumours: WHO Classification of Tumours, Volume 6, 5th Ed. (Geneva: World Health Organization, 2021). ISBN: 978-92-832-4508-7.* 5th ed. International agency for research on cancer; 2021.
28. Louis DN, Perry A, Wesseling P, et al. The 2021 WHO Classification of Tumors of the Central Nervous System: a summary. *Neuro-Oncol.* 2021;23(8):1231-1251. doi:10.1093/neuonc/noab106
29. Capper D, Jones DTW, Sill M, et al. DNA methylation-based classification of central nervous system tumours. *Nature.* 2018;555(7697):469-474. doi:10.1038/nature26000
30. Capper D, Reifenberger G, French PJ, et al. EANO guideline on rational molecular testing of gliomas, glioneuronal, and neuronal tumors in adults for targeted therapy selection. *Neuro-Oncol.* 2023;25(5):813-826. doi:10.1093/neuonc/noad008
31. Sahm F, Bertero L, Brandner S, et al. European Association of Neuro-Oncology guideline on molecular testing of meningiomas for targeted therapy selection. *Neuro-Oncol.* 2025;27(4):869-883. doi:10.1093/neuonc/noae253

32. Association of Population-based Cancer Registries in Germany (GEKID) and the German Centre for Cancer Registry Data (ZfKD) at the Robert Koch Institute. Cancer in Germany 2019/2020 - Central nervous system.
33. Association of Population-based Cancer Registries in Germany (GEKID) and the German Centre for Cancer Registry Data (ZfKD) at the Robert Koch Institute. Cancer in Germany 2019/2020 - Cancer in Children.
34. Northcott PA, Korshunov A, Witt H, et al. Medulloblastoma Comprises Four Distinct Molecular Variants. *J Clin Oncol*. 2011;29(11):1408-1414. doi:10.1200/JCO.2009.27.4324
35. Northcott PA, Robinson GW, Kratz CP, et al. Medulloblastoma. *Nat Rev Dis Primer*. 2019;5(1):11. doi:10.1038/s41572-019-0063-6
36. Gilbertson RJ, Ellison DW. The Origins of Medulloblastoma Subtypes. *Annu Rev Pathol Mech Dis*. 2008;3(1):341-365. doi:10.1146/annurev.pathmechdis.3.121806.151518
37. Wang J, Wechsler-Reya RJ. The role of stem cells and progenitors in the genesis of medulloblastoma. *Exp Neurol*. 2014;260:69-73. doi:10.1016/j.expneurol.2012.11.014
38. AbdelBaki MS, Boué DR, Finlay JL, Kieran MW. Desmoplastic nodular medulloblastoma in young children: a management dilemma. *Neuro-Oncol*. 2018;20(8):1026-1033. doi:10.1093/neuonc/nox222
39. Das A, Zameer L, Vinarkar S, et al. TP53 Mutation, MYCN Amplification, and Large Cell/Anaplastic Histology in Medulloblastoma. *Indian J Pediatr*. 2018;85(8):684-685. doi:10.1007/s12098-017-2527-6
40. Taylor MD, Northcott PA, Korshunov A, et al. Molecular subgroups of medulloblastoma: the current consensus. *Acta Neuropathol (Berl)*. 2012;123(4):465-472. doi:10.1007/s00401-011-0922-z
41. Cavalli FMG, Remke M, Rampasek L, et al. Intertumoral Heterogeneity within Medulloblastoma Subgroups. *Cancer Cell*. 2017;31(6):737-754.e6. doi:10.1016/j.ccell.2017.05.005
42. Northcott PA, Buchhalter I, Morrissy AS, et al. The whole-genome landscape of medulloblastoma subtypes. *Nature*. 2017;547(7663):311-317. doi:10.1038/nature22973
43. Sharma T, Schwalbe EC, Williamson D, et al. Second-generation molecular subgrouping of medulloblastoma: an international meta-analysis of Group 3 and Group 4 subtypes. *Acta Neuropathol (Berl)*. 2019;138(2):309-326. doi:10.1007/s00401-019-02020-0
44. Schwalbe EC, Lindsey JC, Nakjang S, et al. Novel molecular subgroups for clinical classification and outcome prediction in childhood medulloblastoma: a cohort study. *Lancet Oncol*. 2017;18(7):958-971. doi:10.1016/S1470-2045(17)30243-7
45. Hovestadt V, Ayrault O, Swartling FJ, Robinson GW, Pfister SM, Northcott PA. Medulloblastomics revisited: biological and clinical insights from thousands of patients. *Nat Rev Cancer*. 2020;20(1):42-56. doi:10.1038/s41568-019-0223-8
46. SIOP Europe / ERN PaedCan. Medulloblastoma: Standard Clinical Practice Recommendations. Published online December 15, 2022. <https://siope.eu/media/documents/escp-medulloblastoma.pdf>

47. Chang CH, Housepian EM, Herbert C. An Operative Staging System and a Megavoltage Radiotherapeutic Technic for Cerebellar Medulloblastomas. *Radiology*. 1969;(VOL. 93, NO. 6). doi:<https://doi.org/10.1148/93.6.1351>
48. Ramaswamy V, Remke M, Bouffet E, et al. Risk stratification of childhood medulloblastoma in the molecular era: the current consensus. *Acta Neuropathol (Berl)*. 2016;131(6):821-831. doi:10.1007/s00401-016-1569-6
49. Cooney T, Lindsay H, Leary S, Wechsler-Reya R. Current studies and future directions for medulloblastoma: A review from the pacific pediatric neuro-oncology consortium (PNO) disease working group. *Neoplasia*. 2023;35:100861. doi:10.1016/j.neo.2022.100861
50. Ellison DW, Dalton J, Kocak M, et al. Medulloblastoma: clinicopathological correlates of SHH, WNT, and non-SHH/WNT molecular subgroups. *Acta Neuropathol (Berl)*. 2011;121(3):381-396. doi:10.1007/s00401-011-0800-8
51. Jones DTW, Jäger N, Kool M, et al. Dissecting the genomic complexity underlying medulloblastoma. *Nature*. 2012;488(7409):100-105. doi:10.1038/nature11284
52. Kool M, Jones DTW, Jäger N, et al. Genome Sequencing of SHH Medulloblastoma Predicts Genotype-Related Response to Smoothed Inhibition. *Cancer Cell*. 2014;25(3):393-405. doi:10.1016/j.ccr.2014.02.004
53. Northcott PA, Shih DJH, Peacock J, et al. Subgroup-specific structural variation across 1,000 medulloblastoma genomes. *Nature*. 2012;488(7409):49-56. doi:10.1038/nature11327
54. Robinson GW, Rudneva VA, Buchhalter I, et al. Risk-adapted therapy for young children with medulloblastoma (SJYC07): therapeutic and molecular outcomes from a multicentre, phase 2 trial. *Lancet Oncol*. 2018;19(6):768-784. doi:10.1016/s1470-2045(18)30204-3
55. Korshunov A, Sahm F, Stichel D, et al. Molecular characterization of medulloblastomas with extensive nodularity (MBEN). *Acta Neuropathol (Berl)*. 2018;136(2):303-313. doi:10.1007/s00401-018-1840-0
56. Zhukova N, Ramaswamy V, Remke M, et al. Subgroup-Specific Prognostic Implications of TP53 Mutation in Medulloblastoma. *J Clin Oncol*. 2013;31(23):2927-2935. doi:10.1200/jco.2012.48.5052
57. Rausch T, Jones DTW, Zapatka M, et al. Genome Sequencing of Pediatric Medulloblastoma Links Catastrophic DNA Rearrangements with TP53 Mutations. *Cell*. 2012;148(1-2):59-71. doi:10.1016/j.cell.2011.12.013
58. Reardon DA, Jenkins JJ, Sublett JE, Burger PC, Kun LE. Multiple Genomic Alterations Including N-myc Amplification in a Primary Large Cell Medulloblastoma. *Pediatr Neurosurg*. 2000;32(4):187-191. doi:10.1159/000028932
59. Bunt J, Hasselt NE, Zwijnenburg DA, et al. OTX2 directly activates cell cycle genes and inhibits differentiation in medulloblastoma cells. *Int J Cancer*. 2012;131(2). doi:10.1002/ijc.26474
60. Northcott PA, Lee C, Zichner T, et al. Enhancer hijacking activates GFI1 family oncogenes in medulloblastoma. *Nature*. 2014;511(7510):428-434. doi:10.1038/nature13379

61. Hilden JM, Meerbaum S, Burger P, et al. Central Nervous System Atypical Teratoid/Rhabdoid Tumor: Results of Therapy in Children Enrolled in a Registry. *J Clin Oncol.* 2004;22(14):2877-2884. doi:10.1200/jco.2004.07.073
62. Underiner RM, Eltobgy M, Stanek JR, Finlay JL, AbdelBaki MS. Meta-Analysis of Treatment Modalities in Metastatic Atypical Teratoid/Rhabdoid Tumors in Children. *Pediatr Neurol.* 2020;108:106-112. doi:10.1016/j.pediatrneurol.2020.03.003
63. Biegel JA, Rorke LB, Packer RJ, Emanuel BS. Monosomy 22 in rhabdoid or atypical tumors of the brain. *J Neurosurg.* 1990;73(5):710-714. doi:10.3171/jns.1990.73.5.0710
64. Biegel JA, Zhou JY, Rorke LB, Stenstrom C, Wainwright LM, Fogelgren B. Germ-line and acquired mutations of INI1 in atypical teratoid and rhabdoid tumors. *Cancer Res* 1999 Jan 15;59:174-9. Published online January 1, 1999. doi:PMID:%209892189
65. Versteeg I, Sévenet N, Lange J, et al. Truncating mutations of hSNF5/INI1 in aggressive paediatric cancer. *Nature.* 1998;394(6689):203-206. doi:10.1038/28212
66. Seeringer A, Reinhard H, Hasselblatt M, et al. Synchronous congenital malignant rhabdoid tumor of the orbit and atypical teratoid/rhabdoid tumor—feasibility and efficacy of multimodal therapy in a long-term survivor. *Cancer Genet.* 2014;207(9):429-433. doi:10.1016/j.cancergen.2014.06.028
67. Sredni ST, Tomita T. Rhabdoid Tumor Predisposition Syndrome. *Pediatr Dev Pathol.* 2015;18(1):49-58. doi:10.2350/14-07-1531-MISC.1
68. Foulkes WD, Kamihara J, Evans DGR, et al. Cancer Surveillance in Gorlin Syndrome and Rhabdoid Tumor Predisposition Syndrome. *Clin Cancer Res.* 2017;23(12):e62-e67. doi:10.1158/1078-0432.CCR-17-0595
69. Holdhof D, Johann PD, Spohn M, et al. Atypical teratoid/rhabdoid tumors (ATRTs) with SMARCA4 mutation are molecularly distinct from SMARCB1-deficient cases. *Acta Neuropathol (Berl).* 2021;141(2):291-301. doi:10.1007/s00401-020-02250-7
70. Wu JI, Lessard J, Crabtree GR. Understanding the Words of Chromatin Regulation. *Cell.* 2009;136(2):200-206. doi:10.1016/j.cell.2009.01.009
71. Euskirchen G, Auerbach RK, Snyder M. SWI/SNF Chromatin-remodeling Factors: Multiscale Analyses and Diverse Functions. *J Biol Chem.* 2012;287(37):30897-30905. doi:10.1074/jbc.R111.309302
72. Kadoch C, Hargreaves DC, Hodges C, et al. Proteomic and bioinformatic analysis of mammalian SWI/SNF complexes identifies extensive roles in human malignancy. *Nat Genet.* 2013;45(6):592-601. doi:10.1038/ng.2628
73. Torchia J, Picard D, Lafay-Cousin L, et al. Molecular subgroups of atypical teratoid rhabdoid tumours in children: an integrated genomic and clinicopathological analysis. *Lancet Oncol.* 2015;16(5):569-582. doi:10.1016/S1470-2045(15)70114-2
74. Frühwald MC, Biegel JA, Bourdeaut F, Roberts CWM, Chi SN. Atypical teratoid/rhabdoid tumors—current concepts, advances in biology, and potential future therapies. *Neuro-Oncol.* 2016;18(6):764-778. doi:10.1093/neuonc/nov264
75. Johann PD, Erkek S, Zpatka M, et al. Atypical Teratoid/Rhabdoid Tumors Are Comprised of Three Epigenetic Subgroups with Distinct Enhancer Landscapes. *Cancer Cell.* 2016;29(3):379-393. doi:10.1016/j.ccell.2016.02.001

76. Ho B, Johann PD, Grabovska Y, et al. Molecular subgrouping of atypical teratoid/rhabdoid tumors—a reinvestigation and current consensus. *Neuro-Oncol.* 2020;22(5):613-624. doi:10.1093/neuonc/noz235
77. Ho DMT, Hsu CY, Wong TT, Ting LT, Chiang H. Atypical teratoid/rhabdoid tumor of the central nervous system: a comparative study with primitive neuroectodermal tumor/medulloblastoma. *Acta Neuropathol (Berl).* 2000;99(5):482-488. doi:10.1007/s004010051149
78. Geyer JR, Sposto R, Jennings M, et al. Multiagent Chemotherapy and Deferred Radiotherapy in Infants With Malignant Brain Tumors: A Report From the Children's Cancer Group. *J Clin Oncol.* 2005;23(30):7621-7631. doi:10.1200/jco.2005.09.095
79. Chi SN, Zimmerman MA, Yao X, et al. Intensive Multimodality Treatment for Children With Newly Diagnosed CNS Atypical Teratoid Rhabdoid Tumor. *J Clin Oncol.* 2009;27(3):385-389. doi:10.1200/JCO.2008.18.7724
80. Finkelstein-Shechter T, Gassas A, Mabbott D, et al. Atypical Teratoid or Rhabdoid Tumors: Improved Outcome With High-dose Chemotherapy. *J Pediatr Hematol Oncol.* 2010;32(5):e182-e186. doi:10.1097/MPH.0b013e3181dce1a2
81. Frühwald MC, Hasselblatt M, Nemes K, et al. Age and DNA methylation subgroup as potential independent risk factors for treatment stratification in children with atypical teratoid/rhabdoid tumors. *Neuro-Oncol.* 2020;22(7):1006-1017. doi:10.1093/neuonc/noz244
82. Japp AS, Klein-Hitpass L, Denkhaus D, Pietsch T. OTX2 Defines a Subgroup of Atypical Teratoid Rhabdoid Tumors With Close Relationship to Choroid Plexus Tumors. *J Neuropathol Exp Neurol.* Published online December 26, 2016:nlw101. doi:10.1093/jnen/nlw101
83. Federico A, Thomas C, Miskiewicz K, et al. ATRT–SHH comprises three molecular subgroups with characteristic clinical and histopathological features and prognostic significance. *Acta Neuropathol (Berl).* 2022;143(6):697-711. doi:10.1007/s00401-022-02424-5
84. Rheinbay E, Nielsen MM, Abascal F, et al. Analyses of non-coding somatic drivers in 2,658 cancer whole genomes. *Nature.* 2020;578(7793):102-111. doi:10.1038/s41586-020-1965-x
85. The Wellcome Trust Case Control Consortium, Conrad DF, Pinto D, et al. Origins and functional impact of copy number variation in the human genome. *Nature.* 2010;464(7289):704-712. doi:10.1038/nature08516
86. Pang AW, MacDonald JR, Pinto D, et al. Towarchards a comprehensive structural variation map of an individual human genome. Published online 2010.
87. Audano PA, Sulovari A, Graves-Lindsay TA, et al. Characterizing the Major Structural Variant Alleles of the Human Genome. *Cell.* 2019;176(3):663-675.e19. doi:10.1016/j.cell.2018.12.019
88. Lupski JR. Genomic disorders: structural features of the genome can lead to DNA rearrangements and human disease traits. *Trends Genet.* 1998;14(10):417-422. doi:10.1016/S0168-9525(98)01555-8

89. Lupski JR. Genomic rearrangements and sporadic disease. *Nat Genet.* 2007;39(S7):S43-S47. doi:10.1038/ng2084
90. Stankiewicz P, Lupski JR. Structural Variation in the Human Genome and its Role in Disease. *Annu Rev Med.* 2010;61(1):437-455. doi:10.1146/annurev-med-100708-204735
91. Hollox EJ, Huffmeier U, Zeeuwen PLJM, et al. Psoriasis is associated with increased β -defensin genomic copy number. *Nat Genet.* 2008;40(1):23-25. doi:10.1038/ng.2007.48
92. Fanciulli M, Norsworthy PJ, Petretto E, et al. FCGR3B copy number variation is associated with susceptibility to systemic, but not organ-specific, autoimmunity. *Nat Genet.* 2007;39(6):721-723. doi:10.1038/ng2046
93. Girirajan S, Brkanac Z, Coe BP, et al. Relative Burden of Large CNVs on a Range of Neurodevelopmental Phenotypes. Orr HT, ed. *PLoS Genet.* 2011;7(11):e1002334. doi:10.1371/journal.pgen.1002334
94. Pinto D, Pagnamenta AT, Klei L, et al. Functional impact of global rare copy number variation in autism spectrum disorders. *Nature.* 2010;466(7304):368-372. doi:10.1038/nature09146
95. Lee C, Scherer SW. The clinical context of copy number variation in the human genome. *Expert Rev Mol Med.* 2010;12:e8. doi:10.1017/S1462399410001390
96. Weischenfeldt J, Symmons O, Spitz F, Korbel JO. Phenotypic impact of genomic structural variation: insights from and for human disease. *Nat Rev Genet.* 2013;14(2):125-138. doi:10.1038/nrg3373
97. Dubois F, Sidiropoulos N, Weischenfeldt J, Beroukhi R. Structural variations in cancer and the 3D genome. *Nat Rev Cancer.* 2022;22(9):533-546. doi:10.1038/s41568-022-00488-9
98. Carvalho CMB, Lupski JR. Copy number variation at the breakpoint region of isochromosome 17q. *Genome Res.* 2008;18(11):1724-1732. doi:10.1101/gr.080697.108
99. Kloosterman WP, Hoogstraal M, Paling O, et al. Chromothripsis is a common mechanism driving genomic rearrangements in primary and metastatic colorectal cancer. *Genome Biol.* 2011;12(10):R103. doi:10.1186/gb-2011-12-10-r103
100. Stankiewicz P, Lupski JR. Genome architecture, rearrangements and genomic disorders. *Trends Genet.* 2002;18(2):74-82. doi:10.1016/S0168-9525(02)02592-1
101. Carvalho CMB, Lupski JR. Mechanisms underlying structural variant formation in genomic disorders. *Nat Rev Genet.* 2016;17(4):224-238. doi:10.1038/nrg.2015.25
102. Hastings PJ, Lupski JR, Rosenberg SM, Ira G. Mechanisms of change in gene copy number. *Nat Rev Genet.* 2009;10(8):551-564. doi:10.1038/nrg2593
103. Gu W, Zhang F, Lupski JR. Mechanisms for human genomic rearrangements. *PathoGenetics.* 2008;1(1):4. doi:10.1186/1755-8417-1-4
104. Bailey JA, Yavor AM, Massa HF, Trask BJ, Eichler EE. Segmental Duplications: Organization and Impact Within the Current Human Genome Project Assembly. *Genome Res.* 2001;11(6):1005-1017. doi:10.1101/gr.187101

105. Bailey JA, Eichler EE. Primate segmental duplications: crucibles of evolution, diversity and disease. *Nat Rev Genet.* 2006;7(7):552-564. doi:10.1038/nrg1895
106. Eichler EE, Archidiacono N, Rocchi M. CAGGG Repeats and the Pericentromeric Duplication of the Hominoid Genome. *Genome Res.* 1999;9(11):1048-1058. doi:10.1101/gr.9.11.1048
107. Barbouti A, Stankiewicz P, Nusbaum C, et al. The Breakpoint Region of the Most Common Isochromosome, i(17q), in Human Neoplasia Is Characterized by a Complex Genomic Architecture with Large, Palindromic, Low-Copy Repeats. *Am J Hum Genet.* 2004;74(1):1-10. doi:10.1086/380648
108. Mendrzyk F, Korshunov A, Toedt G, et al. Isochromosome breakpoints on 17p in medulloblastoma are flanked by different classes of DNA sequence repeats. *Genes Chromosomes Cancer.* 2006;45(4):401-410. doi:10.1002/gcc.20304
109. Weterings E, Van Gent DC. The mechanism of non-homologous end-joining: a synopsis of synapsis. *DNA Repair.* 2004;3(11):1425-1435. doi:10.1016/j.dnarep.2004.06.003
110. Lee JA, Carvalho CMB, Lupski JR. A DNA Replication Mechanism for Generating Nonrecurrent Rearrangements Associated with Genomic Disorders. *Cell.* 2007;131(7):1235-1247. doi:10.1016/j.cell.2007.11.037
111. Lieber MR. The Mechanism of Human Nonhomologous DNA End Joining. *J Biol Chem.* 2008;283(1):1-5. doi:10.1074/jbc.R700039200
112. Rausch T, Snajder R, Leger A, et al. Long-read sequencing of diagnosis and post-therapy medulloblastoma reveals complex rearrangement patterns and epigenetic signatures. *Cell Genomics.* 2023;3(4):100281. doi:10.1016/j.xgen.2023.100281
113. Magrangeas F, Avet-Loiseau H, Munshi NC, Minvielle S. Chromothripsis identifies a rare and aggressive entity among newly diagnosed multiple myeloma patients. *Blood.* 2011;118(3):675-678. doi:10.1182/blood-2011-03-344069
114. Molenaar JJ, Koster J, Zwijnenburg DA, et al. Sequencing of neuroblastoma identifies chromothripsis and defects in neuritogenesis genes. *Nature.* 2012;483(7391):589-593. doi:10.1038/nature10910
115. Bianchi JJ, Murigneux V, Bedora-Faure M, Lescale C, Deriano L. Breakage-Fusion-Bridge Events Trigger Complex Genome Rearrangements and Amplifications in Developmentally Arrested T Cell Lymphomas. *Cell Rep.* 2019;27(10):2847-2858.e4. doi:10.1016/j.celrep.2019.05.014
116. Stephens PJ, Greenman CD, Fu B, et al. Massive Genomic Rearrangement Acquired in a Single Catastrophic Event during Cancer Development. *Cell.* 2011;144(1):27-40. doi:10.1016/j.cell.2010.11.055
117. Shoshani O, Brunner SF, Yaeger R, et al. Chromothripsis drives the evolution of gene amplification in cancer. *Nature.* 2021;591(7848):137-141. doi:10.1038/s41586-020-03064-z
118. Baca SC, Prandi D, Lawrence MS, et al. Punctuated Evolution of Prostate Cancer Genomes. *Cell.* 2013;153(3):666-677. doi:10.1016/j.cell.2013.03.021
119. Berger MF, Lawrence MS, Demichelis F, et al. The genomic complexity of primary human prostate cancer. *Nature.* 2011;470(7333):214-220. doi:10.1038/nature09744

120. Shen MM. Chromoplexy: A New Category of Complex Rearrangements in the Cancer Genome. *Cancer Cell*. 2013;23(5):567-569. doi:10.1016/j.ccr.2013.04.025
121. Mahmoud M, Gobet N, Cruz-Dávalos DI, Mounier N, Dessimoz C, Sedlazeck FJ. Structural variant calling: the long and the short of it. *Genome Biol*. 2019;20(1):246. doi:10.1186/s13059-019-1828-7
122. Mertens F, Johansson B, Fioretos T, Mitelman F. The emerging complexity of gene fusions in cancer. *Nat Rev Cancer*. 2015;15(6):371-381. doi:10.1038/nrc3947
123. Heisterkamp N, Stam K, Groffen J, De Klein A, Grosveld G. Structural organization of the bcr gene and its role in the Ph^t translocation. *Nature*. 1985;315(6022):758-761. doi:10.1038/315758a0
124. Gröschel S, Sanders MA, Hoogenboezem R, et al. A Single Oncogenic Enhancer Rearrangement Causes Concomitant EVI1 and GATA2 Deregulation in Leukemia. *Cell*. 2014;157(2):369-381. doi:10.1016/j.cell.2014.02.019
125. Valentijn LJ, Koster J, Zwijnenburg DA, et al. TERT rearrangements are frequent in neuroblastoma and identify aggressive tumors. *Nat Genet*. 2015;47(12):1411-1414. doi:10.1038/ng.3438
126. Cooper GM. *The Cell: A Molecular Approach*. 2nd edition. Sunderland (MA): Sinauer Associates; 2000. Tumor Suppressor Genes. Available from: <https://www.ncbi.nlm.nih.gov/books/NBK9894/>.
127. Chen WY, Baylin SB. Inactivation of Tumor Suppressor Genes: Choice Between Genetic and Epigenetic Routes. *Cell Cycle*. 2005;4(1):10-12. doi:10.4161/cc.4.1.1361
128. Delves PJ, Roitt IM, eds. *Encyclopedia of Immunology*. 2nd ed. Academic Press; 1998.
129. Lupski JR, Wise CA, Kuwano A, et al. Gene dosage is a mechanism for Charcot-Marie-Tooth disease type 1A. *Nat Genet*. 1992;1(1):29-33. doi:10.1038/ng0492-29
130. Rice AM, McLysaght A. Dosage-sensitive genes in evolution and disease. *BMC Biol*. 2017;15(1):78. doi:10.1186/s12915-017-0418-y
131. The Wellcome Trust Case Control Consortium, Conrad DF, Pinto D, et al. Origins and functional impact of copy number variation in the human genome. *Nature*. 2010;464(7289):704-712. doi:10.1038/nature08516
132. Beroukhi R, Mermel CH, Porter D, et al. The landscape of somatic copy-number alteration across human cancers. *Nature*. 2010;463(7283):899-905. doi:10.1038/nature08822
133. Zhang X, Choi PS, Francis JM, et al. Identification of focally amplified lineage-specific super-enhancers in human epithelial cancers. *Nat Genet*. 2016;48(2):176-182. doi:10.1038/ng.3470
134. Takeda DY, Spisák S, Seo JH, et al. A Somatic Acquired Enhancer of the Androgen Receptor Is a Noncoding Driver in Advanced Prostate Cancer. *Cell*. 2018;174(2):422-432.e13. doi:10.1016/j.cell.2018.05.037
135. Espejo Valle-Inclán J, Besselink NJM, De Bruijn E, et al. A multi-platform reference for somatic structural variation detection. *Cell Genomics*. 2022;2(6):100139. doi:10.1016/j.xgen.2022.100139

136. Bates SE. Classical Cytogenetics: Karyotyping Techniques. In: Schwartz PH, Wesselschmidt RL, eds. *Human Pluripotent Stem Cells*. Vol 767. Methods in Molecular Biology. Humana Press; 2011:177-190. doi:10.1007/978-1-61779-201-4_13
137. Wan TSK. Cancer Cytogenetics: Methodology Revisited. *Ann Lab Med*. 2014;34(6):413-425. doi:10.3343/alm.2014.34.6.413
138. Speicher MR, Carter NP. The new cytogenetics: blurring the boundaries with molecular biology. *Nat Rev Genet*. 2005;6(10):782-792. doi:10.1038/nrg1692
139. Schröck E, Du Manoir S, Veldman T, et al. Multicolor Spectral Karyotyping of Human Chromosomes. *Science*. 1996;273(5274):494-497. doi:10.1126/science.273.5274.494
140. Snijders AM, Nowak N, Segreaves R, et al. Assembly of microarrays for genome-wide measurement of DNA copy number. *Nat Genet*. 2001;29(3):263-264. doi:10.1038/ng754
141. Campbell PJ, Stephens PJ, Pleasance ED, et al. Identification of somatically acquired rearrangements in cancer using genome-wide massively parallel paired-end sequencing. *Nat Genet*. 2008;40(6):722-729. doi:10.1038/ng.128
142. Li H, Durbin R. Fast and accurate short read alignment with Burrows–Wheeler transform. *Bioinformatics*. 2009;25(14):1754-1760. doi:10.1093/bioinformatics/btp324
143. Shanker A, ed. *Bioinformatics: Sequences, Structures, Phylogeny*. Springer Singapore; 2018. doi:10.1007/978-981-13-1562-6
144. Sedlazeck FJ, Rescheneder P, Smolka M, et al. Accurate detection of complex structural variations using single-molecule sequencing. *Nat Methods*. 2018;15(6):461-468. doi:10.1038/s41592-018-0001-7
145. Nagarajan N, Pop M. Sequence assembly demystified. *Nat Rev Genet*. 2013;14(3):157-167. doi:10.1038/nrg3367
146. Hakeem KR, Tombuloğlu H, Tombuloğlu G, eds. *Plant Omics: Trends and Applications*. Springer International Publishing; 2016. doi:10.1007/978-3-319-31703-8
147. Sanchis-Juan A, Stephens J, French CE, et al. Complex structural variants in Mendelian disorders: identification and breakpoint resolution using short- and long-read genome sequencing. *Genome Med*. 2018;10(1):95. doi:10.1186/s13073-018-0606-6
148. Bocklandt S, Hastie A, Cao H. Bionano Genome Mapping: High-Throughput, Ultra-Long Molecule Genome Analysis System for Precision Genome Assembly and Haploid-Resolved Structural Variation Discovery. In: Suzuki Y, ed. *Advances in Experimental Medicine and Biology*. Springer Singapore; 2019. doi:10.1007/978-981-13-6037-4_7
149. Barseghyan H, Tang W, Wang RT, et al. Next-generation mapping: a novel approach for detection of pathogenic structural variants with a potential utility in clinical diagnosis. *Genome Med*. 2017;9(1):90. doi:10.1186/s13073-017-0479-0
150. D'cunja J, Shalaby T, Rivera P, et al. Antisense treatment of IGF-1R induces apoptosis and enhances chemosensitivity in central nervous system atypical teratoid/rhabdoid tumours cells. *Eur J Cancer*. 2007;43(10):1581-1589. doi:10.1016/j.ejca.2007.03.003

151. Xu J, Margol A, Asgharzadeh S, Erdreich-Epstein A. Pediatric Brain Tumor Cell Lines: PEDIATRIC BRAIN TUMOR CELL LINES. *J Cell Biochem.* 2015;116(2):218-224. doi:10.1002/jcb.24976
152. Erdreich-Epstein A, Robison N, Ren X, et al. *PID1 (NYGGF4)*, a New Growth-Inhibitory Gene in Embryonal Brain Tumors and Gliomas. *Clin Cancer Res.* 2014;20(4):827-836. doi:10.1158/1078-0432.CCR-13-2053
153. Xu J, Erdreich-Epstein A, Gonzalez-Gomez I, et al. Novel cell lines established from pediatric brain tumors. *J Neurooncol.* 2012;107(2):269-280. doi:10.1007/s11060-011-0756-5
154. Friedman HS, Burger PC, Bigner SH, et al. Establishment and characterization of the human medulloblastoma cell line and transplantable xenograft D283 Med. *J Neuropathol Exp Neurol.* 1985;44(6):592-605. doi:10.1097/00005072-198511000-00005
155. Jacobsen PF, Jenkyn DJ, Papadimitriou JM. Establishment of a Human Medulloblastoma Cell Line and Its Heterotransplantation into Nude Mice: *J Neuropathol Exp Neurol.* 1985;44(5):472-485. doi:10.1097/00005072-198509000-00003
156. Milde T, Lodrini M, Savelyeva L, et al. HD-MB03 is a novel Group 3 medulloblastoma model demonstrating sensitivity to histone deacetylase inhibitor treatment. *J Neurooncol.* 2012;110(3):335-348. doi:10.1007/s11060-012-0978-1
157. Dietl S, Schwinn S, Dietl S, et al. MB3W1 is an orthotopic xenograft model for anaplastic medulloblastoma displaying cancer stem cell- and Group 3-properties. *BMC Cancer.* 2016;16(1):115. doi:10.1186/s12885-016-2170-z
158. Yamada M, Shimizu K, Tamura K, et al. [Establishment and biological characterization of human medulloblastoma cell lines]. *No To Shinkei.* 1989;41(7):695-702.
159. Keles GE, Berger MS, Srinivasan J, Kolstoe DD, Bobola MS, Silber JR. Establishment and characterization of four human medulloblastoma-derived cell lines. *Oncol Res.* 1995;7(10-11):493-503.
160. Capper D, Stichel D, Sahm F, et al. Practical implementation of DNA methylation and copy-number-based CNS tumor diagnostics: the Heidelberg experience. *Acta Neuropathol (Berl).* 2018;136(2):181-210. doi:10.1007/s00401-018-1879-y
161. Hovestadt V, Zapatka M. conumee: Enhanced Copy-Number Variation Analysis Using Illumina DNA Methylation Arrays. R Package Version 1.9.0. 2015. <http://bioconductor.org/packages/conumee/>
162. Aryee MJ, Jaffe AE, Corrada-Bravo H, et al. Minfi: a flexible and comprehensive Bioconductor package for the analysis of Infinium DNA methylation microarrays. *Bioinformatics.* 2014;30(10):1363-1369. doi:10.1093/bioinformatics/btu049
163. Seshan V, Olshen A. DNACopy: DNA Copy Number Data Analysis. R package version 1.80.0. <https://bioconductor.org/packages/release/bioc/html/DNACopy.html>
164. Bionano Genomics. Bionano Solve Theory of Operation: Structural Variant Calling - CG-30110, Rev G. Published online 2020.
165. R Core Team. R: A Language and Environment for Statistical Computing. R Foundation for Statistical Computing, Vienna. Published online 2021. <https://www.R-project.org/>

166. Wickham H. *Ggplot2: Elegant Graphics for Data Analysis*. Springer New York; 2009. doi:10.1007/978-0-387-98141-3
167. Wickham H, Averick M, Bryan J, et al. Welcome to the Tidyverse. *J Open Source Softw*. 2019;4(43):1686. doi:10.21105/joss.01686
168. Pauck D, Picard D, Maue M, et al. An in vitro pharmacogenomic approach reveals subtype-specific therapeutic vulnerabilities in atypical teratoid/rhabdoid tumors (AT/RT). *Pharmacol Res*. 2025;213:107660. doi:10.1016/j.phrs.2025.107660
169. Ewels P, Peltzer A, Fillinger S, et al. The nf-core framework for community-curated bioinformatics pipelines. *Nat Biotechnol*. 2020;38(3):276-278. doi:10.1038/s41587-020-0439-x.
170. Krueger F. Trim Galore. Published online November 19, 2019. https://www.bioinformatics.babraham.ac.uk/projects/trim_galore/
171. Dobin A, Davis CA, Schlesinger F, et al. STAR: ultrafast universal RNA-seq aligner. *Bioinformatics*. 2013;29(1):15-21. doi:10.1093/bioinformatics/bts635
172. Patro R, Duggal G, Love MI, Irizarry RA, Kingsford C. Salmon provides fast and bias-aware quantification of transcript expression. *Nat Methods*. 2017;14(4):417-419. doi:10.1038/nmeth.4197
173. Love MI, Huber W, Anders S. Moderated estimation of fold change and dispersion for RNA-seq data with DESeq2. *Genome Biol*. 2014;15(12):550. doi:10.1186/s13059-014-0550-8
174. Uhrig S, Ellermann J, Walther T, et al. Accurate and efficient detection of gene fusions from RNA sequencing data. *Genome Res*. 2021;31(3):448-460. doi:10.1101/gr.257246.119
175. Nicorici D, Şatalan M, Edgren H, et al. **FusionCatcher** – a tool for finding somatic fusion genes in paired-end RNA-sequencing data. Preprint posted online November 19, 2014. doi:10.1101/011650
176. Azatyan A, Zaphiropoulos PG. Circular and Fusion RNAs in Medulloblastoma Development. *Cancers*. 2022;14(13):3134. doi:10.3390/cancers14133134
177. Forget A, Martignetti L, Puget S, et al. Aberrant ERBB4-SRC Signaling as a Hallmark of Group 4 Medulloblastoma Revealed by Integrative Phosphoproteomic Profiling. *Cancer Cell*. 2018;34(3):379-395.e7. doi:10.1016/j.ccell.2018.08.002
178. Russo J, Sheriff F, de Cicco RL, Pogash TJ, Nguyen T, Russo IH. Methodology for Studying the Compartments of the Human Breast. In: Russo J, Russo IH, eds. *Techniques and Methodological Approaches in Breast Cancer Research*. Springer New York; 2014:75-102. doi:10.1007/978-1-4939-0718-2_3
179. Ben-David U, Amon A. Context is everything: aneuploidy in cancer. *Nat Rev Genet*. 2020;21(1):44-62. doi:10.1038/s41576-019-0171-x
180. Bierkens M, Krijgsman O, Wilting SM, et al. Focal aberrations indicate *EYA2* and *hsa-miR-375* as oncogene and tumor suppressor in cervical carcinogenesis. *Genes Chromosomes Cancer*. 2013;52(1):56-68. doi:10.1002/gcc.22006

181. Belli C, Trapani D, Viale G, et al. Targeting the microenvironment in solid tumors. *Cancer Treat Rev*. 2018;65:22-32. doi:10.1016/j.ctrv.2018.02.004
182. Bain BJ. *Blood Cells: A Practical Guide*. 1st ed. Wiley; 2022. doi:10.1002/9781119820307
183. Kahlke T. Metrics: N50. 2019. https://github.com/timkahlke/LongRead_tutorials/blob/master/docs/APP_MET.md
184. Lobón-Iglesias MJ, Andrianteranagna M, Han ZY, et al. Imaging and multi-omics datasets converge to define different neural progenitor origins for ATRT-SHH subgroups. *Nat Commun*. 2023;14(1):6669. doi:10.1038/s41467-023-42371-7
185. Sun CX, Daniel P, Bradshaw G, et al. Generation and multi-dimensional profiling of a childhood cancer cell line atlas defines new therapeutic opportunities. *Cancer Cell*. 2023;41(4):660-677.e7. doi:10.1016/j.ccell.2023.03.007
186. Johann PD, Altendorf L, Efremova EM, et al. Recurrent atypical teratoid/rhabdoid tumors (AT/RT) reveal discrete features of progression on histology, epigenetics, copy number profiling, and transcriptomics. *Acta Neuropathol (Berl)*. 2023;146(3):527-541. doi:10.1007/s00401-023-02608-7
187. Guo G, Zhuang J, Zhang K, Zhou Z, Wang Y, Zhang Z. Atypical Teratoid/Rhabdoid Tumor of the Central Nervous System in Children: Case Reports and Literature Review. *Front Surg*. 2022;9:864518. doi:10.3389/fsurg.2022.864518
188. Skowron P, Farooq H, Cavalli FMG, et al. The transcriptional landscape of Shh medulloblastoma. *Nat Commun*. 2021;12(1):1749. doi:10.1038/s41467-021-21883-0
189. Northcott PA, Nakahara Y, Wu X, et al. Multiple recurrent genetic events converge on control of histone lysine methylation in medulloblastoma. *Nat Genet*. 2009;41(4):465-472. doi:10.1038/ng.336
190. Okonechnikov K, Joshi P, Körber V, et al. Oncogene aberrations drive medulloblastoma progression, not initiation. *Nature*. 2025;642(8069):1062-1072. doi:10.1038/s41586-025-08973-5
191. Daenekas B, Pérez E, Boniolo F, et al. Conumee 2.0: enhanced copy-number variation analysis from DNA methylation arrays for humans and mice. Kelso J, ed. *Bioinformatics*. 2024;40(2):btac029. doi:10.1093/bioinformatics/btac029
192. Domcke S, Sinha R, Levine DA, Sander C, Schultz N. Evaluating cell lines as tumour models by comparison of genomic profiles. *Nat Commun*. 2013;4(1):2126. doi:10.1038/ncomms3126
193. Ivanov DP, Coyle B, Walker DA, Grabowska AM. In vitro models of medulloblastoma: Choosing the right tool for the job. *J Biotechnol*. 2016;236:10-25. doi:10.1016/j.jbiotec.2016.07.028
194. Ben-David U, Siranosian B, Ha G, et al. Genetic and transcriptional evolution alters cancer cell line drug response. *Nature*. 2018;560(7718):325-330. doi:10.1038/s41586-018-0409-3
195. Quinlan AR, Hall IM. Characterizing complex structural variation in germline and somatic genomes. *Trends Genet*. 2012;28(1):43-53. doi:10.1016/j.tig.2011.10.002

196. Malhotra A, Lindberg M, Faust GG, et al. Breakpoint profiling of 64 cancer genomes reveals numerous complex rearrangements spawned by homology-independent mechanisms. *Genome Res.* 2013;23(5):762-776. doi:10.1101/gr.143677.112
197. Uhlén M, Fagerberg L, Hallström BM. Tissue-based map of the human proteome. *Science.* 2015;347(1260419). doi:DOI:%2010.1126/science.126041
198. Torchia J, Golbourn B, Feng S, et al. Integrated (epi)-Genomic Analyses Identify Subgroup-Specific Therapeutic Targets in CNS Rhabdoid Tumors. *Cancer Cell.* 2016;30(6):891-908. doi:10.1016/j.ccell.2016.11.003
199. Chun HJE, Lim EL, Heravi-Moussavi A, et al. Genome-Wide Profiles of Extra-cranial Malignant Rhabdoid Tumors Reveal Heterogeneity and Dysregulated Developmental Pathways. *Cancer Cell.* 2016;29(3):394-406. doi:10.1016/j.ccell.2016.02.009
200. Hasselblatt M, Nagel I, Oyen F, et al. SMARCA4-mutated atypical teratoid/rhabdoid tumors are associated with inherited germline alterations and poor prognosis. *Acta Neuropathol (Berl).* 2014;128(3):453-456. doi:10.1007/s00401-014-1323-x
201. Kumar R, Liu APY, Northcott PA. Medulloblastoma genomics in the modern molecular era. *Brain Pathol.* 2020;30(3):679-690. doi:10.1111/bpa.12804
202. Negrini S, Gorgoulis VG, Halazonetis TD. Genomic instability — an evolving hallmark of cancer. *Nat Rev Mol Cell Biol.* 2010;11(3):220-228. doi:10.1038/nrm2858
203. Yi E, Chamorro González R, Henssen AG, Verhaak RGW. Extrachromosomal DNA amplifications in cancer. *Nat Rev Genet.* 2022;23(12):760-771. doi:10.1038/s41576-022-00521-5
204. Lange JT, Rose JC, Chen CY, et al. The evolutionary dynamics of extrachromosomal DNA in human cancers. *Nat Genet.* 2022;54(10):1527-1533. doi:10.1038/s41588-022-01177-x
205. Wu S, Turner KM, Nguyen N, et al. Circular ecDNA promotes accessible chromatin and high oncogene expression. *Nature.* 2019;575(7784):699-703. doi:10.1038/s41586-019-1763-5
206. Purshouse K, Friman ET, Boyle S, et al. Oncogene expression from extrachromosomal DNA is driven by copy number amplification and does not require spatial clustering in glioblastoma stem cells. *eLife.* 2022;11:e80207. doi:10.7554/eLife.80207
207. Kim H, Nguyen NP, Turner K, et al. Extrachromosomal DNA is associated with oncogene amplification and poor outcome across multiple cancers. *Nat Genet.* 2020;52(9):891-897. doi:10.1038/s41588-020-0678-2
208. Yang L, Jia R, Ge T, et al. Extrachromosomal circular DNA: biogenesis, structure, functions and diseases. *Signal Transduct Target Ther.* 2022;7(1):342. doi:10.1038/s41392-022-01176-8
209. Häcker U, Nybakken K, Perrimon N. Heparan sulphate proteoglycans: the sweet side of development. *Nat Rev Mol Cell Biol.* 2005;6(7):530-541. doi:10.1038/nrm1681
210. Sarrazin S, Lamanna WC, Esko JD. Heparan Sulfate Proteoglycans. *Cold Spring Harb Perspect Biol.* 2011;3(7):a004952-a004952. doi:10.1101/cshperspect.a004952

211. Ortiz MV, Roberts SS, Glade Bender J, Shukla N, Wexler LH. Immunotherapeutic Targeting of GPC3 in Pediatric Solid Embryonal Tumors. *Front Oncol.* 2019;9:108. doi:10.3389/fonc.2019.00108
212. Williamson D, Selfe J, Gordon T, et al. Role for Amplification and Expression of *Glypican-5* in Rhabdomyosarcoma. *Cancer Res.* 2007;67(1):57-65. doi:10.1158/0008-5472.CAN-06-1650
213. Li Y, Yang P. GPC5 Gene and Its Related Pathways in Lung Cancer. *J Thorac Oncol.* 2011;6(1):2-5. doi:10.1097/JTO.0b013e3181fd6b04
214. Chui MH, Have C, Hoang LN, Shaw P, Lee C, Clarke BA. Genomic profiling identifies *GPC5* amplification in association with sarcomatous transformation in a subset of uterine carcinosarcomas. *J Pathol Clin Res.* 2018;4(1):69-78. doi:10.1002/cjp.2.89
215. Zhang Y, Wang J, Dong F, Li H, Hou Y. The role of GPC5 in lung metastasis of salivary adenoid cystic carcinoma. *Arch Oral Biol.* 2014;59(11):1172-1182. doi:10.1016/j.archoralbio.2014.07.009
216. Guo L, Wang J, Zhang T, Yang Y. Glypican-5 is a tumor suppressor in non-small cell lung cancer cells. *Biochem Biophys Rep.* 2016;6:108-112. doi:10.1016/j.bbrep.2016.03.010
217. Chen Y, Banda M, Speyer CL, Smith JS, Rabson AB, Gorski DH. Regulation of the Expression and Activity of the Antiangiogenic Homeobox Gene *GAX / MEOX2* by ZEB2 and MicroRNA-221. *Mol Cell Biol.* 2010;30(15):3902-3913. doi:10.1128/MCB.01237-09
218. Epifanova E, Babaev A, Newman AG, Tarabykin V. Role of Zeb2/Sip1 in neuronal development. *Brain Res.* 2019;1705:24-31. doi:10.1016/j.brainres.2018.09.034
219. Hill L, Browne G, Tulchinsky E. ZEB/miR-200 feedback loop: At the crossroads of signal transduction in cancer. *Int J Cancer.* 2013;132(4):745-754. doi:10.1002/ijc.27708
220. Potts PR, Yu H. Human MMS21/NSE2 Is a SUMO Ligase Required for DNA Repair. *Mol Cell Biol.* 2005;25(16):7021-7032. doi:10.1128/MCB.25.16.7021-7032.2005
221. Potts PR, Porteus MH, Yu H. Human SMC5/6 complex promotes sister chromatid homologous recombination by recruiting the SMC1/3 cohesin complex to double-strand breaks. *EMBO J.* 2006;25(14):3377-3388. doi:10.1038/sj.emboj.7601218
222. Potts PR, Yu H. The SMC5/6 complex maintains telomere length in ALT cancer cells through SUMOylation of telomere-binding proteins. *Nat Struct Mol Biol.* 2007;14(7):581-590. doi:10.1038/nsmb1259
223. Behlke-Steinert S, Touat-Todeschini L, Skoufias DA, Margolis RL. SMC5 and MMS21 are required for chromosome cohesion and mitotic progression. *Cell Cycle.* 2009;8(14):2211-2218. doi:10.4161/cc.8.14.8979
224. Faber ZJ, Chen X, Gedman AL, et al. The genomic landscape of core-binding factor acute myeloid leukemias. *Nat Genet.* 2016;48(12):1551-1556. doi:10.1038/ng.3709
225. Zou L, Li H, Han X, Qin J, Song G. Runx1t1 promotes the neuronal differentiation in rat hippocampus. *Stem Cell Res Ther.* 2020;11(1):160. doi:10.1186/s13287-020-01667-x

226. Kumar P, Verma V, Mohania D, et al. Leukemia associated RUNX1T1 gene reduced proliferation and invasiveness of glioblastoma cells. *J Cell Biochem.* 2021;122(11):1737-1748. doi:10.1002/jcb.30126
227. Kopp F, Mendell JT. Functional Classification and Experimental Dissection of Long Noncoding RNAs. *Cell.* 2018;172(3):393-407. doi:10.1016/j.cell.2018.01.011
228. Zhao S, Zhang X, Chen S, Zhang S. Long noncoding RNAs: fine-tuners hidden in the cancer signaling network. *Cell Death Discov.* 2021;7(1):283. doi:10.1038/s41420-021-00678-8
229. Xu S, Liu D, Chang T, et al. Cuproptosis-Associated lncRNA Establishes New Prognostic Profile and Predicts Immunotherapy Response in Clear Cell Renal Cell Carcinoma. *Front Genet.* 2022;13:938259. doi:10.3389/fgene.2022.938259
230. Feng Y, Yang Z, Wang J, Zhao H. Cuproptosis: unveiling a new frontier in cancer biology and therapeutics. *Cell Commun Signal.* 2024;22(1):249. doi:10.1186/s12964-024-01625-7
231. Lv C, Sun J, Ye Y, et al. Long noncoding RNA *EIF1AX-AS1* promotes endometrial cancer cell apoptosis by affecting *EIF1AX* mRNA stabilization. *Cancer Sci.* 2022;113(4):1277-1291. doi:10.1111/cas.15275
232. Desgrosellier JS, Cheresch DA. Integrins in cancer: biological implications and therapeutic opportunities. *Nat Rev Cancer.* 2010;10(1):9-22. doi:10.1038/nrc2748
233. Wenfei Liu, Surong Fang, Zhenhua Yang, et al. ITGA9-AS1 up-regulates ITGA9 by targeting miR-4765 and recruiting HNRNPU to affect the proliferation and apoptosis of non-small cell lung cancer cells. *Cell Mol Biol.* 2023;69(14):22-28. doi:10.14715/cmb/2023.69.14.4
234. Wiśniowiecka-Kowalnik B, Nesteruk M, Peters SU, et al. Intragenic rearrangements in *NRXN1* in three families with autism spectrum disorder, developmental delay, and speech delay. *Am J Med Genet B Neuropsychiatr Genet.* 2010;153B(5):983-993. doi:10.1002/ajmg.b.31064
235. Viñas-Jornet M, Esteba-Castillo S, Gabau E, et al. A common cognitive, psychiatric, and dysmorphic phenotype in carriers of *NRXN1* deletion. *Mol Genet Genomic Med.* 2014;2(6):512-521. doi:10.1002/mgg3.105
236. Südhof TC. Neuroligins and neuroligins link synaptic function to cognitive disease. *Nature.* 2008;455(7215):903-911. doi:10.1038/nature07456
237. Südhof TC. Synaptic Neurexin Complexes: A Molecular Code for the Logic of Neural Circuits. *Cell.* 2017;171(4):745-769. doi:10.1016/j.cell.2017.10.024
238. Bang HJ, Shim HJ, Park MR, et al. NRXN1 as a Prognostic Biomarker: Linking Copy Number Variation to EMT and Survival in Colon Cancer. *Int J Mol Sci.* 2024;25(21):11423. doi:10.3390/ijms252111423
239. Haarhuis JHI, Elbatsh AMO, Rowland BD. Cohesin and Its Regulation: On the Logic of X-Shaped Chromosomes. *Dev Cell.* 2014;31(1):7-18. doi:10.1016/j.devcel.2014.09.010
240. Solomon DA, Kim T, Diaz-Martinez LA, et al. Mutational Inactivation of *STAG2* Causes Aneuploidy in Human Cancer. *Science.* 2011;333(6045):1039-1043. doi:10.1126/science.1203619

241. Lawrence MS, Stojanov P, Mermel CH, et al. Discovery and saturation analysis of cancer genes across 21 tumour types. *Nature*. 2014;505(7484):495-501. doi:10.1038/nature12912
242. Balbás-Martínez C, Sagrera A, Carrillo-de-Santa-Pau E, et al. Recurrent inactivation of STAG2 in bladder cancer is not associated with aneuploidy. *Nat Genet*. 2013;45(12):1464-1469. doi:10.1038/ng.2799
243. Kim JS, He X, Orr B, et al. Intact Cohesion, Anaphase, and Chromosome Segregation in Human Cells Harboring Tumor-Derived Mutations in STAG2. Sullivan BA, ed. *PLoS Genet*. 2016;12(2):e1005865. doi:10.1371/journal.pgen.1005865
244. Nam H, Jeon S, An H, et al. Critical roles of ARHGAP36 as a signal transduction mediator of Shh pathway in lateral motor columnar specification. *eLife*. 2019;8:e46683. doi:10.7554/eLife.46683
245. Zhang B, Zhuang T, Lin Q, et al. Patched1–ArhGAP36–PKA–Inversin axis determines the ciliary translocation of Smoothed for Sonic Hedgehog pathway activation. *Proc Natl Acad Sci*. 2019;116(3):874-879. doi:10.1073/pnas.1804042116
246. Rack PG, Ni J, Payumo AY, et al. Arhgap36-dependent activation of Gli transcription factors. *Proc Natl Acad Sci*. 2014;111(30):11061-11066. doi:10.1073/pnas.1322362111
247. Deckert M, Rottapel R. The Adapter 3BP2: How It Plugs into Leukocyte Signaling. In: Tsoukas C, ed. *Lymphocyte Signal Transduction*. Vol 584. Advances in Experimental Medicine and Biology. Springer US; 2006:107-114. doi:10.1007/0-387-34132-3_8
248. Reichenberger EJ, Levine MA, Olsen BR, Papadaki ME, Lietman SA. The role of SH3BP2 in the pathophysiology of cherubism. *Orphanet J Rare Dis*. 2012;7(Suppl 1):S5. doi:10.1186/1750-1172-7-S1-S5
249. Bell SM, Shaw M, Jou YS, Myers RM, Knowles MA. Identification and Characterization of the Human Homologue of SH3BP2, an SH3 Binding Domain Protein within a Common Region of Deletion at 4p16.3 Involved in Bladder Cancer. *Genomics*. 1997;44(2):163-170. doi:10.1006/geno.1997.4849
250. Serrano-Candelas E, Ainsua-Enrich E, Navinés-Ferrer A, et al. Silencing of adaptor protein SH 3 BP 2 reduces KIT / PDGFRA receptors expression and impairs gastrointestinal stromal tumors growth. *Mol Oncol*. 2018;12(8):1383-1397. doi:10.1002/1878-0261.12332
251. Janssens B, Goossens S, Staes K, et al. α T-Catenin: a novel tissue-specific β -catenin-binding protein mediating strong cell-cell adhesion. *J Cell Sci*. 2001;114(17):3177-3188. doi:10.1242/jcs.114.17.3177
252. Bacchelli E, Ceroni F, Pinto D, et al. A CTNNA3 compound heterozygous deletion implicates a role for α T-catenin in susceptibility to autism spectrum disorder. *J Neurodev Disord*. 2014;6(1):17. doi:10.1186/1866-1955-6-17
253. Kawauchi D, Robinson G, Uziel T, et al. A Mouse Model of the Most Aggressive Subgroup of Human Medulloblastoma. *Cancer Cell*. 2012;21(2):168-180. doi:10.1016/j.ccr.2011.12.023
254. Chapman OS, Luebeck J, Wani S, et al. *The Landscape of Extrachromosomal Circular DNA in Medulloblastoma*. *Cancer Biology*; 2021. doi:10.1101/2021.10.18.464907

255. Chapman OS, Luebeck J, Sridhar S, et al. Circular extrachromosomal DNA promotes tumor heterogeneity in high-risk medulloblastoma. *Nat Genet.* 2023;55(12):2189-2199. doi:10.1038/s41588-023-01551-3
256. Sasai N, Saitoh N, Saitoh H, Nakao M. The Transcriptional Cofactor MCAF1/ATF7IP Is Involved in Histone Gene Expression and Cellular Senescence. Viola JPB, ed. *PLoS ONE.* 2013;8(7):e68478. doi:10.1371/journal.pone.0068478
257. Tsusaka T, Shimura C, Shinkai Y. ATF7IP regulates SETDB1 nuclear localization and increases its ubiquitination. *EMBO Rep.* 2019;20(12):e48297. doi:10.15252/embr.201948297
258. Dong H, Ma L, Gan J, et al. PTPRO represses ERBB2-driven breast oncogenesis by dephosphorylation and endosomal internalization of ERBB2. *Oncogene.* 2017;36(3):410-422. doi:10.1038/onc.2016.213
259. Ming F, Sun Q. Epigenetically silenced PTPRO functions as a prognostic marker and tumor suppressor in human lung squamous cell carcinoma. *Mol Med Rep.* 2017;16(1):746-754. doi:10.3892/mmr.2017.6665
260. Dai W, Xiang W, Han L, et al. PTPRO represses colorectal cancer tumorigenesis and progression by reprogramming fatty acid metabolism. *Cancer Commun.* 2022;42(9):848-867. doi:10.1002/cac2.12341
261. Zhu Y, Sun D, Jakovcevski M, Jiang Y. Epigenetic mechanism of SETDB1 in brain: implications for neuropsychiatric disorders. *Transl Psychiatry.* 2020;10(1):115. doi:10.1038/s41398-020-0797-7
262. Mossink B, Negwer M, Schubert D, Nadif Kasri N. The emerging role of chromatin remodelers in neurodevelopmental disorders: a developmental perspective. *Cell Mol Life Sci.* 2021;78(6):2517-2563. doi:10.1007/s00018-020-03714-5
263. Jiang W, Wei M, Liu M, et al. Identification of Protein Tyrosine Phosphatase Receptor Type O (PTPRO) as a Synaptic Adhesion Molecule that Promotes Synapse Formation. *J Neurosci.* 2017;37(41):9828-9843. doi:10.1523/JNEUROSCI.0729-17.2017
264. Yao Z, Dong H, Zhu J, et al. Age-related decline in hippocampal tyrosine phosphatase PTPRO is a mechanistic factor in chemotherapy-related cognitive impairment. *JCI Insight.* 2023;8(14):e166306. doi:10.1172/jci.insight.166306
265. Bignell GR, Santarius T, Pole JCM, et al. Architectures of somatic genomic rearrangement in human cancer amplicons at sequence-level resolution. *Genome Res.* 2007;17(9):1296-1303. doi:10.1101/gr.6522707
266. Li C, Chen L, Pan G, Zhang W, Li SC. Deciphering complex breakage-fusion-bridge genome rearrangements with Ambigram. *Nat Commun.* 2023;14(1):5528. doi:10.1038/s41467-023-41259-w
267. Phan NN, Wang CY, Chen CF, Sun Z, Lai MD, Lin YC. Voltage-gated calcium channels: Novel targets for cancer therapy. *Oncol Lett.* 2017;14(2):2059-2074. doi:10.3892/ol.2017.6457
268. Ghasemi DR, Okonechnikov K, Rademacher A, et al. Compartments in medulloblastoma with extensive nodularity are connected through differentiation along the granular precursor lineage. *Nat Commun.* 2024;15(1):269. doi:10.1038/s41467-023-44117-x

269. Maklad A, Sedeeq M, Milevskiy MJG, Azimi I. Calcium Signalling in Medulloblastoma: An In Silico Analysis of the Expression of Calcium Regulating Genes in Patient Samples. *Genes*. 2021;12(9):1329. doi:10.3390/genes12091329
270. Sedeeq M, Maklad A, Dutta T, et al. T-Type Calcium Channel Inhibitors Induce Apoptosis in Medulloblastoma Cells Associated with Altered Metabolic Activity. *Mol Neurobiol*. 2022;59(5):2932-2945. doi:10.1007/s12035-022-02771-0
271. Cook A, Bono F, Jinek M, Conti E. Structural Biology of Nucleocytoplasmic Transport. *Annu Rev Biochem*. 2007;76(1):647-671. doi:10.1146/annurev.biochem.76.052705.161529
272. David V, Hochstenbach F, Rajagopalan S, Brenner MB. Interaction with newly synthesized and retained proteins in the endoplasmic reticulum suggests a chaperone function for human integral membrane protein IP90 (calnexin). *J Biol Chem*. 1993;268(13):9585-9592. doi:10.1016/S0021-9258(18)98391-2
273. Ciechanover A, Kwon YT. Degradation of misfolded proteins in neurodegenerative diseases: therapeutic targets and strategies. *Exp Mol Med*. 2015;47(3):e147-e147. doi:10.1038/emm.2014.117
274. Moon HW, Han HG, Jeon YJ. Protein Quality Control in the Endoplasmic Reticulum and Cancer. *Int J Mol Sci*. 2018;19(10):3020. doi:10.3390/ijms19103020
275. Iglesia RP, Prado MB, Alves RN, et al. Unconventional Protein Secretion in Brain Tumors Biology: Enlightening the Mechanisms for Tumor Survival and Progression. *Front Cell Dev Biol*. 2022;10:907423. doi:10.3389/fcell.2022.907423
276. Mantere T, Neveling K, Pebrel-Richard C, et al. Optical genome mapping enables constitutional chromosomal aberration detection. *Am J Hum Genet*. 2021;108(8):1409-1422. doi:10.1016/j.ajhg.2021.05.012
277. Smith AC, Neveling K, Kanagal-Shamanna R. Optical genome mapping for structural variation analysis in hematologic malignancies. *Am J Hematol*. 2022;97(7):975-982. doi:10.1002/ajh.26587
278. Gerding WM, Tembrink M, Nilius-Eliiwi V, et al. Optical genome mapping reveals additional prognostic information compared to conventional cytogenetics in AML / MDS patients. *Int J Cancer*. 2022;150(12):1998-2011. doi:10.1002/ijc.33942
279. Yang H, Garcia-Manero G, Sasaki K, et al. High-resolution structural variant profiling of myelodysplastic syndromes by optical genome mapping uncovers cryptic aberrations of prognostic and therapeutic significance. *Leukemia*. 2022;36(9):2306-2316. doi:10.1038/s41375-022-01652-8
280. Balducci E, Kaltenbach S, Villarese P, et al. Optical genome mapping refines cytogenetic diagnostics, prognostic stratification and provides new molecular insights in adult MDS/AML patients. *Blood Cancer J*. 2022;12(9):126. doi:10.1038/s41408-022-00718-1
281. Brandes D, Yasin L, Nebral K, et al. Optical Genome Mapping Identifies Novel Recurrent Structural Alterations in Childhood ETV6::RUNX1+ and High Hyperdiploid Acute Lymphoblastic Leukemia. *HemaSphere*. 2023;7(8):e925. doi:10.1097/HS9.0000000000000925

282. Zou YS, Klausner M, Ghabrial J, et al. A comprehensive approach to evaluate genetic abnormalities in multiple myeloma using optical genome mapping. *Blood Cancer J.* 2024;14(1):78. doi:10.1038/s41408-024-01059-x
283. Shieh JT, Penon-Portmann M, Wong KHY, et al. Application of full-genome analysis to diagnose rare monogenic disorders. *Npj Genomic Med.* 2021;6(1):77. doi:10.1038/s41525-021-00241-5
284. Sahajpal NS. Clinical Validation and Diagnostic Utility of Optical Genome Mapping in Prenatal Diagnostic Testing.
285. Lühmann JL, Stelter M, Wolter M, et al. The Clinical Utility of Optical Genome Mapping for the Assessment of Genomic Aberrations in Acute Lymphoblastic Leukemia. *Cancers.* 2021;13(17):4388. doi:10.3390/cancers13174388
286. Levy B, Baughn LB, Akkari Y, et al. Optical genome mapping in acute myeloid leukemia: a multicenter evaluation. *Blood Adv.* 2023;7(7):1297-1307. doi:10.1182/bloodadvances.2022007583
287. Barford R, Whittle E, Weir L, et al. Use of Optical Genome Mapping to Detect Structural Variants in Neuroblastoma. *Cancers.* 2023;15(21):5233. doi:10.3390/cancers15215233
288. Baelen J, Dewaele B, Debiec-Rychter M, et al. Optical Genome Mapping for Comprehensive Cytogenetic Analysis of Soft-Tissue and Bone Tumors for Diagnostic Purposes. *J Mol Diagn.* 2024;26(5):374-386. doi:10.1016/j.jmoldx.2024.02.003
289. Ghabrial J, Stinnett V, Ribeiro E, et al. Diagnostic and Prognostic/Therapeutic Significance of Comprehensive Analysis of Bone and Soft Tissue Tumors Using Optical Genome Mapping and Next-Generation Sequencing. *Mod Pathol.* 2025;38(4):100684. doi:10.1016/j.modpat.2024.100684
290. Bornhorst M, Eze A, Bhattacharya S, et al. Optical genome mapping identifies a novel pediatric embryonal tumor with a *ZNF532::NUTM1* fusion. *J Pathol.* 2023;260(3):329-338. doi:10.1002/path.6085
291. Singh H, Sahajpal NS, Mondal AK, et al. Clinical Utility of Optical Genome Mapping for Improved Cytogenomic Analysis of Gliomas. *Biomedicines.* 2024;12(8):1659. doi:10.3390/biomedicines12081659
292. Sie D, Snijders PJF, Meijer GA, et al. Performance of amplicon-based next generation DNA sequencing for diagnostic gene mutation profiling in oncopathology. *Cell Oncol.* 2014;37(5):353-361. doi:10.1007/s13402-014-0196-2
293. Millán-Esteban D, Reyes-García D, García-Casado Z, et al. Suitability of melanoma FFPE samples for NGS libraries: time and quality thresholds for downstream molecular tests. *BioTechniques.* 2018;65(2):79-85. doi:10.2144/btn-2018-0016
294. Xiao B, Luo X, Liu Y, et al. Combining optical genome mapping and RNA-seq for structural variants detection and interpretation in unsolved neurodevelopmental disorders. *Genome Med.* 2024;16(1):113. doi:10.1186/s13073-024-01382-9
295. Jain M, Olsen HE, Paten B, Akeson M. The Oxford Nanopore MinION: delivery of nanopore sequencing to the genomics community. *Genome Biol.* 2016;17(1):239. doi:10.1186/s13059-016-1103-0

296. Eid J, Fehr A, Gray J, et al. Real-Time DNA Sequencing from Single Polymerase Molecules. 2009;323.
297. De Boer EN, Vroom V, Scheper AJ, et al. Cas9-directed long-read sequencing to resolve optical genome mapping findings in leukemia diagnostics. *Sci Rep.* 2024;14(1):8508. doi:10.1038/s41598-024-59092-6
298. Marwaha S, Knowles JW, Ashley EA. A guide for the diagnosis of rare and undiagnosed disease: beyond the exome. *Genome Med.* 2022;14(1):23. doi:10.1186/s13073-022-01026-w
299. Amarasinghe SL, Su S, Dong X, Zappia L, Ritchie ME, Gouil Q. Opportunities and challenges in long-read sequencing data analysis. *Genome Biol.* 2020;21(1):30. doi:10.1186/s13059-020-1935-5
300. Logsdon GA, Vollger MR, Eichler EE. Long-read human genome sequencing and its applications. *Nat Rev Genet.* 2020;21(10):597-614. doi:10.1038/s41576-020-0236-x
301. Optional fragmentation of gDNA. July 22, 2024. <https://nanoporetech.com/document/extraction-method-group/optional-fragmentation-of-gdna>
302. Bionano Genomics Data Collection Guidelines RevE. Published online February 13, 2021.
303. Infinium methylation microarrays: solutions for epigenetic researchers.
304. Sequencing 101: Comparing long-read sequencing technologies. July 18, 2024. <https://www.pacb.com/blog/sequencing-101-comparing-long-read-sequencing-technologies/>
305. Long-read sequencing myths: debunked. Part 1- HiFi sequencing. April 4, 2024. <https://www.pacb.com/blog/long-read-sequencing-myths-debunked-part-1-hifi-sequencing/>
306. Bionano Genomics Product Ordering Guide 2.0 RevF. Published online April 8, 2023.
307. Cores and Genomic Services - NUSEq Core Pricing. Published online July 22, 2025. <https://www.cgm.northwestern.edu/cores/nuseq/pricing.html>

8 Appendix

8.1 Abbreviations

3D	Three-dimensional
µg	Microgram
µL	Microliter
µm	Micrometer
ABL1	Abelson Murine Leukemia Proto-Oncogene 1, Non-Receptor Tyrosine Kinase
AFDN	Afadin, Adherens Junction Formation Factor
AHR	Allelic homologous recombination
AKT3	AKT Serine/Threonine Kinase 3
AML	Acute myeloid leukemia
ANOVA	Analysis of variance
APC	Adenomatous Polyposis Coli Regulator Of Wnt Signaling Pathway
ARHGAP36	Rho GTPase Activating Protein 36
AS1	Antisense RNA 1
ASCL1	Achaete-Scute Family BHLH Transcription Factor 1
ATF7IP	Activating Transcription Factor 7 Interacting Protein
ATP	Adenosine triphosphate
ATRT	Atypical teratoid/rhabdoid tumor
ATRX	Alpha Thalassemia/Mental Retardation Syndrome X-Linked Chromatin Remodeler
BCR	Breakpoint Cluster Region Activator Of RhoGEF And GTPase
BFB	Breakage–fusion–bridge
BMP	Bone Morphogenetic Protein
BOC	Brother Of CDO Cell Adhesion Associated, Oncogene Regulated
bp	Base pair
BSA	Bovine serum albumin
CACNA	Calcium Voltage-Gated Channel Subunit Alpha
CANX	Calnexin
CASC19	Cancer Susceptibility 19
CBFB	Core-Binding Factor Subunit Beta
CCND1	Cyclin D1
CCND2	Cyclin D2
CDK6	Cyclin Dependent Kinase 6

CDKN2A	Cyclin Dependent Kinase Inhibitor 2A
cDNA	Complementary DNA
CEBPB	CCAAT Enhancer Binding Protein Beta
CGC	Cancer Gene Census
CGH	Comparative genomic hybridization
CHD1	Chromodomain Helicase DNA Binding Protein 1
CI	Confidence interval
chr	Chromosome
CN	Copy number
CNA	Copy number alteration
CNS	Central nervous system
CNV	Copy number variation
COSMIC	Catalogue Of Somatic Mutations In Cancer
CRACR2A	Calcium Release Activated Channel Regulator 2A
CREBBP	CREB Binding Lysine Acetyltransferase
CSF	Cerebrospinal fluid
CSI	Craniospinal irradiation
CTCF	CCCTC-Binding Factor
CTNNA2	Catenin Alpha 2
CTNNA3	Catenin Alpha 3
CTNNB1	Catenin Beta 1
CV	Coefficient of variation
DCC	Deleted In Colorectal Carcinoma Netrin 1 Receptor
DCT	Dopachrome Tautomerase
DDX3X	DEAD-Box Helicase 3 X-Linked
DEL	Deletion
DLE-1	Direct Labelling Enzyme 1
DLS	Direct Label and Stain
D/N	Desmoplastic/nodular
DMEM	Dulbecco's Modified Eagle Medium
DMSO	Dimethyl sulfoxide
DNA	Deoxyribonucleic acid
DNP	<i>De novo</i> Assembly Pipeline
DSB	Double-strand break

DT	Diverse transcript?
DTX1	Deltex E3 Ubiquitin Ligase 1
DUP	Duplication
EB	Elution buffer
ecDNA	Extrachromosomal DNA
EGF	Epidermal Growth Factor
EIF1B	Eukaryotic Translation Initiation Factor 1B
EMT	Epithelial–mesenchymal transition
ER	Endoplasmic reticulum
ERG	ETS Transcription Factor ERG
EtOH	Ethanol
ETV6	ETS Variant Transcription Factor 6
FANCC	FA Complementation Group C
FAS	Fas Cell Surface Death Receptor
FBS	Fetal bovine serum
FFPE	Formalin-Fixed Paraffin-Embedded
FGF	Fibroblast Growth Factor
FGFR2	Fibroblast Growth Factor Receptor 2
FGFR1OP	FGFR1 Oncogene Partner 2
FH	Fumarate Hydratase
FHIT	Fragile Histidine Triad Diadenosine Triphosphatase
FISH	Fluorescence <i>in situ</i> hybridisation
FNBP1	Formin Binding Protein 1
FoSTeS	Fork Stalling and Template Switching
FOXK1	Forkhead Box K1
FOXP1	Forkhead Box P1
g	gravitational force
Gbp	Gigabase pair
gDNA	Genomic DNA
GFI1	Growth Factor Independent 1 Transcriptional Repressor
GFI1B	Growth Factor Independent 1B Transcriptional Repressor
GLI	Glioma-Associated Oncogene
GLI1	GLI Family Zinc Finger 1
GLI2	GLI Family Zinc Finger 2

GPC3	Glypican 3
GPC5	Glypican 5
GSTA1	Glutathione S-Transferase Alpha 1
GSTA6P	Glutathione S-Transferase Alpha 6, Pseudogene
GTR	Gross total resection
h	Hours
HES1	Hes Family BHLH Transcription Factor 1
HGF	Hepatocyte Growth Factor
HIF1 α	Hypoxia Inducible Factor 1 Subunit Alpha
HMW	High molecular weight
HSD	Honestly Significant Difference
HSPG	Heparan sulfate proteoglycans
HOXC	Homeobox C
HOXC9	HOXC Cluster
HPYR1	Helicobacter Pylori Responsive 1
IGL	Immunoglobulin Lambda Locus
IMDM	Iscove's Modified Dulbecco's Medium
indel	Insertion/deletion
INS	Insertion
INV	Inversion
isochr	Isochromosome
ITGA9	Integrin Alpha-9
JAK	Janus Kinase
KANSL1	KAT8 Regulatory NSL Complex Subunit 1
kbp	Kilobase pair
KDM6A	Lysine Demethylase 6A
KMT2C	Lysine Methyltransferase 2C
KMT2D	Lysine methyltransferase 2D
LBB	Lysis and binding buffer
LCA	Large-cell anaplastic
LCR	Low-copy repeat
lncRNA	Long non-coding RNA
LOF	Loss-of-function
LRP1BLDL	Receptor Related Protein 1B

MAP2K2	Mitogen-Activated Protein Kinase Kinase 2
MB	Medulloblastoma
MBEN	Medulloblastoma with extensive nodularity
Mbp	Megabase pair
MEM	Minimum Essential Medium
MF	Methylation family
min	Minute
MITF	Melanocyte Inducing Transcription Factor
mg	Milligram
mL	Milliliter
MLLT3	Myeloid/Lymphoid Or Mixed-Lineage Leukemia Translocated To Chromosome 3 Super Elongation Complex Subunit
mm	Millimeter
MMP11	Matrix Metalloproteinase 11
MN1	Meningioma Proto-Oncogene, Transcriptional Regulator
MRI	Magnetic resonance imaging
mRNA	Messenger ribonucleic acid
MSH2	MutS Homolog 2
MYC	MYC Proto-Oncogene, BHLH Transcription Factor
MYCN	MYCN Proto-Oncogene, BHLH Transcription Factor
MYRIP	Myosin VIIA And Rab Interacting Protein
NAHR	Non-allelic homologous recombination
NEAA	Non-essential amino acids
ng	Nanogram
NGS	Next-generation sequencing
NHEJ	Non-homologous endjoining
NOTCH2	Notch Receptor 2
NPIP2	Nuclear Pore Complex Interacting Protein Family Member B2
NRXN1	Neurexin-1
ns	Not significant
NCS	Neural stem cell
NSCLC	Non-small cell lung cancer
NSMCE2	Non-SMC Element 2 Homolog SUMO Ligase Component Of SMC5/6 Complex
NTR	Near-total resection

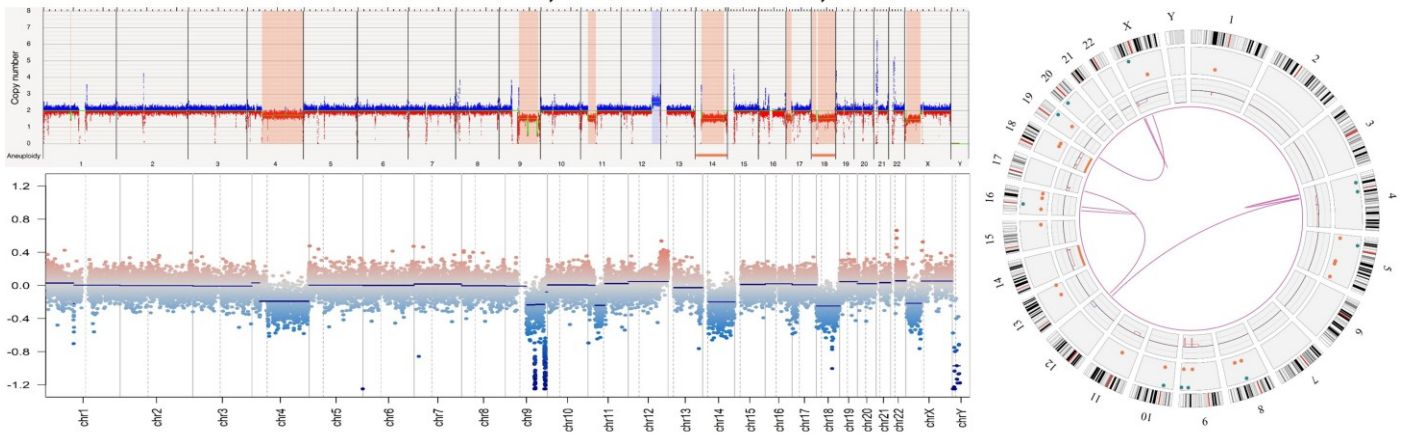
NUDCD1	NudC Domain Containing 1
NUTM1	NUT Midline Carcinoma Family Member 1
OGM	Optical genome mapping
ONT	Oxford Nanopore Technologies
OTX2	Orthodenticle Homeobox 2
OS	Overall survival
PBS	Phosphate buffered saline
PCAT1	Prostate Cancer Associated Transcript 1
pg	Picogram
PLAG1	Pleiomorphic Adenoma Gene 1 Zinc Finger
PMSF	Phenylmethanesulfonyl fluoride
PPIL2	Peptidylprolyl Isomerase Like 2
PRDM6	PR/SET Domain 6
PTCH1	Patched 1
PTCH2	Patched 2
PTEN	Phosphatase And Tensin Homolog
PTPRD	Protein Tyrosine Phosphatase Receptor Type D
PTPRK	Protein Tyrosine Phosphatase Receptor Type K
PTPRO	Protein Tyrosine Phosphatase Receptor Type O
QC	Quality control
RANBP17	RAN Binding Protein 17
RARG	Retinoic Acid Receptor Gamma
RGS7	Regulator Of G Protein Signaling 7
RNA	Ribonucleic acid
RNA-Seq	RNA sequencing
ROBO2	Roundabout Guidance Receptor 2
RPL5	Ribosomal Protein L5
rpm	revolutions per minute
RPMI	Roswell Park Memorial Institute
RRID	Research Resource Identifier
RT	Room temperature
RTPS1	Rhabdoid Tumor Predisposition Syndrome 1
RUNX1	RUNX Family Transcription Factor 1
RUNX1T1	RUNX1 Partner Transcriptional Co-Repressor 1

RVA	Rare Variant Analysis
SACC	Salivary adenoid cystic carcinoma
sd	Standard deviation
SD	Segmental duplication
SET	SET Nuclear Proto-Oncogene
SFMBT1	Scm Like With Four Mbt Domains 1
SH3BP2	SH3 Domain Binding Protein 2
SHH	Sonic Hedgehog
SLC14A2	Solute Carrier Family 14 Member 2
SMARCA4	SWI/SNF Related BAF Chromatin Remodeling Complex Subunit ATPase 4
SMARCB1	SWI/SNF Related BAF Chromatin Remodeling Complex Subunit B1
SMO	Smoothed, Frizzled Class Receptor
SNCAIP	Synuclein Alpha Interacting Protein
SNV	Single-nucleotide variant
SOX11	SRY-Box Transcription Factor 11
STAG2	Sister Chromatid Cohesion 3 Homolog Cohesin Complex Component
STAT	Signal Transducer And Activator Of Transcription
STR	Subtotal resection
SUFU	Suppressor Of Fused Homolog Negative Regulator Of Hedgehog Signaling
SV(s)	Structural variant(s)
TCF7L2	Transcription Factor 7 Like 2
TERT	Telomerase Reverse Transcriptase
TF	Transcription factor
TFBS	Transcription factor-binding site
TMPRSS2	Transmembrane Serine Protease 2
TP53	Tumor Protein P53
TSC1	Tuberous Sclerosis Complex Subunit 1
TYR	Tyrosinase
TYRP	Tyrosinase Related Protein 1
UHMW	Ultra-high molecular weight
UTR	Untranslated region
VAF	Variant allele fraction
VAP	Variant Annotation Pipeline
WGS	Whole genome sequencing

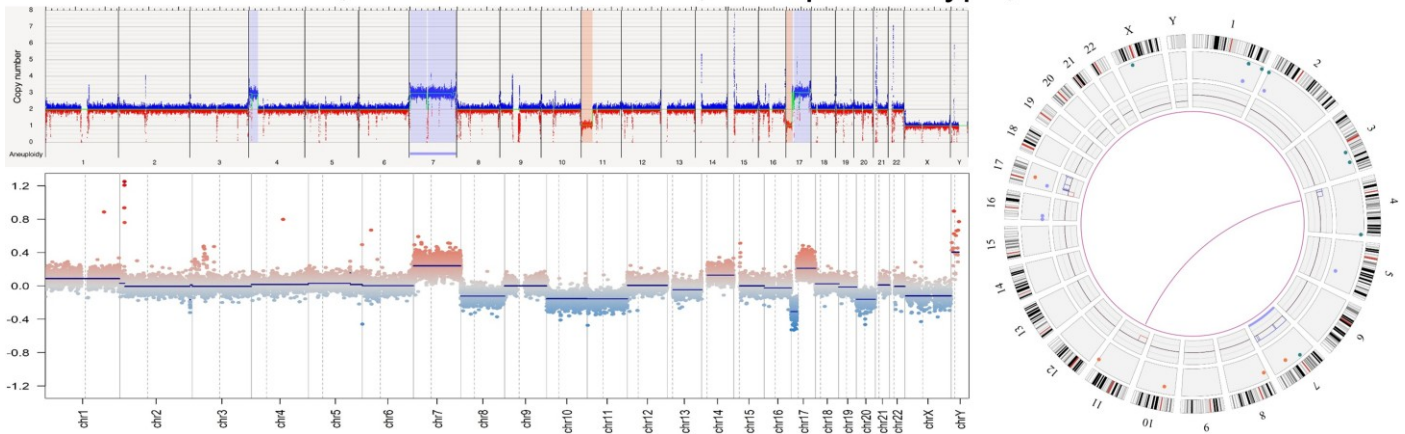
WHO	World Health Organization
WNT	Wingless
XPA	Xeroderma Pigmentosum Group A DNA Damage Recognition And Repair Factor
YAP1	Yes1 Associated Transcriptional Regulator
YWHAE	Tyrosine 3-Monooxygenase/Tryptophan 5-Monooxygenase Activation Protein Epsilon
ZEB2	Zinc Finger E-Box Binding Homeobox 2
ZMYM3	Zinc Finger MYM-Type Containing 3
ZNF532	Zinc Finger Protein 532

8.2 Supplementary Figures and Tables

MB1t: MB, SHH-activated, subclass 4



MB2t: MB, non-WNT/non-SHH, Group 4 subtype, subclass V



MB3t: MB, non-WNT/non-SHH, Group 4 subtype, subclass VIII

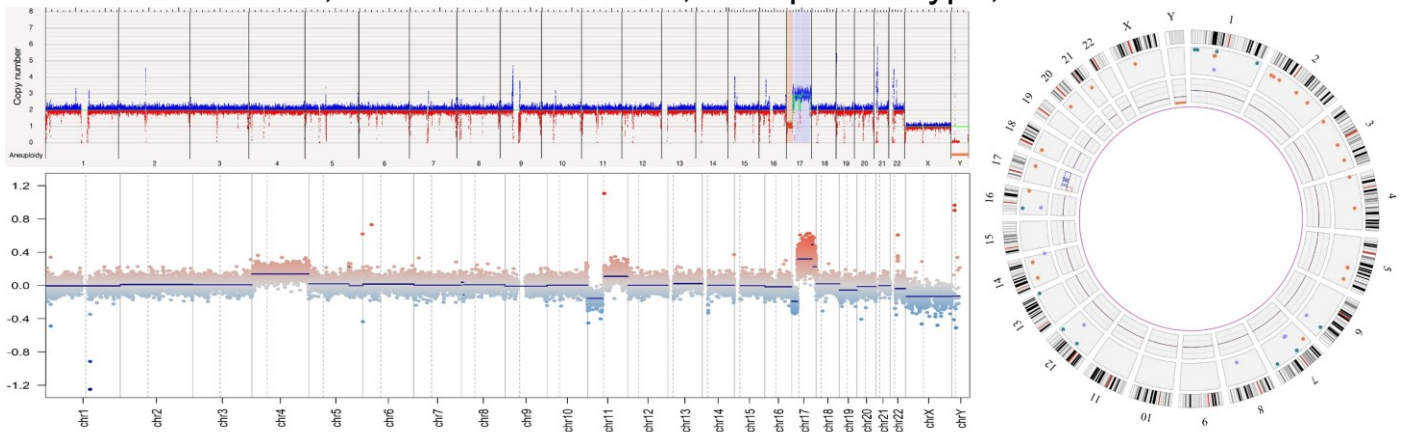
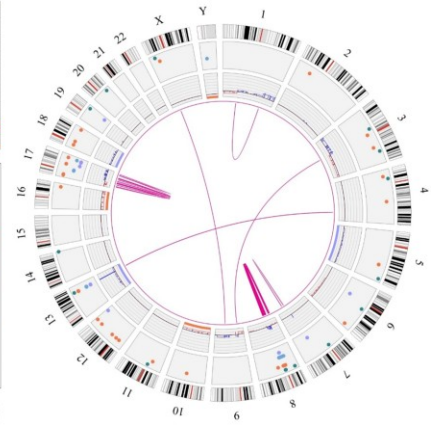
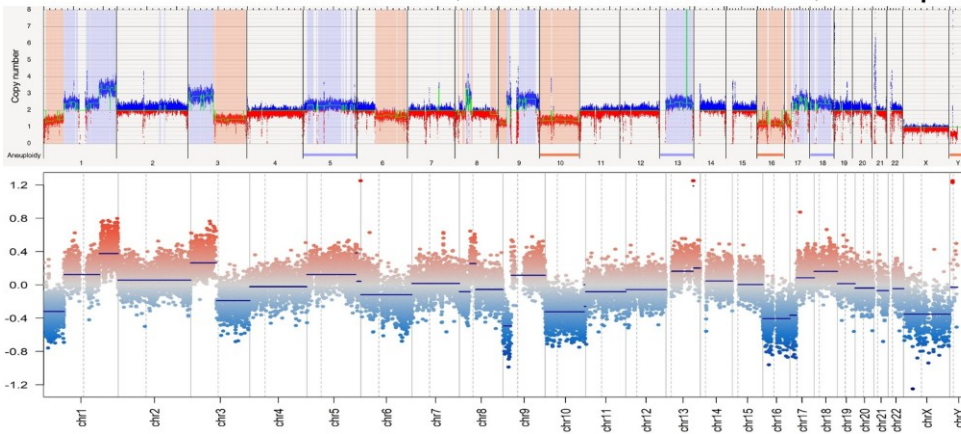
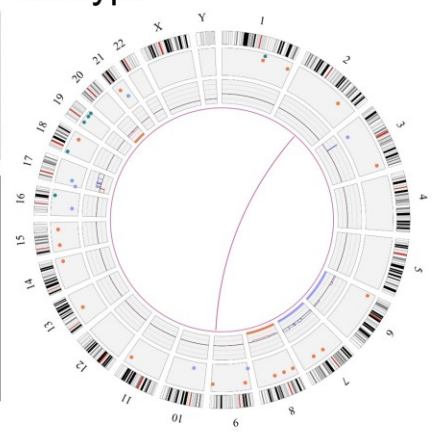
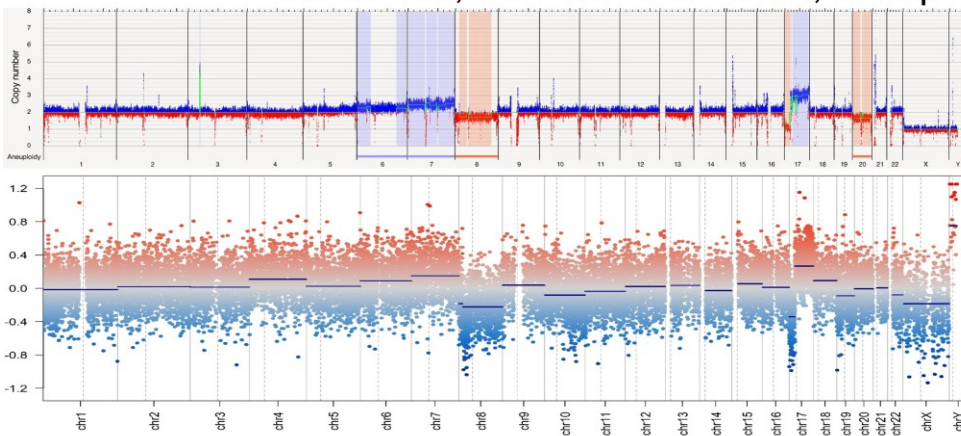


(Figure legend is on pages 174 and 175.)

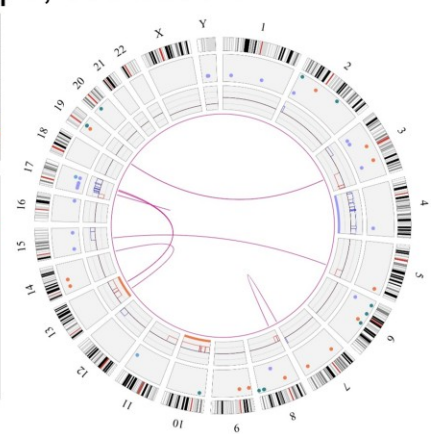
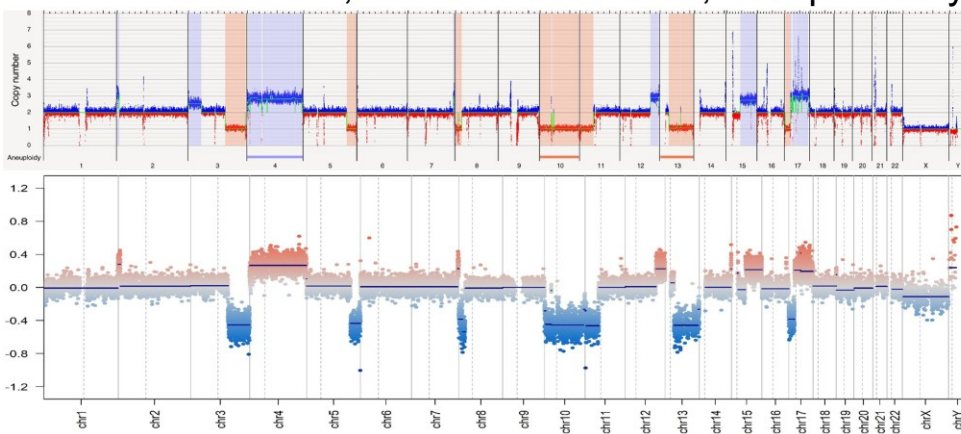
MB4t: MB, non-WNT/non-SHH, Group 3 subtype



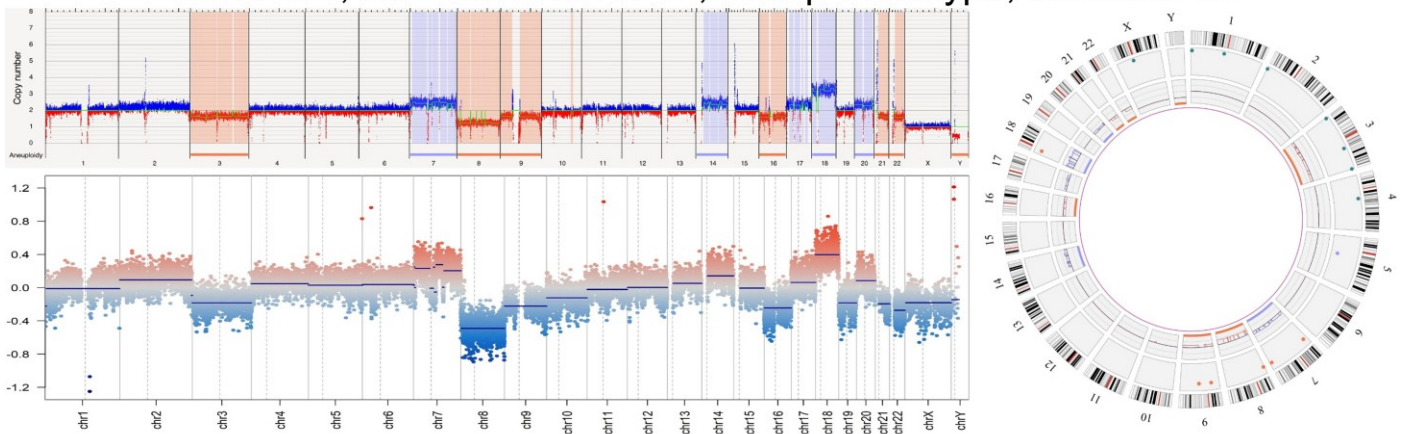
MB5t: MB, non-WNT/non-SHH, Group 4 subtype



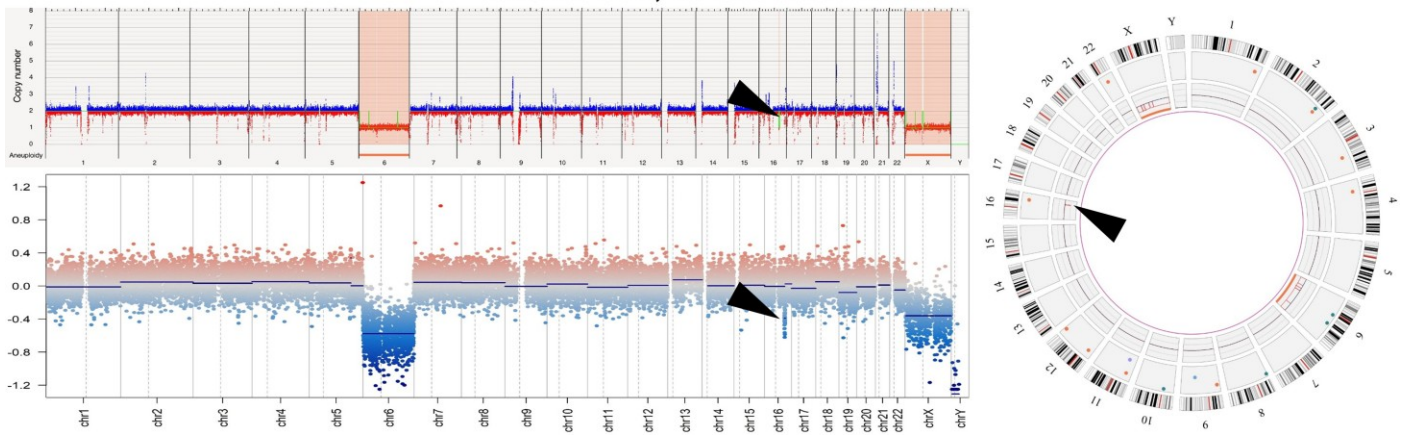
MB6t: MB, non-WNT/non-SHH, Group 4 subtype, subclass V



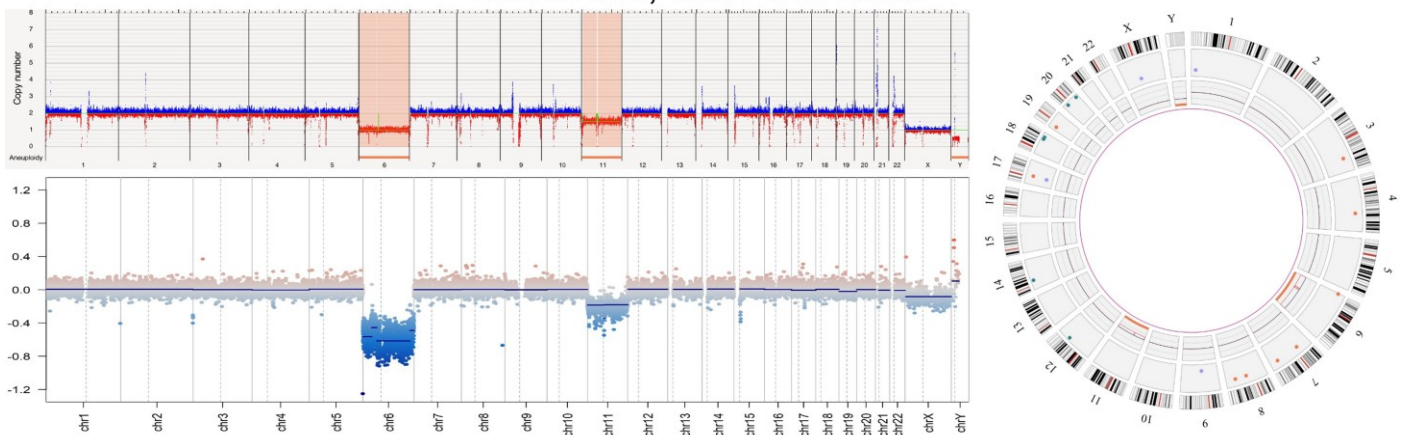
MB7t: MB, non-WNT/non-SHH, Group 4 subtype, subclass VII



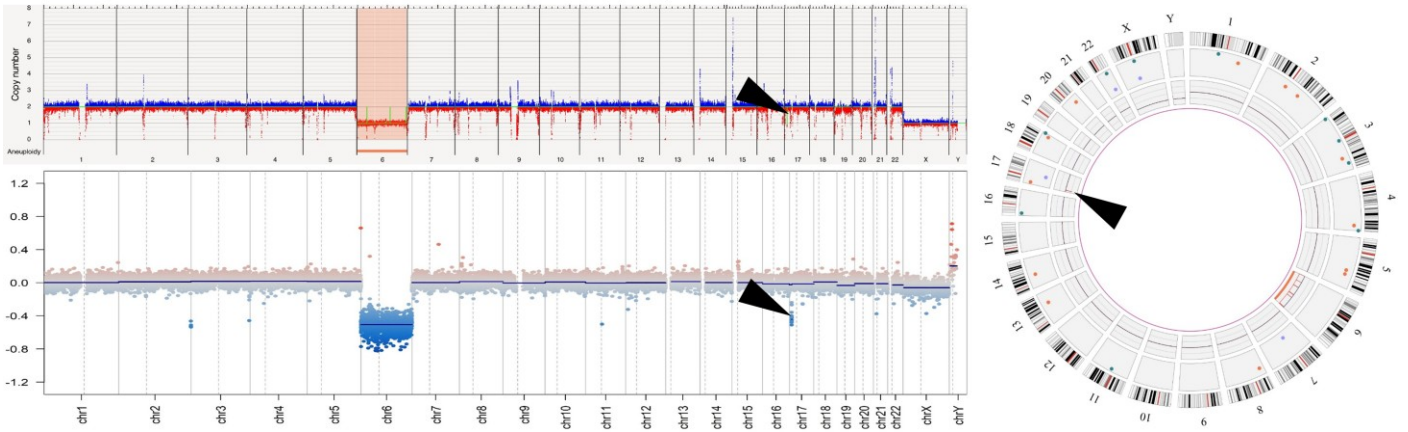
MB8t: MB, WNT-activated



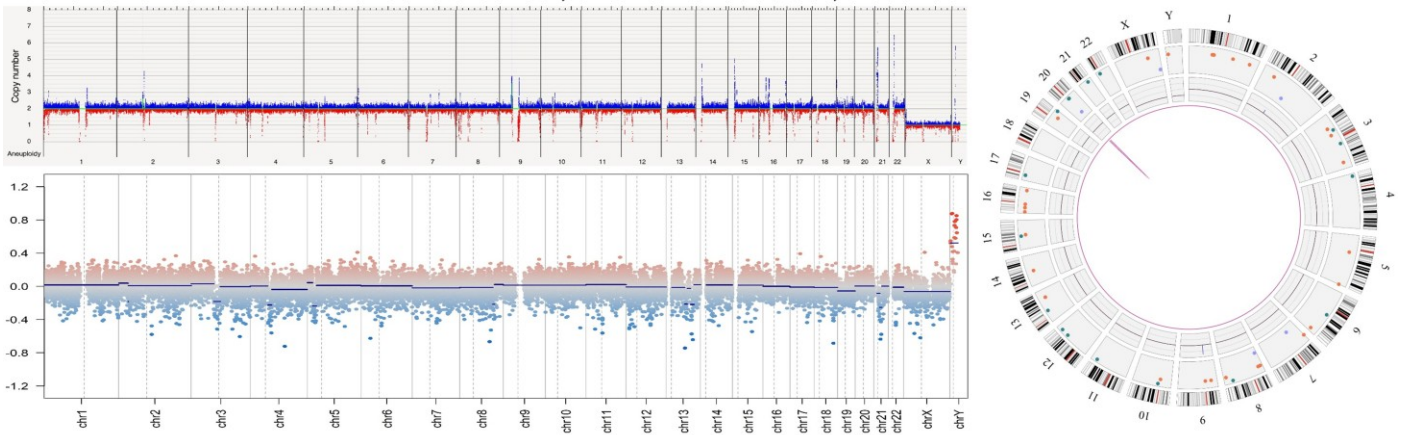
MB9t: MB, WNT-activated



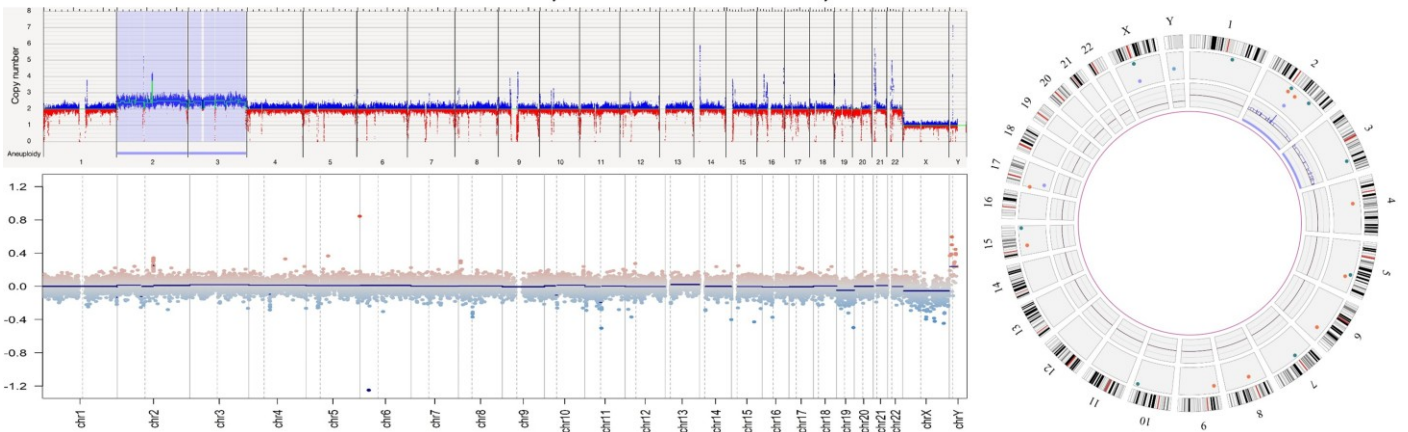
MB10t: MB, WNT-activated



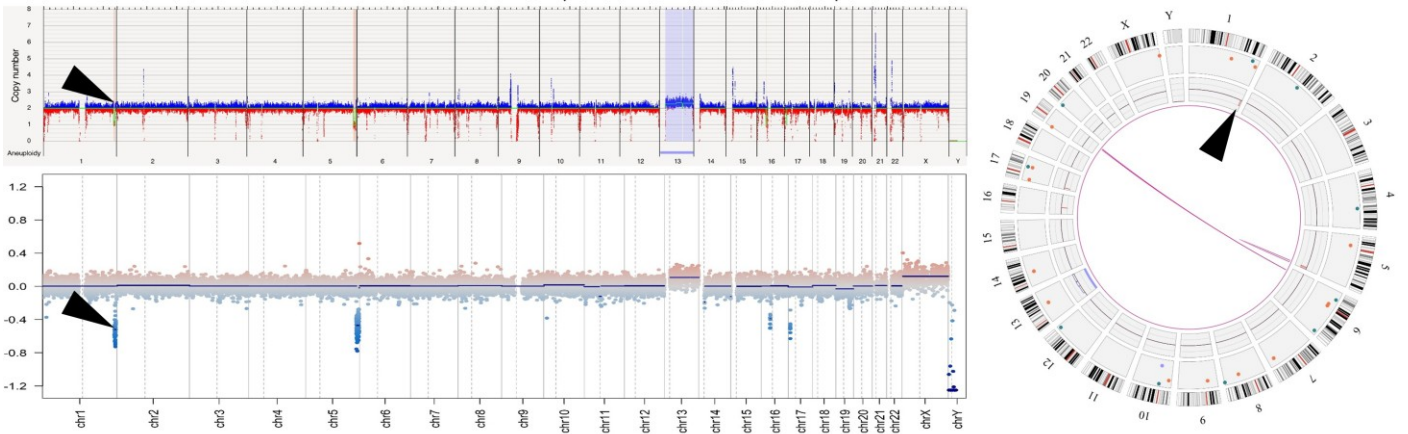
MB11t: MB, SHH-activated, subclass 4



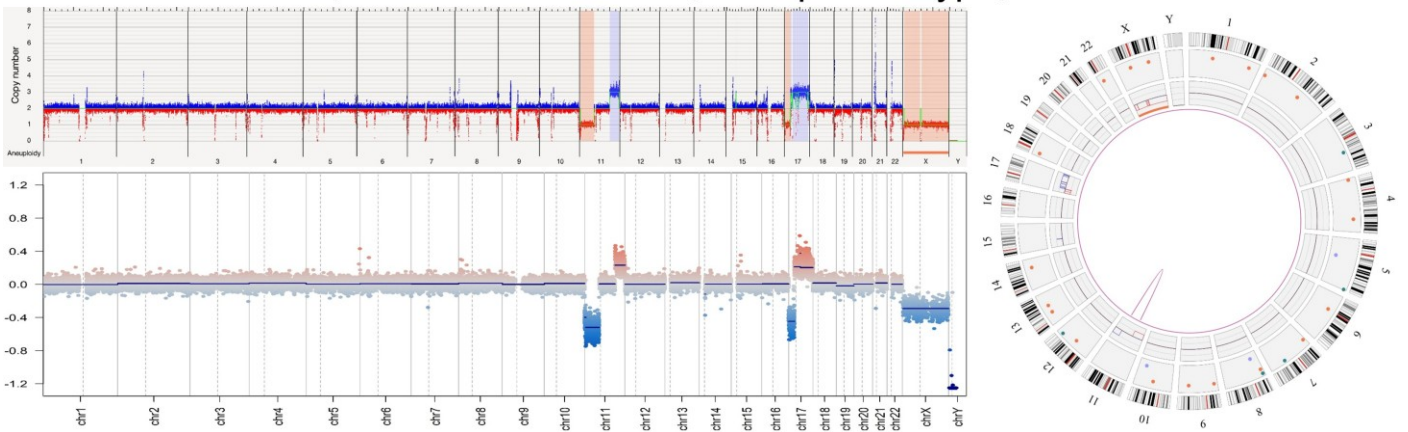
MB12t: MB, SHH-activated, subclass 1



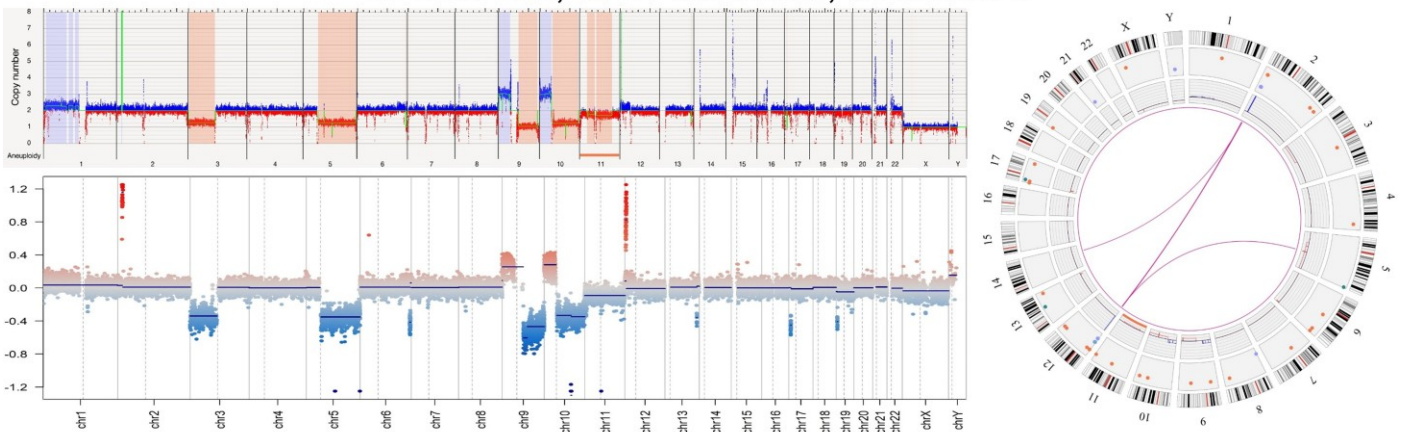
MB13t: MB, SHH-activated, subclass 3



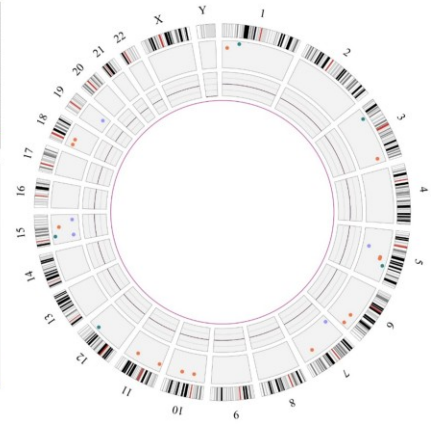
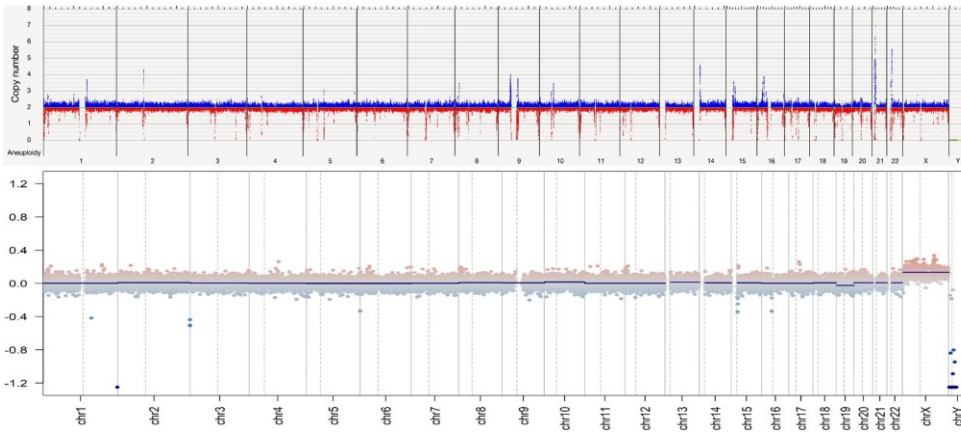
MB14t: MB, non-WNT/non-SHH, Group 4 subtype, subclass VIII



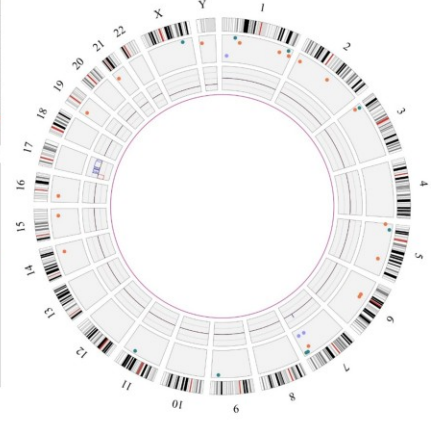
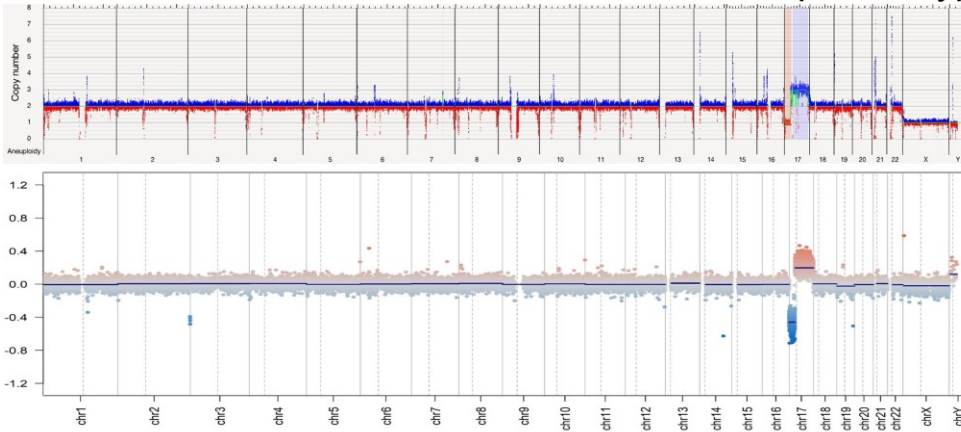
MB15t: MB, SHH-activated, subclass 3



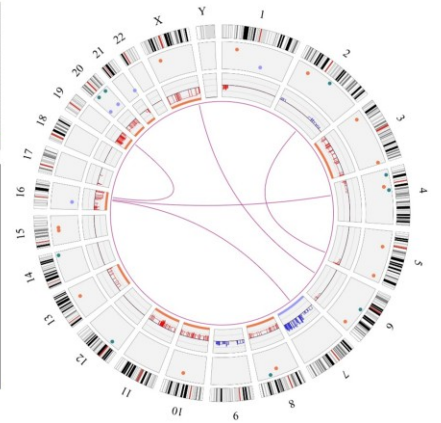
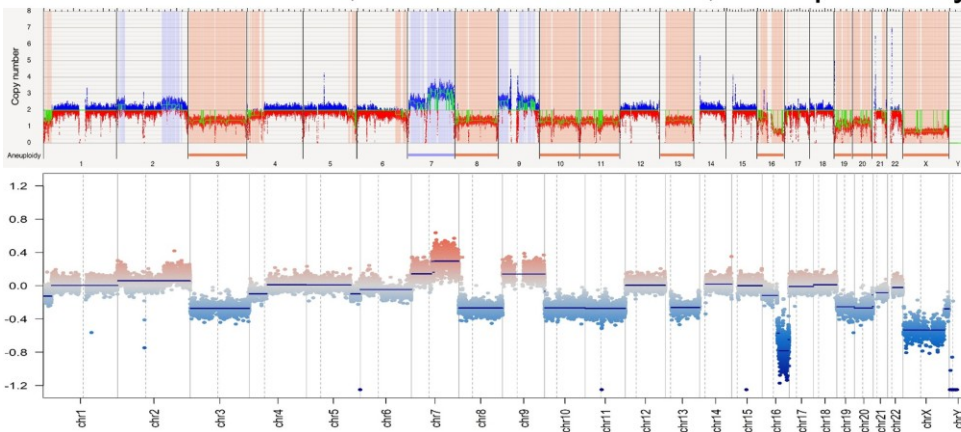
MB16t: MB, SHH-activated, subclass 1



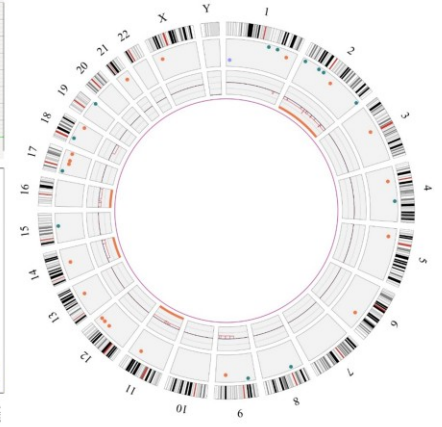
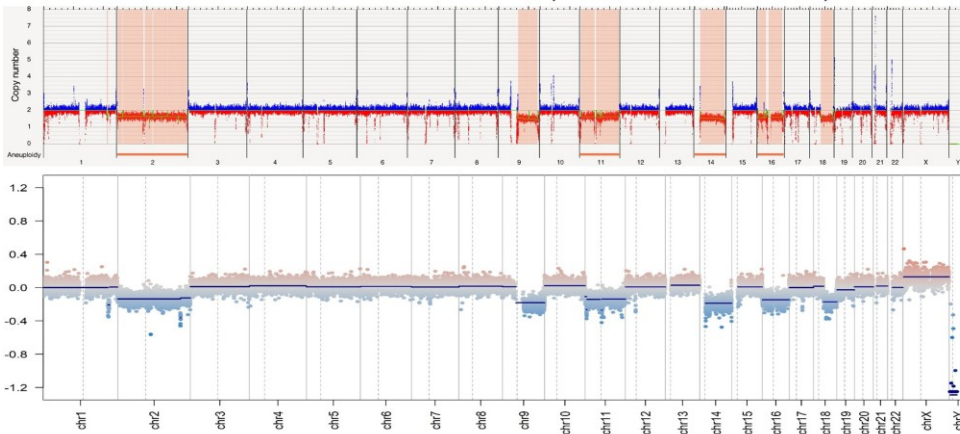
MB17t: MB, non-WNT/non-SHH, Group 4 subtype, subclass VIII



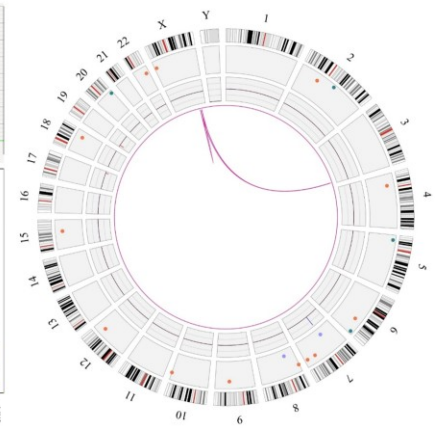
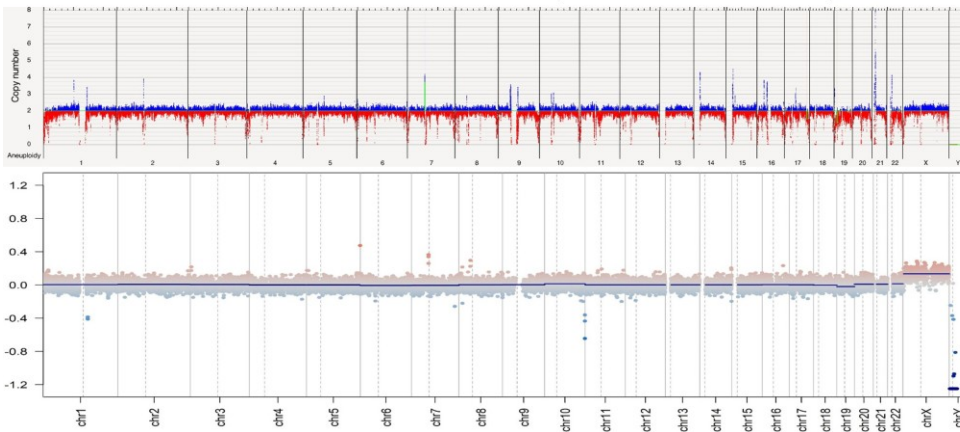
MB18t: MB, non-WNT/non-SHH, Group 3 subtype, subclass IV



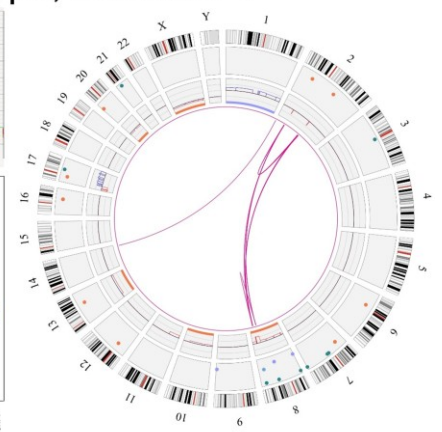
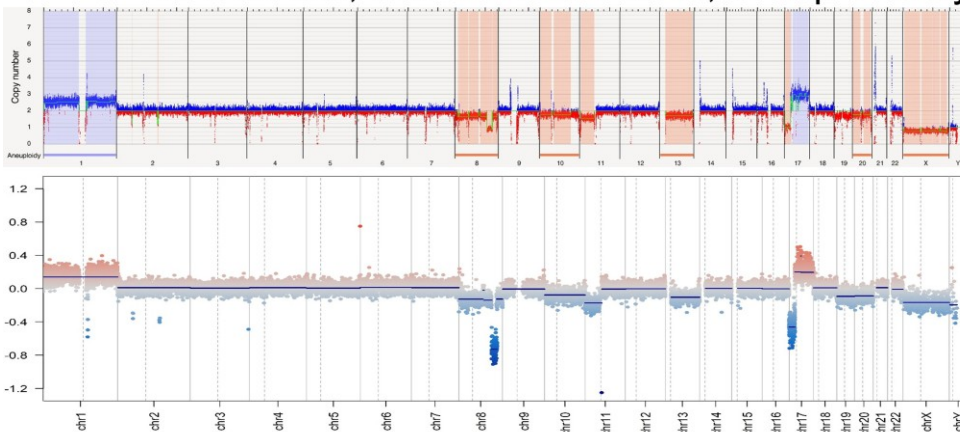
MB19t: MB, SHH-activated, subclass 4



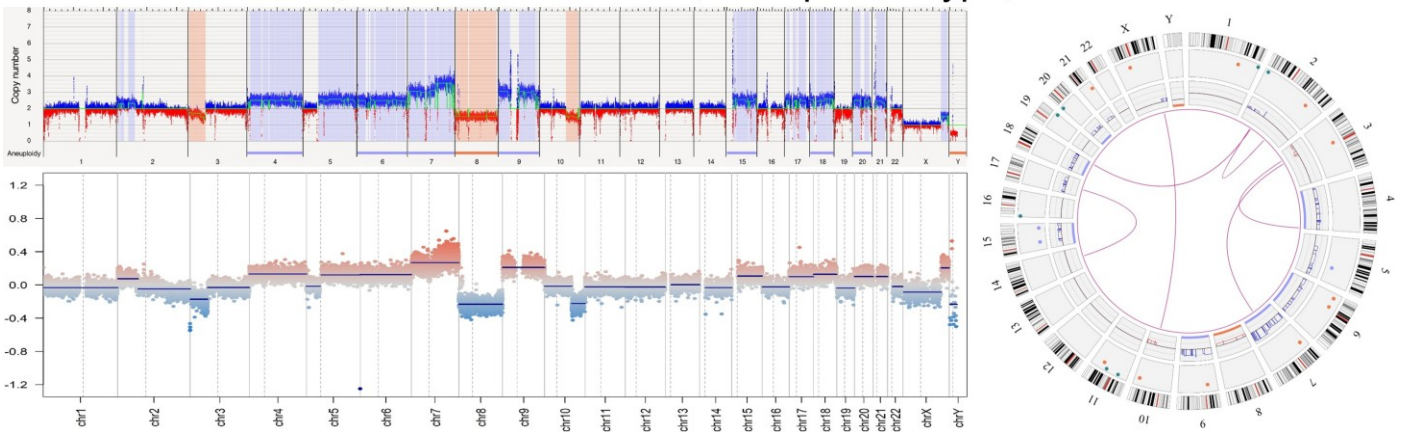
MB20t: MB, SHH-activated, subclass 2



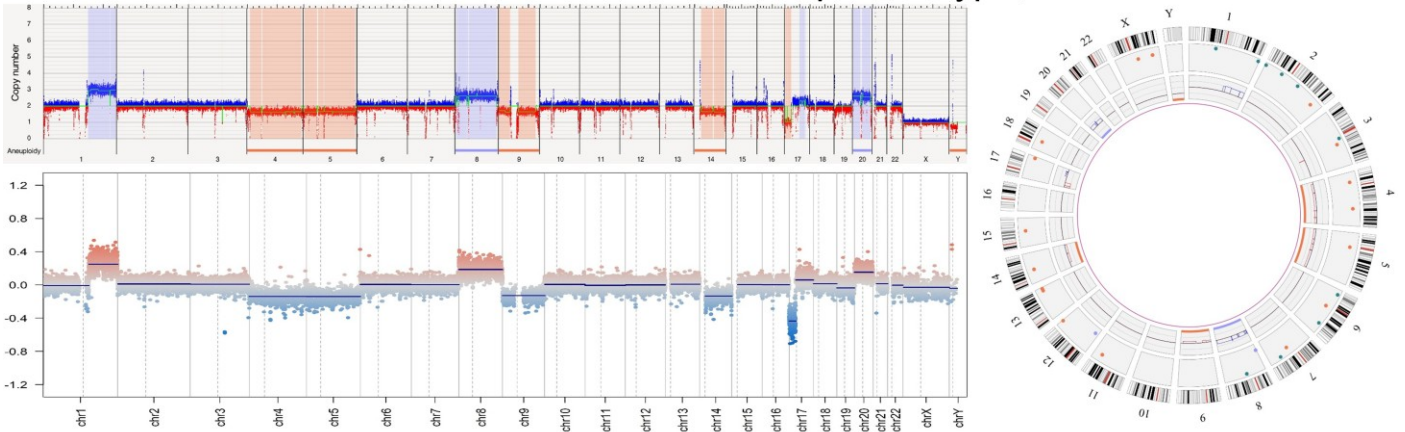
MB21t: MB, non-WNT/non-SHH, Group 4 subtype, subclass V



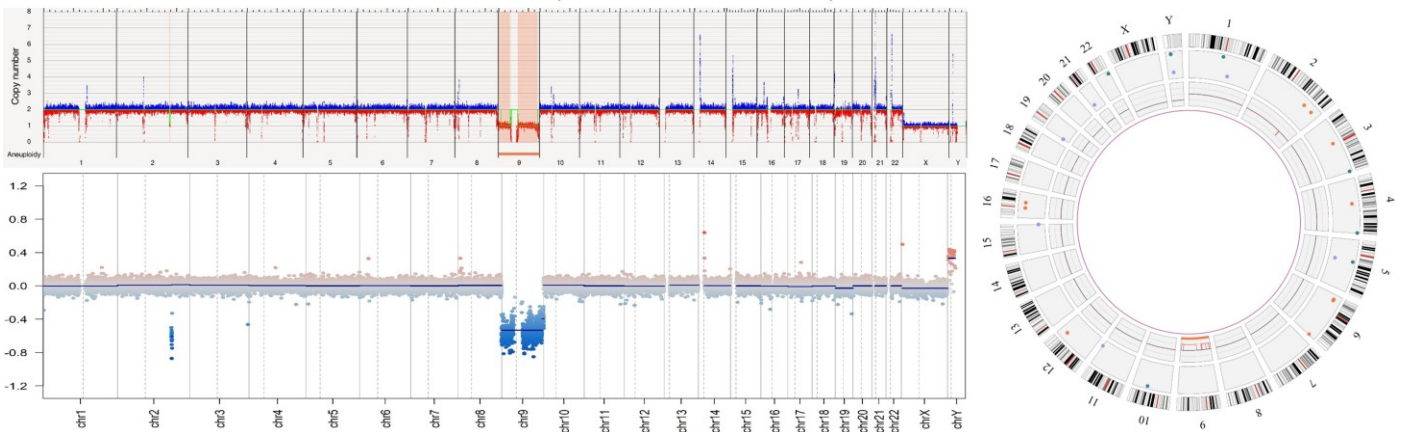
MB22t: MB, non-WNT/non-SHH, Group 4 subtype, subclass VII



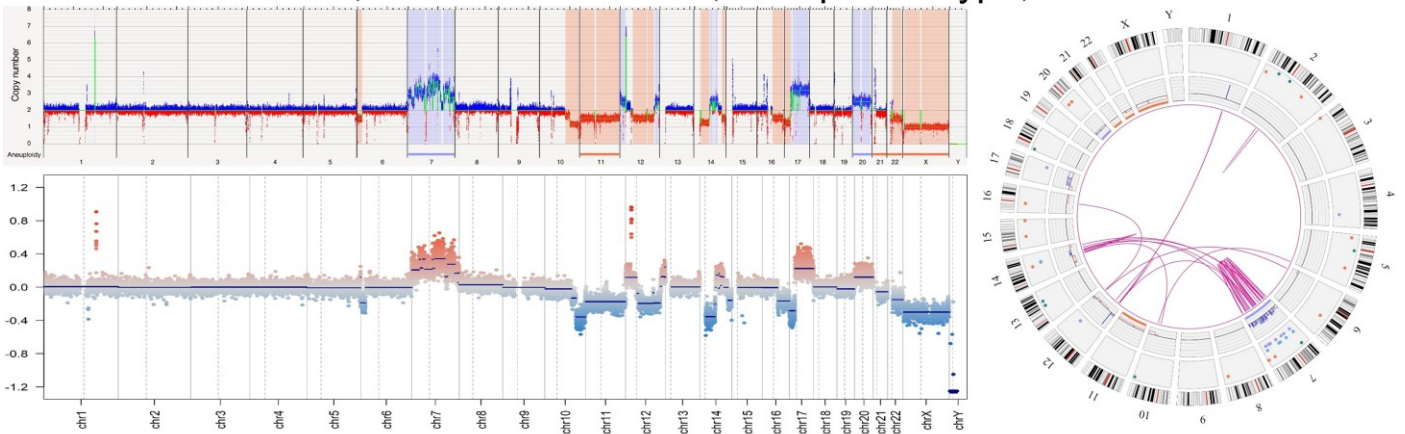
MB23t: MB, non-WNT/non-SHH, Group 3 subtype, subclass II



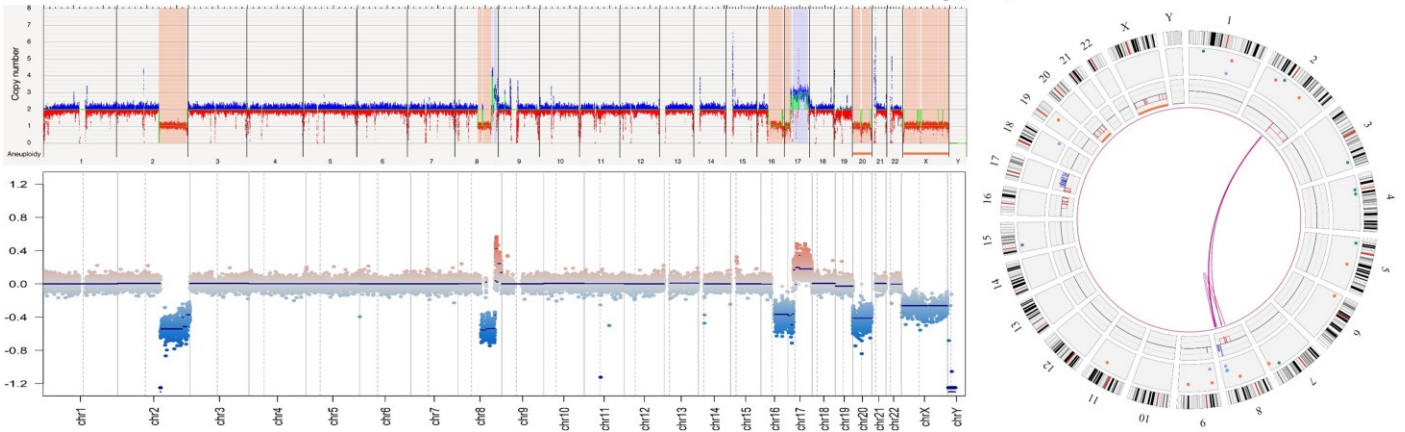
MB24t: MB, SHH-activated, subclass 2



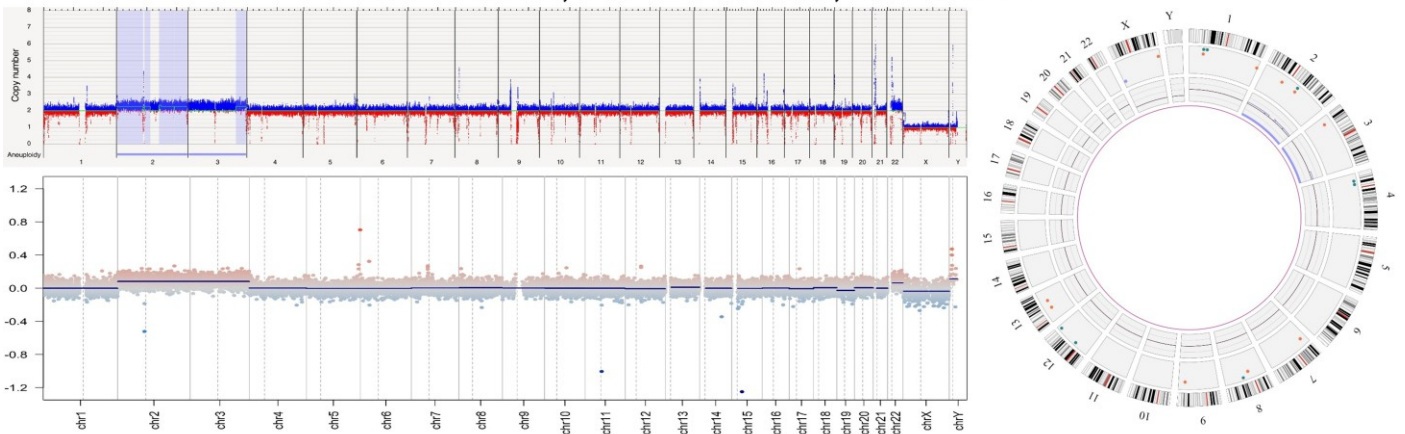
MB25t: MB, non-WNT/non-SHH, Group 4 subtype, subclass VI



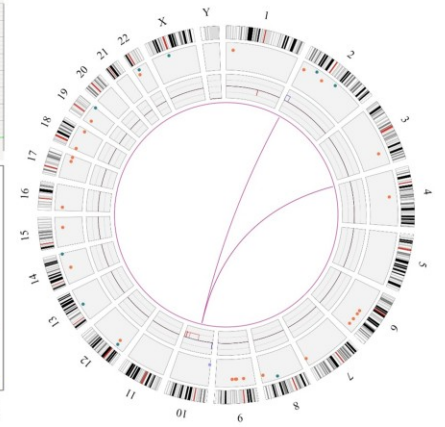
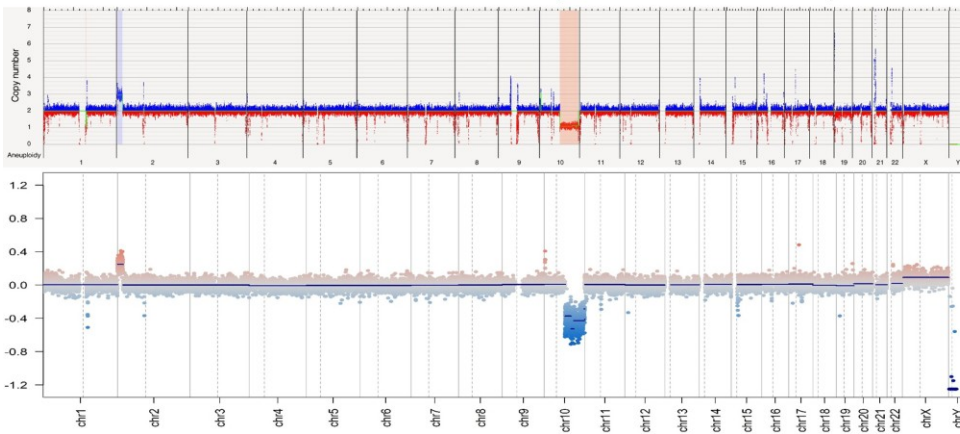
MB26t: MB, non-WNT/non-SHH, Group 4 subtype, subclass VIII



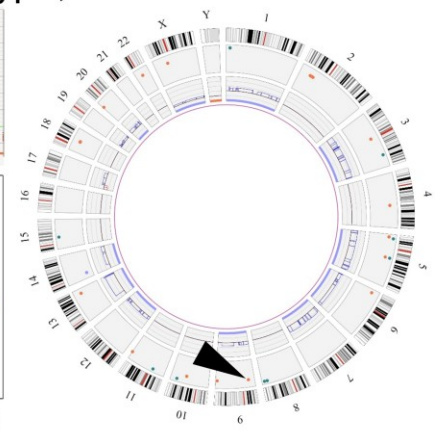
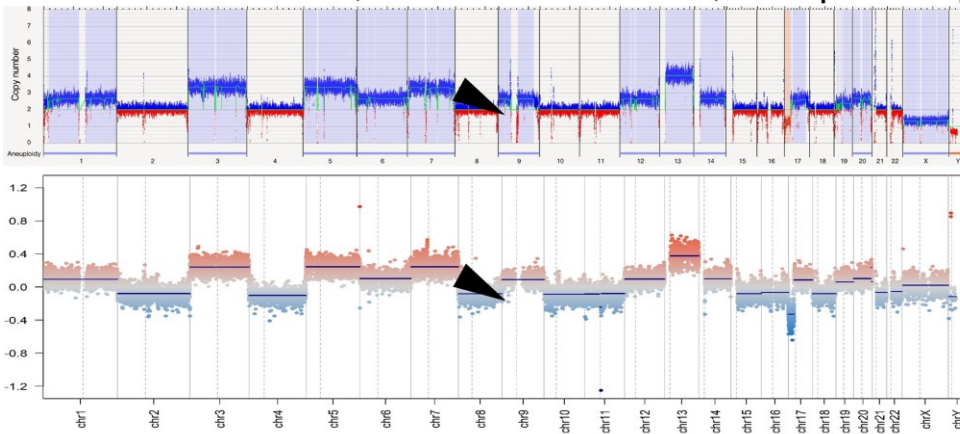
MB27t: MB, SHH-activated, subclass 1



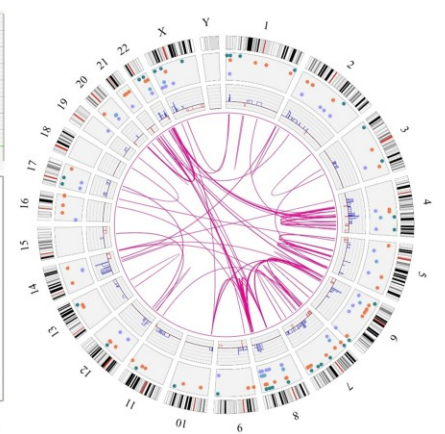
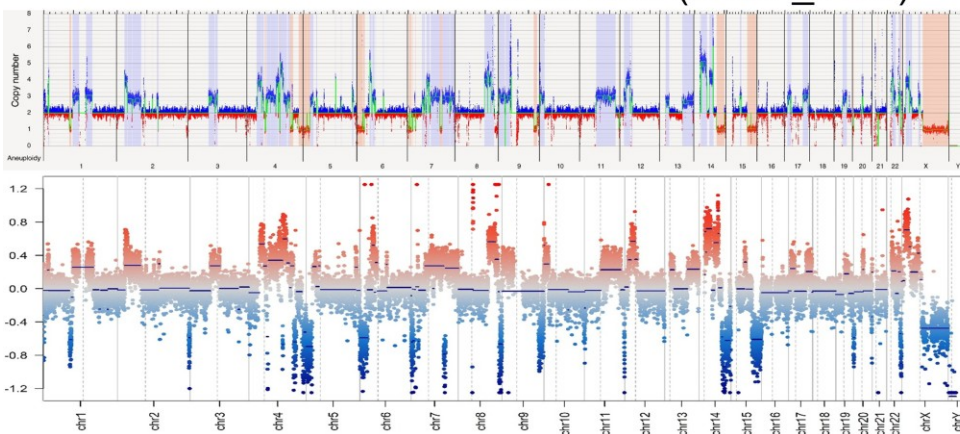
MB28t: MB, SHH-activated, subclass 2



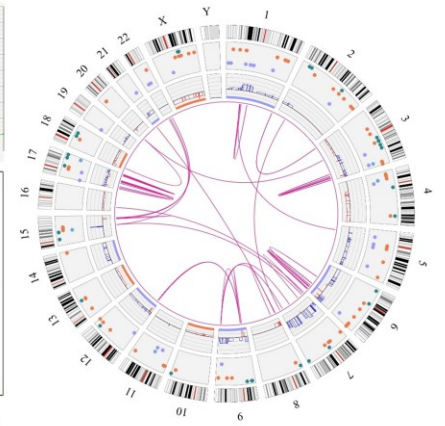
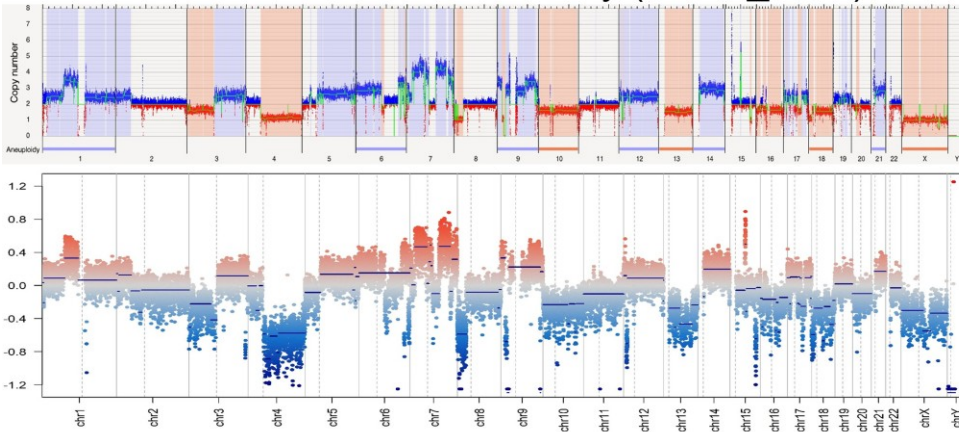
MB29t: MB, non-WNT/non-SHH, Group 3 subtype, subclass IV



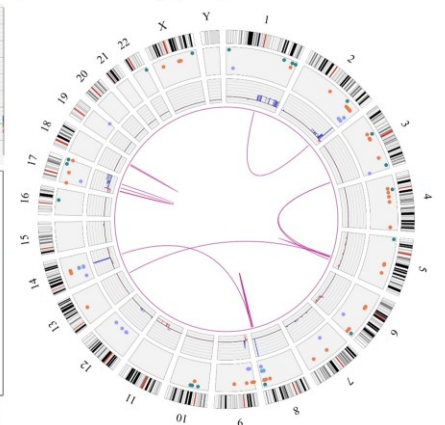
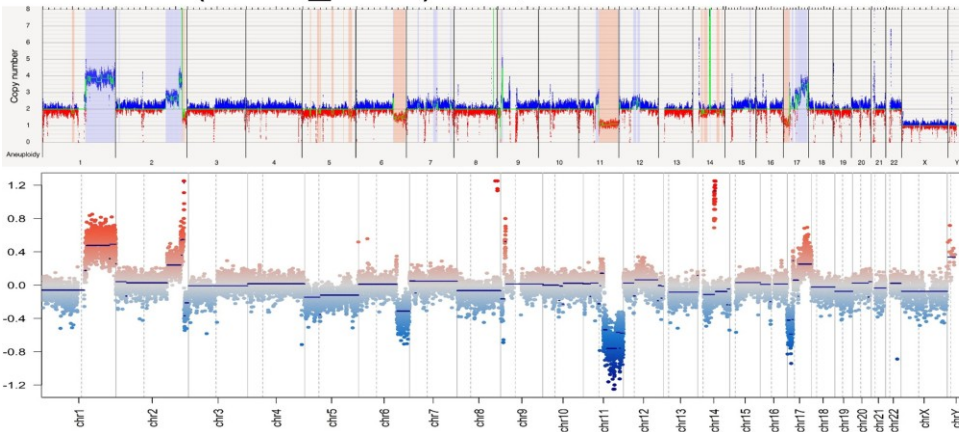
D283 Med (CVCL_1155)



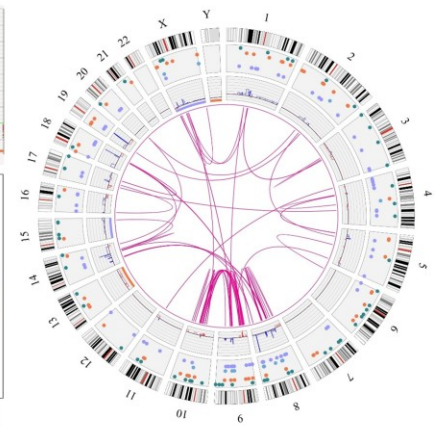
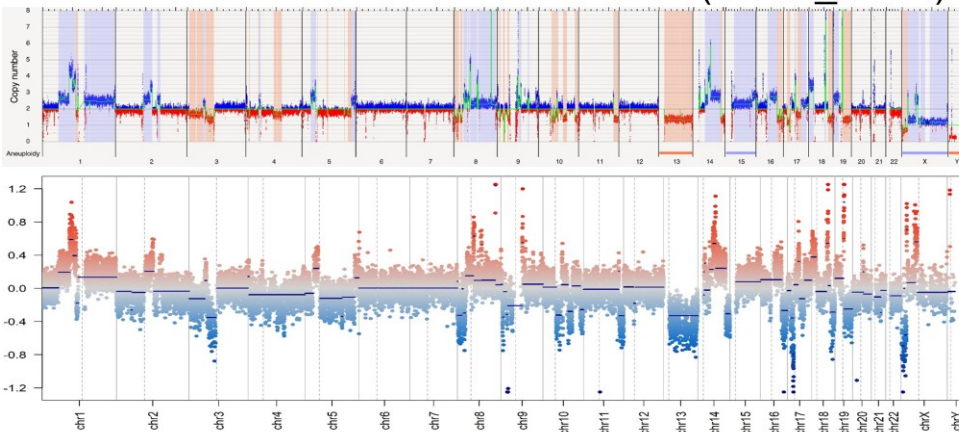
Daoy (CVCL_1167)



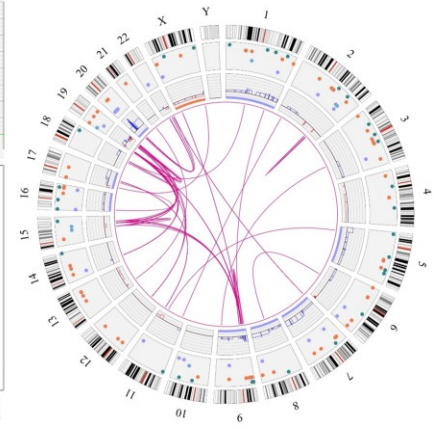
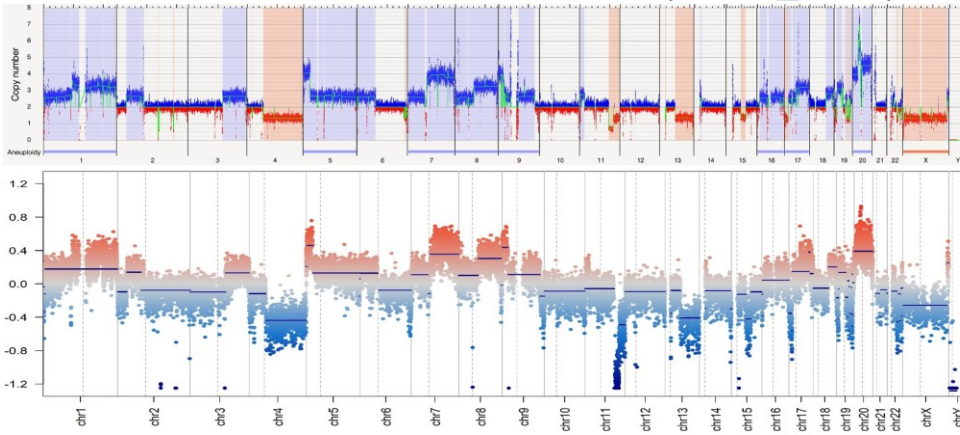
HD-MB03 (CVCL_S506): MB, non-WNT/non-SHH, Group 3 subtype, subclass II



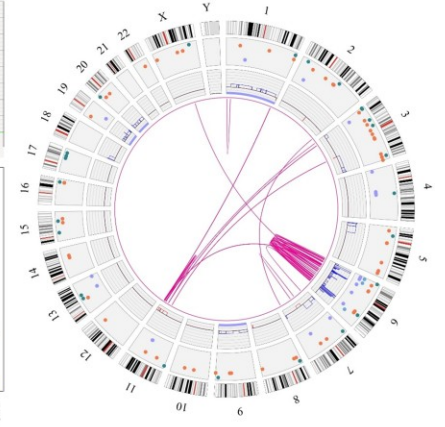
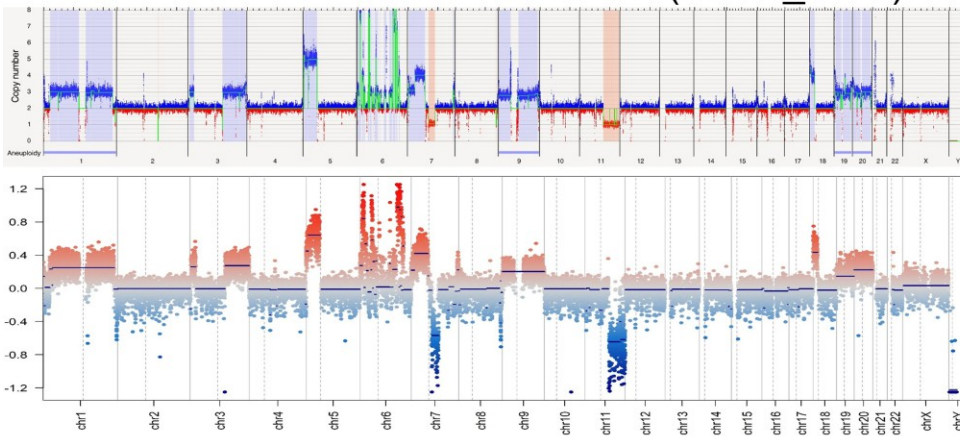
MED-MEB-8A (CVCL_M137)



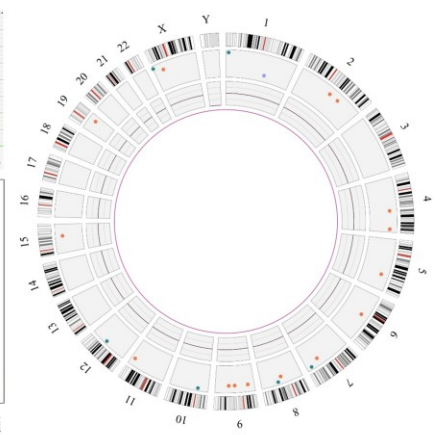
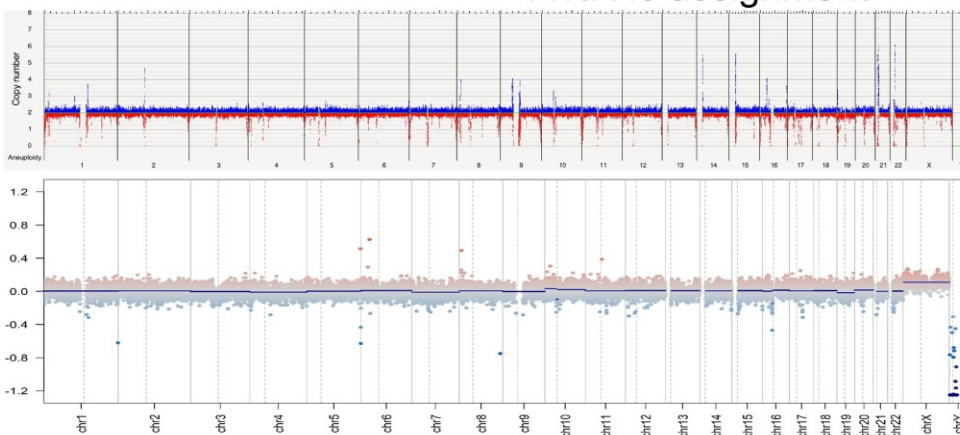
ONS-76 (CVCL_1624)



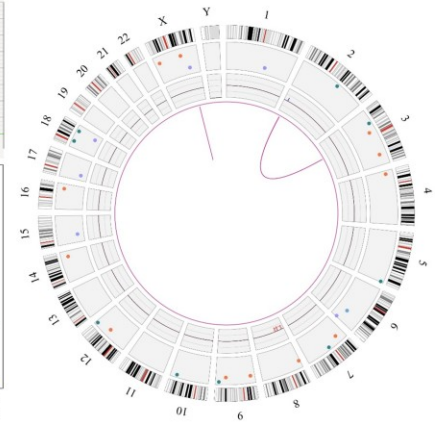
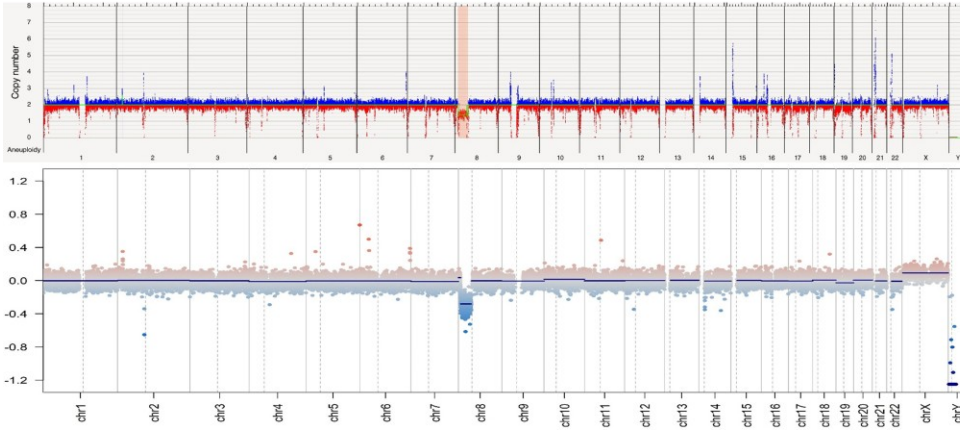
UW228-3 (CVCL_0573)



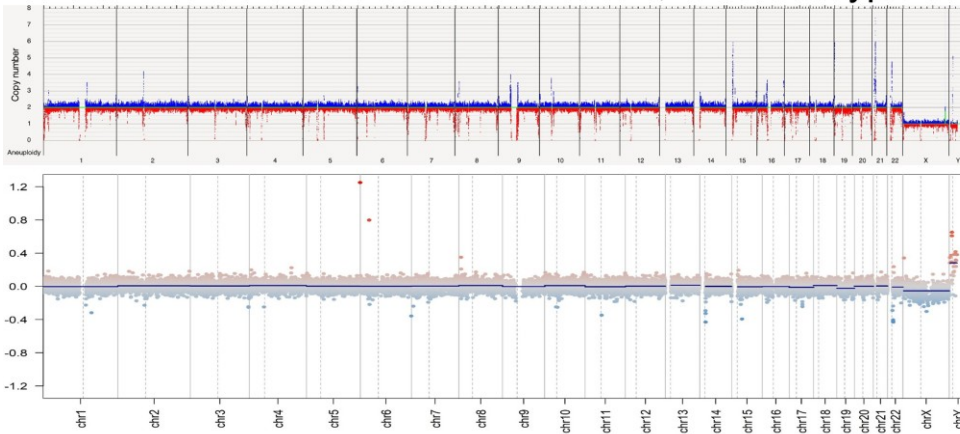
A1t: No assignment



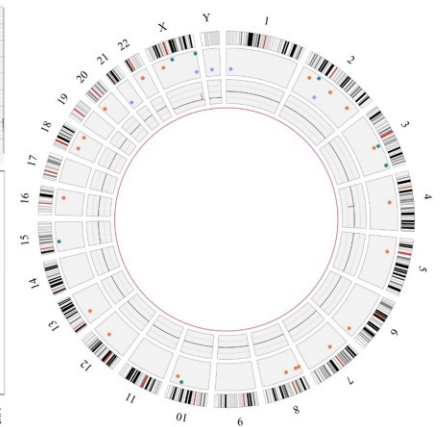
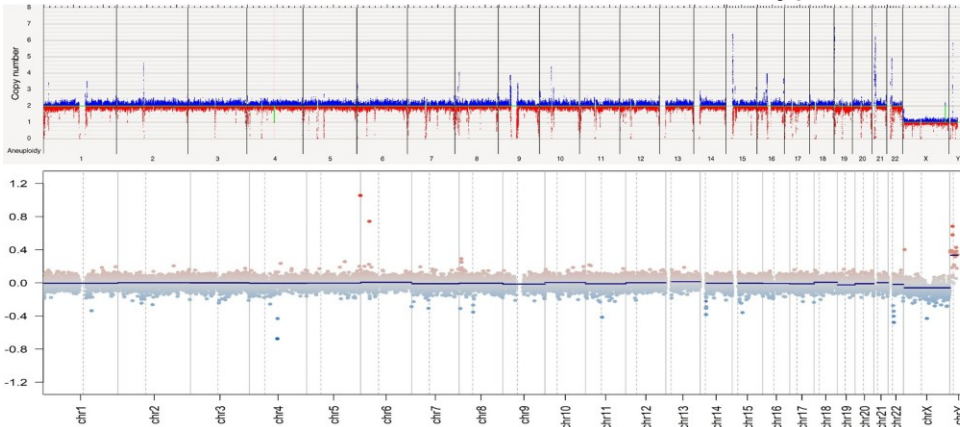
A2t: ATRT, MYC-subtype



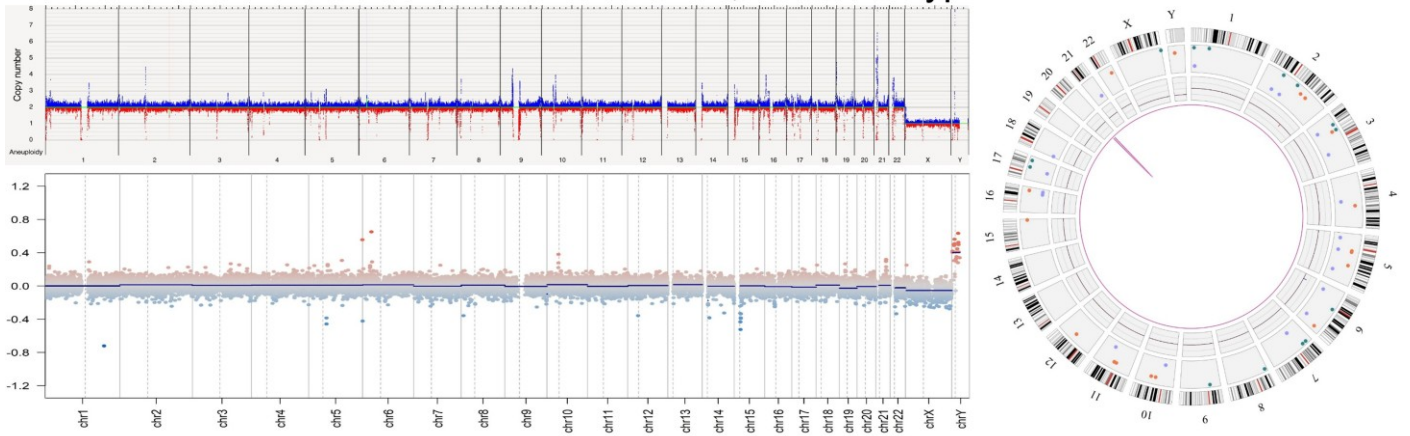
A3t: ATRT, SHH-subtype



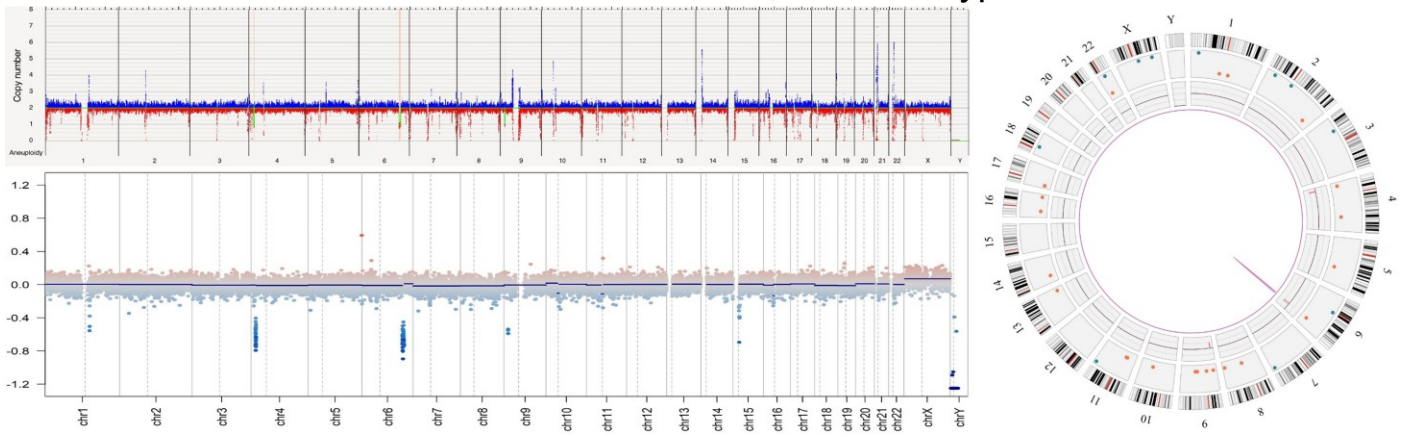
HHU01-ATRT: ATRT, SHH-subtype; cell line from A3t



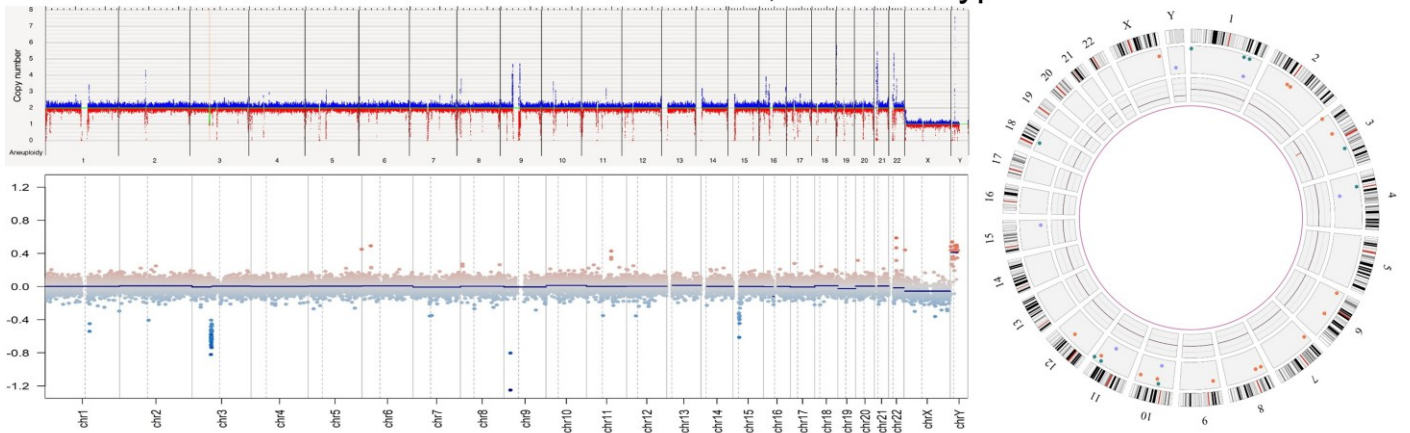
ATRT13808: ATRT, MYC-subtype



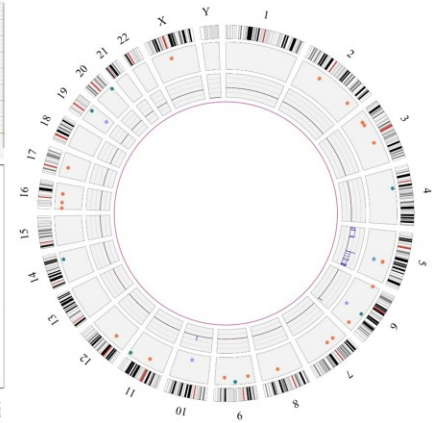
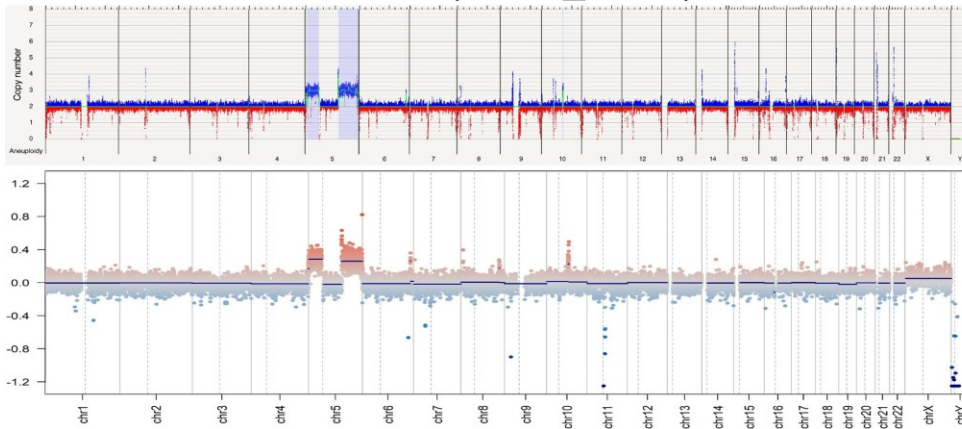
ATRT310-FHTC: ATRT, SHH-subtype



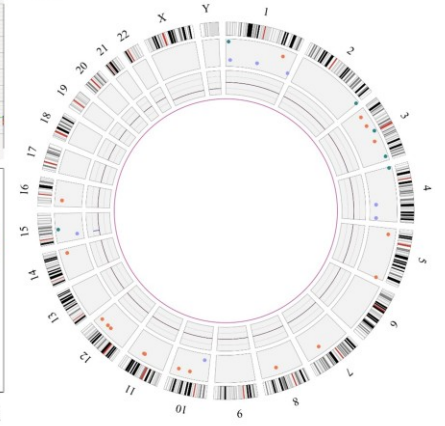
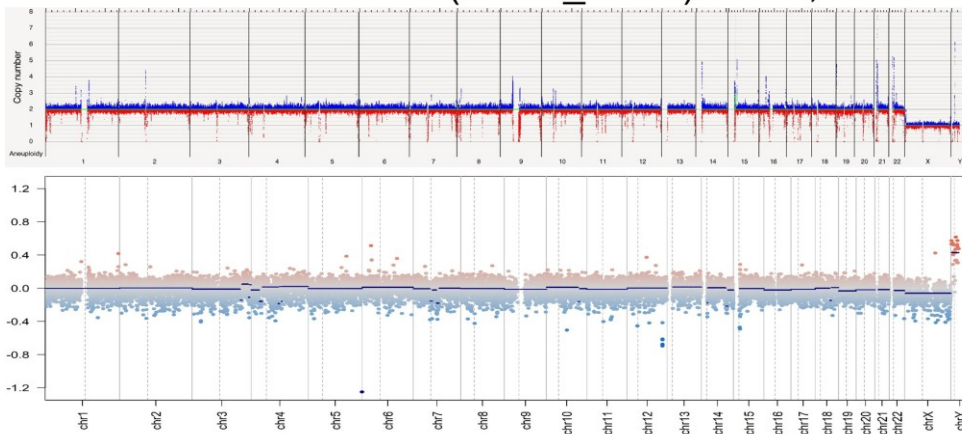
ATRT311-FHTC: ATRT, SHH-subtype



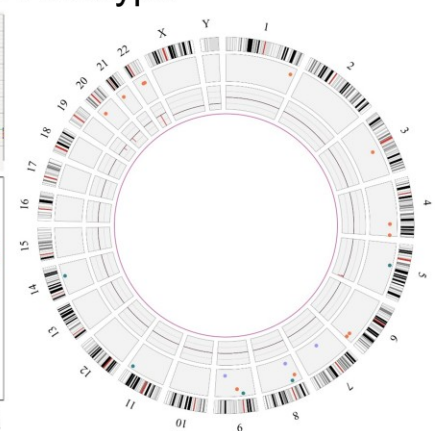
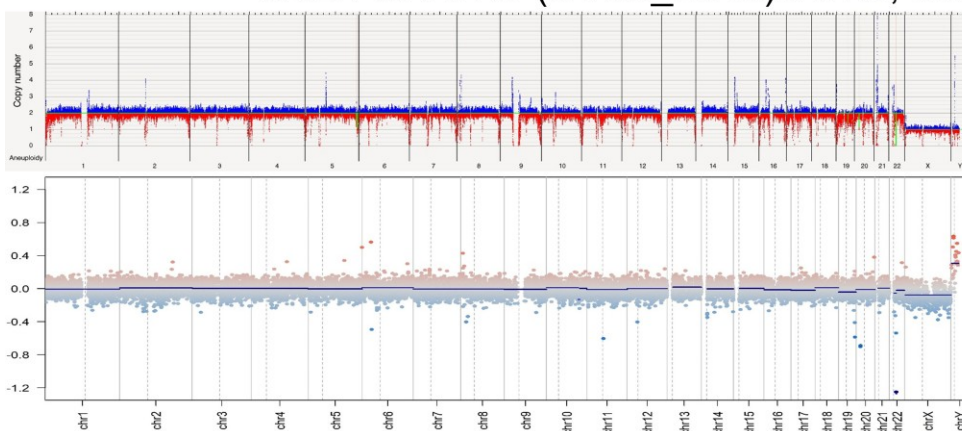
BT-12 (CVCL_M155): ATRT, MYC-subtype



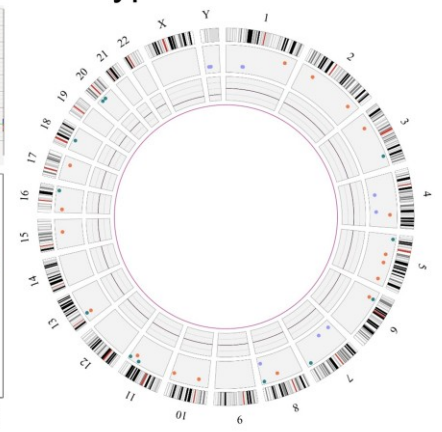
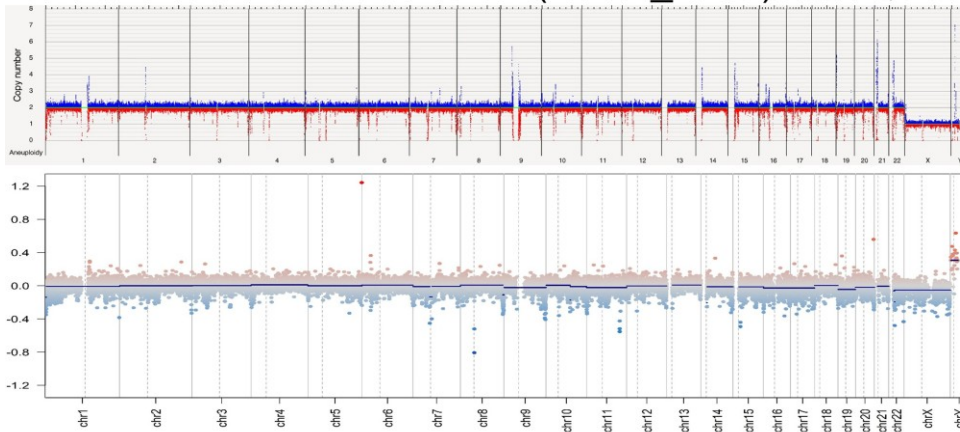
BT-16 (CVCL_M156): ATRT, MYC-subtype



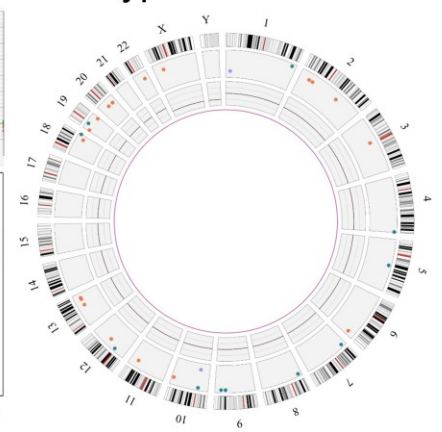
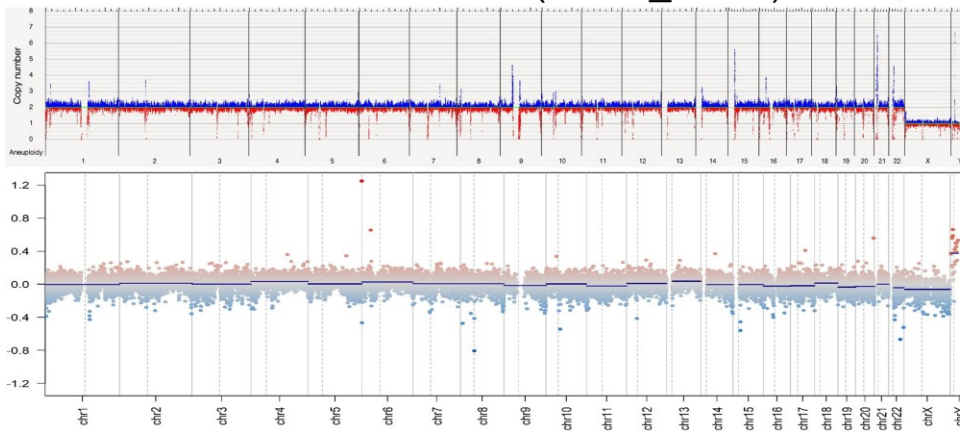
CHLA-02-ATRT (CVCL_B045): ATRT, SHH-subtype



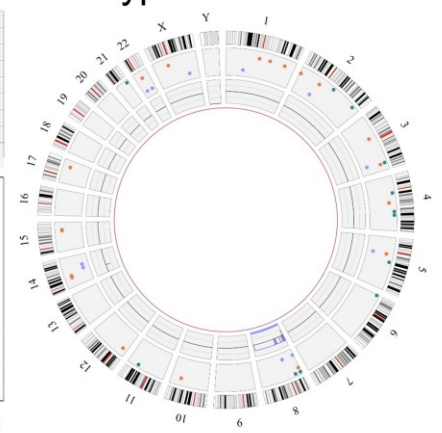
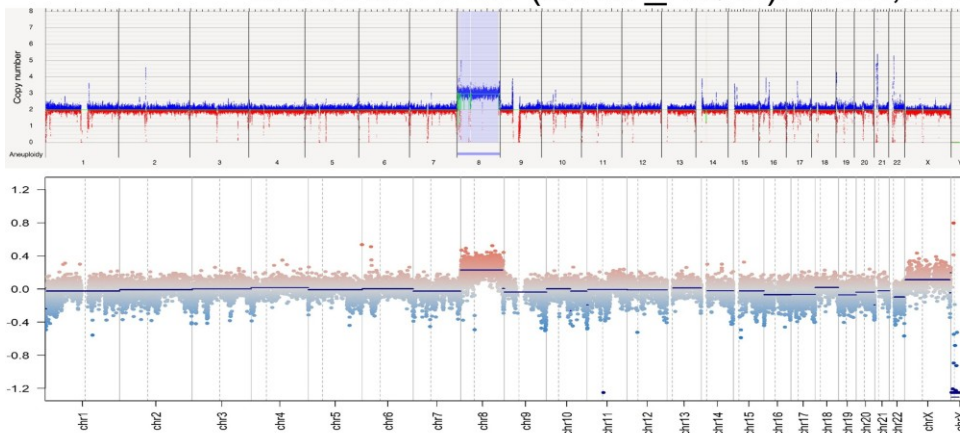
CHLA-04-ATRT (CVCL_0F38): ATRT, SHH-subtype



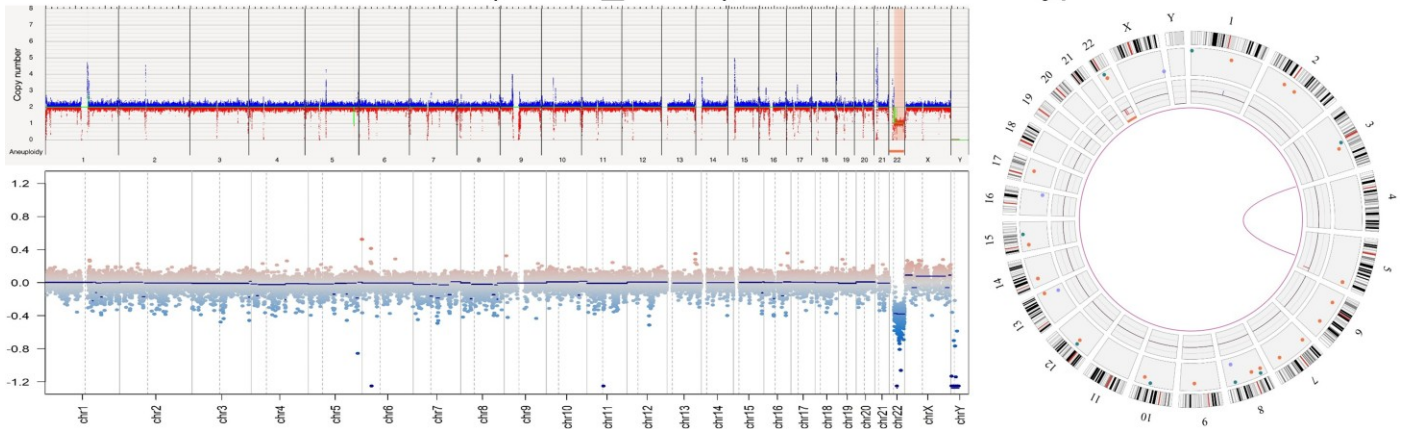
CHLA-05-ATRT (CVCL_AQ41): ATRT, SHH-subtype



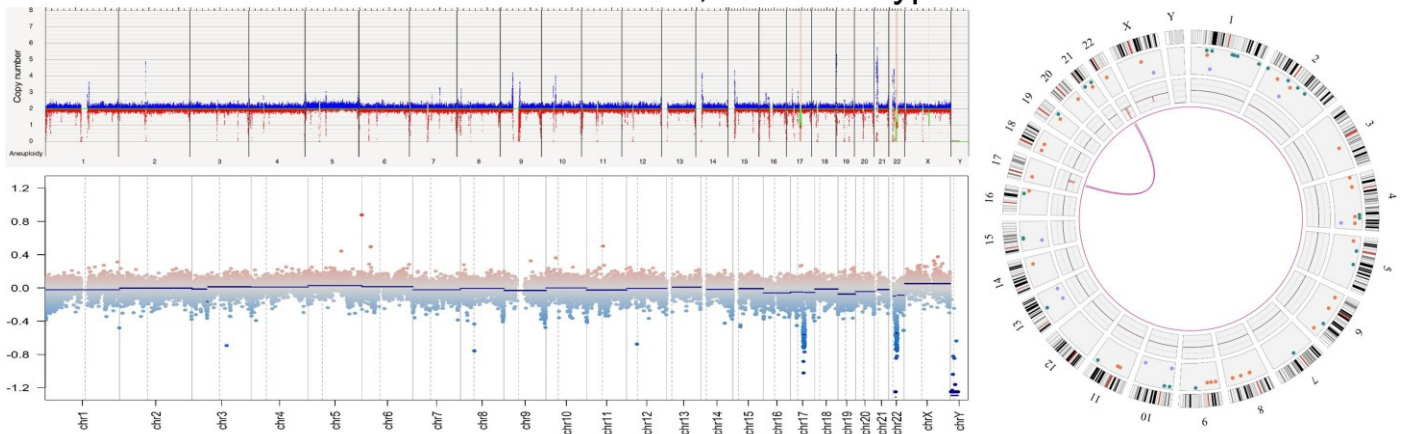
CHLA-06-ATRT (CVCL_AQ42): ATRT, MYC-subtype



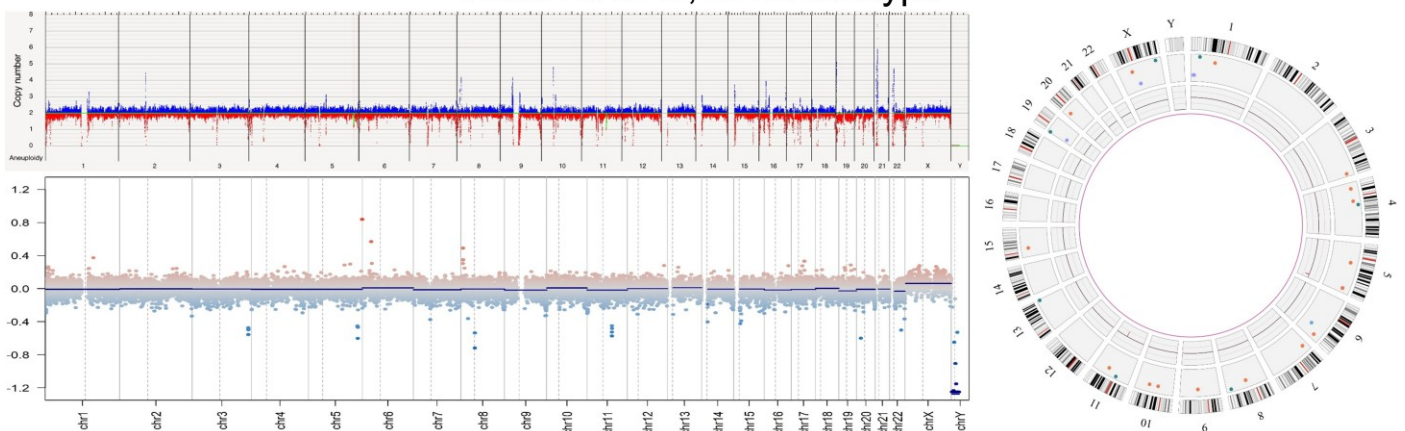
CHLA-266 (CVCL_M149): ATRT, MYC-subtype



JC-ATRT: ATRT, MYC-subtype

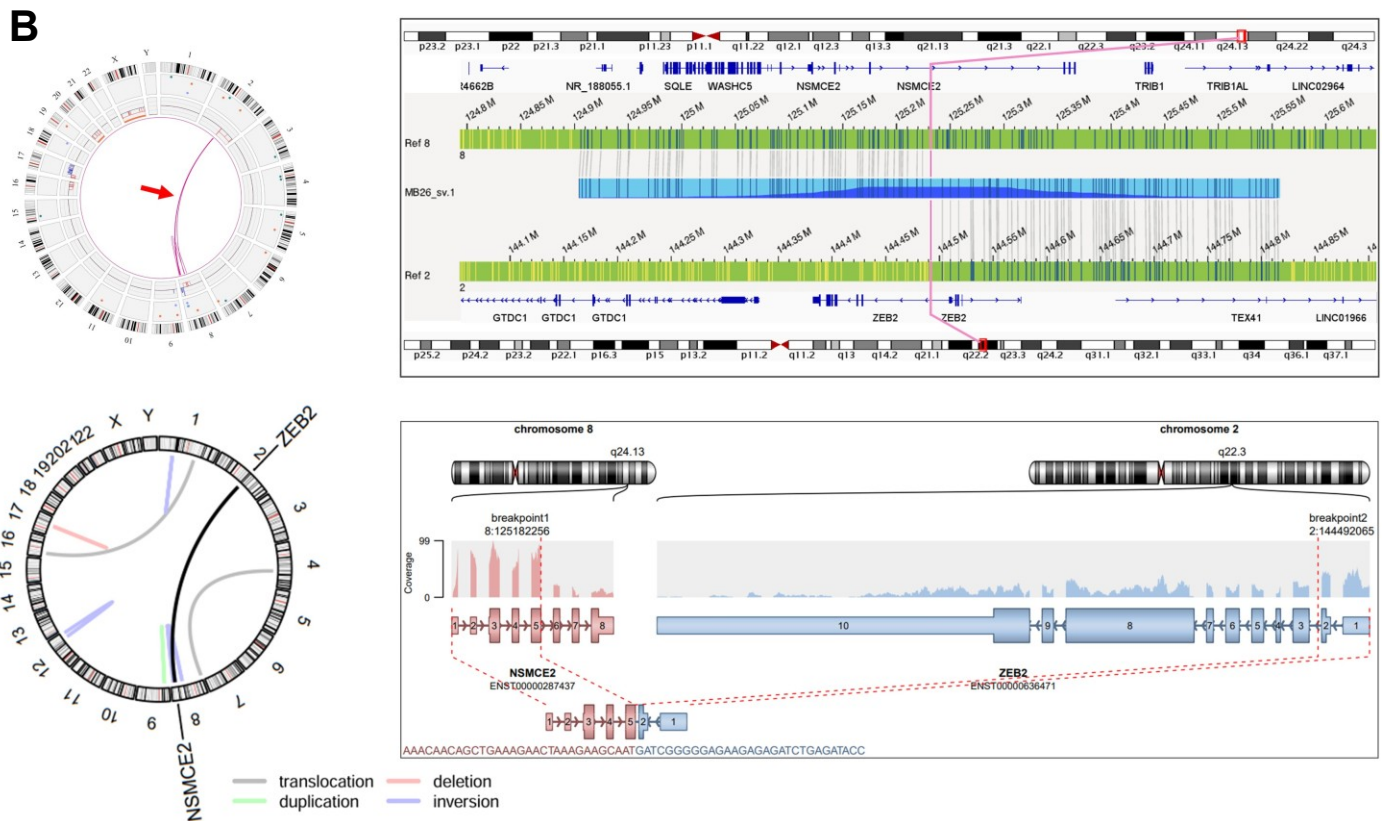
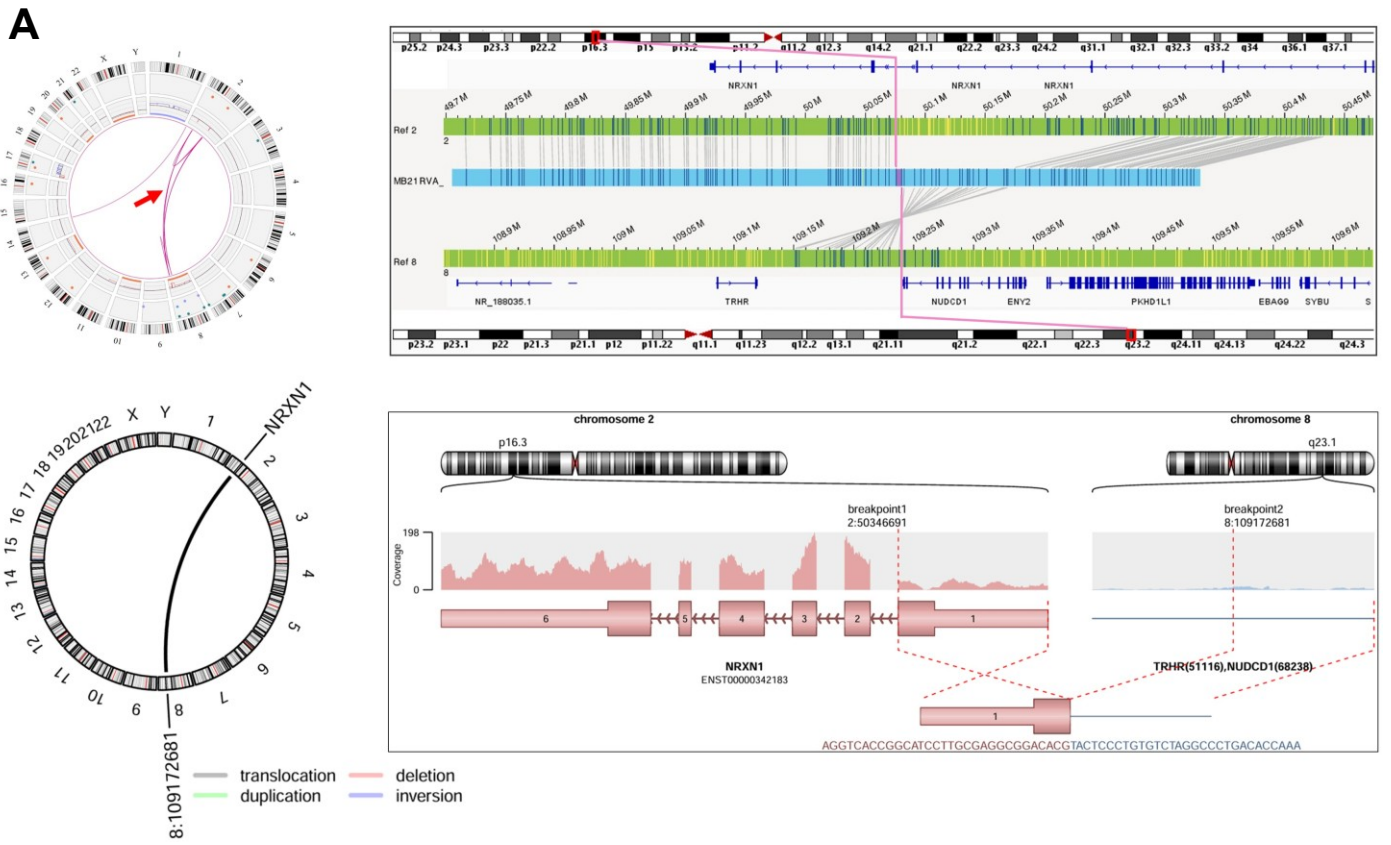


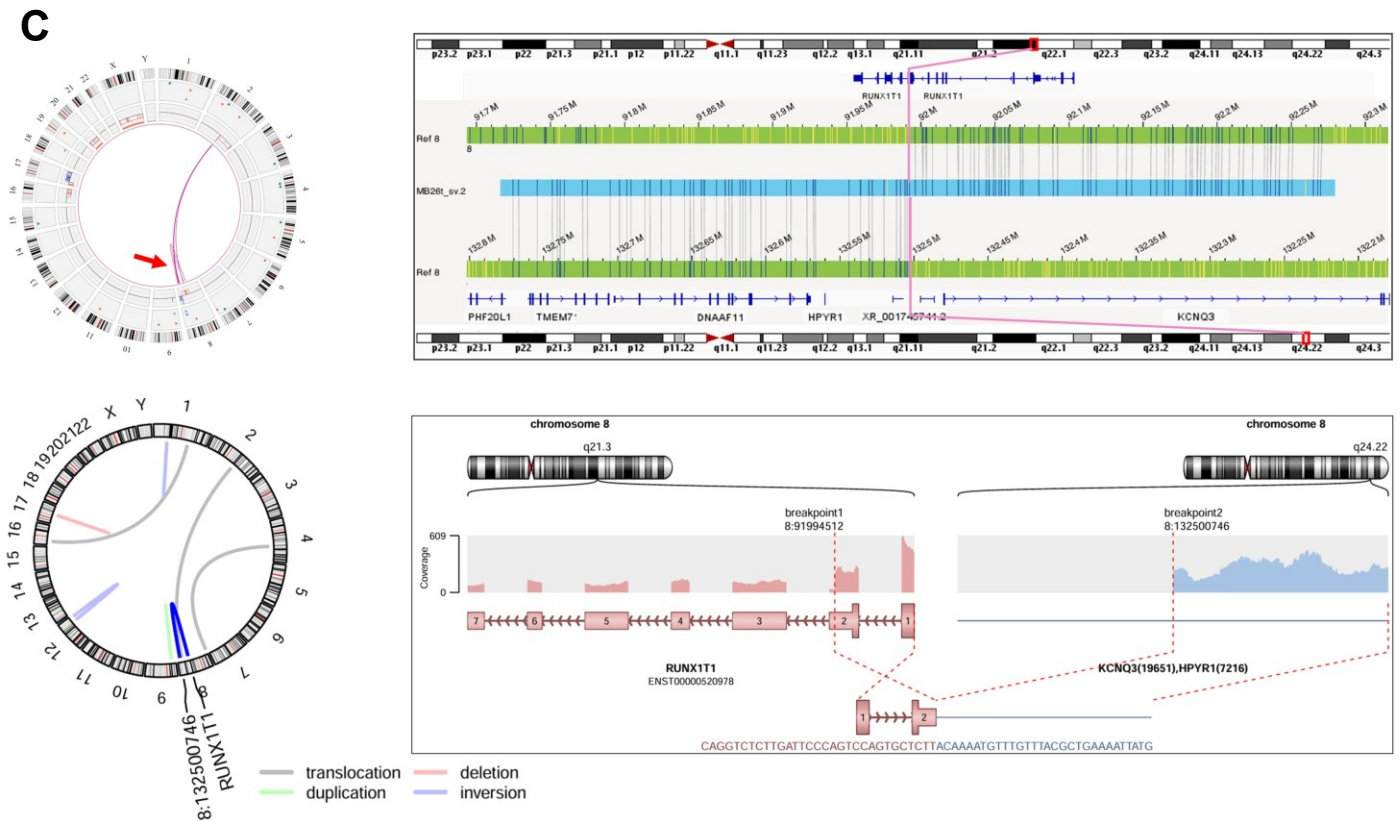
VU397: ATRT, MYC-subtype



Supplementary Figure I. Landscape of CNV alterations and SVs detected by OGM in 29 MB tumors, six MB cell lines, three ATRT tumors and 13 ATRT cell lines. For each case two genome-wide CNV plots (OGM: upper CNV plot, EPIC array: lower CNV plot) and one circos plot summarizing the rare SVs detected in each tumor or cell line are

shown. In the OGM-derived CNV plots, chromosomal regions with copy number losses are indicated in red and regions with copy number gains are indicated in blue. y-axis, CN in the interval [0, 8]; x-axis, Aneuploidy indicators showing whole-chromosome monosomies or total losses (red) and whole-chromosome trisomies or amplifications (blue), and chr1–22 plus sex chromosomes. In the EPIC-derived CNV plots, chromosomal regions with copy number losses are indicated in blue and chromosomal regions with copy number gains are indicated in red. y-axis, log₂ median segment intensity in the interval [-1.2, 1.2]; x-axis, chr1–22 plus sex chromosomes. The circos plots show, from the outside to the center, the chromosome numbers and ideograms, SVs represented as color-coded dots (*red*, deletion; *purple*, duplication; *light-blue*, insertion; *dark-blue*, inversion), the integrated CN plot, and translocations/fusion events of complex rearrangements as connective pink arcs. Black arrowheads point to specific events discussed within the result section.



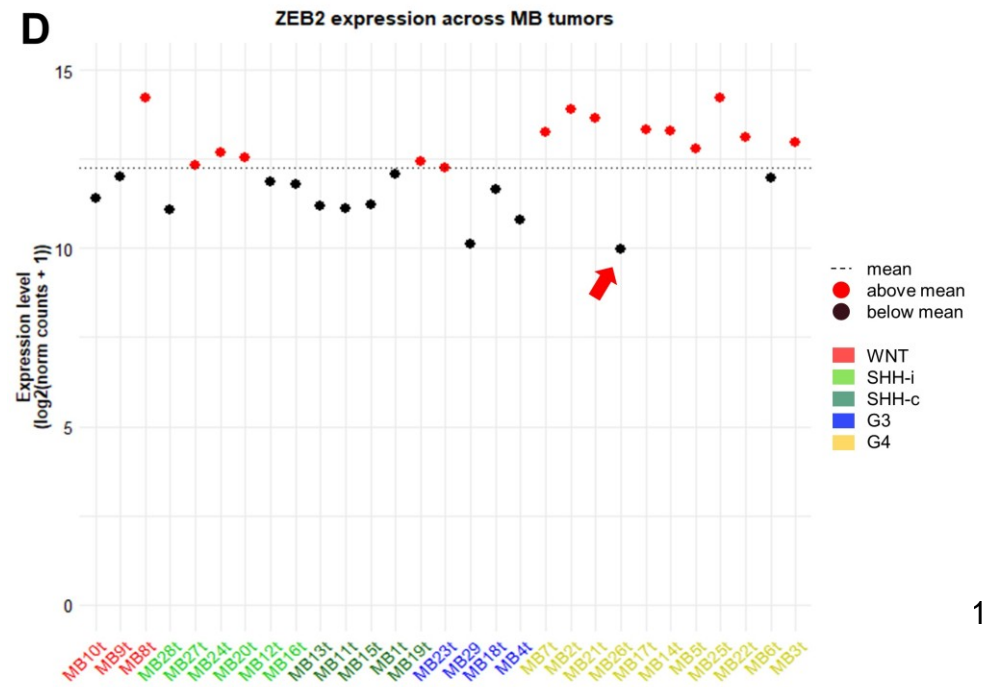
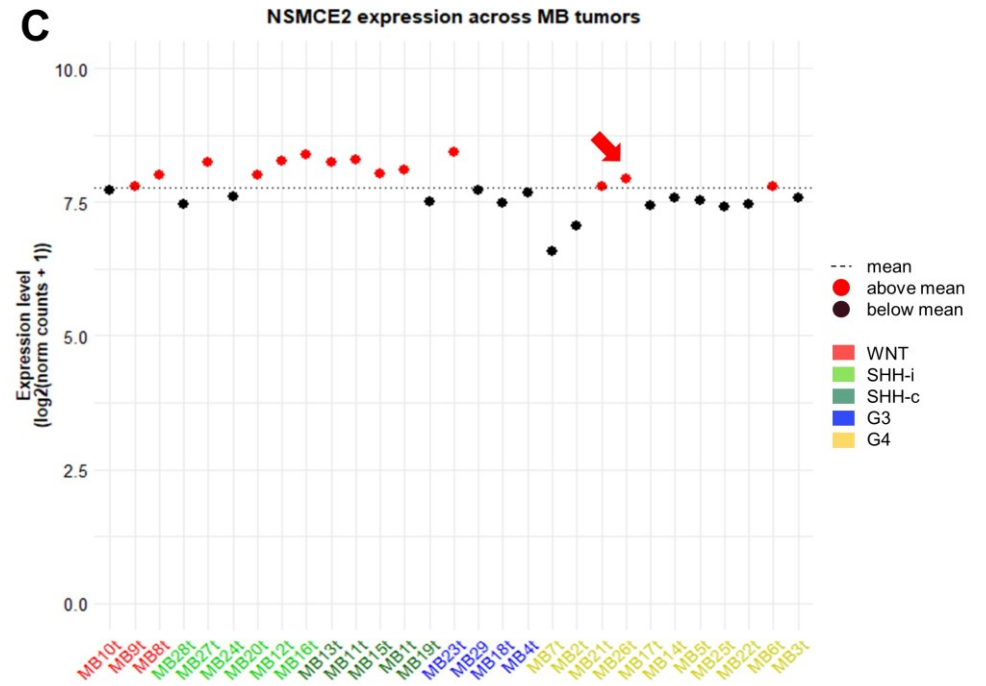
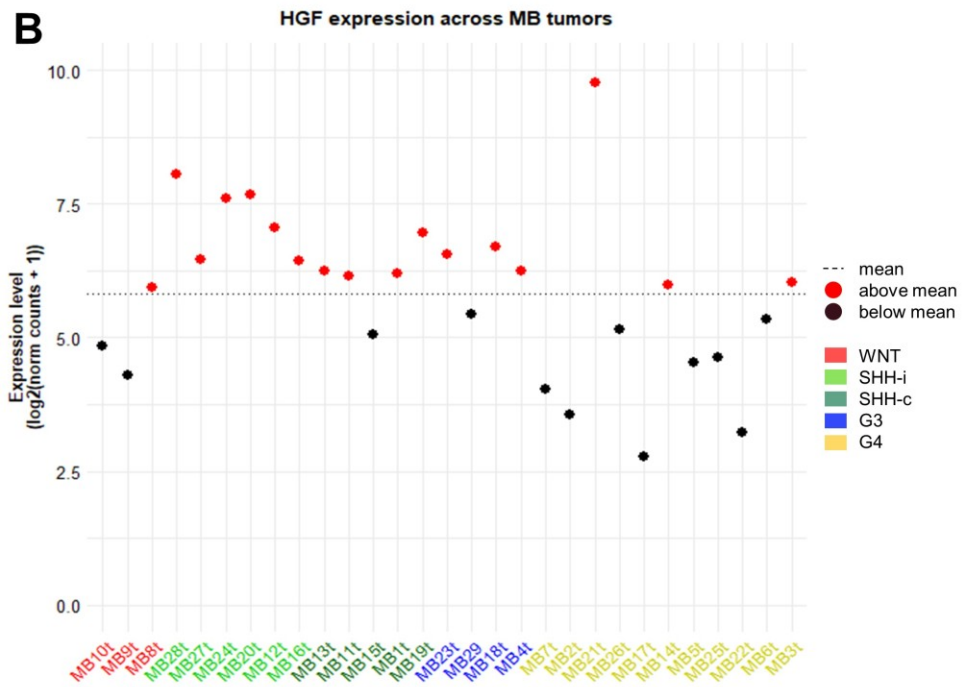
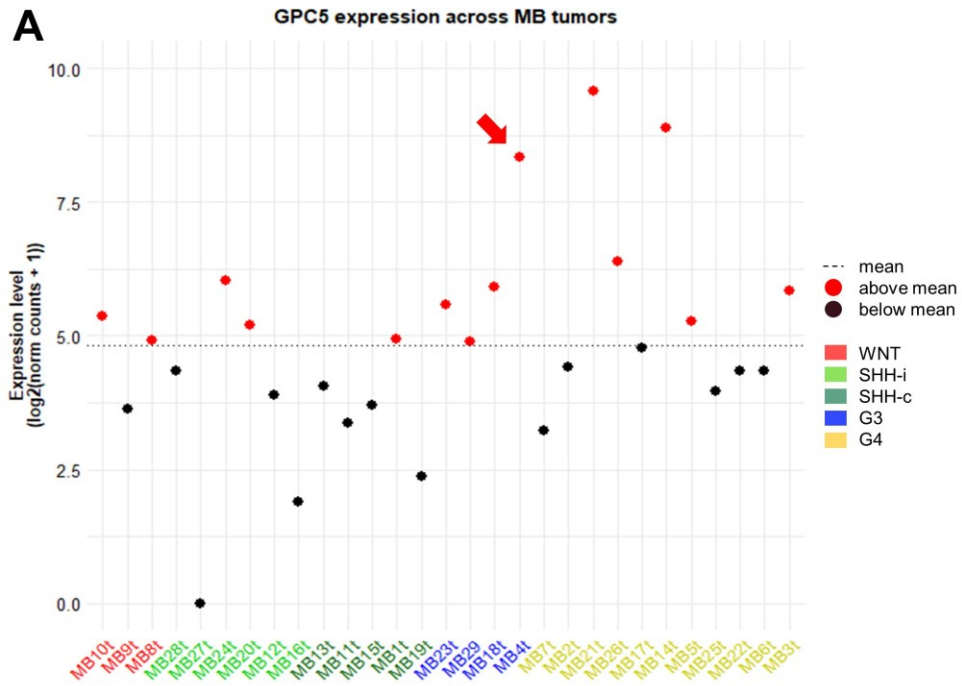


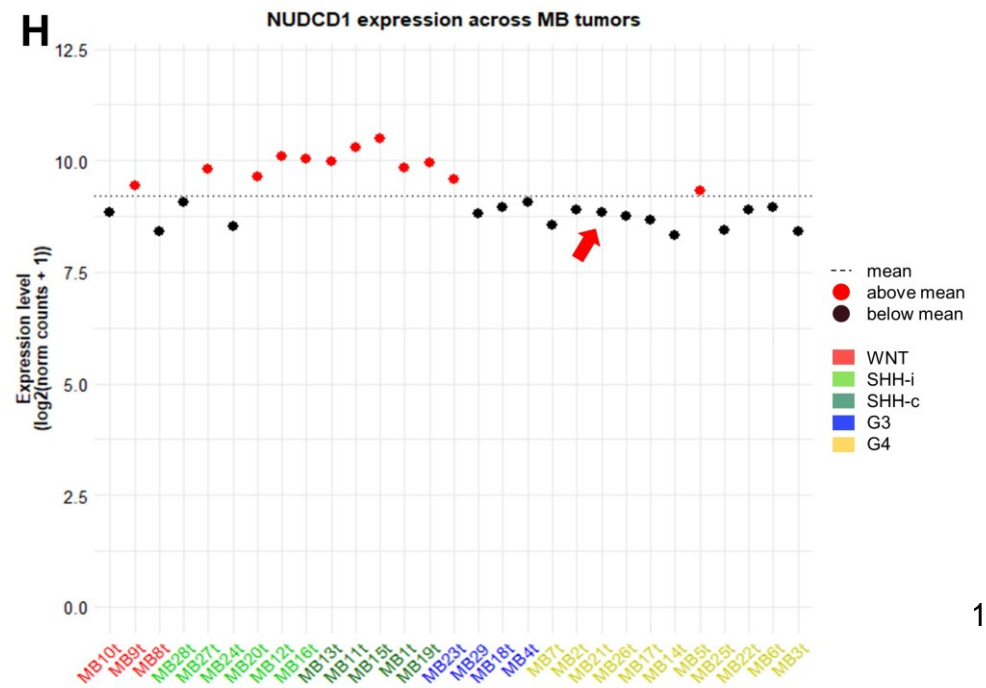
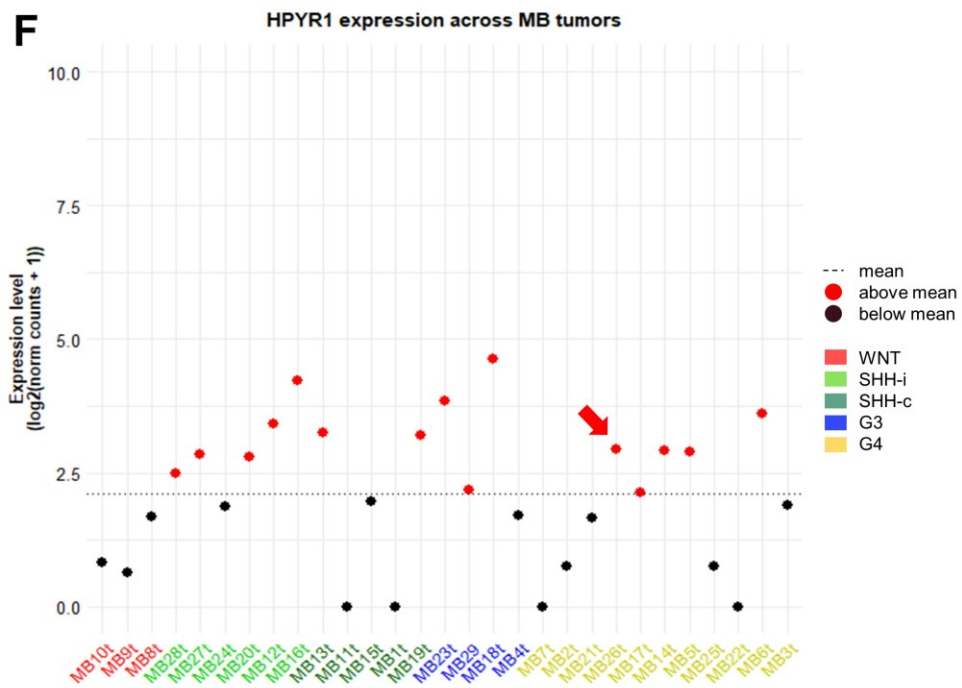
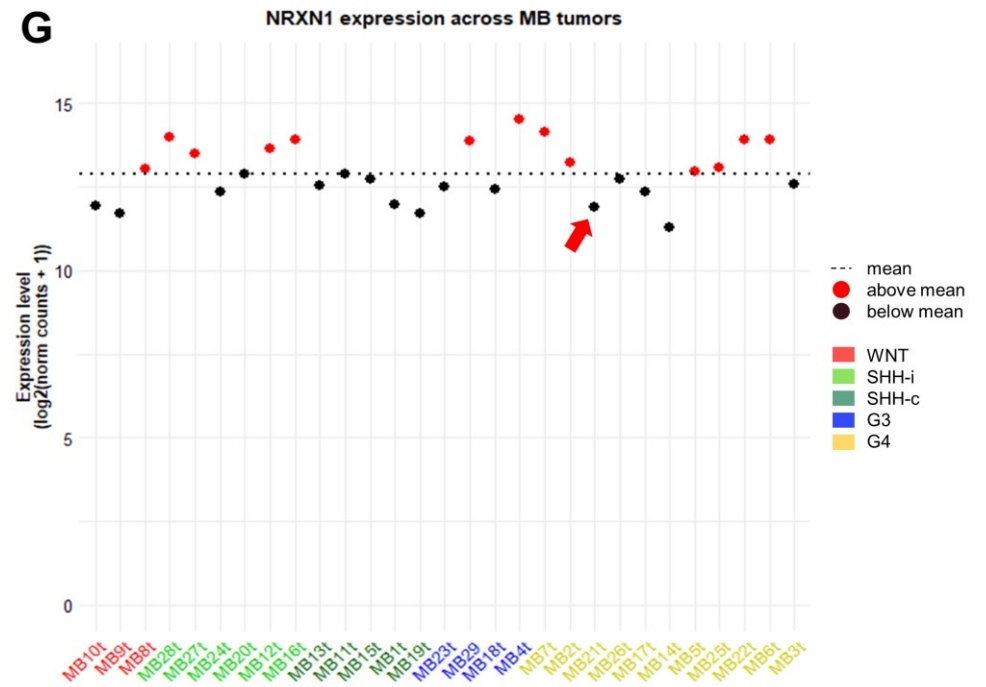
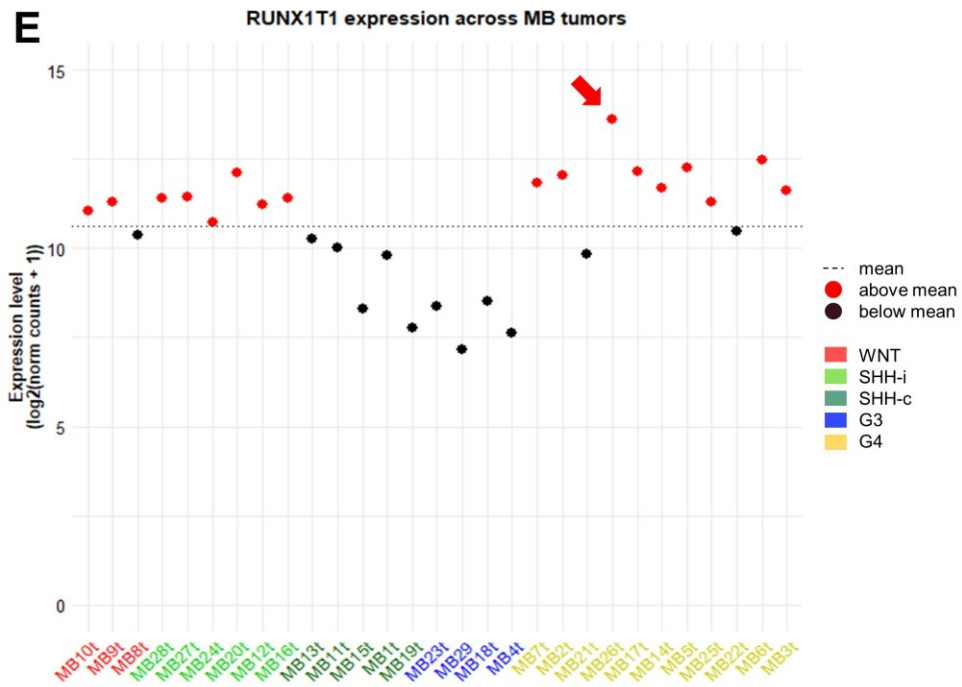
Supplementary Figure II. Novel gene fusions in MB detected by OGM and RNA-Seq of the same tumors. The upper circos plot (left) and SV-view (center-right) are derived from OGM and the lower circos plot (left) and SV-view (center-right) from RNA-Seq data evaluated by Arriba. The circos plots emphasize all structural rearrangements of the analyzed sample, whereas the SV event of interest is designated and both SV views zoom into the specific SV event. In OGM SV view, the reference regions are indicated in green with the respective whole-chromosome on the other rims of the window and in the middle the light blue OGM consensus map (map incorporating the SV), indicating the partial alignment to the reference region. In the Arriba SV view, a schematic visualization of detected transcripts of the fusion partners, their coverage, orientation and the retained exons contributing to the fusion transcript are visualized.

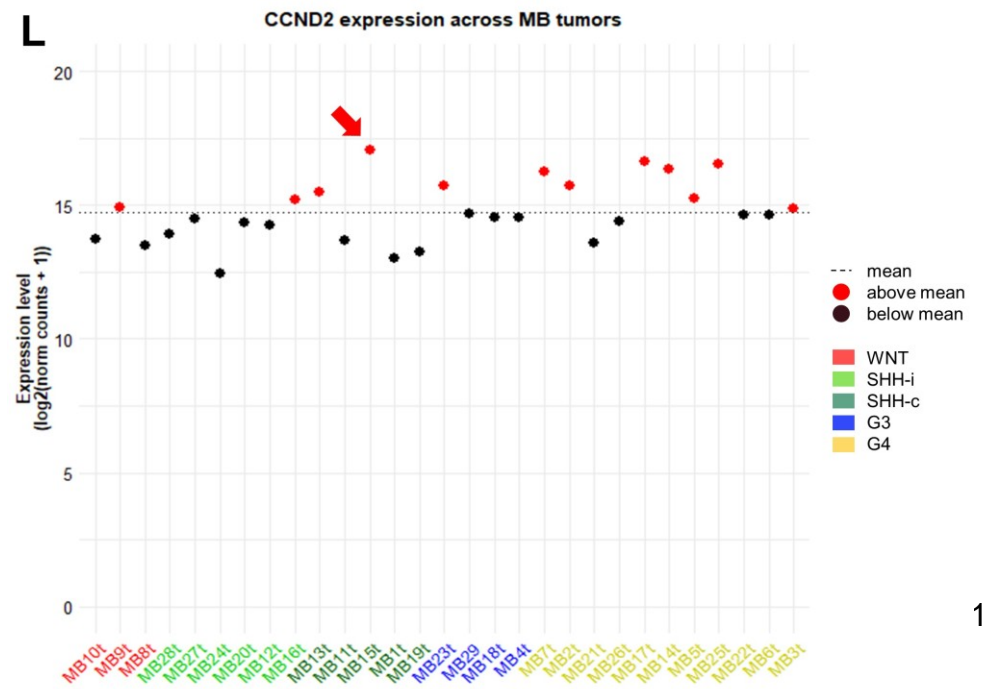
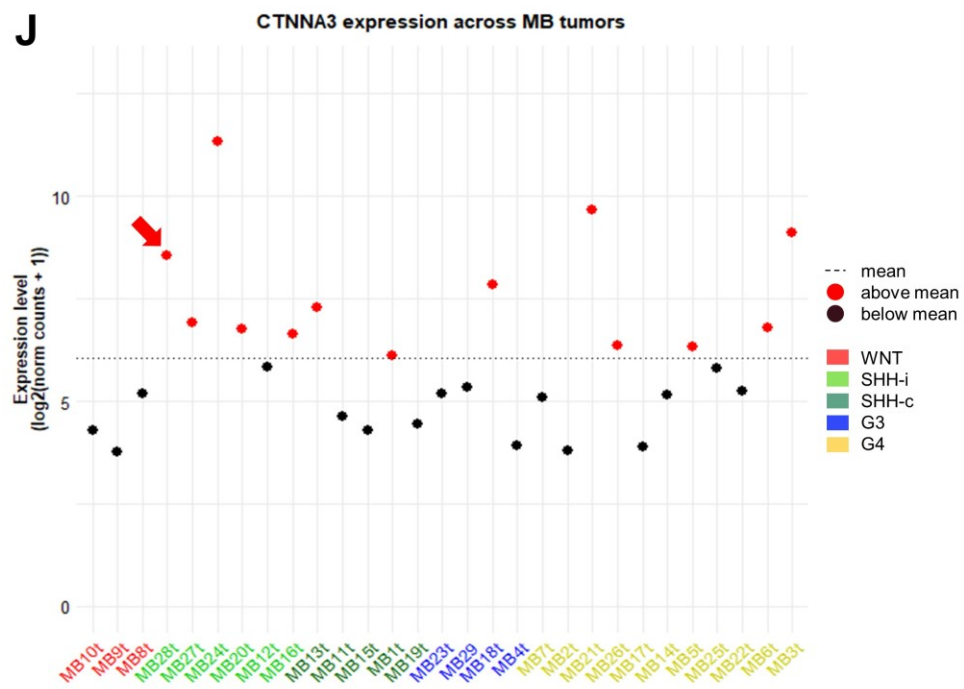
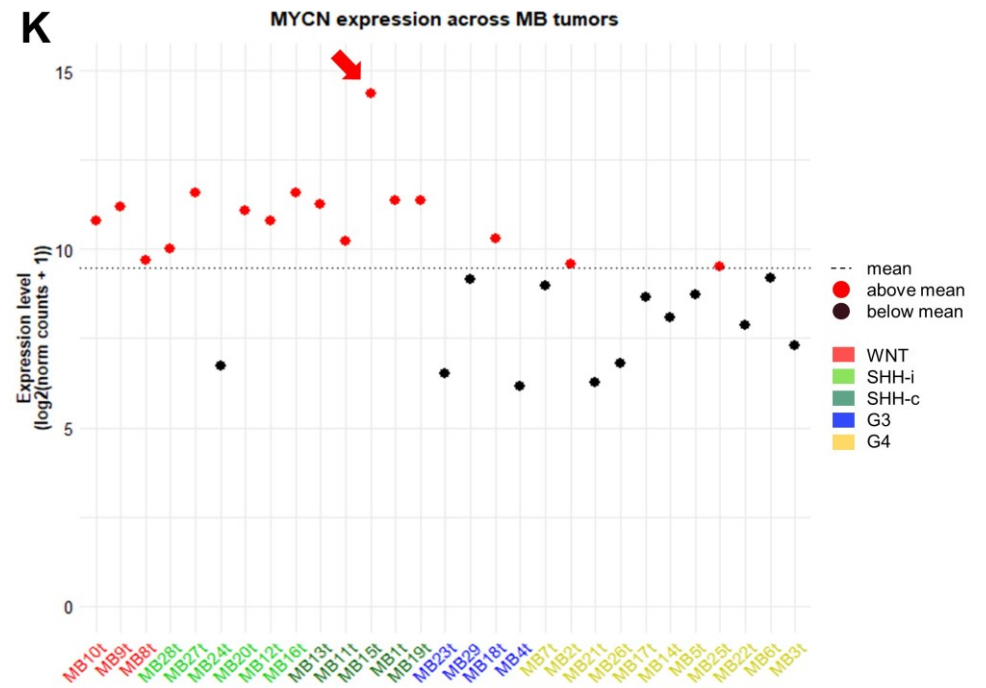
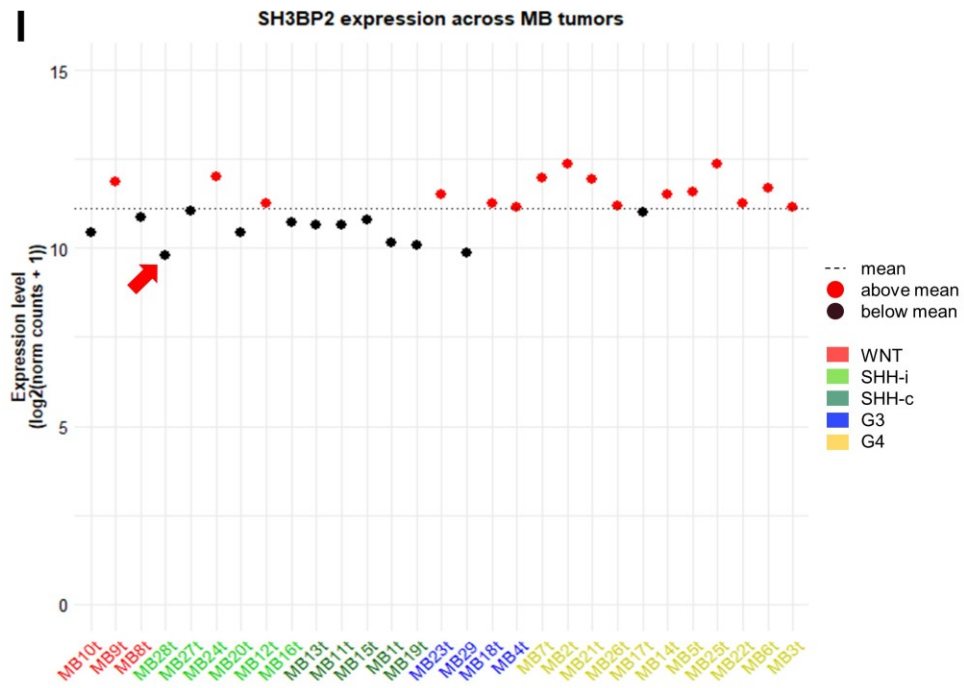
(A) OGM detected in MB21t (MB Group 4) a partially inverted, interchromosomal translocation between the p-arm of chr2 and the q-arm of chr8 overlapping with the genes *NRXN1* and *NUDCD1*. A putative *NRXN1::NUDCD1* gene fusion was predicted by OGM and validated by detection of *NRXN1::NUDCD1* fusion transcripts by Arriba.

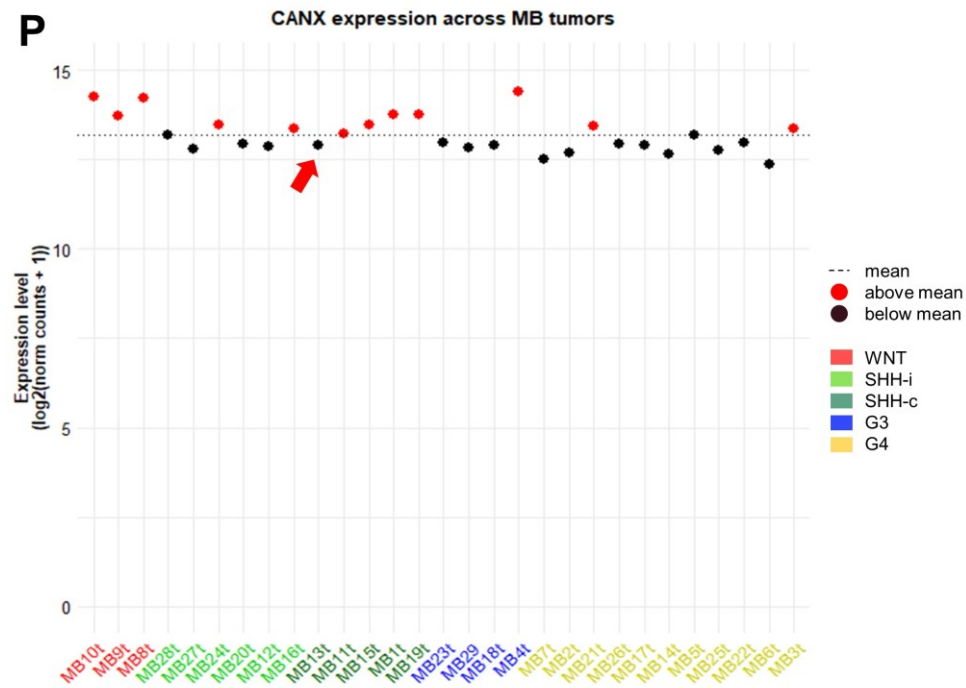
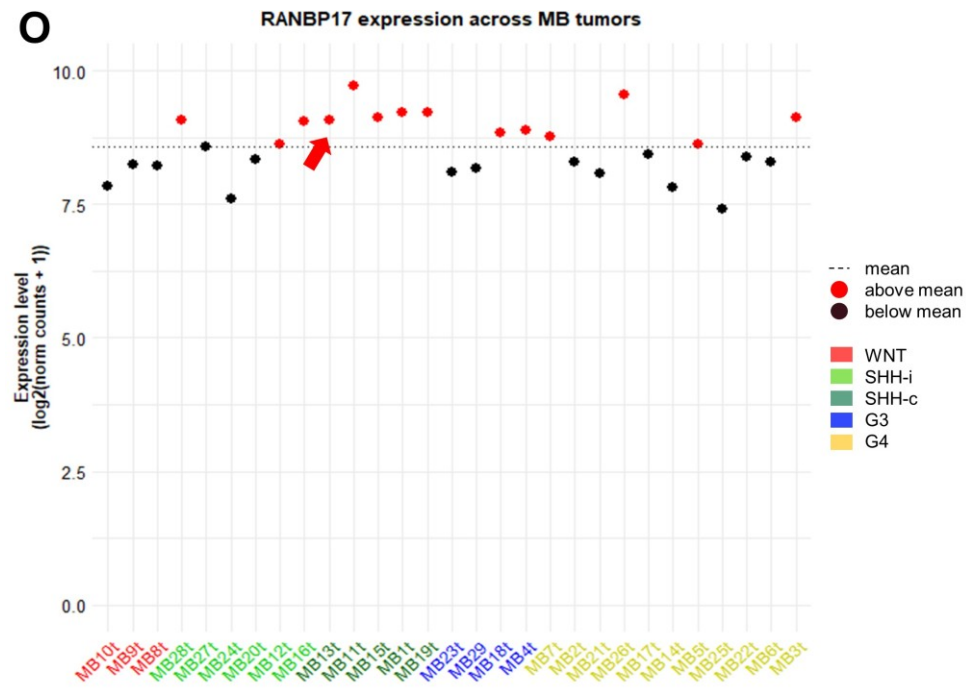
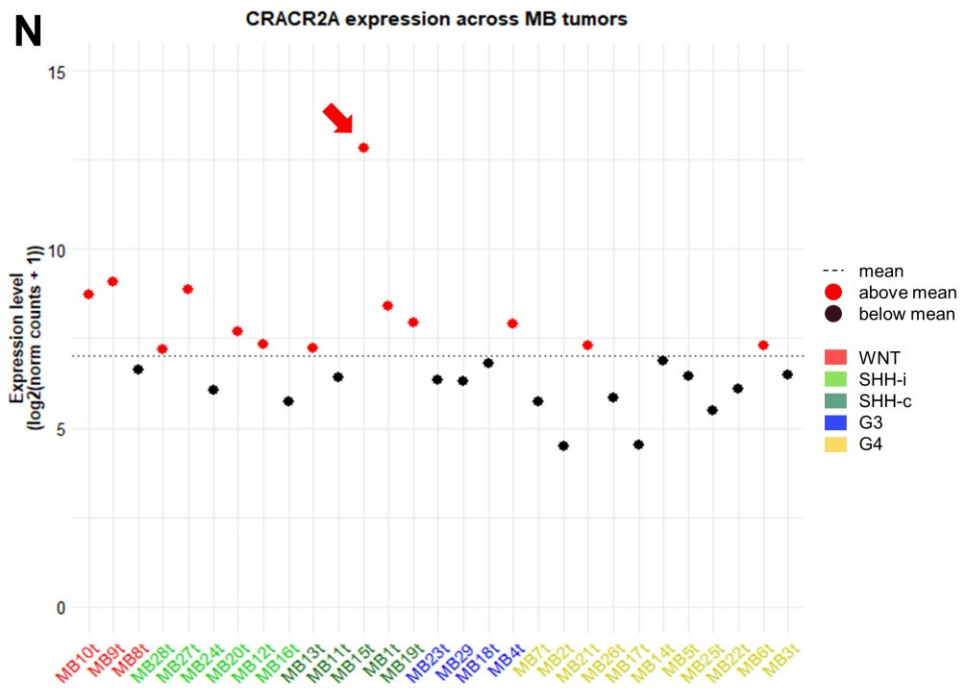
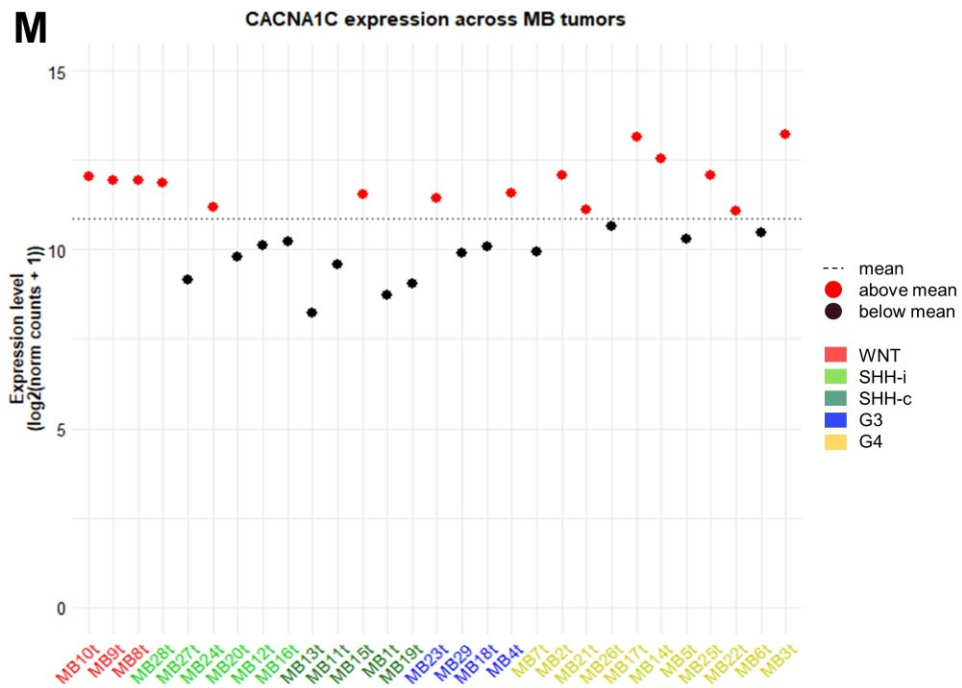
(B) In MB26t (MB Group 4), OGM identified an *NSMCE2::ZEB2* gene fusion, formed through an interchromosomal translocation between the q-arm of chr8 and the q-arm of chr2. Arriba analysis of the RNA-Seq data supported this translocation-dependent gene fusion event.

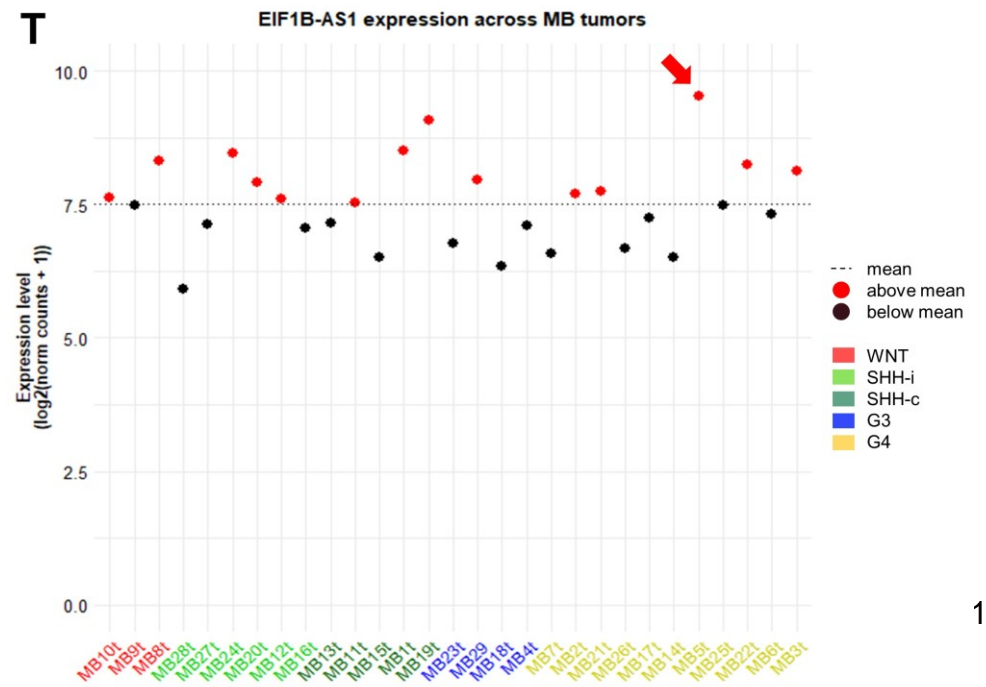
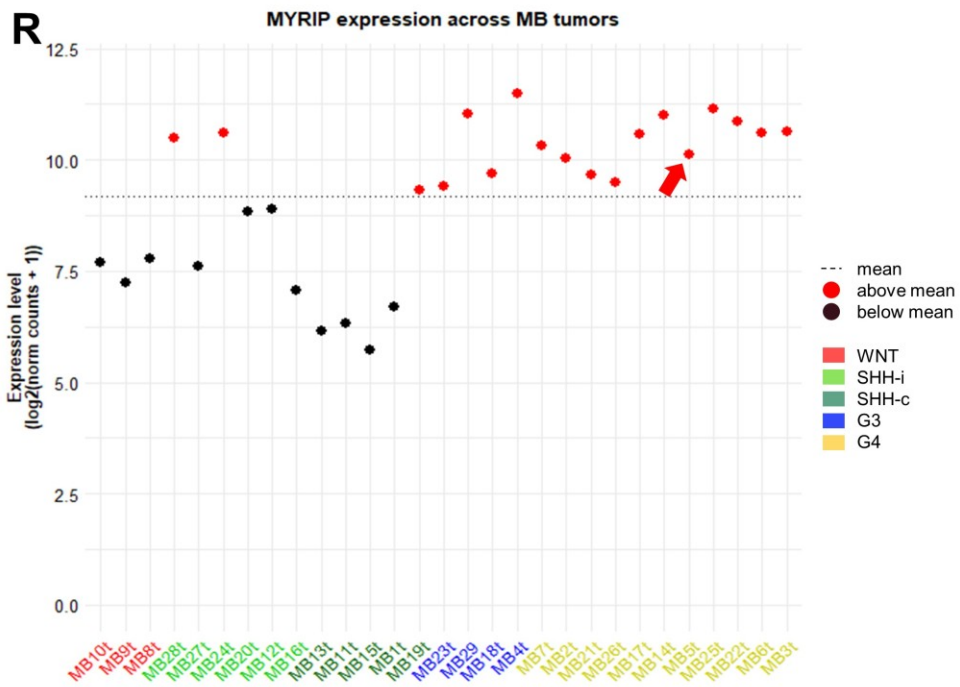
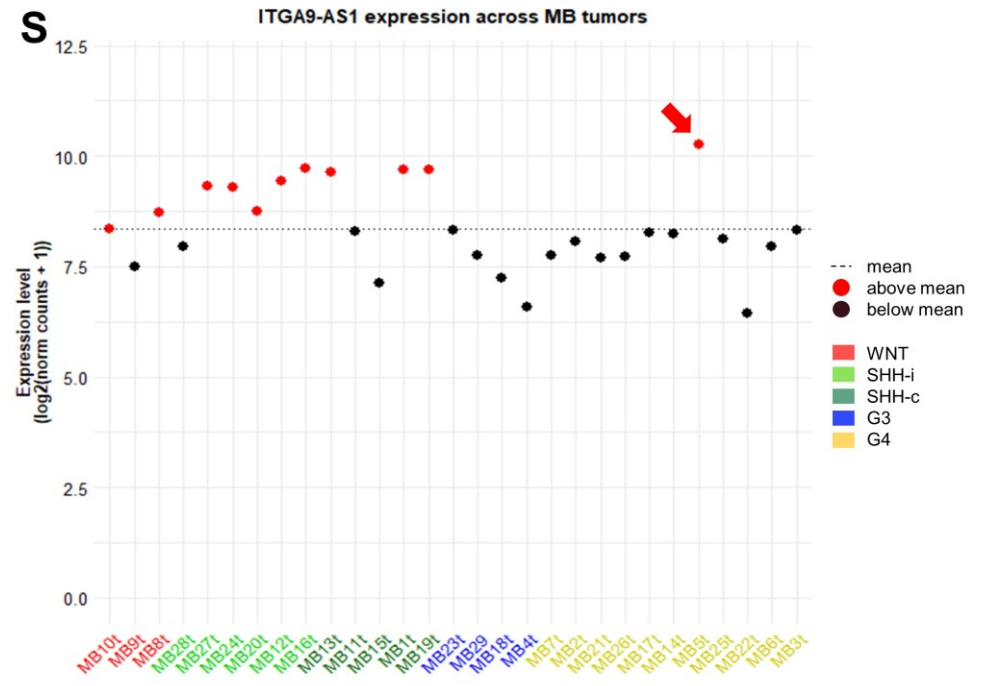
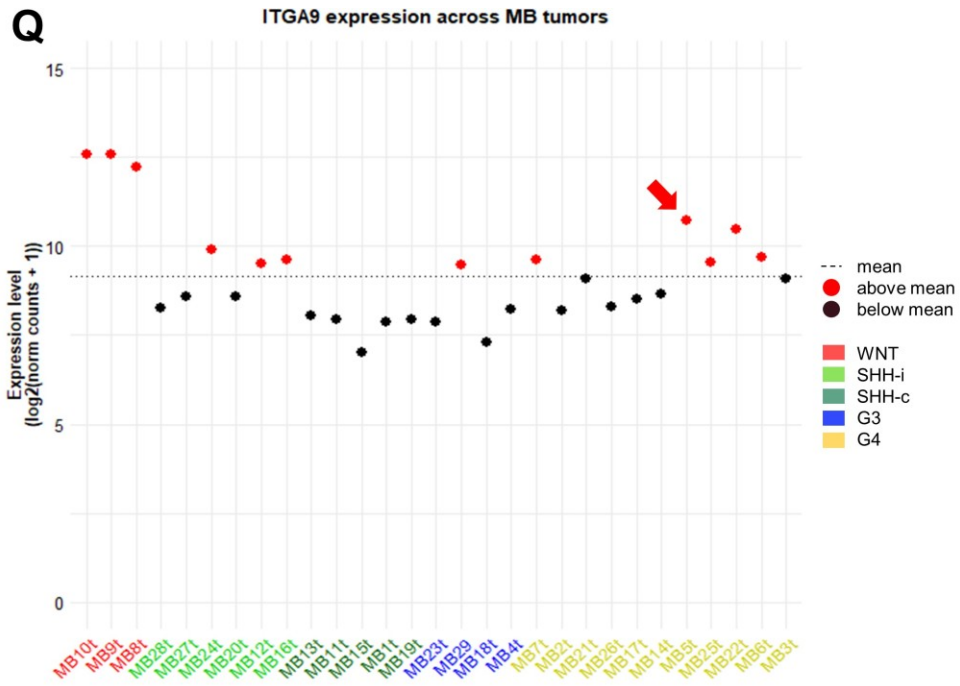
(C) In the same tumor, MB26t (MB Group 4), OGM detected a deletion-associated, intrachromosomal translocation affecting the q-arm of chr8. The breakpoints are within the *RUNX1T1* gene and an intergenic region. Arriba predicted the formation of a partially inverted *RUNX1T1::HPYR1/KCNQ3* fusion transcript from RNA-Seq data.

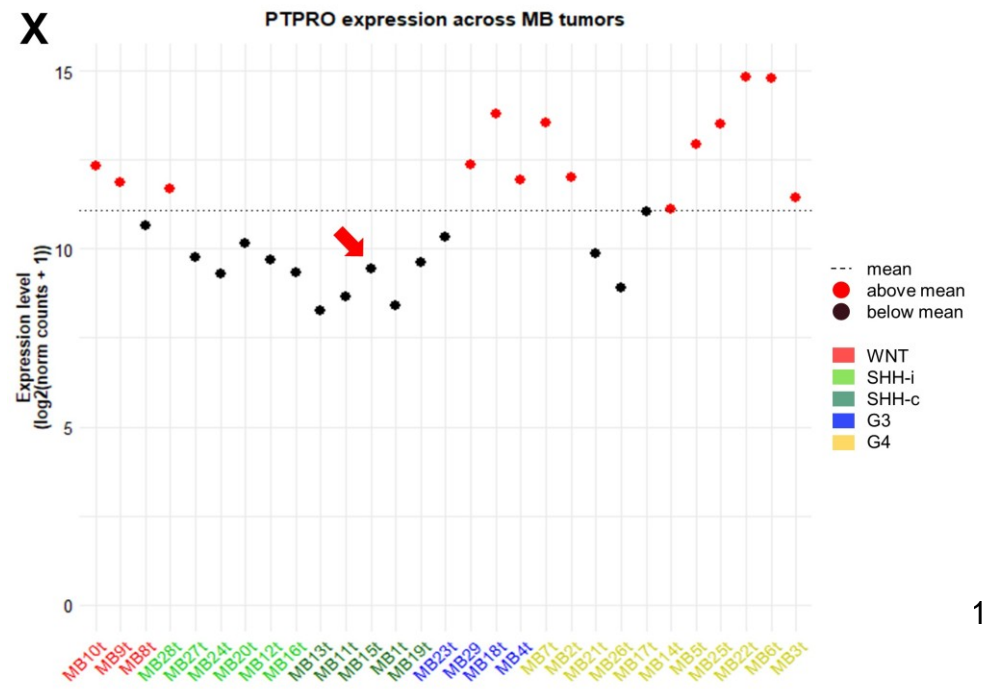
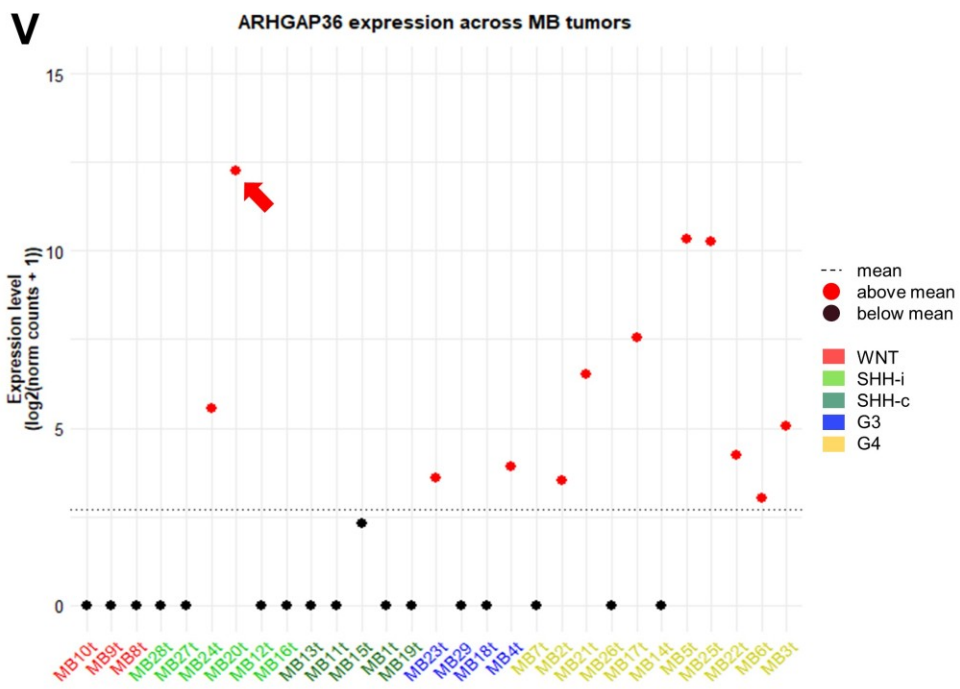
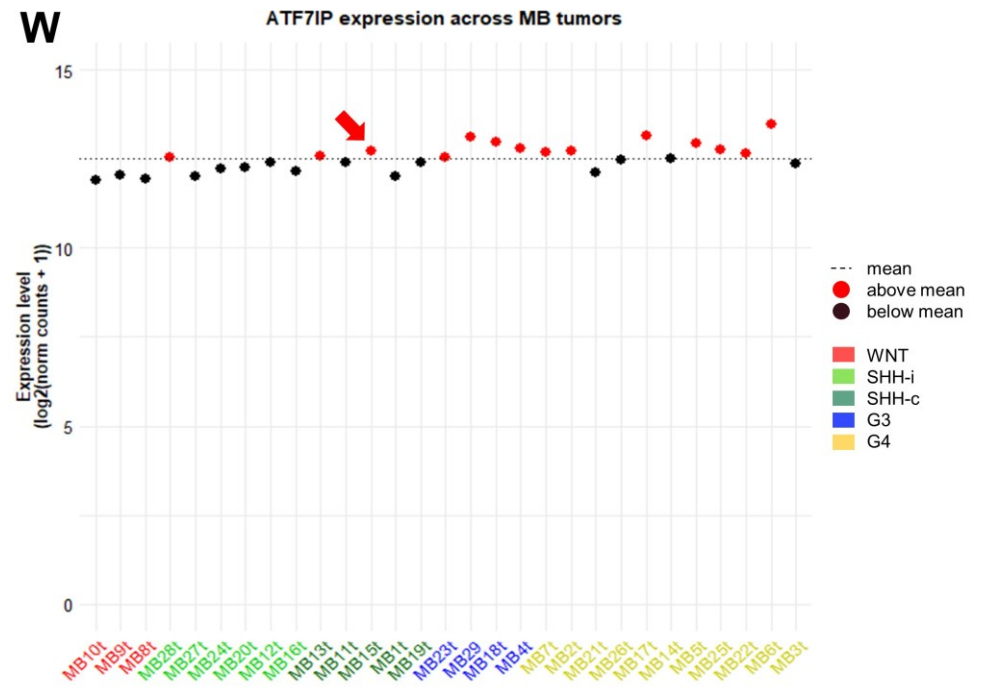
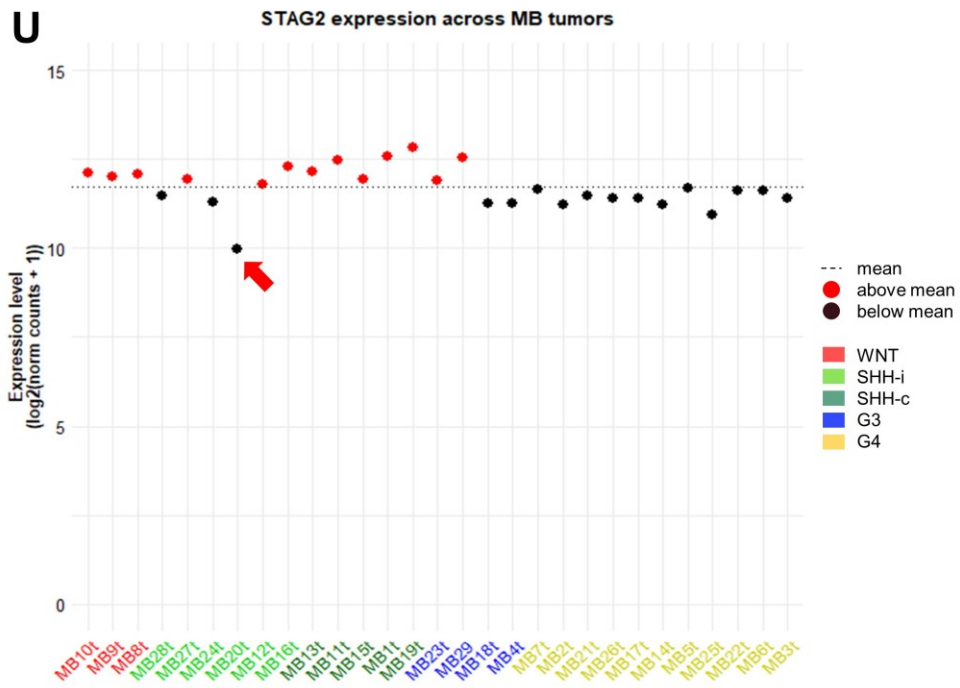












Supplementary Figure III. Expression levels of genes implicated in the MB-associated gene fusions depicted in Figure 23 and Suppl. Figure II across all MB cases and altered genes specifically addressed within the discussion. The expression levels in $\log_2(\text{normalized counts} + 1)$ are plotted vertically against the individual MB samples (horizontally), which are group-wise separated by distinct colours from left to right: *red*, MB WNT; *light-green*, MB SHH–infant; *dark-green*, MB SHH–child; *blue*, MB Group 3; *yellow*, MB Group 4. The red arrows indicate the gene expression levels in the specific MB cases carrying the respective gene fusions or a particularly affected gene. For gene fusions, partners are depicted on the same page, one below the other.

Supplementary Table I. Sample characteristics and Infinium™ MethylationEPIC v1.0 BeadChip-based ("850k EPIC") CNS tumor methylation classification of OGM analyzed MB and ATRT tumors and cell lines. Legend: n.a., not available; MF, methylation family; MC, methylation (sub-)class; *, Capper *et al.* 2018, doi:10.1038/nature26000

Case ID	Tumor ID	Blood ID	CNS Tumor Methylation Classifier v12.8* methylation family (MF)	MF calibrated score	CNS Tumor Methylation Classifier v12.8* methylation (sub-)class (MC)	MC calibrated score
A1	A1t	A1b	-	no score \geq 0.3	-	no score \geq 0.3
A2	A2t	n.a.	Atypical teratoid/rhabdoid tumor	1.00000	Atypical teratoid/rhabdoid tumor, MYC-subtype	0.99999
A3	A3t	n.a.	Atypical teratoid/rhabdoid tumor	1.00000	Atypical teratoid/rhabdoid tumor, SHH-subtype	1.00000
ATRT13808	ATRT13808	n.a.	Atypical teratoid/rhabdoid tumor	0.99075	Atypical teratoid/rhabdoid tumor, MYC-subtype	0.96201
ATRT310-FHTC	ATRT310-FHTC	n.a.	Atypical teratoid/rhabdoid tumor	0.99742	Atypical teratoid/rhabdoid tumor, SHH-subtype	0.99484
ATRT311-FHTC	ATRT311-FHTC	n.a.	Atypical teratoid/rhabdoid tumor	0.59999	Atypical teratoid/rhabdoid tumor, SHH-subtype	0.49257
BT-12 (CVCL_M155)	BT-12	n.a.	Atypical teratoid/rhabdoid tumor	0.92043	Atypical teratoid/rhabdoid tumor, MYC-subtype	0.66682
BT-16 (CVCL_M156)	BT-16	n.a.	Atypical teratoid/rhabdoid tumor	0.85475	Atypical teratoid/rhabdoid tumor, MYC-subtype	0.77544
CHLA-02-ATRT (CVCL_B045)	CHLA-02	n.a.	Atypical teratoid/rhabdoid tumor	0.63227	Atypical teratoid/rhabdoid tumor, MYC-subtype	0.50433
CHLA-04-ATRT (CVCL_0F38)	CHLA-04	n.a.	Atypical teratoid/rhabdoid tumor	0.89967	Atypical teratoid/rhabdoid tumor, SHH-subtype	0.75624
CHLA-05-ATRT (CVCL_AQ41)	CHLA-05	n.a.	Atypical teratoid/rhabdoid tumor	0.88346	Atypical teratoid/rhabdoid tumor, SHH-subtype	0.81965
CHLA-06-ATRT (CVCL_AQ42)	CHLA-06	n.a.	Atypical teratoid/rhabdoid tumor	0.94533	Atypical teratoid/rhabdoid tumor, MYC-subtype	0.85933
CHLA-266 (CVCL_M149)	CHLA-266	n.a.	Atypical teratoid/rhabdoid tumor	0.96190	Atypical teratoid/rhabdoid tumor, MYC-subtype	0.88673
HHU01-ATRT	HHU01-ATRT	n.a.	Atypical teratoid/rhabdoid tumor	0.99574	Atypical teratoid/rhabdoid tumor, SHH-subtype	0.99343
JC-ATRT	JC-ATRT	n.a.	Atypical teratoid/rhabdoid tumor	0.92257	Atypical teratoid/rhabdoid tumor, MYC-subtype	0.82479
VU397	VU397	n.a.	Atypical teratoid/rhabdoid tumor	0.99831	Atypical teratoid/rhabdoid tumor, MYC-subtype	0.99160
MB1	MB1t	MB1b	Medulloblastoma, SHH-activated	0.96042	Medulloblastoma, SHH-activated, subclass 4	0.81579
MB2	MB2t	MB2b	Medulloblastoma, non-WNT/non-SHH activated	0.99729	Medulloblastoma, non-WNT/non-SHH, Group 4 subtype, subclass V	0.92546
MB3	MB3t	MB3b	Medulloblastoma, non-WNT/non-SHH activated	0.99996	Medulloblastoma, non-WNT/non-SHH, Group 4 subtype, subclass VIII	0.99992
MB4	MB4t	n.a.	Medulloblastoma, non-WNT/non-SHH activated	0.94950	Medulloblastoma, non-WNT/non-SHH, Group 3 (no clear subclass)	0.94463

MB5	MB5t	n.a.	Medulloblastoma, non-WNT/non-SHH activated	0.83142	Medulloblastoma, non-WNT/non-SHH, Group 4 (no clear subclass)	0.73809
MB6	MB6t	n.a.	Medulloblastoma, non-WNT/non-SHH activated	0.99866	Medulloblastoma, non-WNT/non-SHH, Group 4 subtype, subclass V	0.90828
MB7	MB7t	n.a.	Medulloblastoma, non-WNT/non-SHH activated	0.99982	Medulloblastoma, non-WNT/non-SHH, Group 4 subtype, subclass VII	0.99867
MB8	MB8t	n.a.	Medulloblastoma, WNT-activated	0.99482	Medulloblastoma, WNT-activated	0.99482
MB9	MB9t	MB9b	Medulloblastoma, WNT-activated	0.99958	Medulloblastoma, WNT-activated	0.99958
MB10	MB10t	n.a.	Medulloblastoma, WNT-activated	0.99988	Medulloblastoma, WNT-activated	0.99988
MB11	MB11t	n.a.	Medulloblastoma, SHH-activated	0.68749	Medulloblastoma, SHH-activated, subclass 4	0.44044
MB12	MB12t	MB12b	Medulloblastoma, SHH-activated	0.99999	Medulloblastoma, SHH-activated, subclass 1	0.99998
MB13	MB13t	n.a.	Medulloblastoma, SHH-activated	0.88277	Medulloblastoma, SHH-activated, subclass 3	0.71393
MB14	MB14t	MB14b	Medulloblastoma, non-WNT/non-SHH activated	0.99996	Medulloblastoma, non-WNT/non-SHH, Group 4 subtype, subclass VIII	0.99993
MB15	MB15t	MB15b	Medulloblastoma, SHH-activated	0.84003	Medulloblastoma, SHH-activated, subclass 3	0.59341
MB16	MB16t	MB16b	Medulloblastoma, SHH-activated	0.99993	Medulloblastoma, SHH-activated, subclass 1	0.99621
MB17	MB17t	MB17b	Medulloblastoma, non-WNT/non-SHH activated	0.99993	Medulloblastoma, non-WNT/non-SHH, Group 4 subtype, subclass VIII	0.99990
MB18	MB18t	MB18b	Medulloblastoma, non-WNT/non-SHH activated	0.99999	Medulloblastoma, non-WNT/non-SHH, Group 3 subtype, subclass IV	0.99990
MB19	MB19t	MB19b	Medulloblastoma, SHH-activated	0.99739	Medulloblastoma, SHH-activated, subclass 4	0.99227
MB20	MB20t	MB20b	Medulloblastoma, SHH-activated	0.99902	Medulloblastoma, SHH-activated, subclass 2	0.95996
MB21	MB21t	MB21b	Medulloblastoma, non-WNT/non-SHH activated	0.99893	Medulloblastoma, non-WNT/non-SHH, Group 4 subtype, subclass V	0.77007
MB22	MB22t	MB22b	Medulloblastoma, non-WNT/non-SHH activated	0.99999	Medulloblastoma, non-WNT/non-SHH, Group 4 subtype, subclass VII	0.99992
MB23	MB23t	MB23b	Medulloblastoma, non-WNT/non-SHH activated	0.99983	Medulloblastoma, non-WNT/non-SHH, Group 3 subtype, subclass II	0.99804
MB24	MB24t	MB24b	Medulloblastoma, SHH-activated	0.99376	Medulloblastoma, SHH-activated, subclass 2	0.63980
MB25	MB25t	n.a.	Medulloblastoma, non-WNT/non-SHH activated	0.99999	Medulloblastoma, non-WNT/non-SHH, Group 4 subtype, subclass VI	0.99949
MB26	MB26t	MB26b	Medulloblastoma, non-WNT/non-SHH activated	0.97570	Medulloblastoma, non-WNT/non-SHH, Group 4 subtype, subclass VIII	0.86189
MB27	MB27t	n.a.	Medulloblastoma, SHH-activated	0.99999	Medulloblastoma, SHH-activated, subclass 1	0.99996
MB28	MB28t	MB28b	Medulloblastoma, SHH-activated	0.99986	Medulloblastoma, SHH-activated, subclass 2	0.99631
MB29	MB29t	n.a.	Medulloblastoma, non-WNT/non-SHH activated	0.99998	Medulloblastoma, non-WNT/non-SHH, Group 3 subtype, subclass IV	0.99821

D283 Med (CVCL_1155)	D283 Med	n.a.	-	no score \geq 0.3	-	no score \geq 0.3
Daoy (CVCL_1167)	Daoy	n.a.	-	no score \geq 0.3	-	no score \geq 0.3
HD-MB03 (CVCL_S506)	HD-MB03	n.a.	Medulloblastoma, non-WNT/non-SHH activated	0.68007	Medulloblastoma, non-WNT/non-SHH, Group 3 subtype, subclass II	0.52865
MED-MEB-8A (CVCL_M137)	MED-MEB-8A	n.a.	-	no score \geq 0.3	-	no score \geq 0.3
ONS-76 (CVCL_1624)	ONS-76	n.a.	-	no score \geq 0.3	-	no score \geq 0.3
UW228-3 (CVCL_0573)	UW228-3	n.a.	-	no score \geq 0.3	-	no score \geq 0.3

Supplementary Table II. OGM-detected copy number alterations in ATRT and MB tumors and cell lines.

Legend: *Chr*, chromosome; *Start*, starting coordinates (GRCh38); *End*, stopping coordinates (GRCh38); *CN*, copy number; *fractCN*, fractional copy number; *fractCNSize*, fractional copy number size with respect to the size of the whole chromosome; *amplif*, amplification.

Tumor ID	Chr	Start	End	CNsize	CNtype	Confidence	fractCN	CN	fractCNSize	Comment
A1t	-	-	-	-	-	-	-	-	-	balanced
A2t	2	17310306	18392791	1082486	gain	1.000	2.584	3	0.005	focal gain on chr2p
A2t	8	8180484	43209791	35029307	loss	1.000	1.342	1	0.241	hemizygous deletion of most chr8p
A3t	X	144375053	145010611	635559	gain	1.000	1.787	2	0.004	focal gain on chrXq
ATRT13808	2	172505755	173188762	683008	loss	1.000	1.549	2	0.003	focal hemizygous deletion on chr2q
ATRT13808	6	24883579	25755476	871898	gain	1.000	2.531	3	0.005	focal gain on chr6p
ATRT-310-FHTC	4	15071380	17301236	2229857	loss	1.000	0.920	1	0.012	focal hemizygous deletion on chr4p
ATRT-310-FHTC	6	135674891	141904905	6230015	loss	1.000	0.953	1	0.037	partial hemizygous deletion on chr6q
ATRT-310-FHTC	9	13360758	14340804	980047	loss	1.000	1.023	1	0.007	focal hemizygous deletion on chr9q
ATRT-311-FHTC	3	63517091	66566485	3049395	loss	1.000	1.026	1	0.015	partial hemizygous deletion on chr3p
BT-12	5	19314	46400789	46381475	gain	1.000	2.981	3	0.256	chr5p trisomy
BT-12	5	112491823	113332944	841122	gain	1.000	3.822	4	0.005	focal amplif on chr5q
BT-12	5	113824858	181472714	67647856	gain	1.000	2.932	3	0.373	partial gain on chr5q
BT-12	6	160715856	161465908	750053	gain	1.000	2.851	3	0.004	focal gain onchr 6q
BT-12	10	69919558	73025737	3106180	gain	1.000	3.095	3	0.023	partial gain on chr10q
BT-16	15	22478126	23367636	889511	gain	1.000	2.991	3	0.009	focal gain on chr15q
CHLA-02	5	174524120	178388450	3864330	loss	0.998	1.070	1	0.021	partial hemizygous deletion on chr5q
CHLA-02	19	38484027	39110436	626410	loss	0.991	1.398	1	0.011	focal hemizygous deletion on chr19q
CHLA-02	20	14581221	15239237	658017	loss	1.000	1.107	1	0.010	focal hemizygous deletion on chr20p
CHLA-02	22	22183401	23997045	1813645	loss	1.000	0.000	0	0.036	focal homozygous deletion on 22q

CHLA-04	-	-	-	-	-	-	-	-	-	balanced
CHLA-05	-	-	-	-	-	-	-	-	-	balanced
CHLA-06	8	3397114	141282390	137885276	loss	1.000	1.070	1	0.950	chr8 monosomy
CHLA-06	14	33045768	33813012	767245	loss	1.000	1.244	1	0.007	focal hemizygous deletion on chr14q
CHLA-266	1	144721959	145278709	556751	gain	1.000	2.767	3	0.002	focal gain on chr1q
CHLA-266	5	166098910	166972359	873450	loss	1.000	0.961	1	0.005	focal hemizygous deletion on chr5q
CHLA-266	22	15809687	50805587	34995900	loss	1.000	1.004	1	0.689	chr22 monosomy
HUU01-ATRT	4	92254851	93477963	1223113	loss	1.000	1.152	1	0.006	focal hemizygous deletion on chr4q
HUU01-ATRT	X	144410593	145023870	613278	gain	1.000	1.967	2	0.004	focal gain on chrXq
JC-ATRT	17	44369993	50562513	3991156	loss	1.000	0.922	1	0.048	partial hemizygous deletion on chr17q
JC-ATRT	22	21674056	23796274	2122219	loss	1.000	0.000	0	0.042	focal homozygous deletion on chr22q
JC-ATRT	22	23818528	29193141	5374614	loss	1.000	1.054	1	0.106	partial hemizygous deletion on chr22q
JC-ATRT	X	81267090	82218714	951625	loss	1.000	1.035	1	0.006	focal hemizygous deletion on chrXq
VU397	5	165469769	166833217	1363449	loss	1.000	1.348	1	0.008	focal hemizygous deletion on chr5q
VU397	11	83514413	84059562	545150	loss	1.000	1.110	1	0.004	focal hemizygous deletion on chr11q
MB1t	1	92479502	94918675	2439174	loss	1.000	1.499	1	0.010	focal hemizygous deletion on chr1p
MB1t	4	49489158	190202564	140713406	loss	0.999	1.694	2	0.740	chr4q monosomy
MB1t	9	66262739	95380097	29117359	loss	1.000	1.528	2	0.210	partial hemizygous deletion on chr9q
MB1t	9	95381401	98655497	3274097	loss	1.000	0.544	1	0.024	partial homozygous deletion on chr9q
MB1t	9	98656730	128352346	29695617	loss	1.000	1.518	2	0.215	partial hemizygous deletion on chr9q
MB1t	9	128375602	132955523	4579922	loss	1.000	0.564	1	0.033	partial homozygous deletion on chr9q
MB1t	11	23469533	50815234	27345702	loss	1.000	1.520	2	0.202	partial hemizygous deletion on chr11p
MB1t	12	104223034	133263960	29040927	gain	1.000	2.504	3	0.218	partial gain on chr12q
MB1t	14	19189529	96618829	77429300	loss	1.000	1.458	2	0.723	chr14 monosomy
MB1t	17	66653	17490490	17423837	loss	1.000	1.511	1	0.209	partial hemizygous deletion on chr17p
MB1t	18	18868	80256374	80237506	loss	1.000	1.530	2	0.998	chr18 monosomy
MB1t	X	3827829	52922365	49094536	loss	1.000	1.385	1	0.315	chrXp monosomy
MB2t	4	12985	30433573	30420588	gain	1.000	2.932	3	0.160	partial gain on chr4p
MB2t	7	1568879	159334984	157766105	gain	1.000	2.967	3	0.990	chr7 trisomy
MB2t	11	60457	37475052	37414596	loss	1.000	1.044	1	0.277	partial hemizygous deletion on chr11p
MB2t	17	66653	19154549	19087897	loss	1.000	1.026	1	0.230	complex; isochr17q
MB2t	17	19168519	83246392	64077873	gain	1.000	2.976	3	0.770	complex; isochr17q
MB3t	17	66653	19154549	19087897	loss	1.000	1.051	1	0.230	complex; isochr17q
MB3t	17	19168519	81131977	61963458	gain	1.000	2.956	3	0.770	complex; isochr17q
MB3t	Y	-	-	51838687	loss	1.000	0.064	0	0.906	homozygous deletion of chrY
MB4t	1	6372303	67762422	61390119	loss	1.000	1.372	1	0.247	complex; partial hemizygous deletion on chr1p
MB4t	1	67765994	190695431	122929437	gain	0.999	2.409	2	0.494	complex; partial gain on chr1pq
MB4t	1	190703764	248633312	57929548	gain	1.000	3.321	3	0.233	complex; partial gain on chr1q

MB4t	2	144491826	150069658	5577833	gain	0.997	2.282	2	0.023	partial gain on chr2q
MB4t	2	162030869	165548175	3517307	gain	0.992	2.308	2	0.015	partial gain on chr2q
MB4t	3	859173	85664618	84805445	gain	1.000	2.910	3	0.428	complex; chr3p trisomy
MB4t	3	85666015	198230596	112564581	loss	1.000	1.438	1	0.568	complex; chr3q monosomy
MB4t	5	12284578	176080060	163795482	gain	0.999	2.324	2	0.902	chr5 trisomy
MB4t	6	61265511	168468413	107202902	loss	0.999	1.631	2	0.628	chr6q monosomy
MB4t	7	105936194	106563716	627523	gain	1.000	3.330	3	0.004	focal gain on chr7q
MB4t	8	8164637	12005087	3840451	loss	0.998	1.715	2	0.027	complex; partial hemizygous deletion on chr8p
MB4t	8	22860296	31333880	8473585	loss	0.999	1.713	2	0.058	complex; partial hemizygous deletion on chr8p
MB4t	8	35590290	54065505	18475215	gain	1.000	2.899	3	0.127	complex; partial gain on chr8p
MB4t	8	54067337	58704017	4636681	loss	0.999	1.695	2	0.032	complex; partial hemizygous deletion on chr8q
MB4t	8	119638971	141269265	21630295	loss	0.995	1.752	2	0.149	complex; partial hemizygous deletion on chr8q
MB4t	9	14566	27286872	27272306	loss	1.000	1.254	1	0.197	complex; partial hemizygous deletion on chr9p
MB4t	9	27291359	39123743	11832384	gain	1.000	2.674	3	0.086	complex; partial gain on chr9p
MB4t	9	39126935	39639985	513051	loss	1.000	1.155	1	0.004	complex; focal hemizygous deletion on chr9p
MB4t	9	69446871	127659395	58212524	gain	1.000	2.627	3	0.421	complex; partial gain on chr9q
MB4t	10	18514	132700753	132682239	loss	1.000	1.401	1	0.992	chr10 monosomy
MB4t	13	18900644	111648249	92747605	gain	0.999	2.478	2	0.811	chr13 trisomy
MB4t	13	90684670	92265557	1580887	gain	1.000	19.537	20	0.014	focal amplif on chr13q
MB4t	16	2174972	90224751	88049779	loss	1.000	1.164	1	0.975	chr16 monosomy
MB4t	17	7119808	22067787	14947979	loss	1.000	1.293	1	0.180	complex; isochr17q
MB4t	17	28918683	78190794	49272111	gain	0.999	2.607	3	0.592	complex; isochr17q
MB4t	18	1021778	72327628	71305850	gain	0.999	2.458	2	0.887	chr18 trisomy
MB4t	19	19887097	20940723	1053627	gain	0.999	2.439	2	0.018	focal gain on chr19p
MB4t	X	71507686	73173899	1666214	loss	0.999	0.803	1	0.011	focal hemizygous deletion on chrXq
MB4t	Y	-	-	49501714	loss	1.000	0.595	1	0.865	homozygous deletion of chrY
MB5t	3	37845688	40066516	2220828	gain	0.999	4.430	4	0.011	focal amplif on chr3p
MB5t	6	76216	169950341	169874125	gain	0.998	2.272	2	0.995	chr6 trisomy
MB5t	7	1299879	159334984	158035105	gain	1.000	2.493	2	0.992	chr7 trisomy
MB5t	8	12337221	123687282	111350061	loss	0.999	1.714	2	0.767	chr8 monosomy
MB5t	17	66653	18258939	18192286	loss	1.000	1.090	1	0.219	complex; isochr17q
MB5t	17	19168519	83246392	64077873	gain	1.000	2.995	3	0.770	complex; isochr17q
MB5t	20	70156	64333718	64263562	loss	0.999	1.655	2	0.997	chr20 monosomy
MB6t	2	15924	7025026	7009103	gain	1.000	3.063	3	0.029	focal gain on chr2p
MB6t	3	12920	43754033	43741114	gain	1.000	2.531	3	0.221	complex; partial gain on chr3p
MB6t	3	126057802	198230596	72172794	loss	1.000	1.004	1	0.364	complex; partial hemizygous deletion on chr3q
MB6t	4	1835991	188383769	186547778	gain	0.999	2.859	3	0.981	chr4 trisomy
MB6t	5	148625237	181472714	32847478	loss	1.000	1.024	1	0.181	partial hemizygous deletion on chr5q

MB6t	7	155424291	159334984	3910694	gain	1.000	2.982	3	0.025	focal gain on chr7q
MB6t	8	61805	21288819	21227014	loss	1.000	1.026	1	0.146	partial hemizygous deletion on chr8p
MB6t	10	18514	133785266	133766752	loss	1.000	1.034	1	0.999	chr10 monosomy
MB6t	11	60457	46196930	46136474	loss	1.000	1.027	1	0.342	chr11p monosomy
MB6t	12	103438531	132112844	28674314	gain	1.000	2.902	3	0.215	partial gain on chr12q
MB6t	13	29641658	114352102	84710444	loss	1.000	1.092	1	0.741	chr13 monosomy
MB6t	15	46407972	101976509	55568537	gain	1.000	2.748	3	0.545	partial gain on chr15q
MB6t	17	1298266	19154549	17856284	loss	1.000	1.041	1	0.214	complex; isochr17q
MB6t	17	19168519	81131977	61963458	gain	1.000	3.003	3	0.744	complex; isochr17q
MB7t	3	12920	198230596	198217676	loss	1.000	1.630	2	0.999	chr3 monosomy
MB7t	7	6726172	159334984	152608812	gain	1.000	2.452	2	0.958	chr7 trisomy
MB7t	8	61805	145076125	145014320	loss	1.000	1.218	1	0.999	chr8 monosomy
MB7t	9	725826	138334464	137608638	loss	1.000	1.646	2	0.994	chr9 monosomy
MB7t	10	99161779	106574388	7412610	loss	0.997	1.781	2	0.055	partial hemizygous deletion on chr10q
MB7t	14	24445861	105710125	81264264	gain	1.000	2.447	2	0.760	chr14 monosomy
MB7t	16	887824	90224751	89336927	loss	1.000	1.619	2	0.989	chr16 monosomy
MB7t	17	8447808	72413150	63965342	gain	0.999	2.402	2	0.768	chr17 trisomy
MB7t	18	292896	80256374	79963478	gain	1.000	3.268	3	0.995	chr18 trisomy
MB7t	20	70156	61861320	61791164	gain	0.999	2.372	2	0.959	chr20 trisomy
MB7t	21	12406577	46697230	34290653	loss	0.999	1.612	2	0.734	chr21 monosomy
MB7t	22	18838071	50805587	31967517	loss	0.999	1.570	2	0.630	chr22 monosomy
MB7t	Y	-	-	52675821	loss	1.000	0.462	0	0.921	homozygous deletion of chrY
MB8t	6	361446	170739897	170378451	loss	1.000	0.988	1	0.998	chr6 monosomy
MB8t	16	66848095	69308976	2460882	loss	1.000	1.014	1	0.027	focal hemizygous deletion on chr16q
MB8t	X	2398562	155778570	153380008	loss	1.000	1.000	1	0.983	chrX monosomy
MB9t	6	76216	170739897	170663681	loss	1.000	1.032	1	0.999	chr6 monosomy
MB9t	11	2157135	135069565	132912430	loss	1.000	1.512	2	0.984	chr11 monosomy
MB9t	Y	-	-	52669805	loss	1.000	0.476	0	0.920	homozygous deletion of chrY
MB10t	6	76216	170739897	170663681	loss	1.000	1.025	1	0.999	chr6 monosomy
MB10t	17	7247855	7857671	609817	loss	0.999	0.940	1	0.007	focal hemizygous deletion on chr17p
MB11t	2	87136416	87736106	599691	gain	0.999	2.596	3	0.003	focal gain on chr2p
MB11t	9	39297411	39817227	519817	gain	1.000	3.544	4	0.004	focal amplif on chr9p
MB12t	2	298743	240127794	239829051	gain	0.999	2.537	3	0.990	chr2 trisomy
MB12t	3	12920	198230596	198217676	gain	1.000	2.484	2	0.999	chr3 trisomy
MB13t	1	241009879	245389674	4379796	loss	1.000	1.035	1	0.018	partial hemizygous deletion on chr1q
MB13t	5	171092165	179711265	8619100	loss	1.000	0.971	1	0.048	partial hemizygous deletion on chr5q
MB13t	13	17542017	114352102	96810085	gain	0.999	2.301	2	0.847	chr13 trisomy
MB13t	16	29527758	30202372	674615	loss	1.000	0.957	1	0.008	focal hemizygous deletion on chr16p

MB13t	17	6582387	7086426	504040	loss	1.000	1.027	1	0.006	focal hemizygous deletion on chr17p
MB14t	11	642511	48370378	47727868	loss	1.000	1.019	1	0.353	complex; chr11p monosomy
MB14t	11	102213184	134752096	32538913	gain	1.000	3.000	3	0.240	complex; partial gain on chr11q
MB14t	15	31639515	32311023	671509	gain	1.000	2.932	3	0.007	focal gain on chr15q
MB14t	17	392403	19168519	18776116	loss	1.000	0.957	1	0.226	complex; isochr17q
MB14t	17	19209737	81131977	61922240	gain	1.000	2.970	3	0.744	complex; isochr17q
MB14t	X	2699955	155828802	153128847	loss	1.000	1.004	1	0.981	chrX monosomy
MB15t	1	7022978	120497627	113474649	gain	0.999	2.321	2	0.456	chr1p trisomy
MB15t	2	14574554	17636935	3062381	gain	1.000	134.222	134	0.013	partial amplif on chr2p
MB15t	3	12920	90544141	90531222	loss	1.000	1.257	1	0.457	chr3p monosomy
MB15t	5	49709239	180882284	131173045	loss	1.000	1.255	1	0.723	chr5q monosomy
MB15t	5	97223181	98607019	1383839	loss	1.000	0.488	0	0.008	focal homozygous deletion on chr5q
MB15t	6	166452816	168651688	2198873	loss	1.000	0.999	1	0.013	focal hemizygous deletion on chr6q
MB15t	9	972570	38885219	37912649	gain	1.000	2.963	3	0.274	complex; isochr9p?
MB15t	9	67868484	133537181	65668697	loss	1.000	1.003	1	0.475	complex; isochr9p?
MB15t	10	18514	39512270	39493756	gain	1.000	2.970	3	0.295	complex; isochr10p?
MB15t	10	42280969	132340952	90059983	loss	1.000	0.968	1	0.673	complex; isochr10p?
MB15t	11	23845862	50722834	26876972	loss	0.998	1.705	2	0.200	partial hemizygous deletion on chr11pq
MB15t	12	2992821	3523546	530726	gain	1.000	12.772	13	0.004	focal amplif on chr12p
MB15t	13	105875150	107165573	1290424	loss	1.000	1.289	1	0.011	focal hemizygous deletion on chr13q
MB15t	17	6500989	7950571	1449583	loss	1.000	0.962	1	0.017	focal hemizygous deletion on chr17p
MB15t	X	29298321	29898098	599778	loss	1.000	0.227	0	0.004	focal homozygous deletion on chrXp
MB16t	-	-	-	-	-	-	-	-	-	-
MB17t	7	119216017	120141430	925414	gain	1.000	2.693	3	0.006	focal gain on chr7q
MB17t	17	66653	19154549	19087897	loss	1.000	0.994	1	0.229	complex; isochr17q
MB17t	17	19168519	81097586	61929067	gain	1.000	2.939	3	0.744	complex; isochr17q
MB18t	1	4371153	27683111	23311958	loss	1.000	1.374	1	0.094	partial hemizygous deletion on chr1p
MB18t	2	4015119	26524207	22509088	gain	1.000	2.348	2	0.093	partial gain on chr2p
MB18t	2	153669491	223534587	69865096	gain	1.000	2.381	2	0.288	partial gain on chr2q
MB18t	3	12920	198230596	198217676	loss	1.000	1.295	1	0.999	chr3 monosomy
MB18t	4	3879140	42185697	38306557	loss	1.000	1.577	2	0.201	partial hemizygous deletion on chr4p
MB18t	5	153784598	181080612	27296014	loss	0.999	1.423	2	0.150	partial hemizygous deletion on chr5q
MB18t	6	130753060	167328435	36575375	loss	0.997	1.743	2	0.214	partial hemizygous deletion on chr6q
MB18t	7	7988386	67887440	59899054	gain	1.000	2.415	2	0.376	partial gain on chr7p
MB18t	7	67895478	157625834	89730356	gain	1.000	3.040	3	0.563	chr7q trisomy
MB18t	8	1611664	141060360	139448696	loss	1.000	1.309	1	0.961	chr8 monosomy
MB18t	9	465528	33207974	32742446	gain	1.000	2.496	2	0.237	partial gain on chr9p
MB18t	9	69346619	125967657	56621038	gain	1.000	2.550	3	0.409	partial gain on chr9q

MB18t	10	770633	131610141	130839508	loss	1.000	1.282	1	0.978	chr10 monosomy
MB18t	11	3743680	112628476	108884796	loss	1.000	1.225	1	0.806	chr11 monosomy
MB18t	13	18480661	112628476	94147815	loss	1.000	1.336	1	0.823	chr13 monosomy
MB18t	16	2174972	50487730	48312758	loss	1.000	1.454	1	0.535	chr16p monosomy
MB18t	16	50492119	88100298	37608179	loss	1.000	0.724	1	0.416	homozygous deletion on chr16q
MB18t	17	7140975	10176906	3035931	loss	0.998	1.465	1	0.037	partial hemizygous deletion on chr17p
MB18t	17	47485955	48111891	625937	loss	0.998	1.532	2	0.008	focal hemizygous deletion on chr17q
MB18t	19	4734667	57963526	53228859	loss	1.000	1.084	1	0.908	chr19 monosomy
MB18t	20	70156	61861320	61791164	loss	1.000	1.219	1	0.959	chr20 monosomy
MB18t	21	31858430	42015742	10157313	loss	0.996	1.334	1	0.218	partial hemizygous deletion on chr21q
MB18t	X	2354773	155799882	153445109	loss	1.000	0.725	1	0.983	homozygous deletion of chrX
MB19t	1	216789415	221089862	4300447	loss	1.000	1.558	2	0.017	partial hemizygous deletion on chr1q
MB19t	2	568536	241486378	240917842	loss	1.000	1.583	2	0.995	chr2 monosomy
MB19t	9	66725106	133526602	66801496	loss	1.000	1.491	1	0.483	chr9q monosomy
MB19t	11	2530605	134858219	132327614	loss	1.000	1.601	2	0.980	chr11 monosomy
MB19t	14	19761872	104061089	84299217	loss	1.000	1.498	1	0.788	chr14 monosomy
MB19t	16	2853516	85069307	82215791	loss	1.000	1.569	2	0.910	chr16 monosomy
MB19t	18	36250115	78382592	42132478	loss	1.000	1.502	2	0.524	partial hemizygous deletion on chr18q
MB20t	7	57273599	57774338	500740	gain	1.000	3.733	4	0.003	focal amplif on chr7p
MB20t	17	17081407	18538685	1457279	loss	0.993	1.426	1	0.018	focal hemizygous deletion on chr17q
MB20t	19	7814629	8560113	745485	loss	0.993	1.286	1	0.013	focal hemizygous deletion on chr19p
MB21t	1	588217	248943333	248355116	gain	1.000	2.530	3	0.998	chr1 trisomy
MB21t	2	50852643	51634280	781637	loss	1.000	1.200	1	0.003	focal hemizygous deletion on chr2p
MB21t	2	139048596	141412278	2363682	loss	1.000	1.203	1	0.010	focal hemizygous deletion on chr2q
MB21t	8	8180484	145076125	136895641	loss	1.000	1.657	2	0.943	chr8 monosomy
MB21t	8	108744512	126934858	18190346	loss	1.000	0.883	1	0.125	partial hemizygous deletion on chr8q
MB21t	10	18514	105540958	105522444	loss	0.994	1.774	2	0.789	chr10 monosomy
MB21t	11	1710443	48981931	47271488	loss	1.000	1.558	2	0.350	chr11p monosomy
MB21t	13	17542017	111649982	94107965	loss	0.999	1.694	2	0.823	chr13 monosomy
MB21t	17	418050	19168519	18750469	loss	1.000	0.960	1	0.225	complex; isochr17q
MB21t	17	19209737	83246392	64036655	gain	1.000	2.920	3	0.769	complex; isochr17q
MB21t	20	70156	61861320	61791164	loss	0.997	1.776	2	0.959	chr20 monosomy
MB21t	X	2681823	151019381	148337558	loss	1.000	0.780	1	0.951	homozygous deletion of chrX
MB22t	2	3202821	87736106	84533285	gain	0.999	2.449	2	0.349	partial gain on chr2p
MB22t	3	12920	58593505	58580585	loss	0.999	1.544	2	0.295	partial hemizygous deletion on chr3p
MB22t	4	4539595	189206782	184667187	gain	1.000	2.523	3	0.971	chr4 trisomy
MB22t	5	50308926	177758099	127449173	gain	1.000	2.532	3	0.702	chr5q trisomy
MB22t	6	76216	169950341	169874125	gain	1.000	2.517	3	0.995	chr6 trisomy

MB22t	7	2170124	93115632	90945508	gain	1.000	2.882	3	0.571	chr7 trisomy
MB22t	7	93498078	157634263	64136185	gain	1.000	3.500	4	0.403	partial gain on chr7q
MB22t	8	1515346	141044848	139529502	loss	1.000	1.502	3	0.961	chr8 monosomy
MB22t	9	14566	133514440	133499874	gain	1.000	2.940	3	0.965	chr9 trisomy
MB22t	10	89082924	132148913	43065989	loss	1.000	1.458	2	0.322	partial hemizygous deletion on chr10q
MB22t	15	22291770	101349306	79057536	gain	1.000	2.536	2	0.775	chr15 trisomy
MB22t	17	5137735	72990914	67853179	gain	1.000	2.487	2	0.815	chr17 trisomy
MB22t	18	18868	79480944	79462076	gain	1.000	2.553	3	0.989	chr18 trisomy
MB22t	20	4627027	56725949	52098922	gain	1.000	2.461	2	0.808	chr20 trisomy
MB22t	21	12406577	41944568	29537991	gain	1.000	2.405	2	0.632	chr21 trisomy
MB22t	X	129612435	155799882	26187447	gain	1.000	1.514	2	0.168	partial gain on chrXq
MB22t	Y	-	-	52689486	loss	1.000	0.499	0	0.921	homozygous deletion of chrY
MB23t	1	152560756	248943333	96382577	gain	1.000	2.969	3	0.387	chr1q trisomy
MB23t	3	115971772	116747115	775343	loss	1.000	1.033	1	0.004	focal hemizygous deletion on chr3q
MB23t	4	9534678	186264194	176729516	loss	1.000	1.599	2	0.929	chr4 monosomy
MB23t	5	1639540	177726957	176087417	loss	1.000	1.663	2	0.970	chr5 monosomy
MB23t	8	1547131	141276133	139729002	gain	0.999	2.622	3	0.963	chr8 trisomy
MB23t	9	14566	127054760	127040194	loss	1.000	1.671	2	0.918	chr9 monosomy
MB23t	14	22541204	104065218	81524014	loss	1.000	1.649	2	0.762	chr14 monosomy
MB23t	17	1315080	21732588	20417508	loss	1.000	1.026	1	0.245	complex; isochr17q
MB23t	17	50293914	71476243	21182329	gain	1.000	2.344	2	0.254	complex; isochr17q
MB23t	20	70156	61800646	61730490	gain	1.000	2.652	3	0.958	chr20 trisomy
MB23t	Y	-	-	50356477	loss	1.000	0.684	1	0.880	total chrY hemizygous deletion
MB24t	2	180151974	182648364	2496391	loss	1.000	1.079	1	0.010	focal hemizygous deletion on chr2q
MB24t	9	14566	133988623	133974057	loss	1.000	0.997	1	0.968	chr9 monosomy
MB25t	1	175471919	176766517	1294598	gain	1.000	6.326	6	0.005	focal amplif on chr1q
MB25t	6	76216	15787695	15711479	loss	1.000	1.492	1	0.092	partial hemizygous deletion on chr6p
MB25t	7	10487	158292061	158281574	gain	1.000	3.188	3	0.993	chr7 trisomy; chromothripsis
MB25t	10	87350880	133785266	46434386	loss	1.000	1.174	1	0.347	partial hemizygous deletion on chr10q
MB25t	11	60457	135069565	135009108	loss	1.000	1.524	2	0.999	chr11 monosomy
MB25t	12	14568	16885609	16871041	gain	1.000	2.551	3	0.127	complex; partial gain on chr12p
MB25t	12	19115207	20312399	1197193	gain	1.000	6.398	6	0.009	complex; focal amplif on chr12p
MB25t	12	42630563	115654025	73023462	loss	1.000	1.518	2	0.548	complex; partial hemizygous deletion on chr12q
MB25t	12	119297608	132130574	12832966	gain	1.000	2.540	3	0.096	complex; partial gain on chr12q
MB25t	14	19761872	51907397	32145525	loss	1.000	1.313	1	0.300	complex; partial hemizygous deletion on chr14q
MB25t	14	53810937	79931496	26120559	gain	1.000	2.541	3	0.244	complex; partial gain on chr14q
MB25t	14	93471653	106873282	13401630	loss	0.999	1.502	2	0.125	complex; partial hemizygous deletion on chr14q
MB25t	16	51501041	89484298	37983257	loss	1.000	1.538	2	0.420	chr16q monosomy

MB25t	17	66653	18312172	18245519	loss	1.000	1.250	1	0.219	complex; isochr17q
MB25t	17	19168519	83246392	64077873	gain	1.000	3.083	3	0.770	complex; isochr17q
MB25t	20	70156	61861320	61791164	gain	1.000	2.638	3	0.959	chr20 trisomy
MB25t	21	4898548	46703983	41805435	loss	0.999	1.777	2	0.895	chr21 monosomy
MB25t	22	15823915	48436898	32612983	loss	1.000	1.533	2	0.642	chr22 monosomy
MB25t	X	2708370	156025612	153317242	loss	1.000	0.990	1	0.983	chrX monosomy
MB26t	2	143331744	144488646	1156903	loss	1.000	0.061	0	0.005	focal homozygous deletion on chr2q
MB26t	2	144491826	240127794	95635968	loss	1.000	1.054	1	0.395	partial hemizygous deletion on chr2q
MB26t	8	76212902	123000842	46787940	loss	1.000	0.990	1	0.322	complex; partial hemizygous deletion on chr8q
MB26t	8	125656741	128302335	2645594	gain	1.000	3.947	4	0.018	complex; focal amplif on chr8q
MB26t	8	132498591	141206866	8708275	gain	1.000	2.980	3	0.060	complex; partial gain on chr8q
MB26t	9	19868073	20658199	790126	gain	1.000	2.900	3	0.006	focal gain on chr9p
MB26t	16	38277017	87285868	49008851	loss	1.000	1.033	1	0.543	chr16q monosomy
MB26t	17	66653	19154549	19087896	loss	1.000	0.926	1	0.229	complex; isochr17q
MB26t	17	19168519	78967042	59798523	gain	0.999	2.851	3	0.718	complex; isochr17q
MB26t	20	70156	61861320	61791164	loss	1.000	0.989	1	0.959	chr20 monosomy
MB26t	X	2391642	156025612	153633970	loss	1.000	1.035	1	0.985	chrX monosomy
MB27t	2	15924	242181357	242165433	gain	0.993	2.254	2	1.000	chr2 trisomy
MB27t	3	12920	198230596	198217676	gain	0.994	2.247	2	1.000	chr3 trisomy
MB28t	1	144398563	145430610	1032048	loss	1.000	1.050	1	0.004	focal hemizygous deletion on chr1q
MB28t	2	15924	17873410	17857487	gain	1.000	2.941	3	0.074	partial gain on chr2p
MB28t	10	2601734	3131919	530186	gain	1.000	3.087	3	0.004	focal gain on chr10p
MB28t	10	67918851	132533463	64614612	loss	1.000	1.086	1	0.483	partial hemizygous deletion on chr10q
MB29t	1	13115518	248943333	235827815	gain	1.000	2.622	3	0.947	chr1 trisomy
MB29t	3	12920	198230596	198217676	gain	1.000	3.308	3	1.000	chr3 trisomy
MB29t	5	1639540	180542114	178902574	gain	1.000	3.254	3	0.986	chr5 trisomy
MB29t	6	945473	169949785	169004312	gain	1.000	2.684	3	0.990	chr6 trisomy
MB29t	7	2143932	157625834	155481902	gain	1.000	3.206	3	0.976	chr7 trisomy
MB29t	9	14566	120501228	120486662	gain	1.000	2.635	3	0.871	chr9 trisomy
MB29t	12	14568	132112844	132098276	gain	1.000	2.632	3	0.991	chr12 trisomy
MB29t	13	17542017	112743749	95201732	gain	1.000	4.061	4	0.832	chr13 amplif
MB29t	14	19761872	104164085	84402213	gain	1.000	2.632	3	0.788	chr14 trisomy
MB29t	17	66653	18950072	18883419	loss	1.000	1.281	1	0.227	complex; isochr17q
MB29t	17	19168519	72582092	53413573	gain	1.000	2.568	3	0.642	complex; isochr17q
MB29t	19	5406776	58605715	53198939	gain	1.000	2.453	3	0.908	chr19 trisomy
MB29t	20	70156	61861320	61791164	gain	1.000	2.666	3	0.959	chr20 trisomy
MB29t	X	2323889	155724702	153400813	gain	1.000	1.342	1	0.983	chrX gain
MB29t	Y	-	-	51829876	loss	1.000	0.793	1	0.906	homozygous deletion of chrY

Daoy	1	13356991	74393309	61036318	gain	1.000	2.675	2	0.245	partial gain on chr1p
Daoy	1	74394466	121608073	47213607	gain	1.000	3.421	3	0.190	partial gain on chr1p
Daoy	1	144349979	246992214	102642235	gain	1.000	2.496	2	0.412	chr1q trisomy
Daoy	2	15924	51097955	51082031	gain	1.000	2.581	3	0.211	partial gain on chr2p
Daoy	3	12920	90544141	90531221	loss	1.000	1.610	2	0.457	chr3p monosomy
Daoy	3	91946512	116601750	24655238	gain	1.000	2.529	2	0.124	complex; chr3q trisomy
Daoy	3	116607648	117248419	640771	loss	1.000	1.408	1	0.003	complex; focal hemizygous deletion on chr3q
Daoy	3	117249906	189416526	72166620	gain	1.000	2.609	3	0.364	complex; chr3q trisomy
Daoy	3	189423192	190368607	945415	loss	1.000	0.974	1	0.005	complex; focal hemizygous deletion on chr3q
Daoy	3	190375207	198230596	7855389	gain	1.000	2.639	3	0.040	complex; chr3q trisomy
Daoy	4	49489158	190202564	140713406	loss	1.000	1.094	1	0.740	chr4q monosomy
Daoy	5	26844560	29593261	2748702	gain	1.000	2.801	3	0.015	focal gain on chr5p
Daoy	5	49709239	180844439	131135200	gain	1.000	2.658	3	0.722	chr5q trisomy
Daoy	6	76216	58445657	58369441	gain	1.000	2.954	3	0.342	chr6p trisomy
Daoy	6	60290031	86128713	25838682	gain	1.000	2.860	3	0.151	complex; partial gain on chr6q
Daoy	6	86132394	95813722	9681328	loss	0.999	1.660	2	0.057	complex; partial hemizygous deletion on chr6q
Daoy	6	129979512	130726062	746550	loss	1.000	0.000	0	0.004	complex; focal hemizygous deletion on chr6q
Daoy	6	143789018	151562746	7773728	gain	1.000	3.338	3	0.046	complex; partial gain on chr6q
Daoy	6	151566111	152835574	1269463	loss	1.000	1.145	1	0.007	complex; focal hemizygous deletion on chr6q
Daoy	6	153548787	164629835	11081048	gain	1.000	3.327	3	0.065	complex; partial gain on chr6q
Daoy	6	165007482	169084485	4077003	loss	1.000	1.175	1	0.024	complex; partial hemizygous deletion on chr6q
Daoy	6	169085404	169950341	864937	gain	1.000	3.455	3	0.005	complex; focal gain on chr6q
Daoy	7	2056060	5767362	3711302	gain	1.000	2.925	3	0.023	complex; partial gain on chr7p
Daoy	7	7049735	17214787	10165052	gain	1.000	2.424	2	0.064	complex; partial gain on chr7p
Daoy	7	17219470	42880847	25661377	gain	1.000	3.975	4	0.161	complex; partial amplif on chr7p
Daoy	7	42884253	47778622	4894369	gain	1.000	4.515	5	0.031	complex; partial amplif on chr7p
Daoy	7	47825750	74773425	26947675	gain	1.000	4.230	4	0.169	complex; partial amplif on chr7pq
Daoy	7	78114241	78719347	605106	loss	0.992	1.498	1	0.004	complex; focal hemizygous deletion on chr7q
Daoy	7	98638257	157255695	58617438	gain	1.000	3.980	4	0.368	complex; partial amplif on chr7q
Daoy	8	1489851	30362334	28872483	loss	1.000	1.027	1	0.199	partial hemizygous deletion on chr8p
Daoy	9	14566	14311451	14296885	gain	1.000	3.350	3	0.103	complex; partial gain on chr9p
Daoy	9	14314600	20877178	6562578	loss	1.000	1.066	1	0.047	complex; partial hemizygous deletion on chr9p
Daoy	9	20879255	26598776	5719521	loss	1.000	0.000	0	0.041	complex; partial homozygous deletion on chr9p
Daoy	9	26886456	39994057	13107602	gain	1.000	2.905	3	0.095	complex; partial gain on chr9p
Daoy	9	67701163	133526602	65825439	gain	1.000	3.161	3	0.476	chr9q trisomy
Daoy	10	1288775	132700753	131411978	loss	1.000	1.554	2	0.982	chr10 monosomy
Daoy	11	57160307	58741873	1581566	gain	1.000	2.462	2	0.012	focal gain on chr11p
Daoy	12	1248900	8795978	7547078	gain	1.000	2.644	3	0.057	complex; partial gain on chr12p

Daoy	12	8798882	12667981	3869099	loss	1.000	0.966	1	0.029	complex; partial hemizygous deletion on chr12p
Daoy	12	12673309	132030708	119357399	gain	1.000	2.497	2	0.896	chr12 trisomy
Daoy	13	18469730	113049822	94580092	loss	1.000	1.515	2	0.827	chr13 monosomy
Daoy	14	19947403	104130265	84182862	gain	1.000	2.872	3	0.786	chr14 trisomy
Daoy	15	49924370	51066988	1142618	gain	1.000	3.483	3	0.011	complex; focal gain on chr15q
Daoy	15	51474493	52585254	1110761	gain	1.000	5.251	5	0.011	complex; focal amplif on chr15q
Daoy	15	83437501	89079631	5642130	loss	1.000	0.970	1	0.055	complex; partial hemizygous deletion on chr15q
Daoy	16	2174972	85069307	82894335	loss	1.000	1.642	2	0.918	chr16 monosomy
Daoy	17	1315080	7596799	6281719	gain	1.000	2.771	3	0.075	complex; partial gain on chr17p
Daoy	17	7611186	10038794	2427608	loss	0.999	1.499	1	0.029	complex; focal hemizygous deletion on chr17p
Daoy	17	10043129	47803490	37760361	gain	1.000	2.512	3	0.454	complex; partial gain on chr17pq
Daoy	17	47826456	61470263	13643807	loss	1.000	1.570	2	0.164	complex; partial hemizygous deletion on chr17q
Daoy	17	61475385	77435041	15959656	gain	1.000	2.568	3	0.192	complex; partial gain on chr17q
Daoy	18	18868	9878625	9859757	loss	1.000	1.095	1	0.123	partial hemizygous deletion on chr18p
Daoy	18	9881048	79500095	69619047	loss	1.000	1.560	2	0.866	chr18 monosomy
Daoy	19	18822329	58605715	39783386	gain	1.000	2.435	2	0.679	partial gain on chr19q
Daoy	20	15012937	26276700	11263763	loss	1.000	1.527	2	0.175	partial hemizygous deletion on chr20p
Daoy	21	12406577	45868535	33461958	gain	1.000	2.801	3	0.716	chr21 trisomy
Daoy	X	2753060	155262939	152509879	loss	1.000	0.982	1	0.977	chrX monosomy
D283 Med	1	14626889	16928353	2301464	gain	1.000	3.091	3	0.009	complex; focal gain on chr1p
D283 Med	1	16935209	18212212	1277003	gain	1.000	4.129	4	0.005	complex; focal amplif on chr1p
D283 Med	1	88266692	94481535	6214843	loss	1.000	1.023	1	0.025	complex; partial hemizygous deletion on chr1p
D283 Med	1	99121098	167085827	67964729	gain	1.000	2.995	3	0.273	complex; partial gain on chr1pq
D283 Med	2	24775678	34908100	10132422	gain	1.000	3.943	4	0.042	complex; focal amplif on chr2p
D283 Med	2	35563008	141323408	105760400	gain	1.000	2.793	3	0.437	complex; partial gain on chr2pq
D283 Med	2	141332146	141999999	667853	loss	1.000	0.973	1	0.003	complex; focal hemizygous deletion on chr2q
D283 Med	3	68940642	99945039	31004397	gain	1.000	2.855	3	0.156	partial gain on chr3pq
D283 Med	4	34851860	48919743	14067883	gain	1.000	3.823	4	0.074	complex; partial amplif on chr4p
D283 Med	4	49489158	56915342	7426184	gain	1.000	3.049	3	0.039	complex; partial gain on chr4p
D283 Med	4	60659137	63460912	2801775	loss	1.000	0.909	1	0.015	complex; focal hemizygous deletion on chr4q
D283 Med	4	64920746	99100014	34179268	gain	1.000	2.842	3	0.180	complex; partial gain on chr4q
D283 Med	4	99109293	109391427	10282134	gain	1.000	3.854	4	0.054	complex; partial amplif on chr4q
D283 Med	4	109394609	111292849	1898240	gain	1.000	2.981	3	0.010	complex; focal gain on chr4q
D283 Med	4	111293581	112988385	1694804	loss	1.000	0.928	1	0.009	complex; focal hemizygous deletion on chr4q
D283 Med	4	113011373	120955161	7943788	gain	1.000	4.893	5	0.042	complex; partial amplif on chr4q
D283 Med	4	120959380	125530538	4571158	gain	1.000	3.891	4	0.024	complex; partial amplif on chr4q
D283 Med	4	125535411	147896927	22361516	gain	1.000	2.795	3	0.118	complex; partial gain on chr4q
D283 Med	4	147899979	158062828	10162849	loss	1.000	1.009	1	0.053	complex; partial hemizygous deletion on chr4q

D283 Med	4	177222954	190202564	12979610	loss	1.000	0.965	1	0.068	complex; partial hemizygous deletion on chr4q
D283 Med	5	19314	22064428	22045114	loss	1.000	0.991	1	0.121	complex; partial hemizygous deletion on chr5p
D283 Med	5	22585848	46400789	23814941	gain	1.000	2.866	3	0.131	complex; partial gain on chr5p
D283 Med	5	109807925	110440302	632377	gain	1.000	4.071	4	0.003	complex; focal amplif on chr5q
D283 Med	5	129162331	129881788	719457	gain	1.000	2.748	3	0.004	complex; focal gain on chr5q
D283 Med	5	166957707	171766873	4809166	gain	1.000	3.191	3	0.026	complex; partial gain on chr5q
D283 Med	6	76216	25110654	25034438	loss	1.000	0.991	1	0.147	complex; partial hemizygous deletion on chr6p
D283 Med	6	41628022	44296092	2668070	gain	1.000	5.203	5	0.016	complex; focal amplif on chr6p
D283 Med	6	44311627	48620477	4308850	gain	1.000	4.156	4	0.025	complex; partial amplif on chr6p
D283 Med	6	51297642	90201079	38903437	gain	1.000	2.905	3	0.228	complex; partial gain on chr6q
D283 Med	7	976977	26156257	25179280	loss	1.000	0.998	1	0.158	complex; partial hemizygous deletion on chr7p
D283 Med	7	47930184	57740993	9810809	gain	1.000	2.898	3	0.062	complex; partial gain on chr7p
D283 Med	7	62926148	74293214	11367066	gain	1.000	3.842	4	0.071	complex; partial amplif on chr7q
D283 Med	7	77768544	109439700	31671156	gain	1.000	2.983	3	0.199	complex; partial gain on chr7q
D283 Med	7	109441794	116771496	7329702	loss	1.000	0.986	1	0.046	complex; partial hemizygous deletion on chr7q
D283 Med	7	116773481	146142967	29369486	gain	1.000	2.934	3	0.184	complex; partial gain on chr7q
D283 Med	7	146144248	147668529	1524281	gain	0.999	2.444	2	0.010	complex; focal gain on chr7q
D283 Med	7	147674767	159334984	11660217	gain	1.000	2.873	3	0.073	complex; partial gain on chr7q
D283 Med	8	99441521	110797625	11356104	gain	1.000	3.907	4	0.078	partial amplif on chr8q
D283 Med	8	111112909	114691853	3578944	gain	1.000	4.532	5	0.025	partial amplif on chr8q
D283 Med	8	114693431	123147723	8454292	gain	1.000	4.075	4	0.058	partial amplif on chr8q
D283 Med	8	123151560	132615410	9463850	gain	1.000	3.036	3	0.065	partial gain on chr8q
D283 Med	9	730103	20860742	20130639	gain	1.000	3.057	3	0.145	complex; partial gain on chr9p
D283 Med	9	21703060	22230588	527528	loss	1.000	0.000	0	0.004	complex; homozygous deletion on chr9p
D283 Med	9	23518686	39123743	15605057	gain	1.000	2.932	3	0.113	complex; partial gain on chr9p
D283 Med	9	42686983	43279152	592169	gain	1.000	4.217	4	0.004	complex; focal amplif on chr9p
D283 Med	9	120656709	131736725	11080016	loss	1.000	1.016	1	0.080	complex; partial hemizygous deletion on chr9q
D283 Med	10	375844	15346001	14970157	gain	1.000	2.967	3	0.112	partial gain on chr10p
D283 Med	11	55733986	122146632	66412646	gain	1.000	2.919	3	0.492	complex; partial gain on chr11q
D283 Med	11	133689197	134806490	1117293	loss	1.000	1.085	1	0.008	complex; focal hemizygous deletion on chr11q
D283 Med	12	11809511	19412187	7602676	gain	1.000	2.993	3	0.057	partial gain on chr12p
D283 Med	12	19415813	32972150	13556337	gain	1.000	3.935	4	0.102	partial amplif on chr12p
D283 Med	12	32976714	33852264	875550	gain	1.000	2.736	3	0.007	focal gain on chr12p
D283 Med	13	18480661	30676295	12195635	gain	1.000	2.767	3	0.107	partial gain on chr13q
D283 Med	13	75844801	114352102	38507301	gain	1.000	2.677	3	0.337	partial gain on chr13q
D283 Med	14	19761872	41442012	21680140	gain	1.000	4.957	5	0.203	complex; partial amplif on chr14q
D283 Med	14	41450254	63152896	21702642	gain	1.000	3.994	4	0.203	complex; partial amplif on chr14q
D283 Med	14	63406892	65519255	2112363	gain	1.000	6.057	6	0.020	complex; focal amplif on chr14q

D283 Med	14	76014435	103237096	27222661	loss	1.000	1.039	1	0.254	complex; partial hemizygous deletion on chr14q
D283 Med	15	45228748	50353158	5124410	gain	1.000	3.034	3	0.050	complex; partial gain on chr15q
D283 Med	15	70310804	101976509	31665705	loss	1.000	1.088	1	0.310	complex; partial hemizygous deletion on chr15q
D283 Med	17	8415275	21722191	13306916	gain	1.000	2.937	3	0.160	partial gain on chr17p
D283 Med	17	61895233	81152500	19257267	gain	1.000	3.016	3	0.231	partial gain on chr17q
D283 Med	19	27185211	42083538	14898327	gain	1.000	2.844	3	0.254	partial gain on chr19q
D283 Med	20	70156	3319937	3249781	loss	1.000	1.024	1	0.050	complex; partial hemizygous deletion on chr20p
D283 Med	20	32355524	34517476	2161952	gain	1.000	2.992	3	0.034	complex; focal gain on chr20q
D283 Med	21	18552517	19827663	1275146	loss	1.000	0.000	0	0.027	focal homozygous deletion on chr21q
D283 Med	22	15825747	20534297	4708550	gain	1.000	4.132	4	0.093	complex; partial amplif on chr22q
D283 Med	22	20556779	42343838	21787059	gain	1.000	3.077	3	0.429	complex; partial gain on chr22q
D283 Med	22	42351019	43165100	814081	gain	1.000	4.020	4	0.016	complex; focal amplif on chr22q
D283 Med	22	43195822	45489964	2294142	gain	1.000	3.046	3	0.045	complex; focal gain on chr22q
D283 Med	22	45491803	49516024	4024221	loss	1.000	1.020	1	0.079	complex; partial hemizygous deletion on chr22q
D283 Med	X	8442038	20130997	11688959	gain	1.000	3.835	4	0.075	complex; partial amplif on chrXp
D283 Med	X	20133894	21020510	886616	gain	1.000	3.049	3	0.006	complex; focal gain on chrXp
D283 Med	X	21294730	22047060	752330	gain	1.000	4.869	5	0.005	complex; focal amplif on chrXp
D283 Med	X	22492356	58514903	36022547	gain	1.000	2.862	3	0.231	complex; partial gain on chrXp
D283 Med	X	66909866	155575923	88666057	loss	1.000	0.976	1	0.568	monosomy of chrXq
HD-MB03	1	94904398	108507412	13603014	loss	1.000	1.634	2	0.055	complex; partial hemizygous deletion on chr1p
HD-MB03	1	146340265	248943333	102603068	gain	1.000	3.643	4	0.412	complex; chr1q amplif
HD-MB03	2	8767546	11786400	3018855	gain	0.999	2.311	2	0.012	partial gain on chr2p
HD-MB03	2	170794749	216166883	45372134	gain	0.999	2.311	2	0.187	complex; partial gain on chr2q
HD-MB03	2	216169562	226607889	10438327	gain	1.000	3.711	4	0.043	complex; partial amplif on chr2q
HD-MB03	2	226609644	227762412	1152768	gain	1.000	10.648	11	0.005	complex; focal amplif on chr2q
HD-MB03	2	227786870	242181357	14394487	loss	1.000	1.508	2	0.059	complex; partial hemizygous deletion on chr2q
HD-MB03	5	2216437	9785475	7569038	loss	1.000	1.670	2	0.042	partial hemizygous deletion on chr5p
HD-MB03	5	10949073	35940005	24990932	loss	1.000	1.698	2	0.138	partial hemizygous deletion on chr5p
HD-MB03	5	38511733	46400789	7889056	loss	1.000	1.682	2	0.043	partial hemizygous deletion on chr5p
HD-MB03	5	96022861	108913041	12890180	loss	1.000	1.685	2	0.071	partial hemizygous deletion on chr5q
HD-MB03	6	125853872	128119357	2265485	gain	1.000	2.590	3	0.013	complex; focal gain on chr6q
HD-MB03	6	128123042	170739897	42616855	loss	1.000	1.464	1	0.250	complex; partial hemizygous deletion on chr6q
HD-MB03	7	21711858	46162007	24450149	gain	0.996	2.247	2	0.153	partial gain on chr7p
HD-MB03	7	64961279	78049169	13087890	gain	0.999	2.274	2	0.082	partial gain on chr7q
HD-MB03	7	90066872	102427110	12360238	gain	0.998	2.268	2	0.078	partial gain on chr7q
HD-MB03	7	127727308	152609930	24882622	gain	0.999	2.313	2	0.156	partial gain on chr7q
HD-MB03	8	133822763	134592958	770195	gain	1.000	95.049	95	0.005	focal amplif on chr8q
HD-MB03	9	2894891	4184041	1289150	loss	1.000	1.402	1	0.009	complex; focal hemizygous deletion on chr9p

HD-MB03	9	9048998	9850919	801921	loss	1.000	0.202	0	0.006	complex; focal homozygous deletion on chr9p
HD-MB03	9	10683155	13918979	3235824	gain	1.000	2.587	3	0.023	complex; partial gain on chr9p
HD-MB03	9	13919886	15557621	1637735	gain	1.000	3.575	4	0.012	complex; focal amplif on chr9p
HD-MB03	9	15564520	17162483	1597963	gain	1.000	4.642	5	0.012	complex; focal amplif on chr9p
HD-MB03	11	59182554	68094196	8911642	gain	1.000	2.617	3	0.066	complex; partial gain on chr11q
HD-MB03	11	68106792	135069565	66962773	loss	1.000	1.071	1	0.496	complex; partial hemizygous deletion on chr11q
HD-MB03	12	43796434	70993180	27196746	gain	1.000	2.380	2	0.204	partial gain on chr12q
HD-MB03	14	25289901	49990868	24700967	loss	1.000	1.663	2	0.231	partial hemizygous deletion on chr14q
HD-MB03	14	54874617	56079707	1205090	gain	1.000	6.967	7	0.011	focal amplif on chr14q
HD-MB03	14	56727294	58581774	1854480	gain	1.000	9.988	10	0.017	focal amplif on chr14q
HD-MB03	14	78726641	90577665	11851024	loss	0.999	1.754	2	0.111	partial hemizygous deletion on chr14q
HD-MB03	15	59939518	84144527	24205009	gain	1.000	2.397	2	0.237	partial gain on chr15q
HD-MB03	17	66653	19137347	19070694	loss	1.000	1.159	1	0.229	complex; isochr17q
HD-MB03	17	19154549	80067060	60912511	gain	1.000	2.988	3	0.732	complex; isochr17q
MED-MEB-8A	1	53962966	91176459	37213493	gain	1.000	2.675	3	0.149	complex; partial gain on chr1p
MED-MEB-8A	1	91184563	113894929	22710366	gain	1.000	3.699	4	0.091	complex; partial amplif on chr1p
MED-MEB-8A	1	113898002	120615069	6717067	loss	0.998	1.715	2	0.027	complex; partial hemizygous deletion on chr1p
MED-MEB-8A	1	121078052	248297734	127219682	gain	1.000	2.568	3	0.511	chr1q trisomy
MED-MEB-8A	2	94052823	124058196	30005373	gain	1.000	2.924	3	0.124	partial gain on chr2q
MED-MEB-8A	2	142189342	152417190	10227848	gain	1.000	2.590	3	0.042	partial gain on chr2q
MED-MEB-8A	3	4949494	52957097	48007603	loss	1.000	1.676	2	0.242	complex; partial hemizygous deletion on chr3p
MED-MEB-8A	3	52960917	59969214	7008297	gain	1.000	2.328	2	0.035	complex; partial gain on chr3p
MED-MEB-8A	3	61038584	90544141	29505557	loss	1.000	1.434	2	0.149	complex; partial hemizygous deletion on chr3p
MED-MEB-8A	4	9478608	11778520	2299912	loss	1.000	1.602	2	0.012	complex; focal hemizygous deletion on chr4p
MED-MEB-8A	4	41484800	43963148	2478348	loss	1.000	1.633	2	0.013	complex; focal hemizygous deletion on chr4p
MED-MEB-8A	4	43965309	49076609	5111300	gain	1.000	2.329	2	0.027	complex; partial gain on chr4p
MED-MEB-8A	4	94368550	122428399	28059849	loss	1.000	1.647	2	0.148	complex; partial hemizygous deletion on chr4q
MED-MEB-8A	5	27986658	45764040	17777382	gain	1.000	2.975	3	0.098	complex; partial gain on chr5p
MED-MEB-8A	5	49709239	51559998	1850760	loss	1.000	1.624	2	0.010	complex; focal hemizygous deletion on chr5q
MED-MEB-8A	5	167651616	181472714	13821098	gain	1.000	2.493	2	0.076	complex; partial gain on chr5q
MED-MEB-8A	8	889815	27097772	26207957	loss	1.000	1.335	1	0.181	complex; partial hemizygous deletion on chr8p
MED-MEB-8A	8	31247366	51208677	19961311	gain	1.000	2.802	3	0.138	complex; partial gain on chr8p
MED-MEB-8A	8	53009044	56102874	3093830	gain	1.000	4.742	5	0.021	complex; partial amplif on chr8q
MED-MEB-8A	8	56103500	76722571	20619071	gain	0.996	2.303	2	0.142	complex; partial gain on chr8q
MED-MEB-8A	8	76724244	81154330	4430086	gain	1.000	3.679	4	0.031	complex; partial amplif on chr8q
MED-MEB-8A	8	81954324	82671485	717161	gain	1.000	2.877	3	0.005	complex; focal gain on chr8q
MED-MEB-8A	8	82672174	126255249	43583075	gain	1.000	2.327	2	0.300	complex; partial gain on chr8q
MED-MEB-8A	8	126257202	127016888	759686	gain	1.000	64.049	64	0.005	complex; focal amplif on chr8q

MED-MEB-8A	8	127030249	127839156	808907	gain	1.000	51.040	51	0.006	complex; focal amplif on chr8q
MED-MEB-8A	8	127845562	142071644	14226082	gain	1.000	2.275	2	0.098	complex; partial gain on chr8q
MED-MEB-8A	9	5006374	21176299	16169925	loss	1.000	1.462	1	0.117	complex; partial hemizygous deletion on chr9p
MED-MEB-8A	9	21177865	24267478	3089613	loss	1.000	0.316	0	0.022	complex; partial homozygous deletion on chr9p
MED-MEB-8A	9	33153487	39626315	6472828	loss	1.000	1.412	1	0.047	complex; partial hemizygous deletion on chr9p
MED-MEB-8A	9	68604705	70405359	1800654	gain	1.000	4.058	4	0.013	complex; focal amplif on chr9q
MED-MEB-8A	9	72113032	79143246	7030214	gain	1.000	2.474	2	0.051	complex; partial gain on chr9q
MED-MEB-8A	9	79151045	80781531	1630486	gain	1.000	3.341	3	0.012	complex; focal gain on chr9q
MED-MEB-8A	9	102489402	108608976	6119574	gain	1.000	2.673	3	0.044	complex; partial gain on chr9q
MED-MEB-8A	10	43337443	61429339	18091896	loss	1.000	1.366	1	0.135	complex; partial hemizygous deletion on chr10q
MED-MEB-8A	10	61790702	63640213	1849511	gain	1.000	2.661	3	0.014	complex; focal gain on chr10q
MED-MEB-8A	10	63650149	66040007	2389858	loss	1.000	1.437	1	0.018	complex; focal hemizygous deletion on chr10q
MED-MEB-8A	10	82648890	96275301	13626411	loss	1.000	1.430	1	0.102	complex; partial hemizygous deletion on chr10q
MED-MEB-8A	10	123244859	133785266	10540407	loss	1.000	1.397	1	0.079	complex; partial hemizygous deletion on chr10q
MED-MEB-8A	11	118221928	119662482	1440554	gain	1.000	2.732	3	0.011	complex; focal gain on chr11q
MED-MEB-8A	11	119670952	135069565	15398613	loss	1.000	1.364	1	0.114	complex; partial hemizygous deletion on chr11q
MED-MEB-8A	13	17542017	114352102	96810085	loss	1.000	1.354	1	0.847	chr13 monosomy
MED-MEB-8A	14	19947403	49521110	29573707	gain	1.000	3.034	3	0.276	complex; partial gain on chr14q
MED-MEB-8A	14	49521952	58420021	8898069	gain	1.000	3.821	4	0.083	complex; partial amplif on chr14q
MED-MEB-8A	14	58423169	58975418	552249	gain	1.000	5.925	6	0.005	complex; focal amplif on chr14q
MED-MEB-8A	14	58991354	93113064	34121710	gain	1.000	2.756	3	0.319	complex; partial gain on chr14q
MED-MEB-8A	14	93120072	99777277	6657205	loss	1.000	1.328	1	0.062	complex; partial hemizygous deletion on chr14q
MED-MEB-8A	15	28391344	90805193	62413849	gain	1.000	2.301	2	0.612	chr15 trisomy
MED-MEB-8A	15	90812043	101976509	11164466	gain	1.000	2.793	3	0.109	partial gain on chr15q
MED-MEB-8A	16	887824	3583915	2696091	gain	0.998	2.623	3	0.030	complex; focal gain on chr16q
MED-MEB-8A	16	38277017	70999200	32722183	gain	1.000	2.716	3	0.362	complex; partial gain on chr16q
MED-MEB-8A	16	71005616	88143333	17137717	loss	1.000	1.358	1	0.190	complex; partial hemizygous deletion on chr16q
MED-MEB-8A	17	11019408	21729630	10710222	loss	1.000	0.964	1	0.129	complex; partial hemizygous deletion on chr17p
MED-MEB-8A	17	36778018	37899072	1121054	gain	1.000	2.765	3	0.013	complex; focal gain on chr17q
MED-MEB-8A	17	38205743	41919439	3713696	gain	1.000	3.746	4	0.045	complex; partial amplif on chr17q
MED-MEB-8A	17	46540894	59338816	12797922	loss	1.000	1.616	2	0.154	complex; partial hemizygous deletion on chr17q
MED-MEB-8A	17	59368395	78421870	19053475	gain	1.000	2.335	2	0.229	complex; partial gain on chr17q
MED-MEB-8A	18	292896	15395376	15102480	gain	1.000	3.400	3	0.188	complex; partial gain on chr18p
MED-MEB-8A	18	53102947	56835233	3732286	gain	1.000	3.712	4	0.046	complex; partial amplif on chr18q
MED-MEB-8A	18	57318342	57949131	630789	gain	1.000	7.434	7	0.008	complex; focal amplif on chr18q
MED-MEB-8A	18	64692405	80256374	15563969	loss	1.000	1.364	1	0.194	complex; partial hemizygous deletion on chr18q
MED-MEB-8A	19	61294	17979878	17918584	gain	1.000	2.653	3	0.306	complex; partial gain on chr19p
MED-MEB-8A	19	28898837	29703033	804196	gain	1.000	7.057	7	0.014	complex; focal amplif on chr19q

MED-MEB-8A	19	29709087	30574588	865501	gain	1.000	20.372	20	0.015	complex; focal amplif on chr19q
MED-MEB-8A	19	31016837	31566287	549450	gain	1.000	39.531	40	0.009	complex; focal amplif on chr19q
MED-MEB-8A	19	31571903	58605715	27033812	loss	1.000	1.399	1	0.461	complex; partial hemizygous deletion on chr19q
MED-MEB-8A	X	223951	18742975	18519024	loss	1.000	0.866	1	0.119	complex; partial hemizygous deletion on chrXp
MED-MEB-8A	X	18746557	20111006	1364449	gain	1.000	2.728	3	0.009	complex; focal gain on chrXp
MED-MEB-8A	X	20111867	47560879	27449012	gain	1.000	1.332	1	0.176	complex; partial gain on chrXp
MED-MEB-8A	X	47565027	55551750	7986723	gain	1.000	3.765	3	0.051	complex; partial amplif on chrXp
MED-MEB-8A	X	55557770	155262939	99705169	gain	1.000	1.226	1	0.639	chrXq gain
MED-MEB-8A	Y	-	-	52689486	loss	1.000	0.499	0	0.921	homozygous deletion of chrY
ONS-76	1	14453	97223511	97209058	gain	1.000	2.695	3	0.390	chr1p trisomy
ONS-76	1	97224917	248943333	151718416	gain	1.000	3.288	3	0.609	partial gain on chr1pq
ONS-76	2	31275960	92093328	60817368	gain	1.000	2.649	3	0.251	complex; partial gain on chr2pq
ONS-76	2	140814785	141575449	760664	loss	1.000	0.519	1	0.003	complex; focal homozygous deletion on chr2q
ONS-76	2	193194049	195585490	2391441	loss	1.000	0.642	1	0.010	complex; focal homozygous deletion on chr2q
ONS-76	3	116960569	198230596	81270027	gain	1.000	2.599	3	0.410	partial gain on chr3q
ONS-76	4	55135423	190202564	135067141	loss	1.000	1.202	1	0.710	chr4q monosomy
ONS-76	5	19314	22327645	22308331	gain	1.000	4.060	4	0.123	partial amplif on chr5p
ONS-76	5	22330105	181472714	159142609	gain	1.000	2.624	3	0.877	chr5 trisomy
ONS-76	6	76216	62410507	62334291	gain	1.000	2.632	3	0.365	chr6p trisomy
ONS-76	6	162329974	168444588	6114614	loss	1.000	1.369	1	0.036	partial hemizygous deletion on chr6q
ONS-76	7	7828448	58027799	50199351	gain	1.000	2.602	3	0.315	chr7p trisomy
ONS-76	7	61875656	156752647	94876991	gain	1.000	3.543	4	0.595	partial amplif on chr7q
ONS-76	8	61805	64082818	64021013	gain	1.000	2.504	2	0.441	chr8p trisomy
ONS-76	8	64087927	145076125	80988198	gain	1.000	3.241	3	0.558	partial gain on chr8q
ONS-76	9	14566	16061369	16046803	gain	1.000	3.592	4	0.116	complex; partial amplif on chr9p
ONS-76	9	16064987	41506439	25441452	gain	1.000	3.885	4	0.184	complex; partial amplif on chr9p
ONS-76	9	66255741	123657918	57402177	gain	1.000	2.841	3	0.415	chr9 trisomy
ONS-76	11	60457	15001068	14940611	gain	1.000	2.714	3	0.111	complex; partial gain on chr11p
ONS-76	11	99232535	114573500	15340965	loss	1.000	0.675	1	0.114	complex; homozygous deletion on chr11q
ONS-76	11	114575408	135069565	20494157	loss	1.000	1.258	1	0.152	complex; partial hemizygous deletion on chr11q
ONS-76	13	17542017	20070014	2527997	loss	1.000	1.324	1	0.022	focal hemizygous deletion on chr13q
ONS-76	13	51167944	114352102	63184158	loss	1.000	1.337	1	0.552	partial hemizygous deletion on chr13q
ONS-76	14	19728320	23016174	3287854	gain	0.993	2.612	3	0.031	focal gain on chr14q
ONS-76	15	48549563	64876006	16326443	loss	1.000	1.348	1	0.160	partial hemizygous deletion on chr15q
ONS-76	16	7138056	77818849	70680793	gain	1.000	2.553	3	0.782	chr16 trisomy
ONS-76	17	66653	11674246	11607593	loss	1.000	1.215	1	0.139	complex; isochr17q
ONS-76	17	11679147	37899072	26219925	gain	1.000	2.479	2	0.315	complex; isochr17q
ONS-76	17	38883052	83246392	44363340	gain	1.000	3.152	3	0.533	complex; partial gain on chr17q

ONS-76	18	54301621	80256374	25954753	gain	1.000	2.751	3	0.323	partial gain in chr18q
ONS-76	19	4934848	7444869	2510021	loss	1.000	1.301	1	0.043	complex; focal hemizygous deletion on chr19p
ONS-76	19	8267877	30025377	21757500	gain	1.000	3.122	3	0.371	complex; partial gain on chr19p
ONS-76	19	36394001	37268099	874098	loss	1.000	1.396	1	0.015	complex; focal hemizygous deletion on chr19q
ONS-76	19	37309822	41458490	4148668	gain	1.000	2.428	2	0.071	complex; partial gain on chr19q
ONS-76	19	43426738	53968446	10541708	loss	1.000	1.236	1	0.180	complex; partial hemizygous deletion on chr19q
ONS-76	20	70156	17721324	17651168	gain	1.000	3.953	4	0.274	complex; partial amplif on chr20p
ONS-76	20	17724353	18736702	1012349	gain	1.000	5.081	5	0.016	complex; focal amplif on chr20p
ONS-76	20	18738280	20703578	1965298	gain	1.000	6.058	6	0.030	complex; focal amplif on chr20p
ONS-76	20	20713688	21650296	936608	gain	1.000	4.804	5	0.015	complex; focal amplif on chr20p
ONS-76	20	21655521	24196248	2540727	gain	1.000	6.461	6	0.039	complex; focal amplif on chr20p
ONS-76	20	24197034	26276700	2079666	gain	1.000	5.134	5	0.032	complex; focal amplif on chr20p
ONS-76	20	31182877	61867015	30684138	gain	1.000	4.470	4	0.476	complex; partial amplif on chr20q
ONS-76	22	23429735	24741589	1311854	gain	1.000	2.540	3	0.026	complex; focal gain on chr22q
ONS-76	22	31965936	44793158	12827222	loss	1.000	1.276	1	0.252	complex; partial hemizygous deletion on chr22q
ONS-76	X	2135979	150940047	148804068	loss	1.000	1.320	1	0.954	chrX monosomy
ONS-76	X	150943747	155778570	4834823	gain	1.000	2.682	3	0.031	focal gain on chrXq
UW228-3	1	50211589	237355370	187143781	gain	1.000	2.938	3	0.752	chr1 trisomy
UW228-3	1	245887973	246410054	522081	loss	1.000	1.178	1	0.002	focal hemizygous deletion on chr1q
UW228-3	2	140759965	141384767	624802	loss	1.000	0.015	0	0.003	focal homozygous deletion on chr2q
UW228-3	2	141391013	142085170	694157	loss	0.998	1.098	1	0.003	focal hemizygous deletion on chr2q
UW228-3	3	2949980	18667748	15717768	gain	1.000	2.999	3	0.079	partial gain on chr3p
UW228-3	3	117336222	198230596	80894374	gain	1.000	3.057	3	0.408	partial gain on chr3q
UW228-3	5	2221165	46400789	44179624	gain	1.000	4.980	5	0.243	partial amplif on chr5q
UW228-3	6	76216	6908652	6832436	gain	1.000	3.076	3	0.040	complex gain; chromothripsis
UW228-3	6	6910738	12824583	5913845	gain	1.000	7.724	8	0.035	complex amplif; chromothripsis
UW228-3	6	16583142	21293280	4710138	gain	1.000	3.983	4	0.028	complex amplif; chromothripsis
UW228-3	6	23263982	37733777	14469795	gain	1.000	2.897	3	0.085	complex gain; chromothripsis
UW228-3	6	38035225	41842804	3807579	gain	1.000	7.677	8	0.022	complex amplif; chromothripsis
UW228-3	6	43113638	44393829	1280191	gain	1.000	4.073	4	0.007	complex amplif; chromothripsis
UW228-3	6	44406571	63377694	18971123	gain	1.000	3.000	3	0.111	complex gain; chromothripsis
UW228-3	6	63379220	64194872	815652	gain	1.000	5.010	5	0.005	complex amplif; chromothripsis
UW228-3	6	64405602	120734551	56328949	gain	1.000	2.939	3	0.330	complex gain; chromothripsis
UW228-3	6	122877660	124120236	1242576	gain	1.000	7.305	7	0.007	complex amplif; chromothripsis
UW228-3	6	124123514	126460562	2337048	gain	1.000	8.430	8	0.014	complex amplif; chromothripsis
UW228-3	6	126463407	129708591	3245184	gain	1.000	7.112	7	0.019	complex amplif; chromothripsis
UW228-3	6	131657232	134810130	3152898	gain	1.000	7.571	8	0.018	complex amplif; chromothripsis
UW228-3	6	137120242	138301122	1180880	gain	1.000	6.729	7	0.007	complex amplif; chromothripsis

UW228-3	6	141640687	143285773	1645086	gain	1.000	3.063	3	0.010	complex gain; chromothripsis
UW228-3	6	143292344	145691089	2398745	gain	1.000	3.888	4	0.014	complex amplif; chromothripsis
UW228-3	7	2821163	23022745	20201582	gain	1.000	3.075	3	0.127	complex; partial gain on chr7p
UW228-3	7	23023594	58027799	35004205	gain	1.000	4.028	4	0.220	complex; partial amplif on chr7p
UW228-3	7	70213733	92524862	22311129	loss	1.000	1.065	1	0.140	complex; partial hemizygous deletion on chr7q
UW228-3	7	154657997	157625834	2967837	gain	1.000	3.168	3	0.019	complex; focal gain on chr7q
UW228-3	8	139775434	140925133	1149699	loss	1.000	0.908	1	0.008	focal hemizygous deletion on chr8q
UW228-3	9	14566	133526602	133512036	gain	1.000	2.824	3	0.965	chr9 trisomy
UW228-3	11	80799790	135069565	54269775	loss	1.000	0.982	1	0.402	partial hemizygous deletion on chr11q
UW228-3	18	18868	15395376	15376508	gain	1.000	4.284	4	0.191	partial amplif on chr18p
UW228-3	19	2458590	58605715	56147125	gain	1.000	3.151	3	0.958	chr19 trisomy
UW228-3	19	35523689	36250381	726692	gain	1.000	3.821	4	0.012	focal amplif on chr19q
UW228-3	20	70156	61867015	61796859	gain	1.000	3.098	3	0.959	chr20 trisomy

Supplementary Table III. Absolute numbers of OGM detected SVs in MB and ATRT tumors and cell lines.

Legend: *n.a.*, not available; SV, structural variant; *VAF*, variant allele frequency; *RVA*, Rare Variant Analysis; *DNP*, De Novo Analysis Pipeline; *VAP*, Variant Annotation Pipeline; *TOT*, total SVs; *DEL*, deletion; *INS*, insertion; *INV*, inversion; *DUP*, duplication; *TRANSL*, intrachromosomal fusion/interchromosomal translocation; *UTR*, untranslated region; *inter*, intergenic; *COSMIC*, number of SVs overlapping COSMIC CGC genes.

Tumor ID	Number of RVA-detected raw SV events (> 5% VAF)						Number of cumulative (RVA & DNP detected) filtered, high-confidence rare SV events ≥ 4.5 kbp											Number of cumulative (RVA- & DNP-VAP detected), rare somatic SV events ≥ 4.5 kbp										
	TOT	DEL	INS	INV	DUP	TRANSL	TOT	DEL	INS	INV	DUP	TRANSL	SV location				COSMIC	TOT	DEL	INS	INV	DUP	TRANSL	SV location				COSMIC
													exon	UTR	intron	inter								exon	UTR	intron	inter	
A1t	1314	597	589	59	69	0	19	12	4	1	2	0	6	8	3	2	1	8	4	2	1	1	0	7	0	0	1	1
A2t	1271	557	591	63	58	2	32	14	10	2	4	2	4	8	8	12	4	n.a.	n.a.	n.a.	n.a.	n.a.	n.a.	n.a.	n.a.	n.a.	n.a.	n.a.
A3t	1581	612	672	73	224	0	29	16	9	1	3	0	9	12	3	5	4	n.a.	n.a.	n.a.	n.a.	n.a.	n.a.	n.a.	n.a.	n.a.	n.a.	n.a.
ATRT13808	1577	633	651	65	226	2	55	17	16	0	21	1	32	6	11	7	7	n.a.	n.a.	n.a.	n.a.	n.a.	n.a.	n.a.	n.a.	n.a.	n.a.	n.a.
ATRT310-FHTC	1211	533	564	50	63	1	42	24	17	0	0	1	14	7	11	10	5	n.a.	n.a.	n.a.	n.a.	n.a.	n.a.	n.a.	n.a.	n.a.	n.a.	n.a.
ATRT311-FHTC	1442	549	562	56	275	0	28	17	9	0	2	0	13	6	5	4	2	n.a.	n.a.	n.a.	n.a.	n.a.	n.a.	n.a.	n.a.	n.a.	n.a.	n.a.
BT-12	1128	500	523	59	46	0	39	23	7	1	8	0	25	5	6	3	5	n.a.	n.a.	n.a.	n.a.	n.a.	n.a.	n.a.	n.a.	n.a.	n.a.	n.a.
BT-16	1496	584	566	61	284	1	42	21	11	1	9	0	17	11	7	7	2	n.a.	n.a.	n.a.	n.a.	n.a.	n.a.	n.a.	n.a.	n.a.	n.a.	n.a.
CHLA-02	1147	489	498	37	122	1	24	13	7	0	4	0	11	6	4	3	0	n.a.	n.a.	n.a.	n.a.	n.a.	n.a.	n.a.	n.a.	n.a.	n.a.	n.a.
CHLA-04	1212	490	549	52	121	0	38	18	12	0	8	0	13	9	5	11	1	n.a.	n.a.	n.a.	n.a.	n.a.	n.a.	n.a.	n.a.	n.a.	n.a.	n.a.
CHLA-05	1879	707	783	94	295	0	36	18	13	0	5	0	14	9	9	4	3	n.a.	n.a.	n.a.	n.a.	n.a.	n.a.	n.a.	n.a.	n.a.	n.a.	n.a.
CHLA-06	1542	638	706	71	127	0	49	20	14	2	13	0	26	3	8	12	6	n.a.	n.a.	n.a.	n.a.	n.a.	n.a.	n.a.	n.a.	n.a.	n.a.	n.a.
CHLA-266	1489	637	671	85	95	1	39	22	11	0	6	0	12	11	6	10	2	n.a.	n.a.	n.a.	n.a.	n.a.	n.a.	n.a.	n.a.	n.a.	n.a.	n.a.
HHU-ATRT1	1556	604	630	57	265	0	36	23	5	2	6	0	15	10	6	5	6	n.a.	n.a.	n.a.	n.a.	n.a.	n.a.	n.a.	n.a.	n.a.	n.a.	n.a.
JC-ATRT	1658	748	724	79	105	2	69	29	28	0	10	2	27	10	18	16	4	n.a.	n.a.	n.a.	n.a.	n.a.	n.a.	n.a.	n.a.	n.a.	n.a.	n.a.
VU397	1322	540	624	53	105	0	29	18	6	1	4	0	10	13	2	4	1	n.a.	n.a.	n.a.	n.a.	n.a.	n.a.	n.a.	n.a.	n.a.	n.a.	n.a.
MB1t	1532	667	695	85	78	7	36	17	10	1	1	7	18	6	6	8	3	15	6	2	0	0	7	12	1	2	0	3
MB2t	1609	585	747	81	194	2	17	3	7	0	6	1	11	0	2	4	1	6	1	2	0	2	1	4	0	1	1	1
MB3t	1652	663	650	75	264	0	36	19	9	0	8	0	16	3	7	10	1	2	0	0	0	2	0	2	0	0	0	0
MB4t	1290	504	518	73	152	43	117	36	13	23	16	29	75	9	5	28	25	n.a.	n.a.	n.a.	n.a.	n.a.	n.a.	n.a.	n.a.	n.a.	n.a.	n.a.
MB5t	1382	588	626	75	91	2	29	15	5	2	5	2	11	6	5	7	3	n.a.	n.a.	n.a.	n.a.	n.a.	n.a.	n.a.	n.a.	n.a.	n.a.	n.a.
MB6t	1846	619	743	84	390	10	53	13	12	4	17	7	25	10	8	10	6	n.a.	n.a.	n.a.	n.a.	n.a.	n.a.	n.a.	n.a.	n.a.	n.a.	n.a.

Supplementary Table IV. Statistics of filtered SV numbers detected by OGM in ATRT and MB cell lines, and ATRT and MB tumors, total and separated by group/subtype. Legend: *sd*, standard deviation; *TOT*, all SVs; *DEL*, deletion; *INS*, insertion; *INV*, inversion; *DUP*, duplication; *TRANSL*, intrachromosomal fusion/interchromosomal translocation.

Samples	TOT		DEL		INS		INV		DUP		TRANSL	
	<i>mean</i>	<i>sd</i>	<i>mean</i>	<i>sd</i>	<i>mean</i>	<i>sd</i>	<i>mean</i>	<i>sd</i>	<i>mean</i>	<i>sd</i>	<i>mean</i>	<i>sd</i>
ATRT cell lines (n = 13)	1435.31	212.98	588.62	78.91	619.31	81.90	63.00	15.04	163.77	87.16	0.61	0.78
ATRT tumors (n = 3)	1388.67	137.13	588.67	23.21	617.33	38.66	65.00	5.89	117.00	75.79	0.67	0.94
ATRT total (n = 16)	1426.60	201.77	588.63	71.84	618.90	75.70	63.38	13.82	155.00	87.08	0.38	0.70
MB cell lines (n = 6)	1812.67	332.67	684.17	75.42	682.33	60.96	99.17	38.24	199.33	116.35	147.67	106.87
MB tumors (n = 29)	1512.79	217.82	612.97	64.14	652.17	72.21	67.93	14.78	172.34	109.37	7.62	15.21
MB WNT (n = 3)	1659.67	139.95	630.00	26.87	701.33	15.58	77.33	6.18	253.33	118.82	0.00	0.00
MB SHH-infant (n = 6)	1431.00	198.62	605.67	53.43	634.50	82.61	60.00	14.16	144.40	87.24	1.17	1.34
MB SHH-child (n = 5)	1640.80	210.74	669.60	70.61	691.20	18.69	81.60	9.67	182.40	127.99	16.00	26.12
MB Group 3 (n = 4)	1292.25	226.74	537.25	72.25	546.00	55.37	54.50	12.44	142.25	103.65	12.25	17.92
MB Group 4 (n = 11)	1539.36	154.81	614.09	35.72	669.27	52.65	69.64	11.06	178.64	95.35	7.73	10.17

Supplementary Table V. Statistics of rare SV numbers detected by OGM in ATRT and MB cell lines, and ATRT and MB tumors, total and separated by group/subtype. Legend: *sd*, standard deviation; *TOT*, all SVs; *DEL*, deletion; *INS*, insertion; *INV*, inversion; *DUP*, duplication; *TRANSL*, intrachromosomal fusion/interchromosomal translocation.

Samples	TOT (rare)			DEL (rare)		INS (rare)		INV (rare)		DUP (rare)		TRANSL (rare)	
	<i>sum</i>	<i>mean</i>	<i>sd</i>	<i>mean</i>	<i>sd</i>	<i>mean</i>	<i>sd</i>	<i>mean</i>	<i>sd</i>	<i>mean</i>	<i>sd</i>	<i>mean</i>	<i>sd</i>
ATRT cell lines (n = 13)	526.00	40.46	11.47	20.23	3.91	12	5.84	0.54	0.75	7.39	5.14	0.31	0.61
ATRT tumors (n = 3)	80.00	26.67	5.56	14.00	1.63	7.67	2.625	1.33	0.471	3.00	0.82	0.67	0.94
ATRT total (n = 16)	606.00	37.88	11.91	19.06	4.34	11.19	5.67	0.69	0.77	6.56	4.95	0.38	0.70
ATRT-MYC (n = 9)	378.00	42.00	13.16	19.67	4.62	12.22	6.39	0.78	0.79	8.78	5.22	0.56	0.83
ATRT-SHH (n = 6)	209.00	34.83	4.91	19.33	3.04	10.83	3.76	0.50	0.76	4.00	2.65	0.17	0.37
MB cell lines (n = 6)	1476.00	246.00	79.06	69.67	12.94	35.00	14.79	26.33	18.98	54.83	32.96	58.33	23.00
MB tumors (n = 29)	943.00	32.52	23.31	13.41	8.06	7.55	2.61	2.24	5.42	4.90	5.39	4.45	7.70
MB WNT (n = 3)	57.00	19.00	4.55	8.00	2.16	7.33	1.70	0.67	0.94	3.33	2.05	0.00	0.00
MB SHH-infant (n = 6)	125.00	20.83	6.91	10.67	5.76	6.17	1.57	0.17	0.37	3.00	1.15	0.83	1.21
MB SHH-child (n = 5)	224.00	44.80	26.42	21.00	9.40	9.00	3.16	4.00	7.51	6.40	8.96	4.40	4.08
MB Group 3 (n = 4)	188.00	47.00	40.50	18.00	10.49	9.25	2.49	5.75	9.96	5.25	6.22	8.75	11.95
MB Group 4 (n = 11)	349.00	31.73	14.72	11.27	4.59	7.09	2.39	1.73	2.49	5.55	4.48	6.09	8.61

Supplementary Table VI. Recurrently SV-affected region on chr2p16.3 in MB Group 3/4 tumors and MB cell lines.

Legend: *n.a.*, not available; *Chr*, chromosome; *UTR*, untranslated region; *Conf*, confidence; *Start*, starting coordinates (GRCh38) on Chr_1; *End*, stopping coordinates (GRCh38) on Chr_2; *SVtype*, type of SV; *SVsize*, size of the SV in bp

Sample ID	MB group	Gene overlap	NrExons Affected	Chr_1	Chr_2	Start	End	Conf	SV type	SV size (bp)	ISCN
MB18t	Group 3	MSH2	UTR	2	2	47679044	47695086	0.99	deletion	10285	ogm[GRCh38] 2p16.3(47679044_47695086)x1
MB21t	Group 4	NRXN1	3	2	2	50075752	50283369	0.99	deletion	108561	ogm[GRCh38] 2p16.3(50075752_50283369)x1
MB4t	Group 3	NRXN1-DT	-	2	2	51272867	51303440	0.99	deletion	9518	ogm[GRCh38] 2p16.3(51272867_51303440)x1
MB26t	Group 4	NRXN1-DT	-	2	2	51293941	51305976	0.99	deletion	9512	ogm[GRCh38] 2p16.3(51293941_51305976)x1
MB29t	Group 3	NRXN1-DT	-	2	2	51293941	51305976	0.99	deletion	9513	ogm[GRCh38] 2p16.3(51293941_51305976)x1
D283 Med	n.a.	NRXN1,ENSG00000283058,MIR8485	1	2	2	50632748	50746609	0.99	deletion	97907	ogm[GRCh38] 2p16.3(50632748_50746608)x1
D283 Med	n.a.	NRXN1,AC007560.1,AC007682.1,AC007402.1	4	2	2	50698392	51048916	0.99	deletion	343770	ogm[GRCh38] 2p16.3(50698392_51048916)x1
D283 Med	n.a.	LOC730100,NRXN1	UTR	2	2	51097955	51337329	0.97	deletion	215653	ogm[GRCh38] 2p16.3(51097955_51337329)x1
D283 Med	n.a.	LOC730100	-	2	2	51456428	51503346	0.99	deletion	37265	ogm[GRCh38] 2p16.3(51456428_51503346)x1
Daoy	n.a.	LOC730100,NRXN1	-	2	7	51125155	157450307	0.88	translocation_interchr	-1	ogm[GRCh38] t(2;7)(p16.3;q36.3)
UW228-3	n.a.	NRXN1,MTCO1P42,ENSG00000283058	multiple	2	2	50564305	50661532	0.99	deletion	97227	ogm[GRCh38] 2p16.3(50564305_50661532)x1

Supplementary Table VII. OGM-called putative gene fusions in ATRT samples and MB tumors, and the corresponding RNA-Seq supported fusion transcripts as identified by Arriba.

Legend: *Classif*, classification; *n.a.*, not available; *OGM*, optical genome mapping; *COSMIC CGC OL*, COSMIC Cancer Gene Census overlap; *chr*, chromosome; *RefStartPos*, first position of the detected SV; *RefEndPos*, last position of the detected SV; *Conf*, confidence; *SVtype*, type of detected SV; *SVsize*, base-pair size of the region affected by the SV; *SVfreq*, frequency of the detected SV; *VAF*, variant allele frequency.

Classif	Sample ID	RNA-Seq Fusion byArriba	OGM Putative Gene Fusion	COSMIC CGC OL/ complex feature	OGM chr1	OGM chr2	OGM RefStartPos	OGM RefEndPos	Conf	OGM SVtype	OGM SVsize [bp]	OGM SVfreq	OGM VAF
ATRT-MYC	A2t	n.a.	AFDN::AL611929.1	AFDN	6	6	167933101	168197312	-1	duplication_split	264212	0.05	1.00
ATRT-SHH	A3t	n.a.	MMP11::SMARCB1	SMARCB1	22	22	23783774	23796274	0.99	deletion	5839	0.14	0.98
ATRT-MYC	ATRT13808	-	AC078883.1::MAP3K20	-	2	2	172510390	173160012	0.99	deletion	645816	0.48	0.29
ATRT-MYC	ATRT13808	-	BMPR1B::UNC5C	-	4	4	95147765	95196675	-1	duplication	48910	0.39	0.06
ATRT-MYC	ATRT13808	-	ERCC8::NDUFAF2	-	5	5	60924299	61088405	0.99	deletion	161539	0.50	0.38
ATRT-MYC	ATRT13808	-	CWC27::ADAMTS6	-	5	5	64972972	65168158	-1	duplication	195186	0.52	1.00
ATRT-MYC	ATRT13808	-	RIPOR2::SLC17A4	-	6	6	24840046	25759608	-1	duplication_split	919562	0.20	1.00
ATRT-MYC	ATRT13808	RP9::BBS9	RP9::BBS9	-	7	7	33096555	33138427	-1	duplication	41872	0.33	NA
ATRT-MYC	ATRT13808	-	AP001528.1::FZD4-DT	-	11	11	86902384	86987485	-1	duplication	85101	0.44	0.11
ATRT-MYC	ATRT13808	-	ADAM11::EFTUD2	-	17	17	44780823	44862048	-1	duplication	81225	0.24	NA

ATRT-MYC	ATRT13808	-	PLXDC1::WIPF2;RDM1P5::WIPF2	CDK12;ERBB2	17	17	39065284	40238971	-1	duplication_split	1173687	1.00	1.00
ATRT-MYC	ATRT13808	-	AP000282.1::IFNAR1;C21orf62-AS1::IFNAR1	OLIG2	21	21	32915289	33359512	-1	duplication_split	444223	0.10	0.30
ATRT-MYC	ATRT13808	-	MGAT3::CACNA1I	-	22	22	39471358	39571613	0.99	deletion	59428	0.55	0.11
ATRT-MYC	ATRT13808	-	RBM1D::RBM1D	-	24	24	21514767	21554925	0.99	deletion	23533	0.45	0.87
ATRT-SHH	ATRT-311-FHTC	-	UGT2B17::UGT2B15	-	4	4	68555236	68658466	-1	duplication	103231	0.57	0.44
ATRT-MYC	BT-12	-	LIMD1::SACM1L	-	3	3	45623648	45696932	0.99	deletion	70945	0.50	0.08
ATRT-MYC	BT-12	GMDS::ENSG00000272279	GMDS::GMDS-DT	-	6	6	1793338	2338403	0.99	deletion	518051	0.50	0.10
ATRT-MYC	BT-12	-	LPA::PRKN	-	6	6	160546951	161465908	-1	duplication_split	918957	0.19	0.23
ATRT-MYC	BT-12	-	COL13A1::P4HA1	PRF1	10	10	69902006	73048666	-1	duplication_split	3146660	0.58	1.00
ATRT-MYC	BT-12	-	SLC38A2::AC008014.1	-	12	12	46369873	46492054	0.99	deletion	119477	0.42	0.06
ATRT-MYC	BT-12	-	AC025031.1::AC008035.1	-	12	12	46386968	46591303	0.97	deletion	204335	0.33	0.06
ATRT-MYC	BT-12	-	AC004223.3::FNDC8;RAD51D::FNDC8	-	17	17	35093405	35124964	0.99	deletion	16609	0.42	0.50
ATRT-MYC	BT-16	-	SRGAP2-AS1::LINC02798;SRGAP2C::LINC02798	-	1	1	121384231	121434665	0.99	deletion	30547	0.16	0.56
ATRT-MYC	BT-16	-	JADE1::SCLT1	-	4	4	128854220	129010106	-1	duplication	155886	0.62	0.16
ATRT-MYC	BT-16	-	HNRNP1::HMG3P22	-	5	5	179632006	179684088	0.99	deletion	22143	0.66	0.80
ATRT-MYC	CHLA-02	-	SLC35F3::TARBP1	-	1	1	234290717	234441833	0.99	deletion	137552	0.50	0.28
ATRT-MYC	CHLA-02	-	TRIM51BP::TRIM49D1	-	11	11	89857270	89915449	0.99	deletion	45629	0.26	0.25
ATRT-MYC	CHLA-02	-	TRIM49D2::TRIM51EP	-	11	11	89929018	89987235	0.99	deletion	45648	0.37	0.38
ATRT-SHH	CHLA-04	-	AL162400.3::ROR1	-	1	1	63011438	63877084	-1	duplication_split	865646	0.46	1.00
ATRT-SHH	CHLA-04	DLAT::ENSG00000258529	ALG9::DLAT;AP001781.2::DLAT	-	11	11	111870483	112043526	0.99	deletion	170235	0.49	0.45
ATRT-SHH	CHLA-05	-	AL392046.1::CREM	-	10	10	35104905	35184991	-1	duplication	80086	0.03	0.16
ATRT-MYC	CHLA-06	-	MYO9A::AC020779.2	-	15	15	72060938	72147613	0.99	deletion	56833	0.55	0.17
ATRT-MYC	CHLA-06	IMP3::SNUPN	SNUPN::AC105020.6;SNUPN::IMP3	-	15	15	75607535	75639834	0.99	deletion	21716	0.51	0.49
ATRT-MYC	CHLA-06	-	DHX40::VMP1	CLTC	17	17	59602864	59805308	0.99	deletion	197856	0.50	0.08
ATRT-MYC	CHLA-266	-	GLDC::AL354707.1	-	9	9	6625126	6724125	-1	duplication	98999	0.41	0.51
ATRT-MYC	CHLA-266	-	GPC6::GPR180	-	13	13	94240441	94616060	-1	duplication_split	375619	0.68	1.00
ATRT-MYC	CHLA-266	-	CCDC43::DBF4B	-	17	17	44685469	44719425	0.99	deletion	5174	0.59	0.60
ATRT-MYC	CHLA-266	-	MMP11::SMARCB1	SMARCB1	22	22	23769856	23791277	0.99	deletion	9211	0.31	0.70
ATRT-SHH	HHU-01	-	MMP11::SMARCB1	SMARCB1	22	22	23783774	23796274	0.99	deletion	5775	0.06	0.64
ATRT-SHH	HHU-01	-	MMP11::SMARCB1	SMARCB1	22	22	23783774	23856402	0.99	deletion	7819	0.19	0.64
ATRT-MYC	JC-ATRT	-	HSDL1::DNAAF1	-	16	16	84142852	84158888	0.99	deletion	11372	0.47	0.56
ATRT-MYC	JC-ATRT	PPIL2::SMARCB1	PPIL2::SMARCB1	MAPK1; IGL locus; BCR locus; SMARCB1	22	22	21674056	23818528	0.99	deletion	2134300	0.34	0.61
ATRT-MYC	VU397	-	AC105233.5::FAM85B	-	8	8	8097356	8217601	0.99	deletion	112837	0.32	0.50
ATRT-MYC	VU397	-	GOLGA8Q::JLK4P2	-	15	15	30553973	30578206	0.99	deletion	5128	0.16	0.53
ATRT-MYC	VU397	-	LDLR::DOCK6	-	19	19	11110705	11223292	-1	duplication	112587	0.31	0.27
MB SHH-c	MB1t	CNN3::GFI (1:92481088/92483586-1:94926838), out-of-frame	-	RPL5	1	1	92491106	94918675	0.99	deletion	2418893	0.50	0.27
MB SHH-c	MB1t	-	F10::PROZ;F10-AS1::PROZ	-	13	13	113128641	113169348	0.99	deletion	20425	0.47	0.91
MB SHH-c	MB1t	-	KDM8::ITFG1	-	16	16	27192335	27209322	0.96	translocation_intrachr	-1	0.52	0.10
MB SHH-c	MB1t	-	KDM8::ITFG1	-	16	16	47329048	47330613	0.96	translocation_intrachr	-1	0.52	0.10
MB SHH-c	MB1t	FAM156B::BTBD2 (X:52900660::19:1987253)	BTBD2::FAM156A	-	19	X	1985314	1999582	0.55	translocation_interchr	-1	1.00	0.35
MB SHH-c	MB1t	FAM156B::BTBD2 (X:52900660::19:1987253)	BTBD2::FAM156A	-	X	19	52934398	52959413	0.55	translocation_interchr	-1	1.00	0.35

MB SHH-c	MB1t	-	ENSG00000285756::WWC3	-	X	X	3827829	3852194	0.77	translocation_intrachr	-1	0.27	0.12
MB SHH-c	MB1t	-	ENSG00000285756::WWC3	-	X	X	10096152	10105390	0.77	translocation_intrachr	-1	0.27	0.12
MB SHH-c	MB11t	-	EPRS::BPNT1	-	1	1	220045638	220085582	0.99	deletion	18786	0.48	0.46
MB SHH-c	MB11t	-	AC112229.4::RGPD6	-	2	2	110400015	110563103	-1	duplication_inverted	163088	0.13	0.49
MB SHH-c	MB11t	-	SOD2::ACAT2;WTAP::ACAT2	-	6	6	159748064	159766333	0.99	deletion	12261	0.40	0.06
MB SHH-c	MB11t	-	CNTNAP3B::AL445584.2;CR788268.1::AL445584.2	-	9	9	41981985	42344202	0.99	deletion	62825	0.11	0.36
MB SHH-c	MB11t	CDK5RAP1::SNTA1 (20:33392142-20:33439026), in-frame	CDK5RAP1::SNTA1	-	20	20	33395320	33436557	-1	duplication	41237	0.02	0.04
MB SHH-i	MB12t	-	AC135983.1::GOLGA8O	-	15	15	32406333	32453636	0.99	deletion	19675	0.39	0.45
MB SHH-c	MB13t	-	RGS7::KIF26B	RGS7, FH, AKT3	1	1	241009879	245374670	0.99	deletion	4355050	0.50	0.46
MB SHH-c	MB13t	2x RANBP17::CANX (5:170968377/171028989-5:179705679), in-frame; RANBP17::HMGB3P22 (5:171028989-5:179694306)	RANBP17::HMGB3P22; RANBP17::CANX	-	5	5	171114775	171123698	1	translocation_intrachr/large_deletion	-1	0.40	0.48
MB SHH-c	MB13t	2x RANBP17::CANX (5:170968377/171028989-5:179705679), in-frame; RANBP17::HMGB3P22 (5:171028989-5:179694306)	RANBP17::HMGB3P22; RANBP17::CANX	-	5	5	179632006	179684088	1	translocation_intrachr/large_deletion	-1	0.40	0.48
MB SHH-c	MB13t	-	CDKAL1::TRPM4	-	6	19	20514836	20616665	0.8	translocation_interchr	-1	0.50	0.33
MB SHH-c	MB13t	-	CDKAL1::TRPM4	-	19	6	49160094	49188222	0.8	translocation_interchr	-1	0.50	0.33
MB SHH-c	MB13t	-	CUBNP1::ENST0000056897.6.2	-	10	10	42713662	42752096	-1	duplication	38434	0.21	0.53
MB SHH-c	MB15t	multiple fusions of different confidences spanning the highly rearranged region	AC068286.1::NBAS; AC068286.2::NBAS	-	2	2	14892930	15524996	0.97	deletion	264880	0.11	0.11
MB SHH-c	MB15t	multiple fusions of different confidences spanning the highly rearranged region	AC068286.2::NBAS	-	2	2	14855509	15524996	0.99	deletion	594972	0.10	0.12
MB SHH-c	MB15t	-	AC068286.1::AC010745.2; AC068286.2::AC010745.2	MYCN	2	2	14892930	16257585	0.99	deletion	1364655	0.06	0.18
MB SHH-c	MB15t	DDX1::ENSG00000287291 (2:15618270-2:14779147), out-of-frame	AC008278.2::DDX1	-	2	2	15566319	15625882	-1	duplication_inverted	59563	0.01	0.47
MB SHH-c	MB15t	multiple fusions of different confidences spanning the highly rearranged region	AC130710.1::AC008164.1	-	2	2	16098251	16766273	-1	duplication_split	668022	0.00	0.07
MB SHH-c	MB15t	multiple fusions of different confidences spanning the highly rearranged region	AC068286.2::AC008012.1; AC068286.2::FGF23	complex rearrangement involving MYCN	2	12	14762145	14772159	0.98	translocation_interchr	-1	0.06	0.21
MB SHH-c	MB15t	multiple fusions of different confidences spanning the highly rearranged region	AC068286.2::AC008012.1; AC068286.2::FGF23	complex rearrangement involving MYCN	12	2	4376310	4388372	0.98	translocation_interchr	-1	0.06	0.21
MB SHH-c	MB15t	multiple fusions of different confidences spanning the highly rearranged region	LINC01804::TEAD4	complex rearrangement involving MYCN	2	12	15707917	15720700	0.66	translocation_interchr	-1	0.12	0.06
MB SHH-c	MB15t	multiple fusions of different confidences spanning the highly rearranged region	LINC01804::TEAD4	complex rearrangement involving MYCN	12	2	2983141	2984128	0.66	translocation_interchr	-1	0.12	0.06
MB SHH-c	MB15t	multiple fusions of different confidences spanning the highly rearranged region	AC068286.2::AC008012.1	complex rearrangement involving MYCN	2	12	14762145	14772159	0.62	translocation_interchr	-1	0.03	0.21

MB SHH-c	MB15t	multiple fusions of different confidences spanning the highly rearranged region	AC068286.2::AC008012.1	complex rearrangement involving MYCN	12	2	4366492	4373643	0.62	translocation_interchr	-1	0.03	0.21
MB SHH-c	MB15t	multiple fusions of different confidences spanning the highly rearranged region	AC010145.1::AC008012.1	complex rearrangement involving MYCN	2	12	16000200	16019644	0.64	translocation_interchr	-1	0.02	0.08
MB SHH-c	MB15t	multiple fusions of different confidences spanning the highly rearranged region	AC010145.1::AC008012.1	complex rearrangement involving MYCN	12	2	4357180	4363861	0.64	translocation_interchr	-1	0.02	0.08
MB SHH-c	MB15t	multiple fusions of different confidences spanning the highly rearranged region	LIX1-AS1::AC005833.1;LIX1-AS1::NDUFA9	CCND2	5	12	97223181	97225848	0.28	translocation_interchr	-1	0.03	0.08
MB SHH-c	MB15t	multiple fusions of different confidences spanning the highly rearranged region	LIX1-AS1::AC005833.1;LIX1-AS1::NDUFA9	CCND2	12	5	4674224	4686651	0.28	translocation_interchr	-1	0.03	0.08
MB SHH-c	MB15t	-	RPS6KA2::SMOC2	FGFR10P,AFDN	6	6	166505446	168620885	0.99	deletion	2089095	0.23	0.38
MB SHH-c	MB15t	-	MYOM2::AC245123.1	-	8	8	2058828	2581419	-1	duplication_split	522591	0.78	1.00
MB SHH-c	MB15t	-	AP000844.2::NTM	-	11	11	131880246	131922969	0.99	deletion	28707	0.36	0.33
MB SHH-c	MB15t	multiple fusions of different confidences spanning the highly rearranged region	CACNA1C::TEAD4	-	12	12	2558106	3026969	-1	duplication_split	468863	0.17	0.18
MB SHH-c	MB15t	multiple fusions of different confidences spanning the highly rearranged region	CACNA1C::AC006063.1	CCND2	12	12	2539552	4839870	-1	duplication_split	2300319	0.19	0.67
MB SHH-c	MB15t	-	TEAD4::PRMT8	-	12	12	2956260	3541891	0.99	inversion	75758	0.10	0.12
MB SHH-c	MB15t	ATF7IP::PTPRO (12:14461133-12:15483974), out-of-frame	ATF7IP::PTPRO	-	12	12	14459432	15470029	0.99	deletion	1006804	0.50	0.18
MB SHH-c	MB15t	2x PRMT8::TIGAR (12:3544829/3545336-12:4357378/4359600)	PRMT8::AC008012.1	CCND2	12	12	3504769	4397016	0.99	deletion	861503	0.07	0.06
MB SHH-c	MB15t	3x TSPAN9::CRACR2A (12:3201256-12:3713317; 12:3201256-12:3733210; 12:3206418-12:3713317) out-of-frame, stop codon	TEAD4::AC005832.4;TEAD4::AC005833.1;TEAD4::NDUFA9	CCND2	12	12	3030873	4654476	0.99	deletion	1608708	0.15	0.06
MB SHH-c	MB15t	-	PITPNM3::CNTROB	T53	17	17	6500989	7948989	0.99	deletion	1448000	0.51	0.48
MB SHH-c	MB15t	-	CACTIN::STAP2	MAP2K2	19	19	3620619	4337185	0.99	deletion	697090	0.46	0.58
MB SHH-c	MB19t	-	CRY1::AC078929.1	-	12	12	107080109	107102798	0.99	deletion	5298	0.19	0.29
MB SHH-c	MB19t	-	ORAI1::MORN3	-	12	12	121632856	121657227	0.99	deletion	7173	0.44	0.57
MB SHH-i	MB20t	-	ADAM9::ADAM32	-	8	8	39001163	39169151	-1	duplication	167988	0.03	0.13
MB SHH-i	MB20t	3x STAG2::ARHGAP36 (X:123961856/123960866/123962106-X:131081760); STAG2::LINC01201 (X:123961856-X:130982052)	-	STAG2	X	X	123995348	124005001	0.77	translocation_intrachr/ large_deletion	-1	0.27	0.30
MB SHH-i	MB20t	3x STAG2::ARHGAP36 (X:123961856/123960866/123962106 :: X:131081760); STAG2::LINC01201 (X:123961856::X:130982052)	-	STAG2	X	X	130938439	130952538	0.77	translocation_intrachr/ large_deletion	-1	0.27	0.30
MB SHH-i	MB27t	-	KRT86::KRT84	-	12	12	52307887	52384666	-1	duplication	76779	0.47	0.51
MB SHH-i	MB28t	-	GRHL3::STPG1	-	1	1	24354474	24378777	0.99	deletion	13503	0.53	0.55
MB SHH-i	MB28t	SH3BP2::CTNNA3 (4:2820753-10:67219870), out-of-frame	SH3BP2::CTNNA3	-	4	10	2804673	2823735	1	translocation_interchr	-1	0.30	0.47

MB SHH-i	MB28t	SH3BP2::CTNNA3 (4:2820753-10:67219870), out-of-frame	SH3BP2::CTNNA3	-	10	4	67336316	67318345	1	translocation_interchr	-1	0.30	0.47
MB SHH-i	MB28t	-	LINC02387::DENND5B	-	12	12	31368815	31384995	0.99	deletion	6660	0.32	0.51
MB SHH-i	MB28t	-	STYX::GNPNAT1	-	14	14	52774967	52789513	0.99	deletion	10164	0.52	0.53
MB WNT	MB10t	-	AC104667.2::AC104667.1	-	2	2	237593953	237622037	0.99	deletion	5197	0.37	0.44
MB WNT	MB10t	GPS2::KDM6B (17:7314597- 17:7842112); KDM6B::ENSG00000261915 (17:7314597-17:7842112)	SLC2A4::KDM6B	TP53	17	17	7286494	7840671	0.99	deletion	523648	0.51	0.69
MB WNT	MB8t	-	AL162595.2::AL162595.1	-	1	1	229237632	229257327	0.99	deletion	8685	0.05	0.55
MB WNT	MB8t	-	PDP2::AC026464.4;PDP2::S NTB2	CBFB;CTCF;CDH 1	16	16	66886992	69305254	0.99	deletion	2413186	0.36	0.48
MB WNT	MB9t	6 possible fusions with ATAD5	AC005562.1::ATAD5	-	17	17	30619365	30872678	0.97	deletion	248930	0.27	0.18
MB WNT	MB9t	-	ZNF791::MAN2B1	-	19	19	12630593	12656793	0.99	deletion	6072	0.47	0.78
MB G4	MB14t	-	CLU::AC013643.2;CLU::CCD C25	-	8	8	27600851	27758240	-1	duplication_split	157389	0.03	0.31
MB G4	MB14t	-	SCARA3::AC013643.2;SCAR A3::CDC25	-	8	8	27657244	27758240	-1	duplication	100996	0.46	0.31
MB G4	MB17t	-	ZNF442::AC008758.4	-	19	19	12358962	12385422	0.99	deletion	10966	0.52	0.45
MB G3	MB18t	-	RANBP10::PRMT1	-	16	19	67770651	67776926	0.47	translocation_interchr	-1	0.36	0.30
MB G3	MB18t	-	RANBP10::PRMT1	-	19	16	49686022	49701206	0.47	translocation_interchr	-1	0.36	0.30
MB G4	MB2t	-	CFHR1::CFHR4	-	1	1	196821223	196930211	-1	duplication	108988	0.08	0.49
MB G4	MB2t	-	GRAPL::AC106017.1;GRAPL ::KYNUP3	-	17	17	19154549	19209737	-1	duplication_split	55188	0.04	0.41
MB G4	MB21t	NRXN1::TRHR,NUDCD1 (2:50346691-8:109172681), out-of-frame	NRXN1::NUDCD1	-	2	8	50075752	50076217	0.97	translocation_interchr	-1	0.24	0.41
MB G4	MB21t	NRXN1::TRHR,NUDCD1 (2:50346691-8:109172681), out-of-frame	NRXN1::NUDCD1	-	8	2	109240072	109242247	0.97	translocation_interchr	-1	0.24	0.41
MB G4	MB21t	-	NRXN1::AC079793.1;NRXN1 ::ARHGAP15	-	2	2	50274326	50282235	0.98	translocation_intrachr	-1	0.22	0.39
MB G4	MB21t	-	NRXN1::AC079793.1;NRXN1 ::ARHGAP15	-	2	2	143393434	143402948	0.98	translocation_intrachr	-1	0.22	0.39
MB G4	MB21t	-	NRXN1-DT::LRP1B	LRP1B	2	2	51931556	51948489	1	translocation_intrachr	-1	0.34	0.47
MB G4	MB21t	-	NRXN1-DT::LRP1B	LRP1B	2	2	141411428	141412278	1	translocation_intrachr	-1	0.34	0.47
MB G4	MB21t	-	NRXN1-DT::AC016074.2	-	2	8	51931556	51948489	0.93	translocation_interchr	-1	0.03	0.30
MB G4	MB21t	-	NRXN1-DT::AC016074.2	-	8	2	125816357	125824135	0.93	translocation_interchr	-1	0.03	0.30
MB G4	MB21t	-	STMN2::AC015522.1	HEY1	8	8	79632188	84138762	-1	duplication_split	4506574	0.49	1.00
MB G4	MB22t	-	ASTN1::BRINP2	-	1	1	177117525	177246952	0.99	deletion	109009	0.50	0.07
MB G4	MB22t	-	PAQR8::EFHC1	-	6	6	52386548	52438936	0.99	deletion	45676	0.46	0.07
MB G4	MB25t	-	CNOT6::ARL3	-	5	10	180502134	180514735	0.97	translocation_interchr	-1	0.54	0.44
MB G4	MB25t	-	CNOT6::ARL3	-	10	5	102681707	102683111	0.97	translocation_interchr	-1	0.54	0.44
MB G4	MB25t	-	LINC01162::SNX10-AS1	chromothripsis	7	7	20895515	20905127	0.86	translocation_intrachr	-1	0.35	0.15
MB G4	MB25t	-	LINC01162::SNX10-AS1	chromothripsis	7	7	26375094	26377336	0.86	translocation_intrachr	-1	0.35	0.15
MB G4	MB25t	-	FOXP2::KIAA1549	chromothripsis	7	7	114203844	114212219	0.97	translocation_intrachr	-1	0.34	0.16
MB G4	MB25t	-	FOXP2::KIAA1549	chromothripsis	7	7	138872714	138862984	0.97	translocation_intrachr	-1	0.34	0.16
MB G4	MB25t	-	VOPP1::ZNF713	-	7	7	55546339	55933272	-1	duplication_split	386933	0.13	0.13
MB G4	MB25t	GRM8::LINC-PINT (7:126902542-7:131108803), out-of-frame; GRM8::ENSG00000285106 (7:126902542-7:131108803), out-of-frame	GRM8::MKLN1	SND1;SMO	7	7	126808252	131115355	-1	duplication_split	4307103	0.44	1.00

MB G4	MB25t	CLIP2::CADPS2 (7:74397406-7:122696141)	CLIP2::CADPS2;CLIP2::RNF 133	chromothripsis	7	7	74395870	74413452	1	translocation_intrachr	-1	0.36	0.21
MB G4	MB25t	CLIP2::CADPS2 (7:74397406-7:122696141)	CLIP2::CADPS2;CLIP2::RNF 133	chromothripsis	7	7	122693421	122698938	1	translocation_intrachr	-1	0.36	0.21
MB G4	MB25t	-	GNG2::LINC01303;LOC1027 23604::LINC01303	-	14	14	51908130	51915127	0.99	translocation_intrachr	-1	0.34	0.21
MB G4	MB25t	-	GNG2::LINC01303;LOC1027 23604::LINC01303	-	14	14	61555073	61557026	0.99	translocation_intrachr	-1	0.34	0.21
MB G4	MB25t	-	LINC02331::FUT8	-	14	14	53747083	53750273	0.99	translocation_intrachr	-1	0.48	0.29
MB G4	MB25t	-	LINC02331::FUT8	-	14	14	65662894	65672556	0.99	translocation_intrachr	-1	0.48	0.29
MB G4	MB25t	-	OIP5::NUSAP1	-	15	15	41321733	41359542	0.99	deletion	29661	0.53	0.47
MB G4	MB25t	PCNX1::ATP6V0A4 (14:71087046-7:138773767)	ATP6V0A4::PCNX1	-	7	14	138765368	138774129	1	translocation_interchr	-1	0.30	0.21
MB G4	MB25t	PCNX1::ATP6V0A4 (14:71087046-7:138773767)	ATP6V0A4::PCNX1	-	14	7	71083344	71092177	1	translocation_interchr	-1	0.30	0.21
MB G4	MB26t	ZEB2::NSMCE2 (2:144492065-8:125182256), out-of-frame	ZEB2::NSMCE2	-	2	8	144488646	144491826	1	translocation_interchr	-1	0.35	0.41
MB G4	MB26t	ZEB2::NSMCE2 (2:144492065-8:125182256), out-of-frame	ZEB2::NSMCE2	-	8	2	125231884	125237107	1	translocation_interchr	-1	0.35	0.41
MB G4	MB26t	2x RUNX1T1::HPYR1 (8:91994512/92005116- 8:132500746/132544809), out-of-frame	-	RUNX1T1	8	8	91989737	91992297	0.99	translocation_intrachr	-1	0.49	0.44
MB G4	MB26t	2x RUNX1T1::HPYR1 (8:91994512/92005116- 8:132500746/132544809), out-of-frame	-	RUNX1T1	8	8	132503026	132498591	0.99	translocation_intrachr	-1	0.49	0.44
MB G4	MB3t	-	AC008073.3::ITSN2;FAM228 A::ITSN2	-	2	2	24180905	24209398	0.99	deletion	6898	0.51	0.96
MB G3	MB4t	-	GNG12::LINC01720	-	1	1	67704295	67713991	0.93	translocation_intrachr	-1	0.50	0.37
MB G3	MB4t	-	GNG12::LINC01720	-	1	1	190703764	190708929	0.93	translocation_intrachr	-1	0.50	0.37
MB G3	MB4t	-	CADM2::EQTN	-	3	9	85686262	85698013	0.99	translocation_interchr	-1	0.48	0.51
MB G3	MB4t	-	CADM2::EQTN	-	9	3	27291359	27293527	0.99	translocation_interchr	-1	0.48	0.51
MB G3	MB4t	GPC5::GPC5 (13:91448922- 13:92228081), out-of-frame	AC002460.2::GPC5	GPC5	4	13	148773170	148792377	1	translocation_interchr	-1	0.24	0.11
MB G3	MB4t	GPC5::GPC5 (13:91448922- 13:92228081), out-of-frame	AC002460.2::GPC5	GPC5	13	4	91866569	91874640	1	translocation_interchr	-1	0.24	0.11
MB G3	MB4t	-	PPP1R3A::POT1-AS1	-	7	7	113976097	113977460	0.62	translocation_intrachr	-1	0.15	0.10
MB G3	MB4t	-	PPP1R3A::POT1-AS1	-	7	7	125006996	125011760	0.62	translocation_intrachr	-1	0.15	0.10
MB G3	MB4t	-	LSM1::AC022034.3	chromothripsis	8	8	38170927	38176638	0.3	translocation_intrachr	-1	0.50	0.15
MB G3	MB4t	-	LSM1::AC022034.3	chromothripsis	8	8	53452880	53453916	0.3	translocation_intrachr	-1	0.50	0.15
MB G3	MB4t	-	PEBP4::SNTG1	chromothripsis	8	8	22862445	22864438	0.94	translocation_intrachr	-1	0.46	0.23
MB G3	MB4t	-	PEBP4::SNTG1	chromothripsis	8	8	50738183	50747417	0.94	translocation_intrachr	-1	0.46	0.23
MB G3	MB4t	-	UNC5D::AC009630.1;UNC5 D::AC009630.2;UNC5D::GIN S4	chromothripsis	8	8	35548473	35557295	0.38	translocation_intrachr	-1	0.31	0.24
MB G3	MB4t	-	UNC5D::AC009630.1;UNC5 D::AC009630.2;UNC5D::GIN S4	chromothripsis	8	8	41538434	41544505	0.38	translocation_intrachr	-1	0.31	0.24
MB G3	MB4t	-	PLAT::POLB	IKBKB	8	8	42195831	42350508	0.99	deletion	140530	0.25	0.09
MB G3	MB4t	-	IKBKB::THAP1	IKBKB	8	8	42323556	42839978	0.99	deletion	516422	0.38	0.11
MB G3	MB4t	-	SPIDR::UBE2V2	-	8	8	47501527	48030637	0.99	deletion	524346	0.30	0.13
MB G3	MB4t	-	SPIDR::PXDNL	-	8	8	47512901	51524900	-1	duplication_split	4011999	0.11	0.08
MB G3	MB4t	-	AC007368.1::AC078878.2	-	12	12	126364285	126883142	-1	duplication_split	518857	0.35	0.13

MB G3	MB4t	-	LINC02359::AC005888.1	-	12	12	126124810	126183280	0.99	deletion	39971	0.52	0.22
MB G3	MB4t	GPC5::GPC5 (13:91448922-13:92228081), out-of-frame	LINC00410::GPC5	GPC5	13	13	90901087	91445185	0.99	deletion	544098	0.32	0.09
MB G3	MB4t	GPC5::GPC5 (13:91448922-13:92228081), out-of-frame	LINC00410::GPC5	GPC5	13	13	90907430	92079619	-1	duplication_split	1172189	0.24	0.34
MB G3	MB4t	-	ABHD17AP6::AC005144.1	chromothripsis	17	17	20823926	20824736	0.71	translocation_intrachr	-1	0.38	0.14
MB G3	MB4t	-	ABHD17AP6::AC005144.1	chromothripsis	17	17	71823692	71844621	0.71	translocation_intrachr	-1	0.38	0.14
MB G3	MB4t	-	USP22::AC015688.4;USP22::KSR1	chromothripsis	17	17	21023935	21034595	0.11	translocation_intrachr	-1	0.42	0.13
MB G3	MB4t	-	USP22::AC015688.4;USP22::KSR1	chromothripsis	17	17	27596211	27624656	0.11	translocation_intrachr	-1	0.42	0.13
MB G3	MB4t	-	AC015908.2::AC005410.2;AC015908.2::DNAH9;AC015908.7::AC005410.2;AC015908.7::DNAH9	-	17	17	10850246	11960110	0.99	deletion	1109864	0.40	0.12
MB G3	MB4t	-	PER1::NTN1	PER1	17	17	8144677	9126107	0.99	deletion	981430	0.50	0.25
MB G3	MB4t	-	LINC02086::TLL6	-	17	17	48649654	48781278	0.99	deletion	122226	0.50	0.13
MB G3	MB4t	-	SLC39A11::DNAH17	chromothripsis	17	17	72826648	72831884	0.41	translocation_intrachr	-1	0.07	0.17
MB G3	MB4t	-	SLC39A11::DNAH17	chromothripsis	17	17	78568402	78574010	0.41	translocation_intrachr	-1	0.07	0.17
MB G3	MB4t	-	CASC17::SLC39A11	-	17	17	71109107	72826648	-1	duplication_split	1717542	0.03	0.09
MB G3	MB4t	-	ENSG00000291214::ARSG	-	17	17	68131918	68339024	-1	duplication_inverted	207106	1.00	1.00
MB G4	MB5t	-	ARHGAP15::GTF3C4	-	2	9	143313934	143314725	1	translocation_interchr	-1	0.43	0.34
MB G4	MB5t	-	ARHGAP15::GTF3C4	-	9	2	132674624	132677825	1	translocation_interchr	-1	0.43	0.34
MB G4	MB5t	9 fusion events in this region, ITGA9::MYRIP (3:37803823/37818891-3:40044271), out-of-frame ; ITGA9-AS1::EIF1B-AS1 (3:37834679/37806079/37808704/37818810/37821014-40065575)	ITGA9::MYRIP;ITGA9-AS1::MYRIP;ITGA9-AS1::EIF1B-AS1	MYD88	3	3	37795982	40073579	-1	duplication_split	2277597	0.52	1.00
MB G4	MB5t	CWD1::DOCK8 (9:172081-9:399494), out-of-frame	ZNG1A::DOCK8	-	9	9	173653	406050	-1	duplication	232397	0.42	0.11
MB G4	MB5t	-	ZNF471::ZFP28	-	19	19	56530051	56549946	0.99	insertion	5095	0.46	0.47
MB G4	MB6t	MINDY1::PIP5K1A (1:151002965-1:151221878)	MINDY1::PIP5K1A	MLLT11	1	1	151005656	151220891	-1	duplication	215235	0.34	1.00
MB G4	MB6t	-	AC117422.1::RANBP3;SLC41A3::RANBP3	-	3	19	126057802	126064112	0.99	translocation_interchr	-1	0.44	0.43
MB G4	MB6t	-	AC117422.1::RANBP3;SLC41A3::RANBP3	-	19	3	5955736	5960256	0.99	translocation_interchr	-1	0.44	0.43
MB G4	MB6t	-	MBOAT1::ENSG00000227803	-	6	6	20157014	20215002	-1	duplication	57988	0.26	0.14
MB G4	MB6t	-	LINC00348::AC005828.1;LINC00348::TANC2	-	13	17	71043861	71065084	1	translocation_interchr	-1	0.14	0.09
MB G4	MB6t	-	LINC00348::AC005828.1;LINC00348::TANC2	-	17	13	63387568	63399950	1	translocation_interchr	-1	0.14	0.09
MB G4	MB6t	-	SRL::TFAP4	-	16	16	4227862	4271184	0.99	deletion	4798	0.39	0.41
MB G4	MB6t	-	CMIP::PLCG2	-	16	16	81654434	81911298	-1	duplication	256864	0.31	1.00
MB G4	MB6t	SRCIN1::CISD3 (17:38533519-17:38732535)	SRCIN1::MLLT6	MLLT6	17	17	38540193	38727584	-1	duplication	187391	0.49	0.27
MB G4	MB6t	-	AC015845.2::AC015813.1;AC015845.2::AC015813.2	-	17	17	57807386	57990621	-1	duplication_inverted	183235	0.06	0.92
MB G4	MB7t	-	NBPF5P::NBPF6;SLC25A24P2::NBPF6	-	1	1	108384641	108459293	-1	duplication	74652	0.02	0.03

Supplementary Table VIII. Final list of Arriba gene fusion calls in MB tumors.

Legend: *MB ID*, medulloblastoma sample ID; *class*, short classification; *G4*, Group 4 MB; *G3*, Group 3 MB; *str1/str2*, orientation of gene fusion on strand 1/2; *chr1/2*, chromosome nr.1/2 implicated in the fusion event; *loc1/2*, fusion breakpoint coordinates (GRCh38) implicated in the fusion event; *site1/2*, genomic regions affected by the fusion event; *type*, type of SV producing the fusion event; *conf*, confidence; *read_frame*, reading frame; *retained_protein_domains*, percentage of the annotated functional protein domain after fusion formation.

MB ID	class	gene1	gene2	str1	str2	chr1	loc1	chr2	loc2	site1	site2	type	conf	read_frame	retained_protein_domains
MB1t	SHH	CNN3	GF11	-/-	-/-	1	94926838	1	92483586	CDS/splice-site	5'UTR/splice-site	deletion	high	out-of-frame	Zinc_finger_C2H2_type(100%)
MB1t	SHH	SEPSECS-AS1	ENSG00000250863	+/+	-/-	4	25160753	4	44025414	exon/splice-site	exon	inversion	high	.	.
MB2t	G4	SMC6	CYRIA	-/-	-/-	2	17678859	2	16651642	CDS/splice-site	intron	deletion	high	out-of-frame	RecF/RecN/SMC_N_terminal_domain(90%) CYRIA/CYRIB_Rac1_binding_domain(100%)
MB2t	G4	SMC6	CYRIA	-/-	-/-	2	17678859	2	16624019	CDS/splice-site	5'UTR/splice-site	deletion	high	out-of-frame	RecF/RecN/SMC_N_terminal_domain(90%) CYRIA/CYRIB_Rac1_binding_domain(100%)
MB2t	G4	INTS4P1	CCT6P1	+/+	+/+	7	65200698	7	65754527	exon/splice-site	exon/splice-site	deletion	high	.	.
MB2t	G4	INTS4P1	CCT6P1	+/+	+/+	7	65209813	7	65754527	exon/splice-site	exon/splice-site	deletion	high	.	.
MB2t	G4	INTS4P1	CCT6P1	+/+	+/+	7	65212432	7	65755780	exon/splice-site	exon/splice-site	deletion	high	.	.
MB4t	G3	ENSG00000279240	TRPC7	-/-	-/-	5	136396888	5	136315779	exon/splice-site	CDS/splice-site	deletion/read-through	high	.	Ion_transport_protein(100%)
MB4t	G3	RPN2	KIAA1755	+/+	-/-	20	37199225	20	38246126	CDS/splice-site	CDS/splice-site	inversion	high	out-of-frame	Oligosaccharyltransferase_subunit_Ribophorin_II(24%)
MB5t	G4	ITGA9-AS1	EIF1B-AS1	-/-	-/-	3	37806079	3	40065575	exon/splice-site	exon/splice-site	duplication	high	.	.
MB5t	G4	ITGA9-AS1	EIF1B-AS1	-/-	-/-	3	37808704	3	40065575	exon/splice-site	exon/splice-site	duplication	high	.	.
MB5t	G4	ITGA9-AS1	EIF1B-AS1	-/-	-/-	3	37818810	3	40065575	exon/splice-site	exon/splice-site	duplication	high	.	.
MB5t	G4	ITGA9-AS1	EIF1B-AS1	-/-	-/-	3	37821014	3	40065575	exon/splice-site	exon/splice-site	duplication	high	.	.
MB5t	G4	MYRIP	ITGA9	+/+	+/+	3	40044271	3	37803823	CDS/splice-site	CDS/splice-site	duplication	high	out-of-frame	FYVE-type_zinc_finger(92%),Rab_effector_MyRIP/melanophilin_C-terminus(0%)
MB5t	G4	MYRIP	ITGA9	+/+	+/+	3	40044271	3	37818891	CDS/splice-site	CDS/splice-site	duplication	high	out-of-frame	FYVE-type_zinc_finger(92%),Rab_effector_MyRIP/melanophilin_C-terminus(0%)
MB5t	G4	ZNG1A	DOCK8	-/-	+/-	9	172081	9	399494	CDS/splice-site	exon	duplication/5'-5'	high	out-of-frame	CobW/HypB/UreG_nucleotide-binding_domain(53%)
MB6t	G4	KHDRBS2	KHDRBS2	-/-	-/-	6	61652255	6	61901371	exon/splice-site	CDS/splice-site	duplication	high	.	Tyrosine-rich_domain_of_Sam68(100%)
MB6t	G4	RNF144A	LINC02564	+/+	+/+	2	7030215	18	15617	CDS/splice-site	exon/splice-site	translocation	high	out-of-frame	IBR_domain_a_half_RING-finger_domain(100%)
MB6t	G4	PSD2	UBE2D2	+/+	+/+	5	139833791	5	139558822	CDS/splice-site	intron	duplication	high	out-of-frame	Sec7_domain(93%) Ubiquitin-conjugating_enzyme(100%)
MB6t	G4	PSD2	UBE2D2	+/+	+/+	5	139833791	5	139600372	CDS/splice-site	CDS/splice-site	duplication	high	in-frame	Sec7_domain(93%) Ubiquitin-conjugating_enzyme(95%)
MB8t	WNT	ENSG00000224481	LINC01731	+/+	-/-	1	148303555	1	148272035	intron	exon/splice-site	inversion	high	.	.
MB8t	WNT	LINC01138	LINC01731	-/+	-/-	1	148303555	1	148272035	intron	exon/splice-site	inversion/3'-3'	high	.	.
MB9t	WNT	ENSG00000214719	ATAD5	+/+	+/+	17	30610942	17	30876374	exon/splice-site	CDS/splice-site	deletion/read-through	high	.	ATPase_family_associated_with_various_cellular_activities(AAA)(3%)
MB9t	WNT	SMURF2P1	ATAD5	+/+	+/+	17	30610942	17	30876374	exon/splice-site	CDS/splice-site	deletion/read-through	high	.	ATPase_family_associated_with_various_cellular_activities(AAA)(3%)
MB10t	WNT	KDM6B	GPS2	+/-	-/-	17	7842112	17	7314597	intron	CDS/splice-site	deletion/3'-3'	high	.	G-protein_pathway_suppressor(90%)

MB10t	WNT	KDM6B	ENSG00000261915	+/-	-/-	17	7842112	17	7314597	intron	3'UTR/splice-site	deletion/3'-3'	high	.	.
MB11t	SHH	CDK5RAP1	SNTA1	-/-	-/-	20	33392142	20	33439026	CDS/splice-site	CDS/splice-site	duplication	high	in-frame	Uncharacterized_protein_family_UPF0004(78%) PDZ_domain(79%),PH_domain(100%)
MB12t	SHH	FAM20C	BET1L	+/+	-/-	7	208976	11	180404	CDS/splice-site	CDS/splice-site	translocation	high	out-of-frame	.
MB13t	SHH	ZMIZ1	NUTM2B	+/+	+/+	10	79139777	10	79706042	5'UTR/splice-site	CDS/splice-site	deletion	high	.	NUT_protein(100%)
MB13t	SHH	LINC01193	LINC02203	+/+	+/+	15	20973303	15	21651926	intron	5'UTR/splice-site	deletion	high	.	Olfactory_receptor(100%)
MB14t	G4	HGSNAT	BHMT	+/-	+/+	8	43180201	5	79130933	intron	CDS/splice-site	translocation/3'-3'	high	.	.
MB15t	SHH	FKBP4	PARP11	+/+	-/-	12	2800697	12	3816131	intron	intron	inversion	high	stop-codon	FKBP-type_peptidyl-prolyl_cis-trans_isomerase(100%),Tetratricopeptide_repeat(37%) Poly(ADP-ribose)_polymerase_catalytic_domain(80%)
MB15t	SHH	FKBP4	PARP11	+/+	-/-	12	2800577	12	3815053	CDS/splice-site	CDS/splice-site	inversion	high	out-of-frame	FKBP-type_peptidyl-prolyl_cis-trans_isomerase(100%),Tetratricopeptide_repeat(37%) Poly(ADP-ribose)_polymerase_catalytic_domain(80%)
MB15t	SHH	TSPAN9	CRACR2A	+/+	-/-	12	3201256	12	3713317	CDS/splice-site	5'UTR/splice-site	inversion	high	out-of-frame	Tetraspanin_family(5%) EF-hand_domain_pair(100%),Ras_family(100%)
MB15t	SHH	TSPAN9	CRACR2A	+/+	-/-	12	3201256	12	3733210	CDS/splice-site	5'UTR/splice-site	inversion	high	out-of-frame	Tetraspanin_family(5%) EF-hand_domain_pair(100%),Ras_family(100%)
MB15t	SHH	ATF7IP	PTPRO	+/+	+/+	12	14461133	12	15483974	CDS/splice-site	CDS/splice-site	deletion	high	out-of-frame	ATF-interacting_protein_binding_domain(100%) Fibronectin_type_III_domain(100%),Protein-tyrosine_phosphatase(100%)
MB15t	SHH	TEAD4	ENSG00000255608	+/+	+/+	12	3022017	12	4839297	CDS/splice-site	exon	deletion	high	.	TEA/ATTS_domain(100%),YAP_binding_domain(37%)
MB15t	SHH	TULP3	PRMT8	+/+	+/+	12	2922402	12	3419754	CDS/splice-site	intron	deletion	high	out-of-frame	Tubby_N-terminal(100%) Ribosomal_protein_L11_methyltransferase(PrmA)(100%)
MB15t	SHH	TIGAR	NBAS	+/+	-/+	12	4337160	2	15169293	CDS/splice-site	intron	translocation/5'-5'	high	out-of-frame	Histidine_phosphatase_superfamily_(branch_1)(43%)
MB15t	SHH	ENSG00000285901	NBAS	+/+	-/+	12	4337160	2	15169293	3'UTR/splice-site	intron	translocation/5'-5'	high	.	.
MB15t	SHH	GALNT8	CACNA1C	+/+	+/+	12	4814783	12	2512812	intron	CDS/splice-site	duplication	high	.	Glycosyl_transferase_family_2(100%),Ricin-type_beta-trefoil_lectin_domain(100%) Ion_transport_protein(73%),Voltage-dependent_L-type_calcium_channel_IQ-associated(100%),Voltage-gated_calcium_channel_subunit_alpha_C-term(100%),Voltage_gated_calcium_channel_IQ_domain(100%)
MB15t	SHH	GALNT8	CACNA1C	+/+	+/+	12	4814778	12	2512812	exon/splice-site	CDS/splice-site	duplication	high	.	Glycosyl_transferase_family_2(100%),Ricin-type_beta-trefoil_lectin_domain(100%) Ion_transport_protein(73%),Voltage-dependent_L-type_calcium_channel_IQ-associated(100%),Voltage-gated_calcium_channel_subunit_alpha_C-term(100%),Voltage_gated_calcium_channel_IQ_domain(100%)
MB15t	SHH	GALNT8	ENSG00000283138	+/+	+/+	12	4814778	12	3757397	exon/splice-site	exon/splice-site	duplication	high	.	Glycosyl_transferase_family_2(100%),Ricin-type_beta-trefoil_lectin_domain(100%)
MB15t	SHH	LINC01193	LINC02203	+/+	+/+	15	20973303	15	21616130	intron	5'UTR/splice-site	deletion	high	.	Olfactory_receptor(100%)
MB15t	SHH	CRACR2A	ENSG00000256988	-/-	-/-	12	3753015	12	4813646	5'UTR/splice-site	exon/splice-site	duplication	high	.	.
MB15t	G3	TMEM244	ARHGAP18	-/-	-/-	6	129861156	6	129642018	CDS/splice-site	CDS/splice-site	deletion/read-through	high	out-of-frame	RhoGAP_domain(100%)
MB15t	SHH	POU6F2	POU6F2-AS2	+/+	-/+	7	39086031	7	38986246	CDS/splice-site	intron	duplication/5'-5'	high	out-of-frame	.
MB15t	SHH	PDCD6IP1	TASP1	+/+	-/-	15	22744698	20	13623514	exon	CDS/splice-site	translocation	high	.	Asparaginase(90%)

MB15t	SHH	RDX	ENSG00000255028	-/-	-/-	11	110124059	11	109583643	3'UTR/splice-site	exon/splice-site	deletion	high	.	Ezrin/radixin/moesin_family_C_terminal(100%),FERM_C-terminal_PH-like_domain(100%),FERM_N-terminal_domain_(100%),FERM_central_domain(100%)
MB20t	SHH	STAG2	LINC01201	+/+	-/+	X	123961856	X	130982052	5'UTR/splice-site	intron	deletion/5'-5'	high	.	.
MB20t	SHH	STAG2	ARHGAP36	+/+	+/+	X	123961856	X	131081760	5'UTR/splice-site	CDS/splice-site	deletion	high	.	RhoGAP_domain(100%)
MB22t	G4	KHDRBS2	KHDRBS2	-/-	-/-	6	61652255	6	62047994	exon/splice-site	CDS/splice-site	duplication	high	.	KH_domain(80%),Tyrosine-rich_domain_of_Sam68(100%)
MB22t	G4	TBX3	DLGAP2	-/-	+/+	12	114679505	8	1258851	CDS/splice-site	CDS/splice-site	translocation	high	out-of-frame	T-box(91%) Guanylate-kinase-associated_protein_(GKAP)_protein(100%)
MB24t	SHH	ENSG00000287406	ENSG00000287372	+/-	-/-	1	90281622	1	90401127	exon	exon/splice-site	duplication/3'-3'	high	.	.
MB24t	SHH	MIR4300HG	ENSG00000287912	-/-	+/-	11	82099974	11	81252969	exon/splice-site	intron	deletion/5'-5'	high	.	.
MB25t	G4	GRM8	LINC-PINT	-/-	-/-	7	126902542	7	131108803	CDS/splice-site	exon/splice-site	duplication	high	out-of-frame	Receptor_family_ligand_binding_region(77%)
MB25t	G4	GRM8	ENSG00000285106	-/-	-/-	7	126902542	7	131108803	CDS/splice-site	exon/splice-site	duplication	high	out-of-frame	Receptor_family_ligand_binding_region(77%)
MB25t	G4	KANSL1	LRRC37A4P	-/-	-/-	17	46152904	17	45545676	exon/splice-site	exon/splice-site	deletion	high	.	.
MB26t	G4	RUNX1T1	HPYR1	-/-	-/+	8	92005116	8	132544809	CDS/splice-site	intron	inversion/5'-5'	high	out-of-frame	NHR1_homology_to_TAF(100%)
MB26t	G4	FOCAD	ENSG00000286685	+/+	+/+	9	20658826	9	19892719	5'UTR/splice-site	exon/splice-site	duplication	high	.	.
MB26t	G4	NSMCE2	ZEB2	+/+	-/+	8	125182256	2	144492065	CDS/splice-site	intron	translocation/5'-5'	high	out-of-frame	.
MB26t	G4	KANSL1	ENSG00000267246	-/-	-/-	17	46152904	17	45551537	exon/splice-site	exon/splice-site	deletion	high	.	.
MB28t	SHH	SH3BP2	CTNNA3	+/+	-/-	4	2820753	10	67219870	CDS/splice-site	CDS/splice-site	translocation	high	out-of-frame	PH_domain(17%) Vinculin_family(78%)
MB29t	G3	TMEM244	ARHGAP18	-/-	-/-	6	129861156	6	129642018	CDS/splice-site	CDS/splice-site	deletion/read-through	high	out-of-frame	RhoGAP_domain(100%)
MB6t	G4	SRCIN1	CISD3	-/-	+/+	17	38533519	17	38732535	intron	intron	inversion	medium	.	Actin_interacting_protein_3(100%) Iron-binding_zinc_finger_CDGSH_type(68%)
MB6t	G4	CISD3	CISD3	+/+	+/+	17	38732679	17	38731322	intron	CDS/splice-site	duplication	medium	.	Iron-binding_zinc_finger_CDGSH_type(31%) Iron-binding_zinc_finger_CDGSH_type(100%)
MB6t	G4	PIP5K1A	MINDY1	+/+	-/+	1	151221878	1	151002965	intron	5'UTR	duplication/5'-5'	medium	.	.
MB13t	SHH	RANBP17	CANX	+/+	+/+	5	170968377	5	179705679	CDS/splice-site	5'UTR/splice-site	deletion	medium	in-frame	Importin-beta_N-terminal_domain(100%) Calreticulin_family(100%)
MB21t	SHH	NRXN1	TRHR	-/-	-/+	2	50346691	8	109172681	CDS/splice-site	intergenic	translocation	high	out-of-frame	EGF-like_domain(100%),Laminin_G_domain(82%)
MB25t	G4	PCNX1	ATP6V0A4	+/+	-/+	14	71087046	7	138773767	intron	intron	translocation/5'-5'	medium	.	.
MB25t	G4	CLIP2	CADPS2	+/+	-/+	7	74397406	7	122696141	intron	intron	deletion/5'-5'	medium	.	CAP-Gly_domain(100%)

Supplementary Table IX. Final list of Arriba gene fusion calls in ATRT cell lines.

Legend: *ATRT ID*, ATRT sample ID; *class*, short classification; *str1/str2*, orientation of gene fusion on strand 1/2; *chr1/2*, chromosome nr.1/2 implicated in the fusion event; *loc1/2*, fusion breakpoint coordinates (GRCh38) implicated in the fusion event; *site1/2*, genomic regions affected by the fusion event; *type*, type of SV producing the fusion event; *conf*, confidence; *read_frame*, reading frame; *retained_protein_domains*, percentage of the annotated functional protein domain after fusion formation.

ATRT ID	class	gene1	gene2	str1	str2	chr1:loc1	chr2:loc2	site1	site2	type	conf	read_frame	retained_protein_domains
JC-ATRT	MYC	HHLA3	CTH	+/+	+/+	1:70368207	1:70415956	intron	CDS/splice-site	deletion/read-through	high	.	Cys/Met_metabolism_PLP-dependent_enzyme(89%)
JC-ATRT	MYC	HGD	GTF2E1	-/+	+/+	3:120675939	3:120750523	intron	5'UTR/splice-site	deletion/read-through/3'-3'	high	.	CTerminal_general_transcription_factor_TFII_E_alpha(100%),TFIIB_zinc-binding(100%),TFII_E_alpha_subunit(100%)
JC-ATRT	MYC	ENSG00000239482	SLC9C1	+/-	-/-	3:112314110	3:112286878	intron	5'UTR/splice-site	deletion/read-through/3'-3'	high	.	Cyclic_nucleotide-binding_domain(100%),Ion_transport_protein(100%),Sodium/hydrogen_exchanger_family(100%)
JC-ATRT	MYC	PPIL2	SMARCB1	+/+	+/+	22:21675115	22:23816770	CDS/splice-site	CDS/splice-site	deletion	high	in-frame	SNF5/_SMARCB1/_INI1(83%)
CHLA-266	MYC	ANAPC1	RMND5A	-/-	+/+	2:111821239	2:86740927	CDS/splice-site	CDS/splice-site	inversion	high	out-of-frame	Anaphase-promoting_complex_subunit_1_WD40_beta-propeller_domain(100%) CTLH/CRA_C-terminal_to_LisH_motif_domain(100%)
CHLA-266	MYC	NDST3	PRSS12	+/-	-/-	4:118251569	4:118298938	intron	CDS/splice-site	duplication/3'-3'	high	.	Scavenger_receptor_cysteine-rich_domain(14%),Trypsin(100%)
CHLA-266	MYC	KHDRBS2	KHDRBS2	-/-	-/-	6:61652255	6:62047994	exon/splice-site	CDS/splice-site	duplication	high	.	KH_domain(80%),Tyrosine-rich_domain_of_Sam68(100%)
CHLA-266	MYC	KHDRBS2	KHDRBS2	-/-	-/-	6:61652255	6:61901371	exon/splice-site	CDS/splice-site	duplication	high	.	Tyrosine-rich_domain_of_Sam68(100%)
CHLA-266	MYC	POU6F2	POU6F2	+/+	+/+	7:39086031	7:38986246	CDS/splice-site	intron	duplication	high	out-of-frame	Homeodomain(100%),Pou_domain_-_N-terminal_to_homeobox_domain(100%)
CHLA-266	MYC	POU6F2	POU6F2-AS2	+/+	-/+	7:39086031	7:38986246	CDS/splice-site	intron	duplication/5'-5'	high	out-of-frame	.
CHLA-266	MYC	AGAP14P	BMS1P1	+/+	+/+	10:46342940	10:46795806	exon/splice-site	exon/splice-site	deletion	high	.	.
CHLA-04	SHH	KCNMB2-AS1	ZMAT3	-/-	-/-	3:178859489	3:179004184	exon/splice-site	CDS/splice-site	duplication	high	.	.
CHLA-04	SHH	KCNMB2-AS1	ZMAT3	-/-	-/-	3:178801793	3:179004184	exon/splice-site	CDS/splice-site	duplication	high	.	.
CHLA-04	SHH	KCNMB2-AS1	ZMAT3	-/-	-/-	3:178749046	3:179004184	exon/splice-site	CDS/splice-site	duplication	high	.	.
CHLA-04	SHH	MUC20	ENSG00000286909	+/+	-/-	3:195729739	3:197650413	CDS/splice-site	exon/splice-site	inversion	high	out-of-frame	.
CHLA-04	SHH	NDST3	PRSS12	+/-	-/-	4:118251569	4:118298938	intron	CDS/splice-site	duplication/3'-3'	high	.	Scavenger_receptor_cysteine-rich_domain(14%),Trypsin(100%)
CHLA-05	SHH	DUX4L50	FAM242A	-/+	-/-	9:63817907	20:30324826	exon	exon/splice-site	translocation/3'-3'	high	.	.
CHLA-05	SHH	RGS6	ENSG00000266869	+/+	+/+	14:71964875	14:71908165	CDS/splice-site	exon/splice-site	duplication	high	out-of-frame	.
VU397	MYC	ITGAV	ZC3H15	+/+	+/+	2:186664641	2:186495233	CDS/splice-site	CDS/splice-site	duplication	high	in-frame	FG-GAP_repeat(100%),Integrin_alpha(50%) CCCH-type_zinc_finger(100%),DRG_Family_Regulatory_Proteins_Tma46(100%)
ATRT-310-FHTC	SHH	CASC17	ENSG00000271239	-/-	-/-	17:71185596	17:70779229	exon/splice-site	exon	deletion	high	.	.
ATRT13808	MYC	HGD	GTF2E1	-/+	+/+	3:120675939	3:120750523	intron	5'UTR/splice-site	deletion/read-through/3'-3'	high	.	CTerminal_general_transcription_factor_TFII_E_alpha(100%),TFIIB_zinc-binding(100%),TFII_E_alpha_subunit(100%)
ATRT13808	MYC	BBS9	RP9	+/+	-/+	7:33146364	7:33094839	CDS/splice-site	3'UTR	duplication/5'-5'	high	out-of-frame	PTHB1_N-terminus(8%)
ATRT13808	MYC	IGFL1P2	HIF3A	-/+	+/+	19:46260672	19:46303898	exon	CDS/splice-site	deletion/read-through/3'-3'	high	.	Hypoxia-inducible_factor-1(100%),PAS_fold(100%)

8.3 List of Figures

Figure 1. Most common tumors in childhood (< 18 years) of all cancer cases during the period of 2012–2021 in Germany.	3
Figure 2. Current standard clinical management scheme for medulloblastoma patients.	5
Figure 3. Overview of the MB WNT and MB SHH groups.	8
Figure 4. Overview of the complex spectrum of MB, non-WNT/non-SHH, Group 3/4.	11
Figure 5. Overview of ATRT molecular subtypes.	14
Figure 6. Three major mechanisms for SV formation in the human genome.	18
Figure 7. Classification of major SV subtypes in cancer genomes.	21
Figure 8. CNV profile of the MB cell line HD-MB03 calculated from 850k EPIC array data. ...	31
Figure 9. Bionano OGM workflow.	32
Figure 10. Mean UHMW gDNA concentrations according to sample types.	44
Figure 11. Post-run quality control parameters.	50
Figure 12. Illustration of the OGM data analysis workflow.	56
Figure 13. RVA-detected CNVs and SVs in the ATRT cell line JC-ARTT.	58
Figure 14. Absolute numbers of OGM RVA-detected SVs in MB (left column) and ATRT samples (right column).	60
Figure 15. Absolute numbers of rare SVs in MB (left column) and ATRT samples (right column).	64
Figure 16. OGM-detected copy number variants in 29 MB tumors.	68
Figure 17. Summary CNV profiles of MB samples derived from DNA methylation array data.	70
Figure 18. Summary genome heatmap of CNV profiles of MB samples as derived from DNA methylation array data.	74
Figure 19. Cumulative SV profiles detected by OGM in 29 MB tumors stratified according to the distinct MB groups and six MB cell lines.	81
Figure 20. Overview of SVs and selected genes in the MB SHH–child tumor MB15t.	82
Figure 21. Overview of SVs and selected genes in the MB Group 3 tumor MB4t.	84
Figure 22. Numbers of high-confidence SVs ≥ 4.5 kbp detected in MB tumor/peripheral blood DNA pairs of 18 patients.	86
Figure 23. Novel gene fusions in MB detected by OGM and RNA-Seq of the same tumors.	90
Figure 24. OGM-detected copy number variants in 15 ATRT samples, separated by ATRT subtype.	97
Figure 25. Summary CNV profiles of ATRT samples derived from DNA methylation array data.	98
Figure 26. Summary genome heatmap of CNV profiles of ATRT samples as derived from DNA methylation array data.	100

Figure 27. Cumulative SV profiles of 13 ATRT cell lines and two ATRT tumors separated according to the ATRT–MYC or ATRT–SHH subtype.....	103
Figure 28. Novel PPIL2::SMARCB1 gene fusion in the cell line JC-ATRT detected by OGM and RNA-Seq.....	106
Supplementary Figure I. Landscape of CNV alterations and SVs detected by OGM in 29 MB tumors, six MB cell lines, three ATRT tumors and 13 ATRT cell lines.....	158
Supplementary Figure II. Novel gene fusions in MB detected by OGM and RNA-Seq of the same tumors.	176
Supplementary Figure III. Expression levels of genes implicated in the MB-associated gene fusions depicted in Figure 23 and Suppl. Figure II across all MB cases and altered genes specifically addressed within the discussion.	178

8.4 List of Tables

Table 1. List of laboratory devices and equipment.....	24
Table 2. Software and packages.	25
Table 3. Overview of investigated ATRT and MB samples.	26
Table 4. Overview of ATRT and MB cell line models and their culture conditions.	28
Table 5. Overview of the different cell culture media (M) compositions.....	28
Table 6. List of cell culture media, supplements and consumables.....	29
Table 7. List of Bionano consumables used for extraction and labelling and of UHMW gDNA.	33
Table 8. List of items and consumables used for extraction and labelling and of UHMW gDNA.	33
Table 9. Assembled OGM data collection parameters for different SV analysis pipelines.	37
Table 10. List of items and consumables used for NGS library preparation.	41
Table 11. Summary and statistics of UHMW gDNA concentrations for each analysed sample.	45
Table 12. Summary of the OGM run and quality control metrics for all analysed samples.	52
Table 13. Summary of investigated MB cell lines and tumors as classified by EPIC 850k DNA methylation analysis and OGM-detected SVs, aneuploidies and subchromosomal CNVs.	75
Table 14. Gene fusions / translocations detected by OGM in the investigated MB and ATRT cohort of this study that affected potentially cancer-relevant genes and were validated by RNA-Seq based fusion callers.	94

Table 15. Summary of investigated ATRT cell lines and tumors as classified by EPIC 850k DNA methylation analysis and OGM-detected SVs, aneuploidies and subchromosomal CNVs.....	104
Table 16. SMARCB1 alterations in ATRT samples as detected by OGM and NGS.....	107
Table 17. Detailed comparison of five major technologies for detection of (epi-)genomic alterations.....	127
Supplementary Table I. Sample characteristics and Infinium™ MethylationEPIC v1.0 BeadChip-based ("850k EPIC") CNS tumor methylation classification of OGM analyzed MB and ATRT tumors and cell lines.....	185
Supplementary Table II. OGM-detected copy number alterations in ATRT and MB tumors and cell lines.	187
Supplementary Table III. Absolute numbers of OGM detected SVs in MB and ATRT tumors and cell lines.	204
Supplementary Table IV. Statistics of filtered SV numbers detected by OGM in ATRT and MB cell lines, and ATRT and MB tumors, total and separated by group/subtype.	206
Supplementary Table V. Statistics of rare SV numbers detected by OGM in ATRT and MB cell lines, and ATRT and MB tumors, total and separated by group/subtype.	206
Supplementary Table VI. Recurrently SV-affected region on chr2p16.3 in MB Group 3/4 tumors and MB cell lines.	207
Supplementary Table VII. OGM-called putative gene fusions in ATRT samples and MB tumors, and the corresponding RNA-Seq supported fusion transcripts as identified by Arriba.	207
Supplementary Table VIII. Final list of Arriba gene fusion calls in MB tumors.	214
Supplementary Table IX. Final list of Arriba gene fusion calls in ATRT cell lines.	217

Curriculum Vitae

Personal Data

Name: Nadezhda Kubon (geb. Bogodukhova)

Date and place of birth: 25 June, 1993 in Volzhsky

Education

03/2020 – present PhD student
Institute of Neuropathology, University Hospital Düsseldorf and
Heinrich-Heine University, Düsseldorf

Doctoral thesis: Detection and characterization of DNA structural variants in pediatric brain tumors using optical genome mapping. (AG Reifenberger)

10/2017 – 09/2019 M. Sc. Immunobiology
Life & Medical Sciences-Institute (LIMES),
Rheinische Friedrich-Wilhelms-University, Bonn

Master thesis: Development of a single-cell platform for personalized medicine with oligonucleotide-tagged antibodies. (AG Schultze)

10/2014 – 09/2017 B.Sc. Biology
Heinrich-Heine University, Düsseldorf

Bachelor thesis: Photopigment-based evaluation of phytoplankton diversity depending on trophic state and disturbance. (AG von Elert, Workgroup Aquatic Chemical Ecology, University of Cologne)

07/2013 Abitur
Gymnasium Koblenzer Straße, Düsseldorf

Publications and presentations

Publication included in this thesis

Kubon N, Bălan M, Koppstein D, Praeger S, Wolter M, Ebert P, Pauck D, Felsberg J, Beez T, Picard D, Remke M, Reifenberger G. *Detection of structural DNA variants in medulloblastomas using optical genome mapping*. *acta neuropathol commun* 14, 50 (2026). <https://doi.org/10.1186/s40478-026-02245-7>

Other publications

Pauck D, Picard D, Maue M, Taban K, Marquardt V, Blümel L, Bartl J, Qin N, Kubon N, Schöndorf D, Meyer F-D, Theruvath J, Mitra S, Hasselblatt M, Frühwald M C, Reifenberger G, Remke M. *An in vitro pharmacogenomic approach reveals subtype-specific therapeutic vulnerabilities in atypical teratoid/rhabdoid tumors (AT/RT)*. *Pharmacological Research*, Volume 213, 2025, 107660, ISSN 1043-6618, <https://doi.org/10.1016/j.phrs.2025.107660>.

Weller M, Felsberg J, Hentschel B, Gramatzki D, Kubon N, Wolter M, Roth P, Krex D, Herrlinger U, Westphal M, Tonn J-C, Regli L, Maurage C-A, von DeimLing A, Pietsch T, Le Rhun E, Reifenberger G. *Improved prognostic stratification of patients with isocitrate dehydrogenase-mutant astrocytoma*. *Acta Neuropathol* 147, 11 (2024). <https://doi.org/10.1007/s00401-023-02662-1>

Weller M, Felsberg J, Hentschel B, Gramatzki D, Kubon N, Wolter M, Roth P, Krex D, Herrlinger U, Westphal M, Tonn J-C, Regli L, Maurage C-A, von DeimLing A, Pietsch T, Le Rhun E, Reifenberger G. *PATH-19. PROGNOSTIC FACTORS, RESPONSE TO TREATMENT, AND OUTCOME OF PATIENTS WITH ISOCITRATE DEHYDROGENASE (IDH)-MUTANT ASTROCYTOMA, CNS WHO GRADE 4*. *Neuro-Oncology*, Volume 25, Issue Supplement_5, November 2023, Page v171, <https://doi.org/10.1093/neuonc/noad179.0649>

Presentations and poster

Detection of structural DNA variants in pediatric brain tumors using optical genome mapping (OGM). Bogodukhova N, Picard D, Knobbe-Thomsen C, Pauck D, Felsberg J, Remke M, Reifenberger G.

e-Poster, 20th International Congress of Neuropathology, 13.09-16.09.2023, Berlin, Germany

Poster, 6th Translational Oncology Symposium (ETOS), 16.02.2023, Essen, Germany

Poster, 24. Jahrestagung der Neurologischen Arbeitsgemeinschaft (NOA), 10.11.2022, Heidelberg, Germany

Molecular characterization of genomic structural variants in pediatric CNS tumors using optical genome mapping.

Talk, Retreat Düsseldorf School of Oncology, 24.05.2022, Düsseldorf, Germany.

Acknowledgements

First, I would like to thank my supervisor Prof. Dr. Guido Reifenberger for giving me the opportunity to work on this interesting project and for proofreading this thesis. I greatly appreciate your constructive feedback, and continuous support and guidance over the last years.

Furthermore, I would like to thank Prof. Dr. Gunnar Klau for evaluating my thesis as a second supervisor.

I would like to acknowledge Düsseldorf School of Oncology (DSO) and the Institute of Neuropathology, Heinrich Heine University, for funding this work.

Also, I would like to thank all of the members of the DSO research network on “Dissolving genetic structural variants underlying childhood malignancies using single molecule long range next generation sequencing and optical mapping techniques” for essential feedback and insightful discussions that helped shape the study. In particular, I would like to thank Prof. Dr. Arndt Borkhardt for coordination of the research network, Dr. Rabea Wagener for valuable discussions concerning analysis of optical genome mapping data and Danielle Brandes for methodological scientific exchange and fruitful discussions. Prof. Dr. Karl Köhrer and his team at the Genomics and Transcriptomics Laboratory of BMFZ, are greatly acknowledged for providing access to the Bionano Saphyr™ Instrument at the and support with its use.

Dr. Bärbel Überlacker, Zotz/Klimas MVZ Düsseldorf-Centrum GbR, is acknowledged for providing access to the Bionano Access Server for OGM data analysis.

I would like to thank Dr. Mirela Bălan and Dr. Peter Ebert at the Core Unit Bioinformatics (CUBI) for their valuable expertise and their help with bioinformatic data analysis. I would also like to thank Prof. Dr. Michael Weller, Prof. Dr. Mark Remke, Dr. David Koppstein and Dr. Daniel Picard for successful collaborations.

Furthermore, I would like to thank all current and former members of the Institute of Neuropathology for the friendly working environment, warm kitchen gatherings and great Christmas celebrations. In particular, I would like to thank Dr. Marietta Wolter and Dr. Kerstin Kaulich for their help during this project, for sharing their great scientific knowledge and for being always so supportive. Also, I would like to thank PD Dr. Jörg Felsberg and Dr. David Pauck for their constant scientific exchange and helpful discussions. My thanks further extend to all the members of the Molecular Diagnostics and Histopathology Laboratory for their technical assistance and camaraderie. Also, I would like to thank all members of AG Leprivier and AG Lim for welcoming me in their journal clubs and for all the friendly support throughout the years.

Finally, I would like to thank my dear friends and family for their invaluable emotional support. A big thank you goes out to my Heimatverein-family, who accompanied me throughout my entire career, from high school to my doctorate. Furthermore, thanks to Jill, Fabienne and Sebastian for being part of this journey, I am very grateful for your constant encouragement and help, and all the good times spent together. I would like to express my deepest gratitude to my parents, thank you for always believing in me and encouraging me, for your unlimited support and love. Especially, I would like to thank my husband Dennis, who always knew how to encourage and motivate me. Thank you for your endless understanding, your patience and for always being there for me throughout the years. Without all of you, this work would have not been possible.

Affirmation

Hereby, I declare on oath that I composed this dissertation independently by myself. I used only the references and resources indicated in this thesis. With the exception of such quotations, the work presented in this thesis is my own. I have accredited all the sources of help. This PhD thesis was never submitted or presented in a similar form to any other institution or examination board. I have not undertaken a doctoral examination without success so far.

Eidesstattliche Erklärung

Ich versichere an Eides Statt, dass die Dissertation von mir selbständig und ohne unzulässige fremde Hilfe unter Beachtung der „Grundsätze zur Sicherung guter wissenschaftlicher Praxis an der Heinrich-Heine-Universität Düsseldorf“ erstellt worden ist. Die Dissertation wurde in dieser oder ähnlicher Weise noch an keiner anderen Fakultät vorgelegt und es wurde kein vorheriger Promotionsversuch unternommen.

Nadezhda Kubon

Düsseldorf, November 2025